EG&G Idaho, Inc

FORM EG&G-398
(Rev. 11-79)

INTERIM REPORT

Accession No. _____

Report No. EGG-CDAP-5144

Contract Program or Project Title: Fuel Behavior Model Development

Subject of this Document: The Licensing Audit Calculation(LACE) Models in the FRAP-T4 Code - Description and Developmental Assessment

Type of Document: Interim Report

Author(s): M. P. Bohn, L. J. Siefken, E. T. Laats, G. P. Engelman, S. O. Peck

Date of Document: April 1980

Responsible NRC Individual and NRC Office or Division: G. P. Marino, NRC-RSR

This document was prepared primarily for preliminary or internal use. It has not received full review and approval. Since there may be substantive changes, this document should not be considered final.

EG&G Idaho, Inc.
Idaho Falls, Idaho 83415

Prepared for the
U.S. Nuclear Regulatory Commission
Washington, D.C.
Under DOE Contract No. DE-AC07-76ID01570
NRC FIN No. A6050

INTERIM REPORT

EGG-CDAP-5144
April 1980

THE LICENSING AUDIT CALCULATION EVALUATION (LACE) MODELS IN THE FRAP-T4 CODE

Description and Developmental Assessment

M. P. Bohn
L. J. Siefken
E. T. Laats
G. P. Engelman
S. O. Peck

EG&G Idaho, Inc.
Idaho Falls, ID U.S.A.

CONTENTS

FIGURES

TABLES

I. INTRODUCTION

The ability to accurately predict the performance of light water reactors (LWRs) under hypothesized accident conditions is a major objective of the reactor safety research program being conducted by the U.S. Nuclear Regulatory Commission (NRC). To achieve this objective, the NRC has sponsored an extensive program of analytical computer code development as well as both in-pile and out-of-pile experiments against which to benchmark and assess the analytical code capabilities. The computer code being developed for the prediction of the transient response of a single fuel rod under hypothesized accident conditions is the Fuel Rod Analysis Program - Transient (FRAP-T) code.

As part of this effort, the NRC is supporting the development of both best-estimate (BE) and evaluation model (EM) versions of the analytical computer codes. The best estimate code versions are designed to predict as accurately as possible the actual fuel rod response. By contrast, the evaluation model code versions are designed to provide a margin of conservatism in the code predictions. This conservatism is in accordance with Appendix K of Part 50, Volume 10 of the Code of Federal Regulations which is based on the philosophy that:

a) The initial stored energy or temperature in the fuel shall not be underestimated.

b) The consequences of a spectrum of design basis transients shall not be underestimated.

The evaluation models incorporated in FRAP-T4 and described in this report were developed by the NRC to meet the objectives outlined in Appendix K. The development of the evaluation model version of FRAP-T is intended to provide the NRC with an additional tool by which

reactor vendor fuel licensing calculations can be audited. Thus, this EM version of FRAP-T4 has been designated the Licensing Audit Calculation Evaluation Model version, or the LACE model version for short.

The LACE version of FRAP-T4 was constructed by adding a number of options which contain the prescribed evaluation models. For a full EM calculation, all the LACE options should be specified. The available LACE options are listed below:

Model	Option
CLADDING AXIAL THERMAL EXPANSION	3
CLADDING DIAMETRAL THERMAL EXPANSION	3
CLADDING SPECIFIC HEAT	4
CLADDING ELASTIC MODULUS	5
CLADDING POISSON'S RATIO	6
CLADDING THERMAL CONDUCTIVITY	7
FUEL SPECIFIC HEAT	8
FUEL ELASTIC MODULUS	9
FUEL EMISSIVITY	10
FUEL POISSON'S RATIO	11
FUEL THERMAL CONDUCTIVITY	12
FUEL THERMAL EXPANSION	13
CLADDING PLASTIC HOOP STRAIN	14
CLADDING SURFACE HEAT TRANSFER COEFFICIENT	15
GAS THERMAL CONDUCTIVITY	16
METAL-WATER REACTION	17
FUEL DEFORMATION	18

GAP CONDUCTANCE	19
OPERATING POWER * 1.02	20
ANS DECAY POWER * 1.2	21

These LACE models have been incorporated in the fourth released version of the FRAP-T code, which was then given the designation FRAP-T4-LACE. Both BE and EM models are incorporated in the same code, with the specification of models being made by the code user through the input.

This report presents detailed descriptions of all the LACE models, as well as results of checkout studies made with these models. Section II presents a description of each of the individual LACE options and where possible compares the LACE option with the corresponding best estimate model or correlation. Section III presents the results of an assessment of the LACE option package as incorporated in FRAP-T4. This assessment consisted of running the LACE version of FRAP-T4 for several hypothesized reactor transients and comparing the LACE code predictions to the best estimate code predictions. This provides a qualitative evaluation of the reasonableness of the LACE code predictions and verification that a reasonable degree of conservatism is present for the cladding temperature predictions for a typical hypothesized loss-of-coolant accident (LOCA).

Section IV compares the LACE code predictions for a typical LOCA with the best estimate code predictions performed using the Uncertainty Analysis Package also available in FRAP-T4. This package calculates the uncertainty bands (as a function of known uncertainties in the input variables) about the nominal BE code predictions by making use of multiple problem calculations and Response Surface Methodology. These comparisons permit an estimate of the degree of conservatism present in the LACE code predictions.

Finally, Section V presents conclusions and recommendations. Documentation of specific changes made in the LACE options from earlier versions is presented in Appendix A. Appendix B presents the results of checkout calculations made for the short core FLECHT reflood model. Appendix C presents the required input for the short core FLECHT model. Appendix D presents the results of LACE calculations of all the FRAP-T standard problems.

II. DESCRIPTION OF LACE MODELS

The LACE (Licensing Audit Code Evaluation) models as incorporated in FRAP-T4 were developed to analyze LOCA events according to guidelines set out in the WREM[1] document. Special LACE model options are available for

(a) Mechanical deformation and failure
(b) Thermal boundary conditions and initial conditions
(c) Material properties of fuel and cladding.

A description of the LACE options for each of the above items is presented in the following subsections. In each case, the LACE code models were examined in detail and hand checked for numerical coding accuracy. A number of minor coding errors present in early versions of the LACE option package were corrected. (These corrections are described in Appendix A.)

1. LACE DEFORMATION AND FAILURE OPTIONS

The LACE mechanical and failure subroutines are described in detail in Section 1.1. Several sample problems of a standard LOCA analysis were analyzed to check the accuracy of the programming of the models and to determine if the LACE mechanical and failure models are conservative per se. These sample problems are discussed in Section 1.2. The problems are followed by a discussion of the LACE models and certain limitations inherent in these models.

1.1 Description of LACE Mechanical and Failure Models

The LACE mechanical and failure models consist of the subroutines LACEDF, PRSINF and EMSTRN. LACEDF performs the fuel and cladding thermal expansion calculations, and also calculates the cladding stress and strain due to fission gas and coolant pressures.

Subroutine EMSTRN predicts cladding failure, plastic strain, and flow blockage at failure as a function of the fission gas and coolant pressure differential. Subroutine PRSINF calculates the interface pressure between the fuel and cladding if pellet-cladding mechanical interaction (PCMI) occurs.

1.1.1 LACEDF - Fuel Thermal Expansion Calculations. The LACEDF fuel expansion model is based on the GAPCON-THERMAL-1 fuel expansion model[2]. The radial expansion of the fuel is shown graphically in Figure 1. The solid curve represents the thermal expansion across the fuel calculated as if each point were a thin ring free to expand. Point A corresponds to the maximum free ring thermal expansion. The dashed curve from A to B represents the displacement at A plus the integral of radial thermal strain from A out to the fuel surface. Point B represents the radial displacement of the fuel surface. Equation 1 below calculates this displacement incrementally by dividing the fuel into fifty radial nodes. The term $(\Delta R_L)_{max}$ in Equation 1 corresponds to the displacement at point A and the summation corresponds to the integral of radial thermal strain from point A to the fuel surface.

$$\Delta R = (\Delta R_L)_{max} + \sum_{i=1}^{L} \Delta t_i \qquad (1)$$

where

ΔR = the increase in fuel pellet radius due to thermal expansion

Δt_i = $\alpha R_i (T_i - T_r)$

= increase in radius of radial increment i

$(\Delta R_L)_{max}$ = maximum ΔR_i (i.e., maximum free ring expansion)

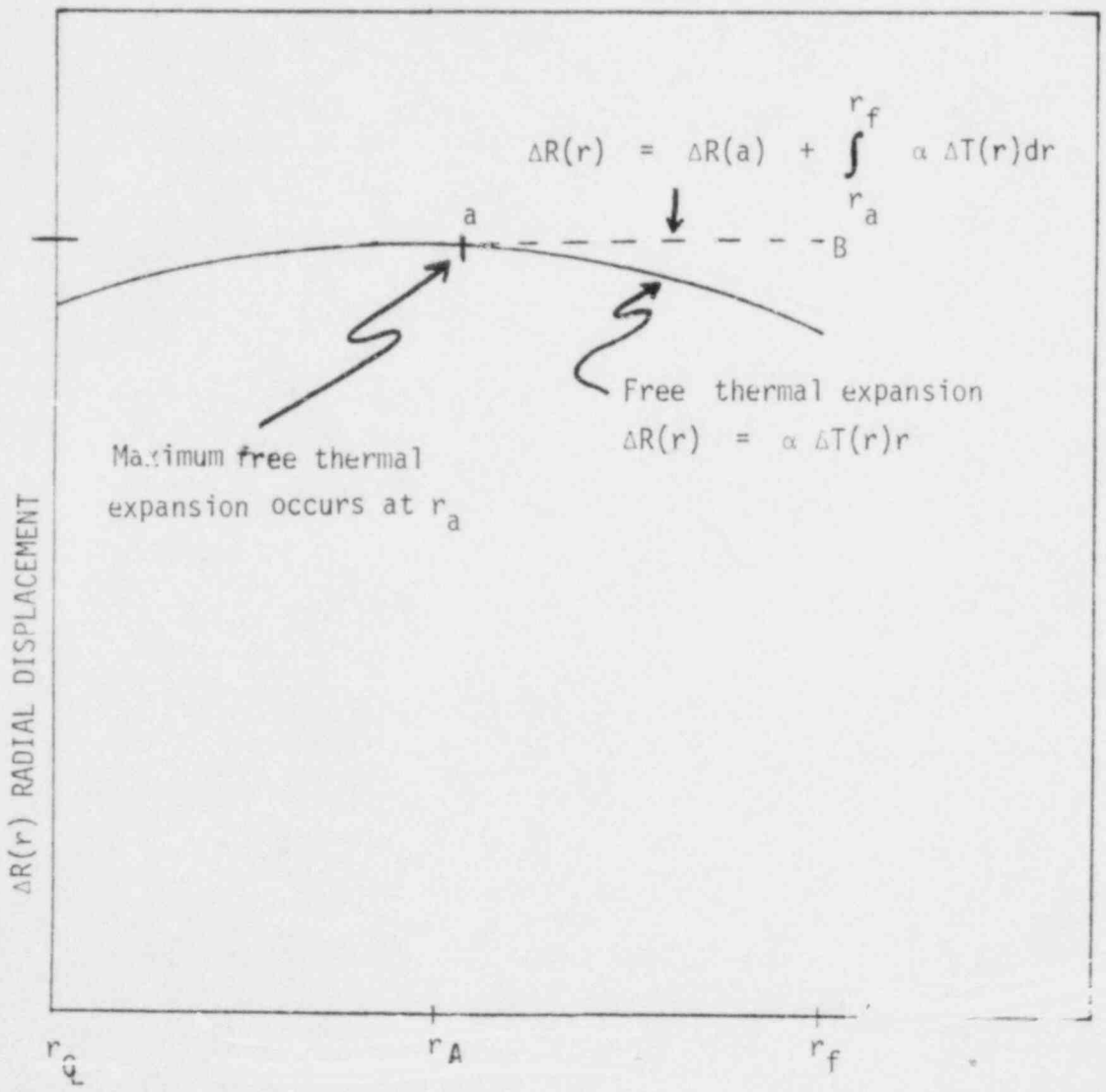

Fig. 1 GAPCON THERMAL-I fuel expansion model.

Δt_i = $\alpha t\ (T_i - T_r)$

= increase in thickness of radial increment i due to thermal expansion

R_i = average radius of radial increment i

T_i = average temperature of radial increment i

T_r = strain-free reference temperature

α = coefficient of thermal expansion

L = the index of the ring with the maximum thermal expansion (rings are numbered from the outer ring to the inner ring)

The contribution to ΔR due to swelling (obtained from a separate correlation) is also added into the fuel surface displacement calculation. The axial length change in the fuel due to thermal expansion is calculated using the temperature at the pellet shoulder.

1.1.2 LACEDF - Fuel Crack Volume Calculations. The volume of the radial cracks per unit length of fuel rod is computed by the equation

$$V_{cn} = 2\pi \sum_{n=1}^{L} \left((R_L)_{max} + \sum_{i=n}^{L} \Delta t_i \right) - \Delta R_n \qquad (2)$$

as described in the FRAP-T1[3] document where

V_{cn} = volume of radial cracks per unit length

$$\Delta R_n = \alpha R_n (T_n - T_r) \quad (3)$$

R_n = average radial increment radius

All other terms have been defined in the previous subsection. The rings are numbered from the surface inward as before.

1.1.3 LACEDF - Cladding Deformation Calculations. LACEDF calculates cladding thermal expansion and material properties from the average[a] cladding temperature. Cladding hoop stress and axial stress are calculated as for a thin cylinder using the equations:

$$\sigma_H = \frac{P_G R_i' - P_C R_o'}{(R_o' - R_i')} \quad (4)$$

$$\sigma_z = \frac{P_G (R_i')^2 - P_C (R_o')^2}{(R_o'^2 - R_i'^2)} \quad (5)$$

where

σ_H = hoop stress

σ_z = axial stress

P_G = fission gas pressure

P_C = coolant pressure

---

a. Cladding temperature is the average of all the cladding node temperatures.

R_i' = new inside cladding radius as calculated at the last calculation step.

R_o' = new outside cladding radius as calculated at the last calculation step.

The cladding strains are computed by the equations

$$\varepsilon_H = \frac{\sigma_H}{E(T)} - \nu(T) \frac{\sigma_Z}{E(T)} + \varepsilon_c + \varepsilon_p \quad (6)$$

$$\varepsilon_Z = \frac{\sigma_Z}{E(T)} - \nu(T) \frac{\sigma_H}{E(T)} \quad (7)$$

where

ε_H = hoop strain

ε_Z = axial strain

ε_p = plastic strain calculated in EMSTRN

$E(T)$ = temperature dependent Young's modulus

T = average cladding temperature

$\nu(T)$ = temperature-dependent Poisson's ratio

ε_c = creep strain (a quantity initialized from steady-state calculations).

The new cladding dimensions are calculated as

$$R_i' = R_m' - \frac{\Delta t}{2} \quad (8)$$

$$R_o' = R_m' + \frac{\Delta t}{2} \tag{9}$$

$$R_m' = \frac{R_i + R_o}{2} (1 + \varepsilon_H + \varepsilon_{TH}) \tag{10}$$

$$\Delta t = \frac{(R_o - R_i)(1 + \varepsilon_{TH})}{(1 + \varepsilon_H)} \quad . \quad \star \tag{11}$$

where

R_i' = new inside cladding radius

R_o' = new outside cladding radius

R_i = cold inside cladding radius

R_o = cold outside cladding radius

ε_{TH} = $\alpha(T)\ (T - T_r)$

= thermal strain

T_r = strain-free reference temperature.

If the deformation of the fuel and the cladding is such that PCMI has occurred, an interface pressure is calculated in subroutine PRSINF as described in Section 1.1.5. In addition, the new cladding coordinates are then calculated from

$$R_i' = R_p' \tag{12}$$

$$R_o' = R_p' + \Delta t \tag{13}$$

---

* See Appendix A for discussion of Equation 11.

where

R'_p = new fuel pellet radius.

1.1.4 LACEDF - Cladding Deformation After Failure. After failure has been predicted to occur the rod internal pressure is assumed to equal the coolant pressure and hence, there is no pressure-induced stress in the cladding. The LACEDF calculations of cladding deformation subsequent to failure utilize Equations 10 and 11 but with the following change. The hoop strain, ε_H, is now defined as

$$\varepsilon_H = \varepsilon_p/0.2 + \varepsilon_c$$

where ε_p is the plastic strain predicted at failure (by subroutine EMSTRN) and ε_c is the creep strain defined earlier. ε_p is multiplied by five because EMSTRN limits the plastic strain to one-fifth the strain at failure found in the Radial Expansion versus ΔP table. (This table is described in Section 1.1.6.)

1.5 Subroutine PRSINF

Subroutine PRSINF calculates the interface pressure due to pellet-cladding interaction. The interface pressure due to interference is calculated as

$$P_i = \frac{\frac{I\,E_c}{R'_i}}{\frac{R'^2_o + R'^2_i}{R'^2_o - R'^2_i} + \nu_c + \frac{E_c(1 - \nu_f)}{E_f}} \qquad (14)$$

where

I = cladding-fuel interference[a]

R_i' = new inside cladding radius

R_o' = new outside cladding radius

ν_f = volume averaged Poisson's ratio of the fuel

$$= \frac{2\pi \int_{r_i}^{r_f} \nu_f(T)\, r\, dr}{\pi r_f^2} \qquad (15)$$

r_f = fuel outside radius

r_i = fuel center radius (i.e., $r_i = 0$ for solid fuel pellets)

$\nu_f(T)$ = temperature dependent value of ν_f at radius r and at T(r)

$T(r)$ = temperature at radius r

ν_c = volume averaged Poisson's ratio of the cladding (calculated similarly to ν_f calculation in Equation 15)

E_f = volume averaged Young's Modulus of the fuel (calculated similarly to ν_f in Equation 15)

---

a. The cladding-fuel interference I is calculated as the overlap between the new fuel radius and the new cladding inside radius, i.e., $I = R'_{fuel} - R'_i$.

E_c = volume averaged Young's Modulus of the cladding (calculated similarly to v_f in Equation 15).

Since the P_i calculation uses the deformed radial coordinates the total interface pressure must also include the contribution from the fission gas pressure so that

$$P = \text{total interface pressure}$$

$$= P_{gas} + P_i \quad * \qquad (16)$$

where

P_{gas} = fission gas pressure

P_i = interface pressure due to interference calculated above.

If the calculated total interface pressure would cause the cladding stress to exceed the yield stress, then the interface pressure is set equal to the pressure required for the cladding stress to equal the yield stress.

1.1.6 Subroutine EMSTRN. Subroutine EMSTRN computes cladding failure, plastic deformation and flow blockage by comparing the cladding pressure differential against tabulated data of cladding failure behavior data. The data are supplied by the user in the form of three tables:

(a) Rupture Temperature versus ΔP
(b) Radial Expansion versus ΔP (Single Rod Data)
(c) Assembly Average Flow Blockage versus ΔP (Multiple Rod Data).

---

* See Appendix A for discussion of Equation 16.

Sample tables are shown in Tables 1, 2, and 3. A description of these tables and how they are to be applied is given in the WREM document. They are utilized in FRAP-T4-LACE as described below.

The prediction of plastic deformation and flow blockage depends upon the pressure differential ΔP across the cladding, where

$$\Delta P = P_{gas} - P_{cool}.$$

The EMSTRN subroutine calculates failure and plastic strains only if the rod internal gas pressure is greater than the coolant pressure, that is, $\Delta P > 0$. If ΔP is greater than zero, the EMSTRN subroutine determines the rupture temperature (T_{rupt}) corresponding to the ΔP value. This rupture temperature is calculated by interpolation from the user input table of Rupture Temperature versus ΔP. EMSTRN defines the differential in rupture temperature and cladding temperature as

$$\Delta T = T_{rupt} - T_{clad}$$

The plastic strain and flow blockage predictions are then calculated for the following three possible cases:

(a) $\Delta T > 200^{o}F$.

For this case there is no plastic strain or flow blockage. Failure is not predicted.

(b) $0 < \Delta T \leq 200^{o}F$.

A value of plastic hoop strain is calculated as

$$\epsilon_p = \frac{F \exp(-0.0153\Delta T)}{5} \qquad (19)$$

TABLE 1
RUPTURE TEMPERATURE VERSUS ΔP

Pressure Difference Across Cladding (psia)	Average Rupture Temperature(°F)
0	2500
100	2200
200	1820
400	1730
600	1660
800	1600
1000	1540
1200	1480
1400	1440
1600	1400
1800	1370
2000	1335
2200	1310
2400	1280

TABLE 2
RADIAL EXPANSION VERSUS ΔP

Pressure Difference Across Cladding (psia)	Best Estimate Radial Expansion (%)
0	60
100	60
200	32
400	25
600	35
800	46
1000	54
1200	60
1400	62
1600	60
1800	56
2000	48
2200	38
2400	30

TABLE 3
ASSEMBLY AVERAGE FLOW BLOCKAGE VERSUS ΔP

Pressure Difference Across Cladding (psia)	Maximum Assembly Average Flow Blockage (%)
0	80
100	80
200	60
400	30
600	35
800	55
1000	70
1200	78
1400	77
1600	73
1800	67
2000	57
2200	52
2400	30

where F is the value of failure strain corresponding to ΔP interpolated from the Radial Expansion versus ΔP table. There is no blockage in this case and failure has not occurred.*

(c) First timestep when $\Delta T \leq 0$.

Failure is predicted and the total plastic hoop strain is defined as

$$\varepsilon_p = F/5. \tag{20}$$

The flow blockage is predicted and calculated by interpolation from the Assembly Average Flow Blockage versus ΔP table.

(d) All timesteps after failure.

After the first timestep at which failure is predicted, the plastic strain is set equal to the experimental failure strain, i.e., $\varepsilon_p = F$.

1.2 Comparison of LACE and BE Mechanical Models

In order to compare the performance of the LACE mechanical models against the better understood best-estimate mechanical models, a hypothesized LOCA problem was analyzed exchanging the LACE mechanics model with the BE mechanics model. In each case, all other LACE options were utilized. (The reader should carefully note that the comparision is not between a BE FRAP calculation and an EM calculation, but rather a comparison between two mechanical models.) The only change involved was the substitution of the best estimate

---

* See Appendix A for further discussion of the EMSTRN calculations.

FRACAS-I cladding analysis model and MATPRO[4] failure analysis models in place of the LACEDF cladding and EMSTRN failure models. This comparison checked the cladding deformation calculations against a separate analysis and compared the LACE failure predictions with the MATPRO failure predictions. The MATPRO failure predictions utilize a similar data base but determine failure by comparing the analytical strain predictions to experimental data for strain to failure. An evaluation of the results is detailed below.

1.2.1 Description of the Comparison Problem and Failure Criteria. The sample problem used for this comparison is the hypothesized Zion PWR LOCA standard problem described in Appendix D. The main parameters for this problem are listed in Table 4. The rod average power, however, was increased to 13.02 kW/ft to force cladding failure. The flow chart in Figure 2 shows a comparison of the two paths for the failure analysis. The significant difference lies in determination of plastic strains and in the criteria of failure as will be seen below.

The LACE-EMSTRN calculations were described in Sections 1.1.4 - 1.1.6. The input tables used in this comparison problem for plastic strain, failure and blockage are shown in Tables 1, 2 and 3 and are taken from the WREM document. By cross-plotting total circumferential strain at failure versus temperature at failure from Tables 1 and 2 in Figures 3 and 4, we can compare this failure data to both the MATPRO failure strain model (CSRUPT) and a second set of cladding failure strain data which includes the Hardy[5] data. It should be noted, however, that the EMSTRN calculation does not base failure on the total strain calculation but strictly on temperature and pressure differential. Figure 3 shows the similarities in the two data sets. No assumptions can be made as to inherent conservatisms because the two failure criteria are totally different. Figure 4 is included primarily to show that the WREM data is not Hardy's data as has been often implied.

TABLE 4
DESCRIPTION OF ZION PWR LOCA PARAMETERS

Characteristic	Value
Fuel Pellet Radius (in.)	0.1829
Gas Gap (in.)	0.0043
Cladding Inside Radius (in.)	0.1872
Cladding Outside Radius (in.)	0.211
Fuel Density (%TD)	94.6
Cladding Cold Work (%)	10
Burnup (MW-s/kg)	0
Active Fuel Stack Length (ft)	12
Fill Gas	He
Fill Pressure (psia)	3.75
Plenum Volume ($in.^3$)	0.78
Coolant Conditions	PWR Double-Ended Cold Leg Break

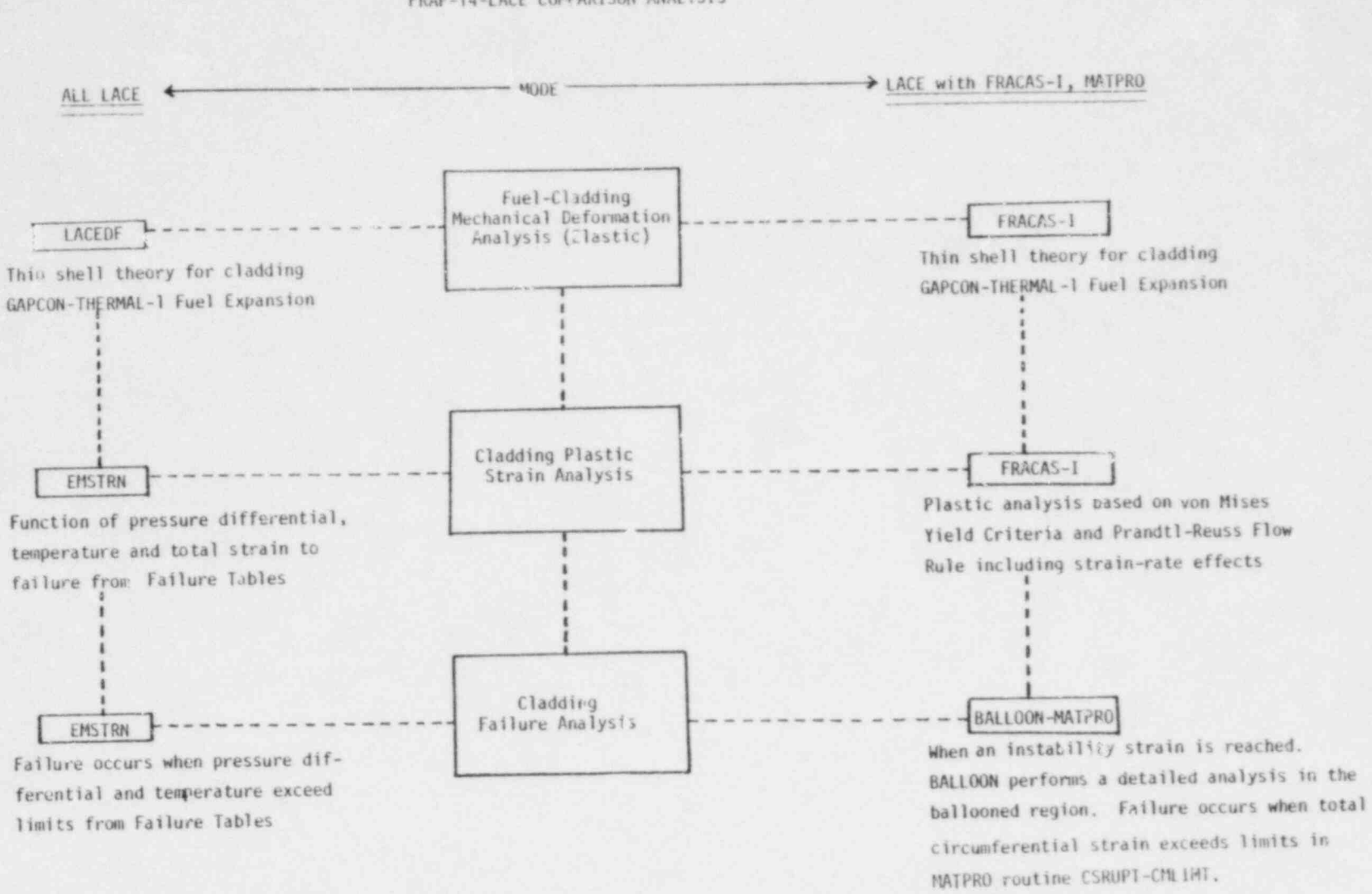

Fig. 2 FRAP-T4-LACE mechanics comparisons.

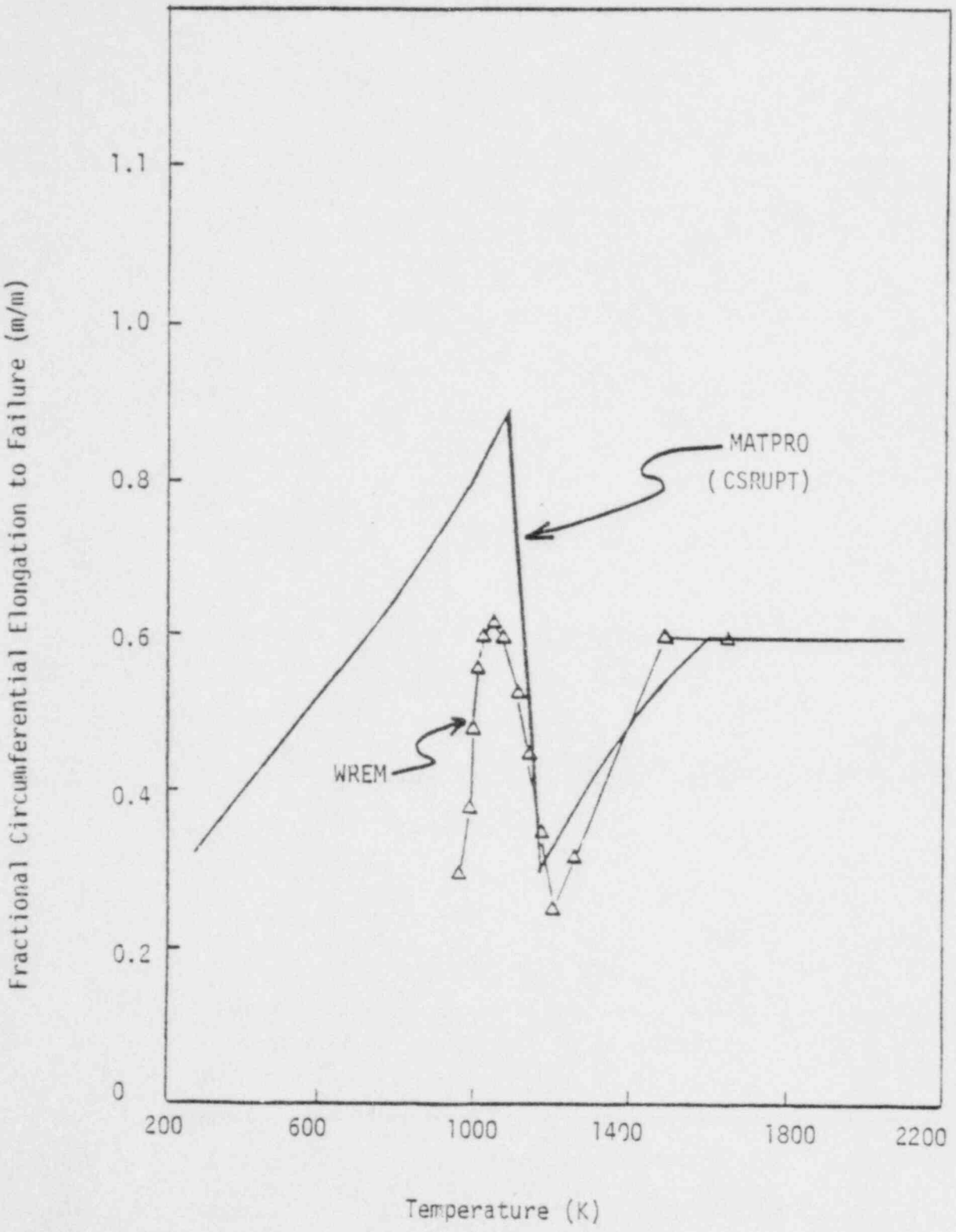

Fig. 3 Cladding strain to failure comparison.

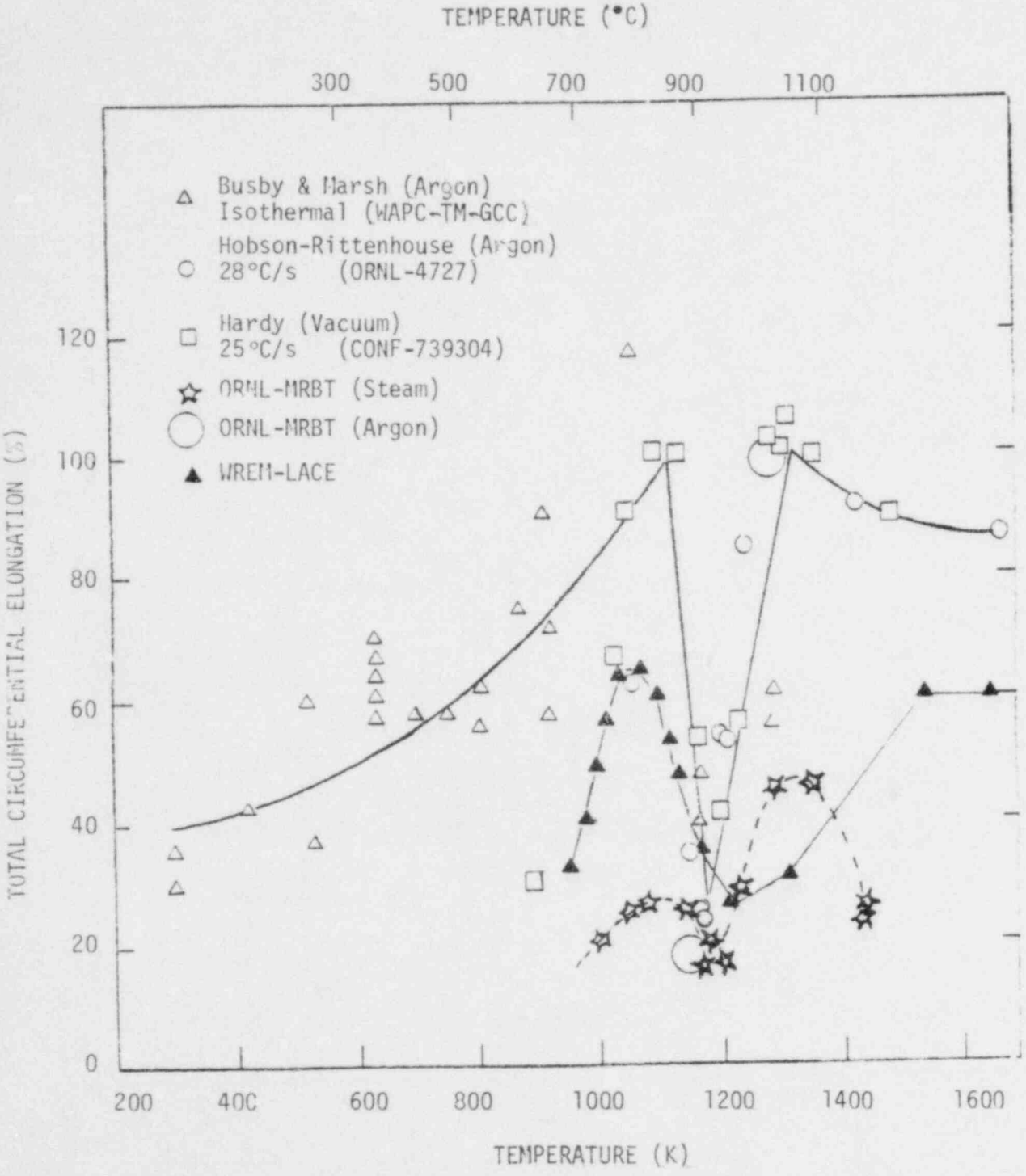

Fig. 4 Total circumferential elongation (TCE) as a function of burst temperature.

The FRACAS-I mechanical model substituted for the LACEDF model is very similar to the LACEDF model for fuel expansion and cladding elastic behavior. However, FRACAS-I calculates cladding plastic strains using multi-axial plasticity theory with the von Mises yield criteria, the Prandtl-Reuss flow rule and strain-rate effects. Once an instability strain (obtained from MATPRO) is reached, ballooning is predicted to occur and a more detailed (large deformation) analysis in the ballooned region is made by the subcode BALLOON. Failure is predicted in the ballooned region when the total cladding strain exceeds the rupture strain from MATPRO subroutine CSRUPT (see Figure 3).

1.2.2 Results. The most significant result of this comparison is that the FRACAS-I model predicts failure well before the LACEDF model, at 16 s as opposed to 35 s.

In this case one might expect that the cladding temperature calculations would also be different. However, from Figure 5 temperature predictions are seen to be almost identical. In fact, when FRACAS-I predicts failure at 14 to 15 s, the cladding temperatures are slightly higher in the LACE prediction. The plots of ΔP (pressure differential across the cladding) for the comparison problem are shown in Figure 6. Until 11 s the two predictions are very close although ΔP for the LACE calculation is always higher. At about 11 s the two predictions diverge. The FRACAS-I model predicts larger plastic hoop strains, and a lowering of the rod internal pressure. Figure 7 shows the two predictions of total hoop strain and time to failure. The LACE prediction of plastic strains remains well below the FRACAS-I prediction until 32 s. It should be noted that the large increase in the LACE prediction of hoop strain after failure occurs because the plastic strain is set to the total strain at failure calculated from the failure table.

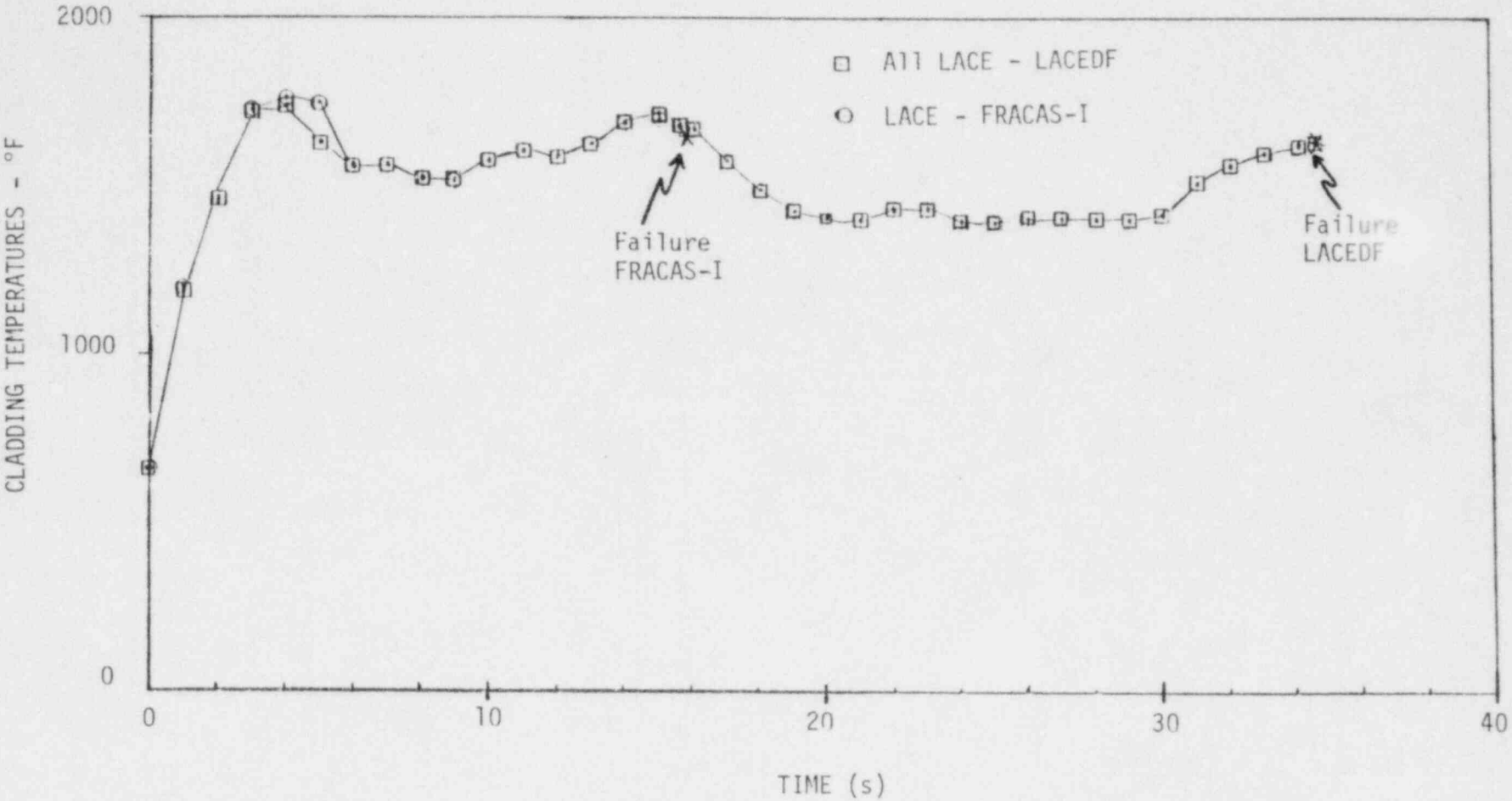

Fig. 5 LACE mechanical comparison problem - cladding temperature.

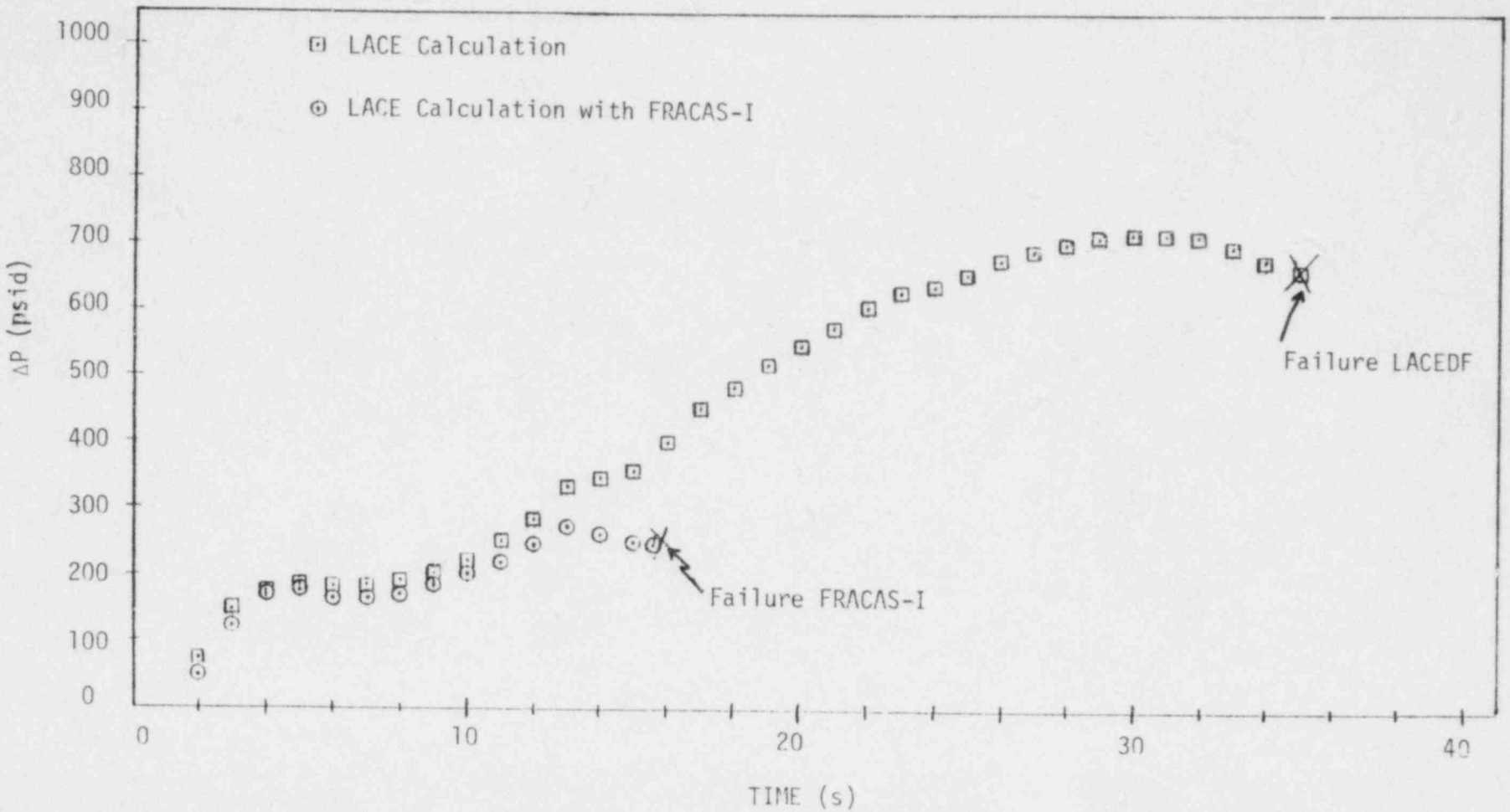

Fig. 6 LACE mechanical comparison problem - pressure differential.

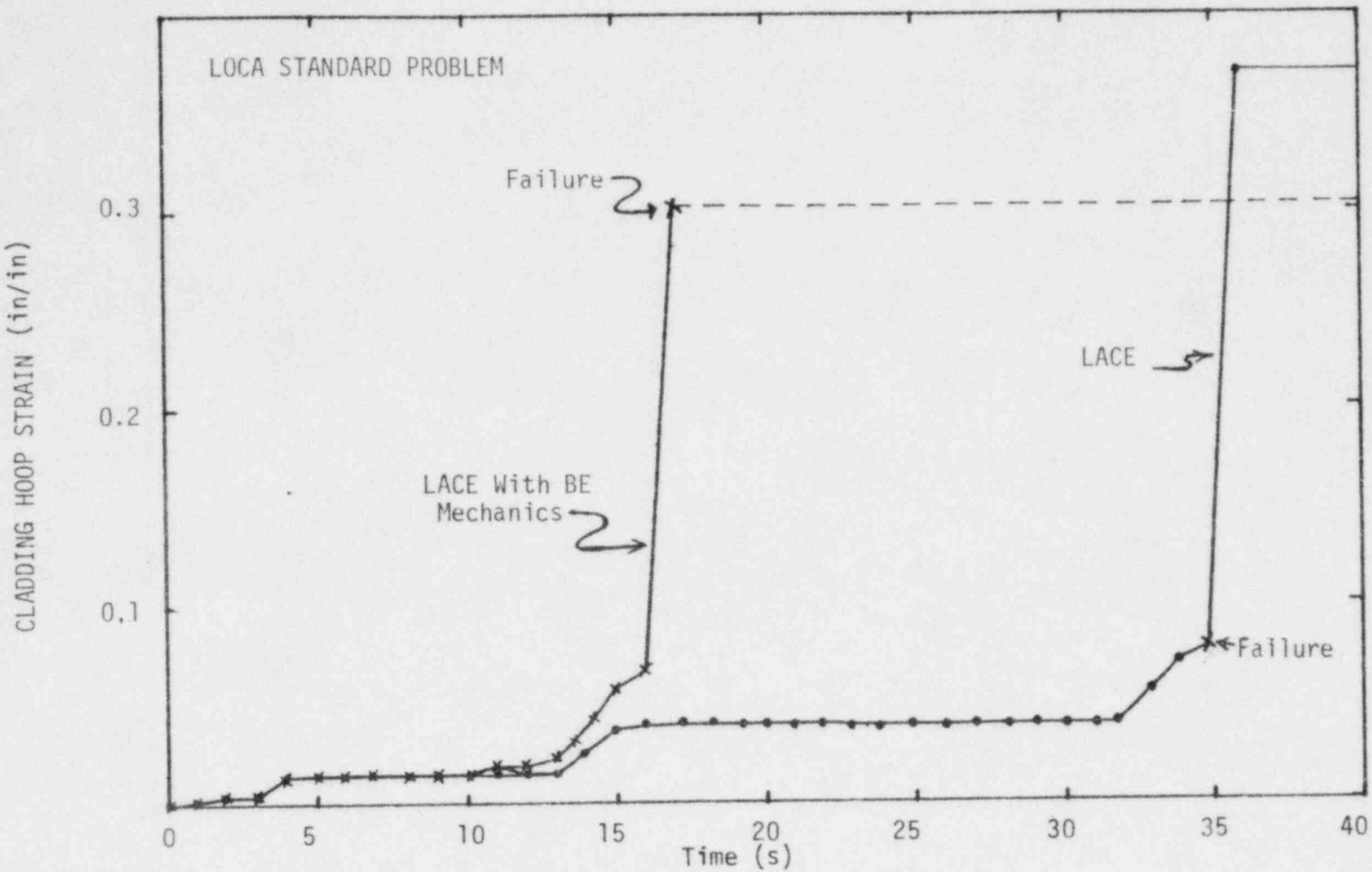

Fig. 7 LACE mechanics comparison problem.

The important point of this comparison is that while the EMSTRN prediction of plastic strain may assure higher cladding temperature and higher pressure differential across the cladding, the EMSTRN criteria for failure per se may not be as conservative as thought.

The user should note that the LACEDF model has a limited ability to analyze cladding plastic behavior and cladding behavior during PCMI. The model does not analyze cladding collapse. For these reasons the model should be limited to analysis of LOCA events.

2. THERMAL INITIAL AND BOUNDARY CONDITIONS

In making the calculations for the temperature distribution in the fuel and the cladding, LACE options are applied to the following:

(a) Operating power prior to transient
(b) Fission product decay heat
(c) Convective heat transfer and CHF correlations
(d) Reflood heat transfer correlations.

These LACE options are described in the following subsections.

2.1 Operating Power Option

As stated in 10 CFR 50 Appendix K, "it shall be assumed that the reactor has been operating continuously at a power level at least 1.02 times the licensed power level" when determining the heat sources during a LOCA. FRAP-T4-LACE accommodates this requirement through option 20, "operating power x 1.02," which increases the input operating power history by 2%.

The influence of this 2% power conservatism upon fuel temperatures and stored energy was examined for a hypothetical LOCA blowdown. This problem was the standard Zion LOCA problem (see

Table 4) with an initial power of 9.11 kW/ft. The effective conductivity and relocation model options were used in these calculations. Two predictions of this blowdown transient were performed. In one, all models were BE. In the second, the same BE models were used except that the power history was increased by 2% (option 20). Results obtained from comparison of these two runs indicated that fuel centerline temperature is increased 1 to 3%, cladding surface temperature is increased 0 to 1%, and stored energy is increased about 1% during the blowdown when option 20 is used.

2.2 Fission Product Decay Heat Option

The best estimate decay heat model used in FRAP-T4 is the proposed ANS 1971 Standard.[6] When LACE option 21 is activated, the decay heat power is obtained from the ANS model for infinite reactor operating time, and is multiplied by 1.2. This procedure is in accordance with 10 CFR 50 Appendix K requirements. The procedure is conservative with respect to the Appendix K requirements, which permit the multiplication factor on decay heat to be less than 1.2 for about the first 50 s following reactor scram.

The same typical blowdown problem of Section 2.1 was analyzed, again with and without the fission product decay heat option (option 21) but with all other models being best estimate. Results from those two runs were compared, and the fuel centerline temperature was found to increase by 1 to 2% during the blowdown when the conservative model was used. Similar increases were noted for the stored energy and cladding surface temperature histories.

2.3 Heat Transfer and Critical Heat Flux Correlations

FRAP-T4-LACE has at least one heat transfer correlation for each convection mode of heat transfer. The various modes of convection heat transfer are illustrated in Figure 8. The appropriate mode of

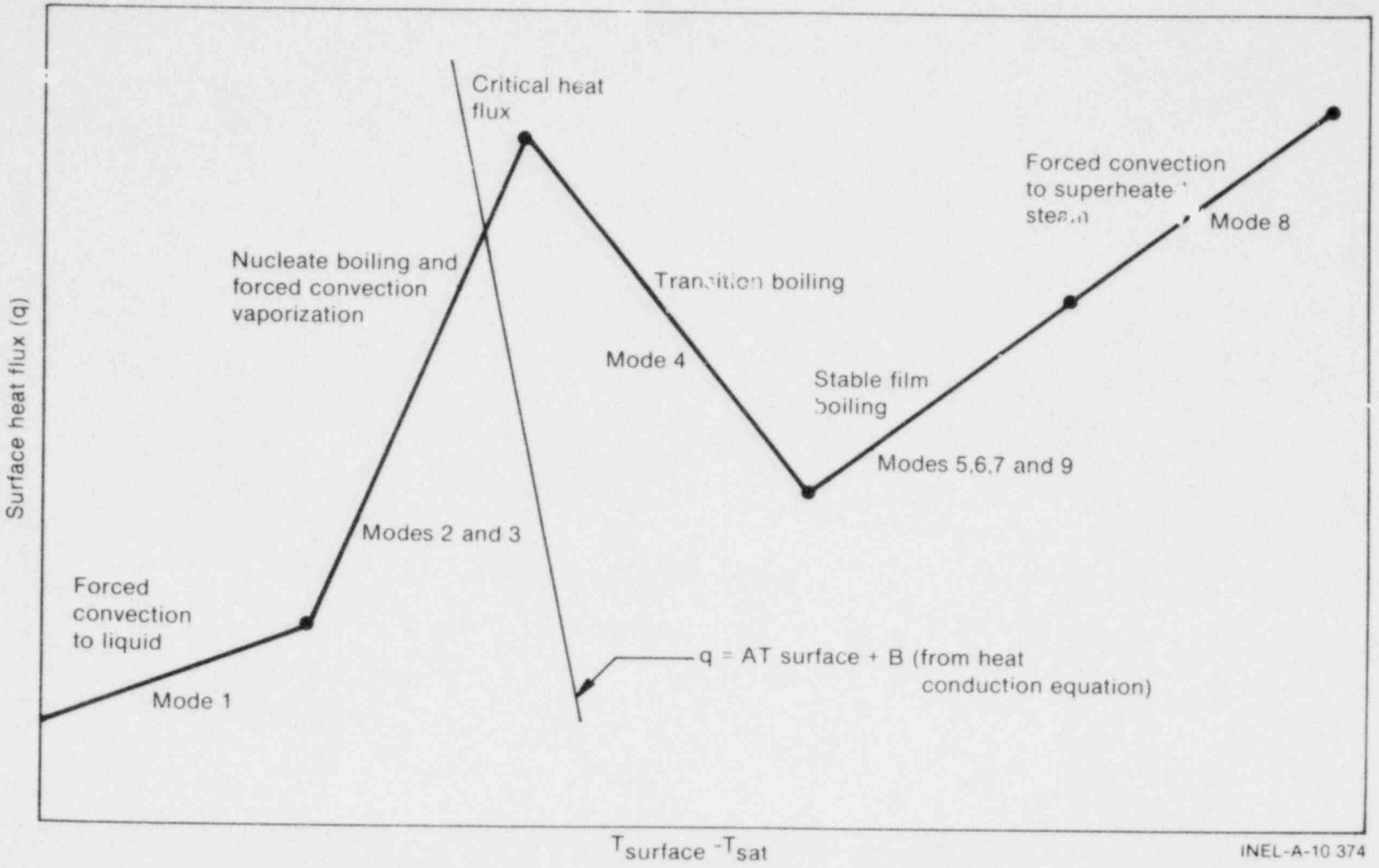

Fig. 8 Heat transfer modes considered in FRAP-T.

heat transfer is determined by the code. As shown in Figure 8, a key quantity in the determination of the mode of heat transfer is the critical heat flux. Several correlations for critical heat flux are contained in the code.

The appropriate convection mode of heat transfer at a given point on the surface of a fuel rod is determined by comparing the heat fluxes given by each applicable mode of heat transfer. The coolant void fraction, mass flux, and pressure are the factors used to determine the applicability of each heat transfer mode. The scheme used to determine the heat transfer mode is outlined in Table 5, which is taken from RELAP4.[7] The scheme of Table 5 is programmed in subroutine HTRC.

The heat transfer and critical heat flux correlations in FRAP-T4-LACE include the correlations specified in 10 CFR 50 Appendix K.

The available correlations for each heat transfer mode are listed in Table 5 and are described in detail in Table 6. The symbols used in Table 6 are defined in Table 7.

The following critical heat flux correlations are available:

(1) Modified Barnett[8]

(2) Barnett[9]

(3) B&W-2 (Gellerstadt)[10]

(4) W-3[11]

(5) LOFT[12]

(6) General Electric[13]

TABLE 5

HEAT TRANSFER MODE SELECTION AND CORRELATIONS

	Heat Transfer Mode	Range[a]	Heat Transfer Correlation[b]
1.	Forced convection to liquid	$T_w < T_{sat}$ or $Q_2 < Q_1 < Q_{crit}$	Dittus-Boelter[16]
2.	Nucleate boiling	$Q_1 < Q_2 < Q_{crit}$; $T_w > T_{sat}$; $\alpha < 0.9$	Thom[17]
3.	Forced convection vaporization	$Q < Q_{crit}$; $\alpha > 0.9$	Shrock-Grossman[18]
4.	Flow transition boiling	Q_2 or $Q_3 > Q_{crit}$; $Q_4 > Q_5$; $G > 200,000$; $P > 500$ or $Q_4 < Q_6$	McDonough, Milich, and King[19]
5.	Flow film boiling	Q_2 or $Q_3 > Q_{crit}$; $Q_5 > Q_4$ $G > 200,000$ or $Q_5 > Q_6$ ($\alpha \leq 0.6$) or Q_7 ($\alpha > 0.6$)	Groeneveld[20]
6.	Pool film boiling	Q_2 or $Q_3 > Q_{crit}$; $G < 200,000$ $Q_6 > Q_5$; $\alpha \leq 0.3$	Modified Bromley[21]
7.	Free convection	Q_2 or $Q_3 > Q_{crit}$; $G < 200,000$ and $Q_7 > Q_5$; $\alpha > 0.3$	Free convection[21] + radiation
8.	Forced convection to gas	$X \geq 1$	Dittus-Boelter[16]
9.	Low pressure film boiling[c]	$P < 500$ and range of mode 5	Dougall-Ronsenow[22]
10.	Reflood	$t \geq t_R$	FLECHT[23]

a The symbols used are:

Q_i	= surface heat flux for i-th heat transfer mode	α	= coolant void fraction
Q_{crit}	= critical heat flux	X	= coolant quality
T_w	= cladding surface temperature	G	= mass flux (lbm/hr-ft^2)
T_{sat}	= saturation temperature of coolant	P	= coolant pressure (psia)
		t	= time (s)
		t_R	= time of initiation of core reflooding (s)

b For each heat transfer mode shown, only one of the listed correlations next to the parameter limits describing the range of the heat transfer mode is used. The correlation to be used is specified on the card input.

c If a flow film boiling correlation other than Groeneveld is specified, mode 9 is not considered.

TABLE 6

HEAT TRANSFER CORRELATIONS[a]

Mode 1 Subcooled Liquid Forced Convection: Ditt:.s and Boelter[16]

$$h = 0.023 \frac{K}{D_e} Pr^{0.4} Re^{0.8}$$

Mode 2 Nucleate Boiling: Thom[17]

$$q = \left[\frac{T_{sat} \exp (P/1,260)}{0.072} \right]^2$$

Mode 3 Forced Convection Vaporization: Schrock and Grossman[18]

$$h = (2.5)\ (0.023)\ \frac{K_f}{D_e} Pr_f^{0.4} \left[Re_f\ (1-X) \right]^{0.8}$$

$$\left[\left(\frac{X}{1 - X} \right)^{0.9} \left(\frac{\mu_g}{\mu_f} \right)^{0.1} \left(\frac{\rho_f}{\rho_g} \right)^{0.5} \right]^{0.75}$$

Mode 4 Transition Boiling: McDonough, Milich, and King[19]

$$q = q_{CHF} - C(P)\ (T_w - T_{w,CHF})$$

Pressure, psi	C(P)
2,000	979.2
1,200	1,180.8
800	1,501.2

where $T_{w,CHF} = T_{sat} + 0.072 \exp (-P/1260)\ (qCHF)^{0.5}$

Mode 5 Stable Film Boiling: Groeneveld[20]

$$h = a \frac{k_g}{D_e} Pr_w^c \left\{ Re_g \left[X + \frac{\rho_g}{\rho_f}\ (1-X) \right] \right\}^b$$

$$\left[1.0 - 0.1\ (1-X)^{0.4}\ \left(\frac{\rho_f}{\rho_g} - 1 \right)^{0.4} \right]^d$$

TABLE 6 (Continued)

Mode 5 Stable Film Boiling (continued)

	Groeneveld Equation (5.9) (cluster geometry)	Groeneveld Equation (5.7) (annular geometry)
a.	0.00327	0.052
b.	0.901	0.688
c.	1.32	1.26
d.	-1.50	-1.06

Mode Low Flow Film Boiling: Modified Bromley[21]

$$h = 0.62\left[\frac{k_g^3 h_{fg} \rho_g g(\rho_f - \rho_g)}{\mu_g L \Delta T_{sat}}\right]^{0.25}$$

$$L = 2\pi\left[\frac{g_c \sigma}{g(\rho_f - \rho_g)}\right]^{0.5}$$

Mode 7 Free Convection plus Radiation[21]

$$h = h_c + h_r$$

$$h_c = 0.4\,(Gr\ Pr_f)^{0.2}$$

$$Gr = \frac{L_g^3 \beta_g \rho_g^2 \Delta T_{sat}}{\mu_g^2}$$

TABLE 6 (Continued)

Mode 7 Free Convection Plus Radiation (continued)

$$L = \frac{D_e}{2}$$

$$h_r = 0.23 \frac{1.714(10^{-9}) \quad (T_w^4 - T_{sat}^4)}{\Delta T_{sat}}$$

Mode 8 Superheated Vapor Forced Convection: Dittus and Boelter[16]

$$h = 0.023 \frac{k}{D_e} Pr^{0.4} Re^{0.8}$$

Mode 9 Low Pressure Flow Film Boiling: Dougall and Rohsenow[22]

$$h = 0.023 \frac{K_g}{D_e} Pr_g^{0.4} \left\{ Re_g \left[X + \frac{\rho_g}{\rho_f} (1-X) \right] \right\}^{0.8}$$

a. Notation definitions follow in the next table.

TABLE 7

SYMBOL DEFINITIONS FOR TABLES 6 and 9

h	=	heat transfer coefficient, Btu/ft^2-hr-^{o}F
k	=	thermal conductivity, Btu/ft-hr-^{o}F
D_e	=	equivalent diameter based on wetted perimeter, in.
D_{HY}	=	$\sqrt{D_r (D_r + D_{HE})} - D_r$, in.
D_{HE}	=	heated equivalent diameter, in.
D_r	=	fuel rod diameter, in.
Pr	=	Prandtl number, $\frac{C_p \mu}{k}$
Re	=	Reynolds number, $\frac{GD_e}{\mu}$
μ	=	viscosity, lbm/ft-hr
C_p	=	specific heat, Btu/lbm-^{o}F
H_{fg}	=	heat of vaporization
T_{sat}	=	saturation temperature, ^{o}F
T_w	=	wall temperature, ^{o}F
ΔT_{sat}	=	$T_w - T_{sat}$, ^{o}F
q	=	heat flux, Btu/ft^2-hr
G	=	mass flow rate, lbm/ft^2-hr

TABLE 7 (Continued)

p	=	pressure, psia
X	=	quality
n	=	X_A/X_E
ρ	=	density, lbm/ft^3
L	=	channel length, in.
g	=	local acceleration due to gravity, ft/s^2
g_c	=	gravitational constant, $ft\text{-}lbm/lbf\text{-}s^2$
σ	=	surface tension, lbf/ft
Q	=	volumetric flow rate, ft^3/s
A_{flow}	=	flow area, ft^2
β	=	coefficient of thermal expansion, $1/^oF$
S	=	ratio of velocity of vapor phase to velocity of liquid phase (slip ratio)

and subscripts

CHF	=	critical heat flux conditions
f	=	saturated liquid conditions
g	=	saturated vapor conditions
v	=	superheated vapor conditions
E	=	equilibrium
w	=	wall
A	=	actual

(7) Savannah River[14]

(8) CE-1[15]

The eight CHF correlations have been combined into five groups. Use of a particular group is specified through the problem input. The available groups are listed on Table 8 and each correlation is described on Table 9.

Two heat transfer mode lockouts are imposed by FRAP-T4-LACE during the blowdown portion of a LOCA. If CHF is exceeded, then return to nucleate boiling is not allowed. Also, if the cladding surface temperature is at least 300°F greater than the coolant saturation temperature, then the transition boiling mode is locked out.

2.4 Reflood Heat Transfer Coefficients

When a LOCA transient is being analysed, a separate set of heat transfer conditions is needed following the blowdown portion of the LOCA during the period when the core is being reflooded by the emergency core cooling system. To meet this need, a separate subcode (REFLOOD) is included in FRAP-T4-LACE for post-blowdown heat transfer coefficient calculations. This subcode is activated at an input-specified time and computes cladding surface heat transfer coefficients during the refill and reflood portions of a LOCA transient. The subcode is based on the FLECHT[23] reflood correlations and includes models for the refill and reflood periods under both high and low flooding rates.

The REFLOOD subcode consists of an input subroutine (FLDINP), the refill-reflood executive subroutine (REFLOOD), a subroutine containing the FLECHT correlation (HCALF), two subroutines containing the steam cooling model (DBINVS and ENRISE), and a subroutine containing the flow blockage model (FIDDLE).

TABLE 8

CHF CORRELATION OPTIONS

JCHF = 0	$p \leq 725$ (psia)	Modified Barnett
	$725 < p < 1000$	Linear interpolation between Modified Barnett and Barnett
	$1000 \leq p \leq 1300$	Barnett
	$1300 \leq p \leq 1500$	Linear interpolation between Barnett and B&W-2
	$p \geq 1500$	B&W-2 (Gellerstadt)
JCHF = 1		GE
JCHF = 2		Savannah River
JCHF = 3	$p \leq 725$	Modified Barnett
	$725 < p < 1000$	Linear Interpolation between Modified Barnett and W-3
	$p \geq 1000$	W-3
JCHF = 4	$1 \times 10^6 < G < 3.5 \times 10^6$ (lbm/hr-ft^2)	
	$1800 < p < 2450$ (psia)	B&W High Flow Regime
	$16 <$ Inlet Subcooling < 299 (Btu/lb)	

TABLE 9

CHF CORRELATION DESCRIPTIONS

Modified Barnett

$$q = \left(\frac{10^6}{3600}\right) \frac{A + B\,(h_f - h_{in})}{C + L}$$

$$A = 73.71\ D_{HE}^{0.052}\ (G')^{0.663} \left(\frac{888.6}{h_{fg}}\right) \left[1 - 0.315 \exp\left(-11.34\ D_{HY}(G')\right)\right]$$

$$B = 0.104\ D_{HE}^{1.445}\ (G')^{0.691}$$

$$C = 45.55\ D_{HY}^{0.0817}\ (G')^{0.5866}$$

Water in rod bundles
Rod diameter: 0.395 to 0.543 in.
Length: 32.9 to 174.8 in.
Pressure: 150 to 725 psia
Mass flux: 0.03×10^6 to 1.7×10^6 lbm/ft^2-hr
Inlet subcooling: 6 to 373 Btu/lbm

Barnett

$$q_{CHF} = \left(\frac{10^6}{3600}\right) \frac{A + B\,(h_f - h_{in})}{C + L}$$

$$A = 67.45\ D_{HE}^{0.68}\ (G')^{0.192} \left[1 - 0.744 \exp(-6.512\ D_{HY}\ (G'))\right]$$

$$B = 0.2587\ D_{HE}^{1.261}\ (G')^{0.817}$$

$$C = 185.0\ D_{HY}^{1.415}\ (G')^{0.212}$$

TABLE 9 (continued)

Babcock and Wilcox B&W-2

$$q_{CHF} = \frac{1.15509 - 0.40703\ D_e}{PFACA\ (12.710)[3.0545\ (G')]^{A}} \left[(0.3702 \times 10^{8})\ 0.59137\ (G')^{B} - 0.15208\ x_{CHF} h_{fg}(G')\right]$$

$$A = 0.71186 + (0.20729 \times 10^{-3})\ (p - 2000)$$

$$B = 0.8340 + (0.68479 \times 10^{-3})\ (p - 2000)$$

PFACA = Axial Power Factor

General Electric Company

$$q_{CHF} = 10^{6}\ (0.8 - X)$$

for $G \leq 0.5 \times 10^{6}$ lbm/ft^2-hr

and

$$q_{CHF} = 10^{6}\ (0.84 - X)$$

for $G > 0.5 \times 10^{6}$ lbm/ft^2-hr

Savannah River

$$q_{CHF} = 188{,}000\ (1.0 + 0.515V)\ (1.0 + 0.069\ T_{SUB})$$

---

where

V = fluid velocity, ft/s

T_{SUB} = fluid saturation temperature minus fluid temperature.

Westinghouse Company, W-3

$$q_{CHF} = 1. \times 10^{6} \left[2.022 - 4.302 \times 10^{-4} p + (0.1722 - 9.84 \times 10^{-5} p) \exp\left((18.177 - 4.129 \times 10^{-3} p) X\right) \right] \left[1.157 - 0.869X \right] \left[(0.1484 + X(-1.596 + 0.1729\,\mathrm{ABS}(X)))G' + 1.037 \right] \left[0.8258 + 7.94 \times 10^{-4} (H_f - H_{IN}) \right] \left[0.2664 + 0.8357 \exp(-3.151\, D_{HE}) \right] F_{CW}/F_{APK}$$

where

H_f = enthalpy of saturated liquid (Btu/lbm)

H_{IN} = enthalpy of coolant at bottom of fuel rods (inlet enthalpy) (Btu/lbm)

F_{CW} = cold wall factor

F_{APK} = axial power profile factor at elevation station K

G' = $G/10^{6}$

X = quality

TABLE 9 (continued)

The cold wall factor is calculated by the equation

$$F_{CW} = 1. - (1-D_e/D_{HE}) \left[13.76-1.372 \exp(1.78X) \right.$$
$$\left. -4.732\ (G/10^6)^{-0.0535} -0.0619(P/1000)^{0.14} \right.$$
$$\left. -8.509\ D_{HE}^{0.107} \right]$$

The axial power profile factor is calculated by the equation

$$F_{APK} = \left\{ S_1 + \sum_{i=2}^{K} \left[\left\{ q_i - (dq/dZ)_i \right\} \exp(C_1(Z_i - Z_K)) \right. \right.$$
$$\left. \left. - \left\{ q_{i-1} - (dq/dZ)_i \right\} \exp(C_1(Z_{i-1} - Z_K)) \right] \right\} \Big/ C_2 q_K$$

where

F_{APK} = axial power profile factor at axial node K

q_i = surface heat flux at axial node i

Z_i = elevation of axial node i (ft)

$(dq/dZ)_i$ = $(q_i - q_{i-1})/C_1(Z_i - Z_{i-1})$

C_1 = $1.8(1-X)^{4.31} / (G/10^6)^{0.478}$

C_2 = $-C_1 Z_K$

S_1 = $q_1 \left[\exp(C_1(Z_1 - Z_K)) - \exp(C_2) \right]$

TABLE 9 (continued)

$$D_{HY} = D_o - D_I$$

$$D_{HE} = \frac{D_o^2 - D_I^2}{D_I}$$

$$D_I = D_{rod}$$

$$D_O = D_{rod}(D_{rod} + D_{HE})^{1/2}$$

$$D_e = \frac{4(\text{flow area})}{S}$$

$$S = \pi D_{rod}$$

Water in annulus: Applied to rod bundles using "equivalent" diameters.

Equivalent diameters: $0.258 \text{ in.} < D_{HE} < 3.792 \text{ in.}$
$0.127 \text{ in.} < D_{HY} < 0.875 \text{ in.}$

Length: 24 to 108 in.

Pressure: 1000 psia

Mass flux: 0.14×10^6 to 6.20×10^6 lbm/ft^2-hr

Inlet subcooling: 0 to 412 Btu/lbm

TABLE 9 (continued)

B&W High Flow Regime

$$q_{CHF} = \left\{ 14.3 \times 10^6 \left(\frac{G}{0.86 \times 10^6}\right)^{(1.09 + 4.16 \times 10^{-4} (P-2000))} + 0.133\, G\, (h_f - h_{in}) \right\} \Bigg/ \left\{ 7.4 \left(\frac{G}{0.268 \times 10^6}\right)^{\left[(1.09 + 4.16 \times 10^{-4} (P-2000))\right.} + 0.133.4 \frac{L}{D_e} \left. P_{APF} \right] \right\}$$

B&W Middle Flow Regime

$$q_{CHF} = \left\{ 0.8284\, G^{-0.2261} \left(1.5353 - \exp\left(0.001178P - 3.0053\right)\right) + \left(2.6028 - \exp\left(0.001084\right)\right) \frac{h_f - h_{in}}{h_{fg}\, 10^6} \right\} \Bigg/ \left\{ \left(1 + 2.6028 \exp\left(0.001084P - 2.5720\right)\right) (0.456) \left(\frac{L}{D_e G\, h_{fg}}\right) P_{APF} \right\}$$

The executive subroutine (REFLOOD) is called from the one-dimensional heat conduction solution subroutine (HTITDP). There are two distinct time dependent phases managed by REFLOOD. The first phase is the user specified time period during which the lower plenum is being refilled (the refill phase). During this phase, the core is assumed to undergo adiabatic heatup.

The second phase is the time period from the beginning of core reflood to the end of the transient. During this phase, fluid is entering the coolant channel and removing heat from the fuel rod surface. In order to comply with the NRC/DSS interpretation of Appendix K, the reflood phase consists of two regime In the first regime, heat transfer is modeled by the FLECHT correlation. In the second regime, heat transfer is modeled by a steam cooling model.

A line of separation (LOS) is determined which defines the upper elevation for which the FLECHT correlation is assumed to apply. The FLECHT correlation is used to calculate the heat transfer coefficient below the LOS, and the steam cooling model is used to calculate the heat transfer coefficient above the LOS.

Depending upon user input, the LOS is determined by one of two options. If the first option is specified, the LOS is the code predicted plane of cladding rupture. If the second option is specified, the LOS is the collapsed liquid level.

If the LOS is specified to be the cladding rupture plane, and cladding rupture does occur, the use of the steam cooling model depends upon the flooding rate. If the flooding rate is greater than 1 in./s, the FLECHT correlation is assumed to apply along the entire length of the fuel rod. But if the flooding rate is less than 1 in./s, the FLECHT correlation is assumed to apply only up to the elevation of the LOS. Above this elevation, the cladding heat transfer coefficient is calculated by the steam cooling model. If,

however, rupture has not occurred, then the FLECHT correlation is applied along the entire length of the rod.

If the LOS is the collapsed liquid level, and the flooding rate is greater than 1 in./s, the FLECHT correlation is assumed to apply along the entire length of the fuel rod. But if the flooding rate is less than 1 in./s, the FLECHT correlation is applied up to the elevation of the LOS, and above this elevation the cladding heat transfer coefficient is calculated by the steam cooling model.

2.4.1 The Refill Model. During the refill phase of the post blowdown analysis, the core undergoes adiabatic heatup. Both the heat transfer coefficient (HTC) and the fuel rod surface heat flux (Q) are set to zero during this phase. The fuel rod surface temperature (TSURF) is calculated from the heat conduction boundary equation (see Appendix C of Reference 24).

$$A * TSURF + B = Q = 0$$

where A and B are coefficients supplied by the FRAP-T subroutine HT1TDP.

2.4.2 The Reflood Model. During the reflood phase of the post blowdown analysis, two heat transfer models are used. They are a generalized FLECHT heat transfer coefficient correlation and a steam cooling model. The FLECHT correlation was generalized for arbitrary length cores by J. C. Lin and documented in Reference 25.

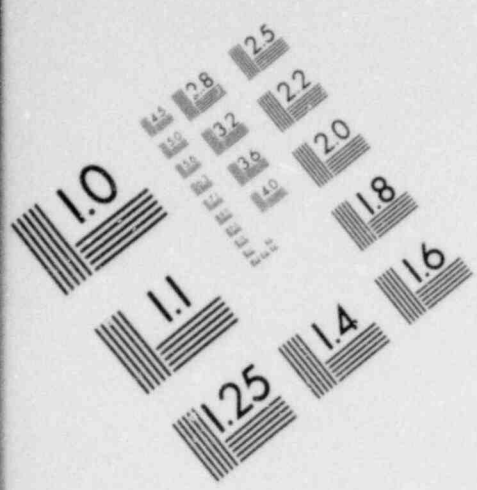

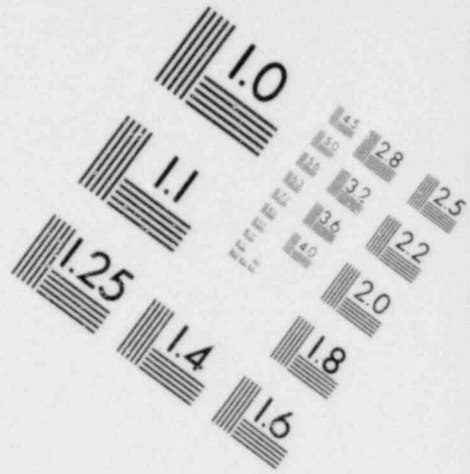

IMAGE EVALUATION
TEST TARGET (MT-3)

MICROCOPY RESOLUTION TEST CHART

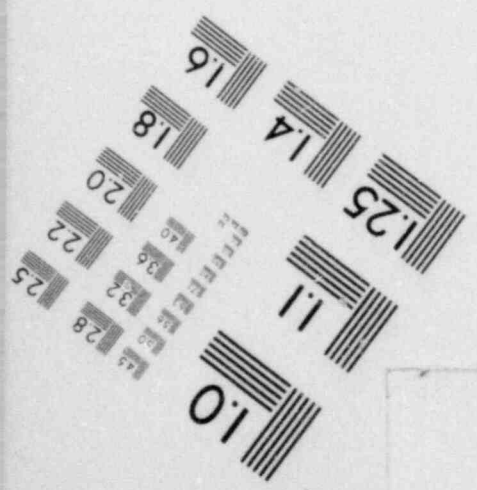

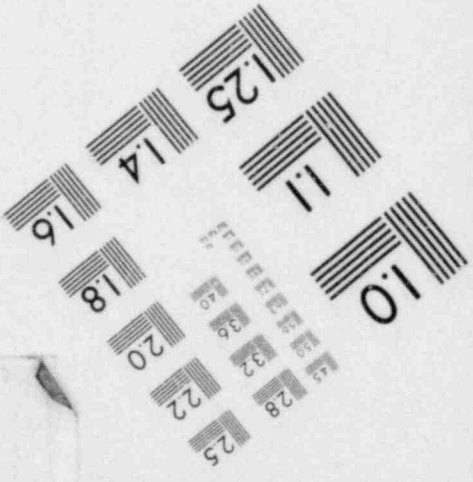

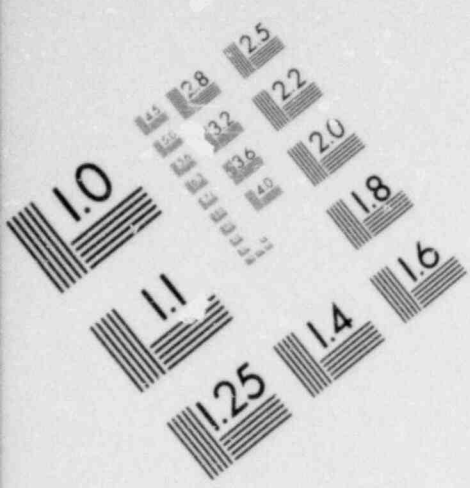

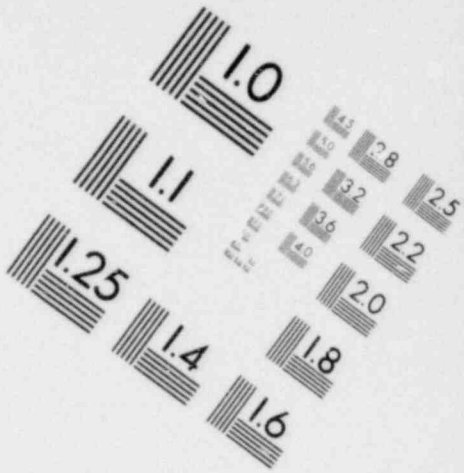

IMAGE EVALUATION
TEST TARGET (MT-3)

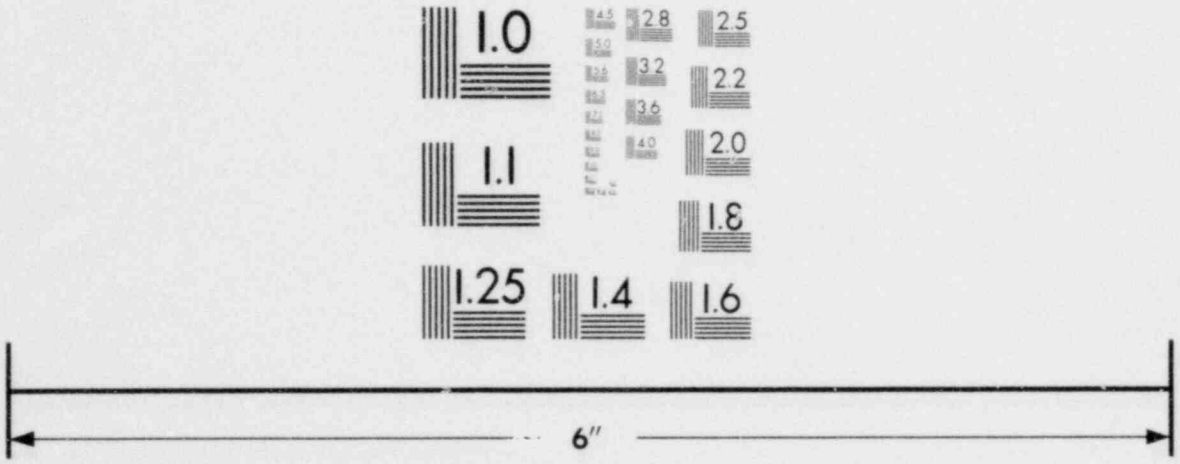

MICROCOPY RESOLUTION TEST CHART

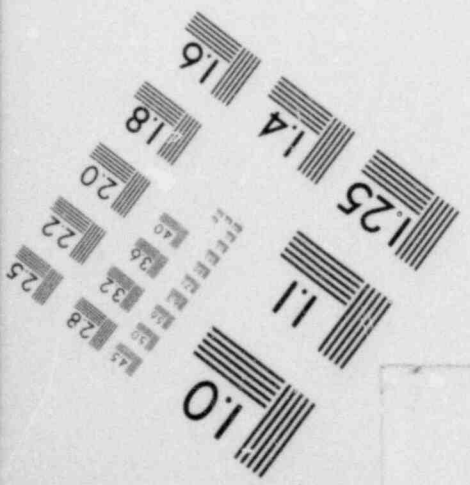

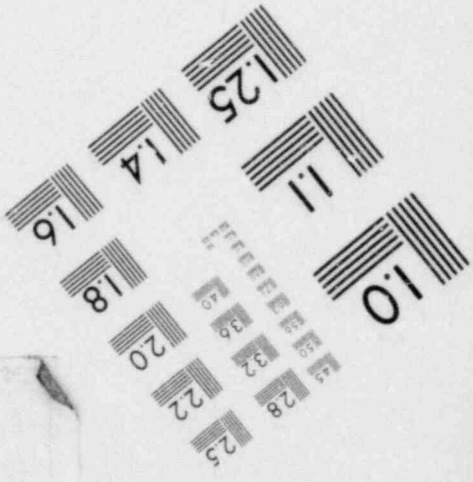

(a) FLECHT Correlation

The generalized FLECHT correlation computes the heat transfer coefficient at the cladding surface during the reflood phase of a LOCA. The heat transfer coefficient is a function of flooding rate, cladding temperature at the start of flooding, fuel rod power at the start of flooding, flood water temperature, vessel pressure, elevation and time. The ranges of these variables for which the correlation is applicable are shown in Table 10. Four different heat transfer correlations are used corresponding to the period of radiation heat transfer only and to the three distinct phases of reflood. Thus four different time periods are considered, and the ranges of these periods are computed within the model. Using the definitions shown on Table 11, the four regimes are described below.

(i) Period of Radiation Only

Only heat transfer due to radiation is modeled during $0 < t \leq t_1$, with the heat transfer coefficient being computed from

$$h = h_o + \Delta h \left[1 - \exp\left(-0.0025\, t^2\right)\right]$$

where

$$t_1 = 274 \exp\left(-0.0034\, T_{init}\right) \exp\left(-0.465\, V_{in}\right) \exp\left(-1.25\, Q'_{max}\right) / \left(1 + 50.^{**} \left\{-0.2\,(P - 30)\right\}\right)$$

$$h_o = \begin{cases} 3.67\, Q'_{max} \left(1 - \exp\left\{-(T_{init} - 700)/435\right\}\right) F, & \text{if } T_{init} > 700^{o}F \\ 0, & \text{if } T_{init} \leq 700^{o}F \end{cases}$$

$$F = F_2 + (1 - F_2)/(1 + 50 ** (Z - 7))$$

TABLE 10

RANGE OF APPLICABILITY OF GENERALIZED FLECHT CORRELATION

Variable	Applicable Range of Variable
Flooding rate (in./s)	0.4 - 10
Reactor vessel pressure (psia)	15 - 90
Inlet coolant subcooling (°F)	16 - 189
Initial cladding temperature (°F)	300 - 2200
Peak fuel rod power (kW/ft)	0.51 - 1.4
Flow blockage (%)	0 - 75
Equivalent elevation in FLECHT facility (ft)	2 - 10

TABLE 11

VARIABLE AND SYMBOL DEFINITIONS IN FLECHT CORRELATION

		Variables
V_{in}	=	flooding rate (in./s)
T_{init}	=	peak cladding temperature at start of flooding (°F)
Q'_{max}	=	fuel rod power at axial peak at start of flooding (kW/ft)
P	=	reactor vessel pressure (psia)
Z	=	equivalent FLECHT elevation (ft)
T_{sub}	=	flood water subcooling at inlet (°F)
t	=	time after start of flooding as adjusted for variable flooding rate (s)
h	=	heat transfer coefficient (Btu/hr-ft^2-°F)
Q_{maxtq}	=	radial power shape factor
	=	1.0 for a nuclear rod
	=	1.1 for electrical rod with radially uniform power
B	=	flow blockage (%) (B always set equal to zero)
		Symb
a**b	=	a^b

$$F_2 = 0.3 + 0.7/(1 + 50 ** (2 - V_{in}))$$
$$\Delta h = 0.0397\ Q'_{max}(T_{init} - 100).$$

(ii) Period I

During Period I, the flow develops from the radiation dominated pre-reflood condition to single phase steam flow, to dispersed flow, and finally to unstable film boiling. If the flooding rate is less than 3 in./s, however, unstable film boiling does not develop. The heat transfer coefficient during this period changes from a low value due to radiation to a relatively high value due to unstable film boiling (high flooding rates) or dispersed flow (low flooding rates). The time range of Period I is

$$t_1 < t$$
and
$$t_q < t_{q2}$$

where the variables in the expression for time range are defined as

$$t_q = \frac{t - t_1}{t_{q6} - t_1}$$

where

$$t_{q6} = 98.39 \left[\exp(-0.0107\ \Delta T_{sub})\left\{1-\exp(-0.667\ V_{in})\right\}\right.$$

$$\left\{1 + 0.5 \exp(-0.000037p^3) + 1.3 \exp(-0.111\ V_{in}^2)\right.$$

$$\left. + 17.3 \exp(-0.00003/p^3) \exp(-0.49\ V_{in}^2)\right\}\ (1.207\ Q'^{1.5}_{maxtq} - 0.667)$$

$$+ \left\{(3.28/V_{in})^{1.1} - 2.8 \exp(-V_{in})\right\} \left\{1 + 0.5 \exp(-0.000037p^3)\right\}\Big]$$

$$(1 + 0.0000588T_{init} - 1.05 \exp(-0.0025\, T_{init}))\,(1 + 0.5/\left\{1 + 50 ** (2-0.667\, V_{in})\right\}) \quad \Big[1 + 0.32/\left\{1 + 50 ** (5-0.1\, P)\right\}\Big]$$

$$t_{q2} = 0.62\,((1 - \exp(-0.192\, Z)) -$$

$$0.115\, Z \exp(-0.0368Z^2))$$

The heat transfer coefficient during Period I is computed using the correlation

$$h = h_1\left[1 - \exp(-10(X_2 - X)/X_2)\right] + \left[h_{12} - h_1\left\{1 - \exp(-10(X_2 - X)/X_2)\right\}\right]$$

$$\left[1 - \exp(-x) - 0.9\, x \exp(-X^2)\right] \left[1 - 2.21 \exp(-0.4\, V_{in})u\exp(-u)\right.$$

$$\exp\left\{-(0.588\, Z_{in} 3.824)^2\right\}\Big/$$

$$(1 + 100 ** \left\{10\ (t_q/\, t_{q2}) - 9\right\})\Big]$$

where

$$h_1 = 3.67\, Q'_{max}\,(1 - \exp\left\{-(T_{init} - 700)/435\right\})$$

$$+ \Delta h\,(1 - \exp(-0.0025\, t_1^2)), \quad \text{if } T_{init} > 700^{o}F$$

$$= \Delta h\,(1 - \exp(-0.0025\, t_1^2)), \quad \text{if } T_{init} \leq 700^{o}F$$

$$x_2 = 17.6 \left[1 + 4.37 \exp\left(-0.0166\ \Delta T_{sub}\right)\right] \left[1 - \exp\left\{ -(0.00075 + 0.0000272\ (V_{in} - 8)^2)\ f_6 \right\}\right]^{t_{q2}\ f_i}$$

$$h_{12} = 2.644 + 1.092\ Q'_{max} + \left[35.7 + (22 - 0.00303\ Z^{4.1})\right.$$

$$\left.(1 - \exp(-0.0383\ P) - 0.034\ P \exp(-0.0011\ P^2))\right] \left[1 - \exp\left(-0.2\ V_{in}\right)\right]$$

$$+ 8 \left[1 - \exp\left(-2\ V_{in}\right)\right] \left[1 - \exp\left(-B/25\right)\right]$$

$$x = 17.6 \left[1 + 4.37 \exp\left(-0.0166\ \Delta T_{sub}\right)\right] \left[1 - \exp\left\{ - (0.00075 + 0.0000272\ (V_{in} - 8)^2)\ f_6 \right\}\right]^{t_q \left(\frac{t - t_1}{t_{q2}(t_{q6} - t_1)}\right)^{f_2}}$$

$$u = 9 \left[f_1\ t_q\ /((t_{q2})^{(1 + f_2\ f_3)})\right]^2$$

$$f_1 = 0.436 + 0.455\ f_5$$

$$f_2 = 0.564 - 0.455\ f_5$$

$$f_3 = 2.8 - 4.8 \exp\left(0.688 - 1.67\ V_{in}\right)$$

$$f_4 = 1 - \exp\left\{-(0.026\ P + 1.041\ V_{in} + 10.28 \exp\left(-3.01\ Q'_{max}\right) - 0.651)\right\}$$

$$f_5 = Q'_{max} + (1.24 - Q'_{max}) \Big/ \left\{1 + 50^{(5 - 2\ V_{in})}\right\}$$

$$f_6 = 0.5 \left[T_{init} - 1000 + \left\{ T_{init}^2 - 2000\, T_{init} + 1.0001(10^6) \right\}^{1/2} \right] + 350$$

(iii) Period II

During this period, the flow pattern has fully developed to a quasi-steady state of either unstable film boiling (high flooding rate) or dispersed flow (low flooding rate), and the heat transfer coefficient reaches a plateau with a rather slow increase. The time range of Period II is:

$$t_{q2} < t_q < t_{q3}$$

where the new variable in the expression for time range is defined as

$$t_{q3} = 1.55 \left((1. - \exp(-0.205\, Z)) - 0.154\, Z \exp(-0.0421\, Z^2) \right) + 0.26 \exp\left(-2.77\,(10^{-6})\, T_{init}^2\right)$$

The heat transfer coefficient during Period II is computed by the equation

$$h = h_2 + b_1 \left[y^2 + b_2 \left(y^2 - b_3\, y^3 \right) + o_4\, y^2 \exp(-6.38\, y) \right] + 60 \exp\left[-2.77\,(10^{-6})\, T_{init}^2\right] (y/y_3) \exp\left[-2.25\,(y/y_3)^2\right]$$

where

$$h_2 = h_{12} \left[(1 - \exp(-x_2)) - 0.9\, x_2 \exp(-x_2^2) \right]$$

$$b_1 = \left[682 - 650 \left\{1 - \exp(4 - Z)\right\}\right]\left[1 - \exp\left\{- 0.95 \ (1 - 0.0488 \ Z) \ V_{in}\right\}\right]$$

$$\left[1 - \exp\left\{- 0.0238 \ \Delta T_{sub}\right\}\right] \left[0.696 + 0.304 \exp \ (-B/25)\right]$$

$$\left[1 + 0.2 \ (1 - f_4)\right] \left[1 + \exp \ (-0.8503 \ Z^2 + 1.0986123 \ Z + 2.3025851)\right]$$

$$y = t_q - t_{q2}$$

$$b_2 = 0.4 \ Z \left[1 - \exp\left\{-2 \ (Z - 3.5)\right\}\right] \left[1.33 \ (1 - \exp(-0.0227 \ P)) - 1\right]$$

$$-2.9 \left[1 - \exp \ (- V_{in}/2.5)\right] \left[1 - \exp \ (-B/25)\right]$$

$$b_3 = 2.55 \ (Z - 3.7)^2 \exp \ (3.7 - Z)$$

$$b_4 = 87.5 \ V_{in} \exp \ (-V_{in}^2) \exp \ (-0.036 \ \Delta T_{sub})$$

If $Z < 4$, $b_3 = b_2 = 0$.

(iv) Period III

During this period, the flow pattern changes to stable film boiling and the heat transfer coefficient increases rapidly as the quench front approaches. The time range of Period III is

$$t_{q3} < t_q$$

where t_q is the time of quenching. The heat transfer coefficient during Period III is computed by the correlation

$$h = h_3 + C \ (t_q - t_{q3})$$

where

$$h_3 = h_2 + b_1 \left[y_3^2 + b_2 \left(y_3^2 - b_3 \; y_3^3 \right) + b_4 \; y_3^2 \exp \left(-6.38 \; y_3 \right) \right]$$

$$C = 420 \left[1 - \exp \left(-0.00625 \; b_1 \right) \right] f_4$$

$$y_3 = t_{q3} - t_{q2}$$

(v) Modification for Low Floodrates

The heat transfer coefficients for Periods I, II, and III given above were based in the original FLECHT tests. Later tests performed at low flooding rates showed that a modification was necessary to best match the data. This modification is accomplished by multiplying the heat transfer coefficients for periods I, II, and III by a factor f where

$$f = f_7 \; f_8$$

and

$$f_7 = 0.978 + 0.022 / \left[1 + 30 \; ** \left\{ t_{q2} - t_q \left\{ \left(t_{q6} - t_1 \right) \right| \right.$$

$$f_8 = f_a + (1 - f_a) / \left[1 + 50 \; ** \; (Z - 7) \right]$$

$$f_a = f_b + (1 - f_b) / \left[1 + 50 \; ** (2 - V_{in}) \right]$$

$$f_b = 0.3 + 0.7 \left[1 - \exp \; (- 1.5 t_q)) \right]$$

(vi) Modification for Variable Floodrates and Variable Rod Length

The variable t in the FLECHT heat transfer correlation is the time after the start of flooding as adjusted for variable flooding rate. The adjustment of time is made according to the equation

$$t = t_A + (0.214\ Z - 0.386)\left[\frac{\int_0^{t_A} V_{in}(t)dt}{V_{in}(t_A)} - t_A\right]$$

where

t = adjusted time (s)

t_A = actual time since start of flooding (s)

Z = equivalent FLECHT elevation (ft)

$V_{in}(t)$ = flooding rate at time t (in./s)

The integral-of-power method[26] is used to calculate the elevation in the FLECHT facility that is equivalent to a given elevation in a nuclear reactor. By inputting the equivalent FLECHT elevation into the FLECHT correlation, the heat transfer coefficient at the given elevation in the nuclear reactor is output. The equation used to calculate the equivalent FLECHT elevation is

$$\int_0^{Z_1} P_F(Z)dZ = \frac{F_F}{F_L}\int_0^{Z_2} P_L(Z)\ dZ$$

where

$P_F(Z)$ = normalized power of FLECHT rod at elevation Z

$P_L(Z)$ = normalized power of nuclear rod at elevation Z

F_F = axial power peaking factor for FLECHT rod = 1.66

F_L = axial power peaking factor for nuclear rod (specified by card input)

Z_2 = elevation on nuclear fuel rods

Z_1 = elevation on FLECHT rods that is equivalent to elevation Z_2 on nuclear fuel rods.

The procedure for solving for the equivalent FLECHT elevation Z_1 that corresponds with the nuclear reactor elevation Z_2 is:

1. Store in computer memory a table of the integral of normalized FLECHT power versus elevation.

2. Numerically integrate the normalized power of the nuclear rod from elevation zero to elevation Z_2.

3. By interpolation in the table of Step 1, find the FLECHT elevation of Z_1 that has the same integral of power as the nuclear reactor elevation Z_2.

(b) Steam Cooling Model

The steam cooling model computes the heat transfer coefficient due to the flow of steam and is used when the FLECHT correlation is not applicable. The model is based on the Dittus-Boelter[16] correlation. The heat capacity term[a] in the Dittus-Boelter correlation is adjusted to match the FLECHT heat transfer coefficient

---

a. $$h = \left(\frac{.023 * THCON}{HYDIAM}\right) \left(\frac{G * HYDIAM}{VISC}\right)^{0.8} \left(\frac{CCP * VISC}{THCON}\right)^{0.4}$$

where THCON is the thermal conductivity of saturated steam at the LOS; HYDIAM is the hydraulic diameter of the flow channel; G is the mass flux, VISC is the viscosity of the saturated steam at the LOS, CCP is the heat capacity of saturated steam, and h is the heat transfer coefficient.

at the maximum elevation for which the FLECHT correlation is applicable. This maximum elevation has been previously defined as the line of separation (LOS).

The heat capacity of saturated steam, CPS, is determined at the LOS and a multiplier CPM=CCP/CPS is determined. This multiplier allows a smooth transition from the FLECHT correlation cooling regime to the steam cooling regime above the LOS. Then for axial elevations above the LOS, the heat capacity of saturated steam (CPS) is calculated using the coolant pressure and temperature at the lower adjacent node. Using the previously determined heat capacity multiplier (CPM), the Dittus-Boelter correlation is solved for the heat transfer coefficient (HTCDTB) using (CPM * CPS) as the vapor heat capacity. The FLECHT heat transfer coefficient (HTCFLC) is also calculated at the same axial elevation. The two heat transfer coefficients (HTCDTB) and (HTCFLC) are compared, and the one which provides the smaller surface heat flux is used. The heat capacity multiplier is recalculated each time step in order to respond to the advancing reflood rate and liquid level.

The mass flux term in the Dittus-Boelter correlation is computed by the equation

$$G = \rho_w (L_2 - L_1) \, 3600/\Delta t$$

where

G = mass flux ($lbm/-ft^2$)

L_1 = collapsed liquid level at start of timestep (ft)

L_2 = collapsed liquid level at end of timestep (ft)

ρ_w = density of flooding water (lbm/ft^3)

Δt = timestep (s)

The collapsed liquid level history is computed by the RELAP/FLOOD code and is input by cards to FRAP-T4-LACE.

If the fuel rod cladding has ruptured, an adjustment is made in the mass flow factor of the Dittus-Boelter correlation for elevations just below the rupture plane and higher. The adjustment is made in subroutine FIDDLE as follows.

Two coefficients F_1 and F_2 are calculated from the relations

$$F_1 = 1.01 - 0.51\ V_{in}$$

$$F_2 = F_2' = 1.0 - (-0.01 + 0.51\ V_{in}) \left(\frac{E_1}{E_2}\right)$$

using V_{in}, the reflood rate, E_1, the current axial node elevation and E_2, the rupture plane elevation.

If $E_1 > E_2$ then $F_2 = F_1$. However, if

$$E_1 > (E_2 + 2), \text{ then } F_2 = F_2' + \frac{(1.0-F_2')\ (E_1 - E_2 - 2.0)^2}{(10-E_2)}$$

Based on this elevation dependent readjustment of the factors F_1 and F_2, the adjusted flow is determined as a function of E_1 and E_2 as follows.

If $E_1 \leq E_2 - 0.91667$, no adjustment is made.

If $E_2 - 0.91667 < E_1 < E_2 + 0.58333$, then the adjusted flow is given by

$$G_2 = F_2\, G_1 \left(\frac{B}{2}\ (\sin(\pi(E_2 - E_1 - 0.41667))-1.0) \quad .0\right).$$

If $E_2 + 0.58222 < E_1$,

then $G_2 = F_2\, G_1\ (1.0 - \frac{B}{2} \exp\ (2.0\ (E_2-E_1 + 0.58333)))$

where

E_1 = the axial elevation

E_2 = the axial rupture elevation

V_{in} = the reflood rate

G_1 = the unmodified mass flow

B = the fraction of channel blockage

G_2 = the returned modified mass flow.

3. MATERIAL PROPERTY CORRELATIONS

LACE options are applied to twelve material properties correlations used in FRAP-T4:

Cladding thermal expansion	(Option 3)
Cladding specific heat	(Option 4)
Cladding elastic modulus	(Option 5)
Cladding Poisson's ratio	(Option 6)
Cladding thermal conductivity	(Option 7)
Fuel specific heat	(Option 8)
Fuel elastic modulus	(Option 9)
Fuel emissivity	(Option 10)
Fuel Poisson's ratio	(Option 11)
Fuel thermal conductivity	(Option 12)
Fuel thermal expansion	(Option 13)
Gas thermal conductivity	(Option 16)

In the following discussion, a brief description of each FRAP-T4-LACE material property correlation is presented. The correlations were compared (where possible) with (a) comparable MATPRO-9 correlation predictions used in the best-estimate version of FRAP-T4, (b) comparable GAPCON-THERMAL-2[27] and -3[28] correlation predictions used in best-estimate and conservative calculations, and (c) available experimental data and associated uncertainties. The influence of each FRAP-T4-LACE material properties option upon fuel temperature and stored energy for a typical LOCA was determined. This was accomplished by running the Zion PWR LOCA problem (see Table 4) with a different LACE option selected for each run. The deviations in temperature and stored energy from the best estimate values gave a measure of the sensitivity of the calculations to the conservative models.

3.1 Cladding Thermal Expansion

A set of thermal expansion correlations is used in FRAP-T4-LACE (for both zircaloy-2 and zircaloy-4) for axial and diametral expansion. For the temperature range 293 to 1116 K,

$$\frac{\Delta L}{L} = 5.76 \times 10^{6} \, (T-293.15)$$

where

$\frac{\Delta L}{L}$ = thermal expansion $\left[\frac{m}{m}\right]$

T = temperature (K).

For the temperature range 1116 to 1241 K, a constant value of 4.74×10^{-3} m/m is used. Above 1241 K,

$$\frac{\Delta L}{L} = 9.54 \times 10^{-6} \, (T-1241) + 4.74 \times 10^{-3}.$$

These cladding thermal expansion correlations are shown in Figures 9 and 10 along with the correlations in MATPRO-9 and GAPCON-THERMAL-3 and the MATPRO-9 data base. The MATPRO-9 correlation is best estimate. The GAPCON-THERMAL correlations produce the most thermal expansion and are not always within the $\pm 2\sigma$ uncertainty limits of the data. The FRAP-T4-LACE correlation underpredicts the best estimate diametral thermal expansion up to 1150 K. The MATPRO-9 data base extends only to 1075 K.

3.2 Cladding Heat Capacity

The cladding heat capacity correlation is

$$C_p = 246.9 + 0.168T - 4.36 \times 10^{-5}T^{-2} \quad \text{for } T \leq 1000K$$
$$= 365.5 \quad \text{for } T > 1000K$$

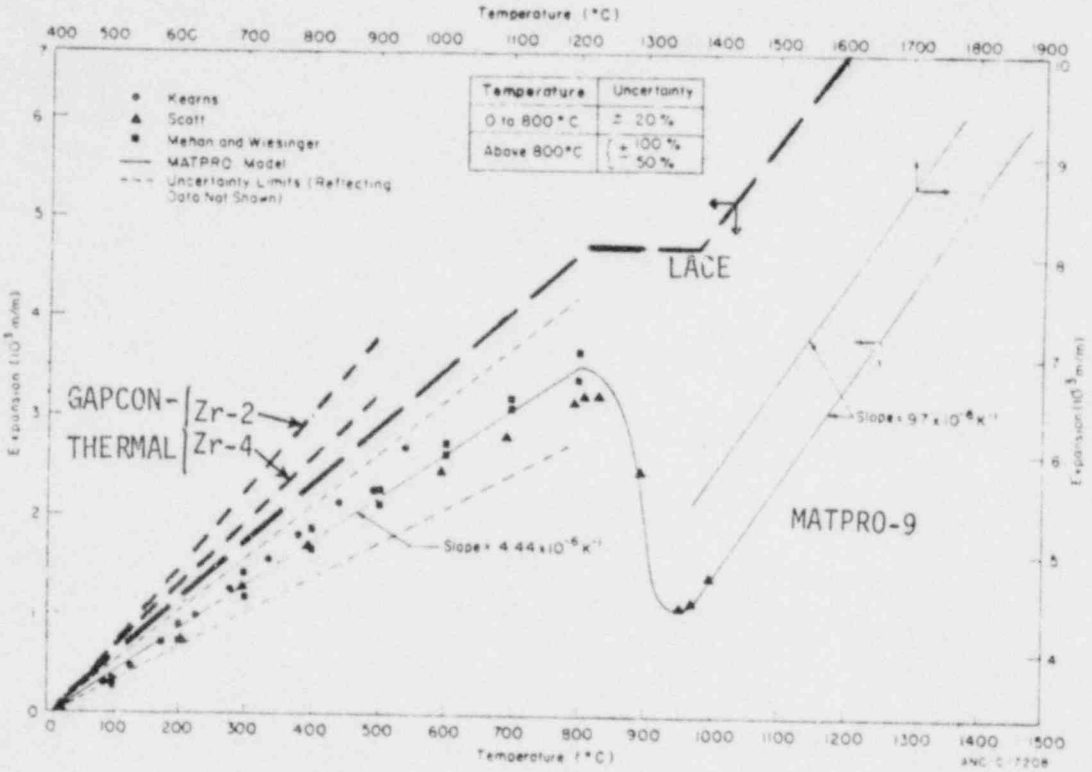

Fig. 9 Cladding axial thermal expansion versus temperature.

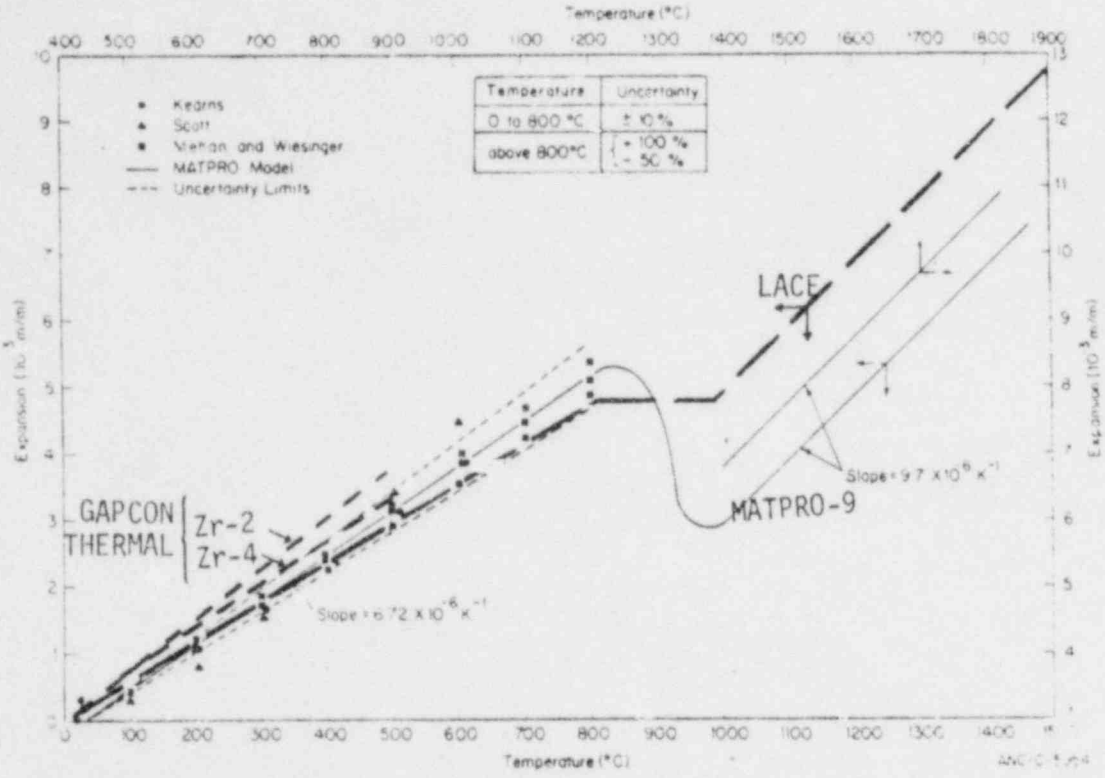

Fig. 10 Cladding diametral thermal expansion versus temperature.

where

C_p = heat capacity (J/kg-K)
T = temperature (K).

This correlation is plotted in Figures 11 and 12, which also present the MATPRO-9 and GAPCON-THERMAL-3 correlations and the MATPRO-9 data base. All correlations are essentially identical up to 1000 K.

3.3 Cladding Elastic Modulus

The FRAP-T4-LACE correlation for cladding elastic modulus is

$$E = 1.148 \times 10^{11} - 5.99 \times 10^{7} T, \quad \text{for } T \leq 750 \text{ K}$$

$$= 1.07981 \times 10^{11} - 5.02236 \times 10^{7} T, \quad \text{for } T > 750 \text{ K}$$

where

E = Young's modulus (N/m^2)
T = temperature (K).

This correlation is compared in Figure 13 with the MATPRO-9 and GAPCON-THERMAL correlations and the MATPRO data base. Nearly all of the correlations including the FRAP-T4-LACE correlation overpredict the data at rod operating and blowdown temperatures.

3.4 Cladding Poisson's Ratio

The cladding Possion's ratio correlation is

$$\nu = 0.32 + 5 \times 10^{-5} T$$

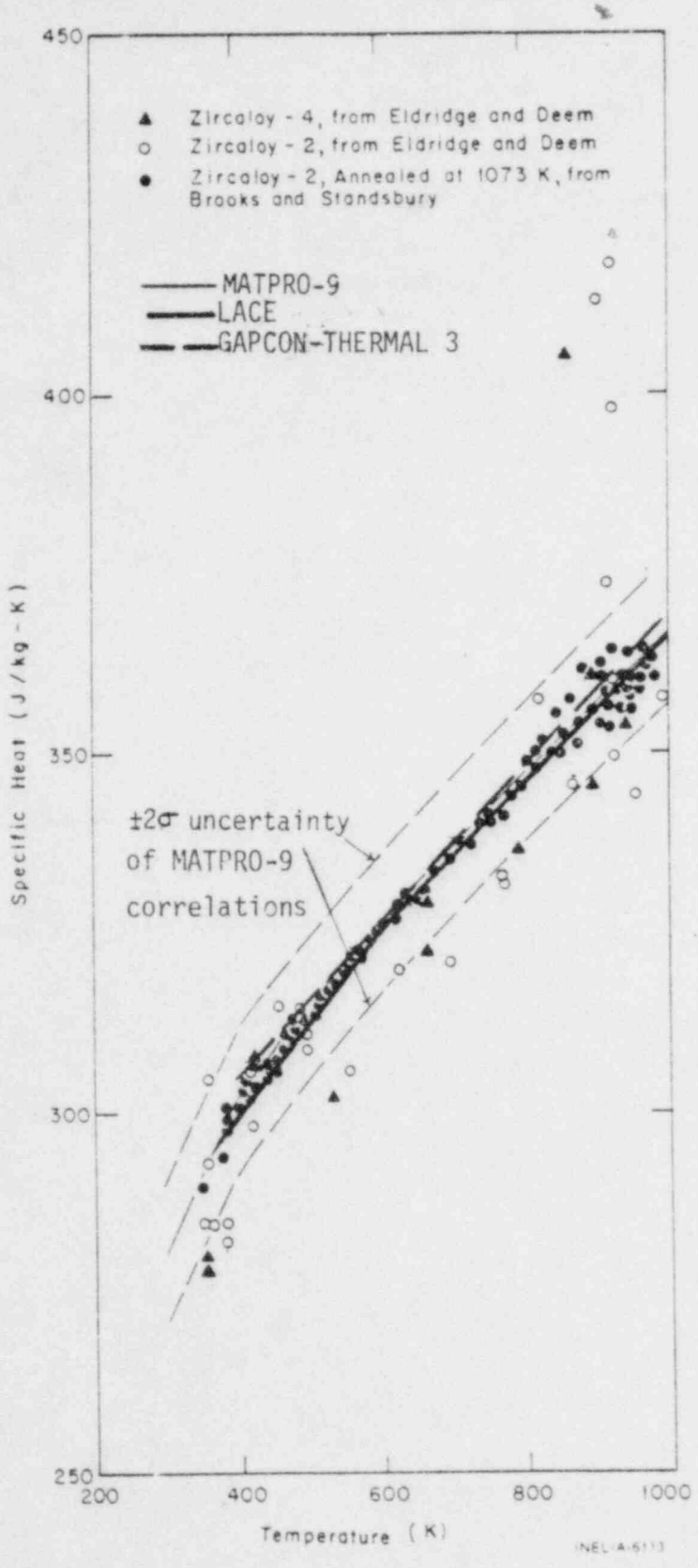

Fig. 11 Low temperature cladding heat capacity.

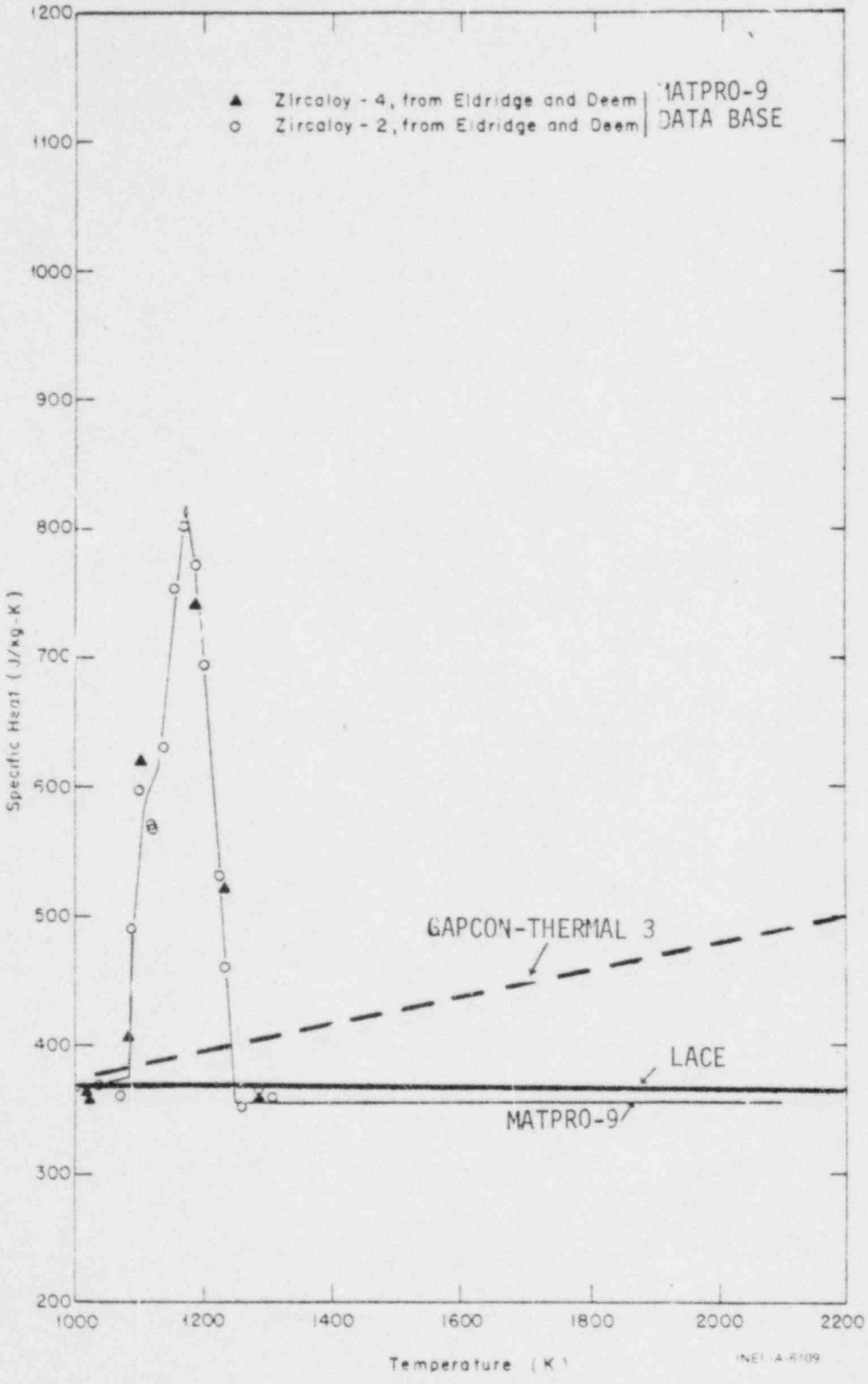

Fig. 12 High temperature cladding heat capacity.

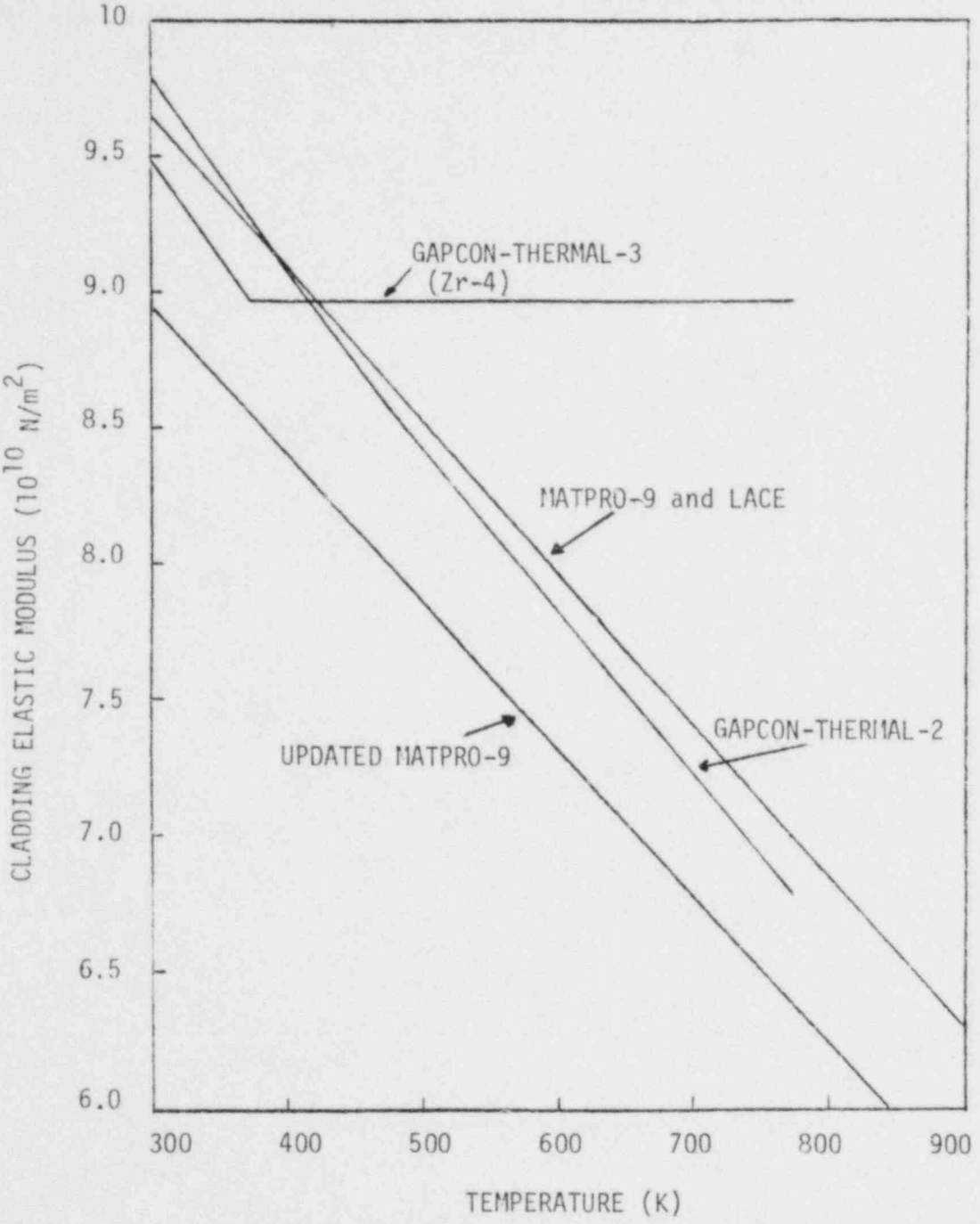

Fig. 13 Cladding elastic modulus versus temperature (alpha region).

where

ν = Poisson's ratio
T = temperature (F).

This correlation and available experimental data versus temperature are presented in Figure 14. Also shown are the MATPRO-9 and GAPCON-THERMAL correlations. Much discrepancy is seen between the correlations and the limited data base.

3.5 Cladding Thermal Conductivity

The correlation for cladding thermal conductivity is

$$k_{Zr} = -3.198 + 5.117 \times 10^{-2}T - 4.114 \times 10^{-5}T^2 + 1.522 \times 10^{-8}T^3$$

where

k_{Zr} = thermal conductivity of zircaloy (W/m-K)
T = temperature (K).

The FRAP-T4-LACE, MATPRO-9, and GAPCON-THERMAL-3 correlations are shown in Figure 15 along with the available experimental data. All correlations produce similar results. The FRAP-T4-LACE values are below best estimate for temperatures less than 700 K.

3.6 Fuel Heat Capacity

The fuel heat capacity correlation is taken from the WREM document,[29] Table 2.4, page 2-30. The correlation is in tabular form, and is given in Table 12. The MATPRO-9, GAPCON-THERMAL, and FRAP-T4-LACE correlations are compared in Figure 16. The fuel was assumed to have a density which is 95% of the theoretical density. All correlations are essentially best-estimate for temperatures up to 2900 K.

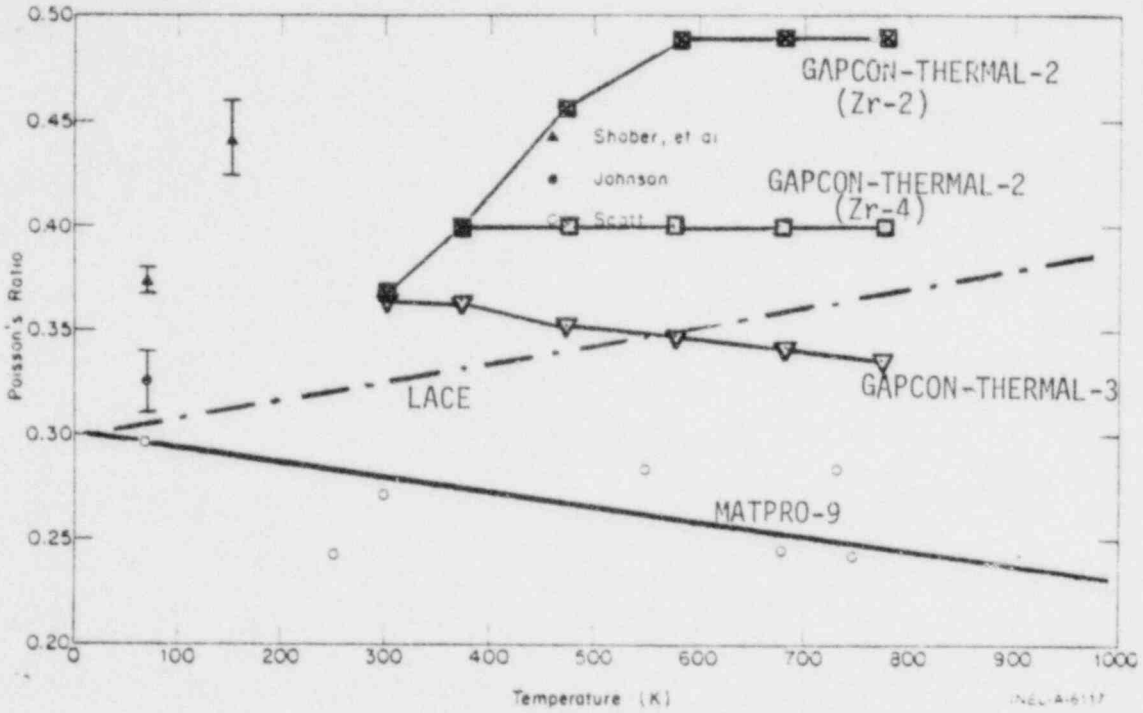

Fig. 14 Cladding Poisson's ratio versus temperature.

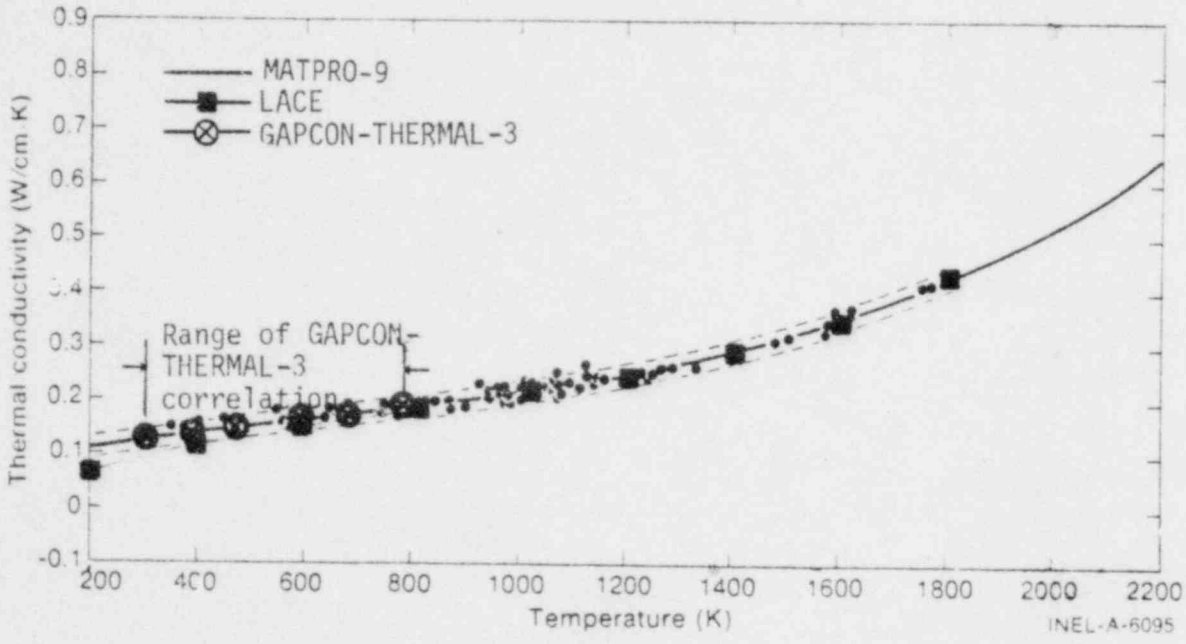

Fig. 15 Cladding thermal conductivity versus temperature.

TABLE 12

UO_2 VOLUMETRIC HEAT CAPACITIES

Temperature (^oF)	Volumetric Capacity (BTU/ft^3-^oF)
32	34.45
122	38.35
212	40.95
392	43.55
752	46.80
2012	51.35
2732	52.65
3092	.55
3452	63.05
3812	72.80
4352	89.70
4532	94.25
4532	98.15
4892	100.10
5144	101.40
8000	101.40

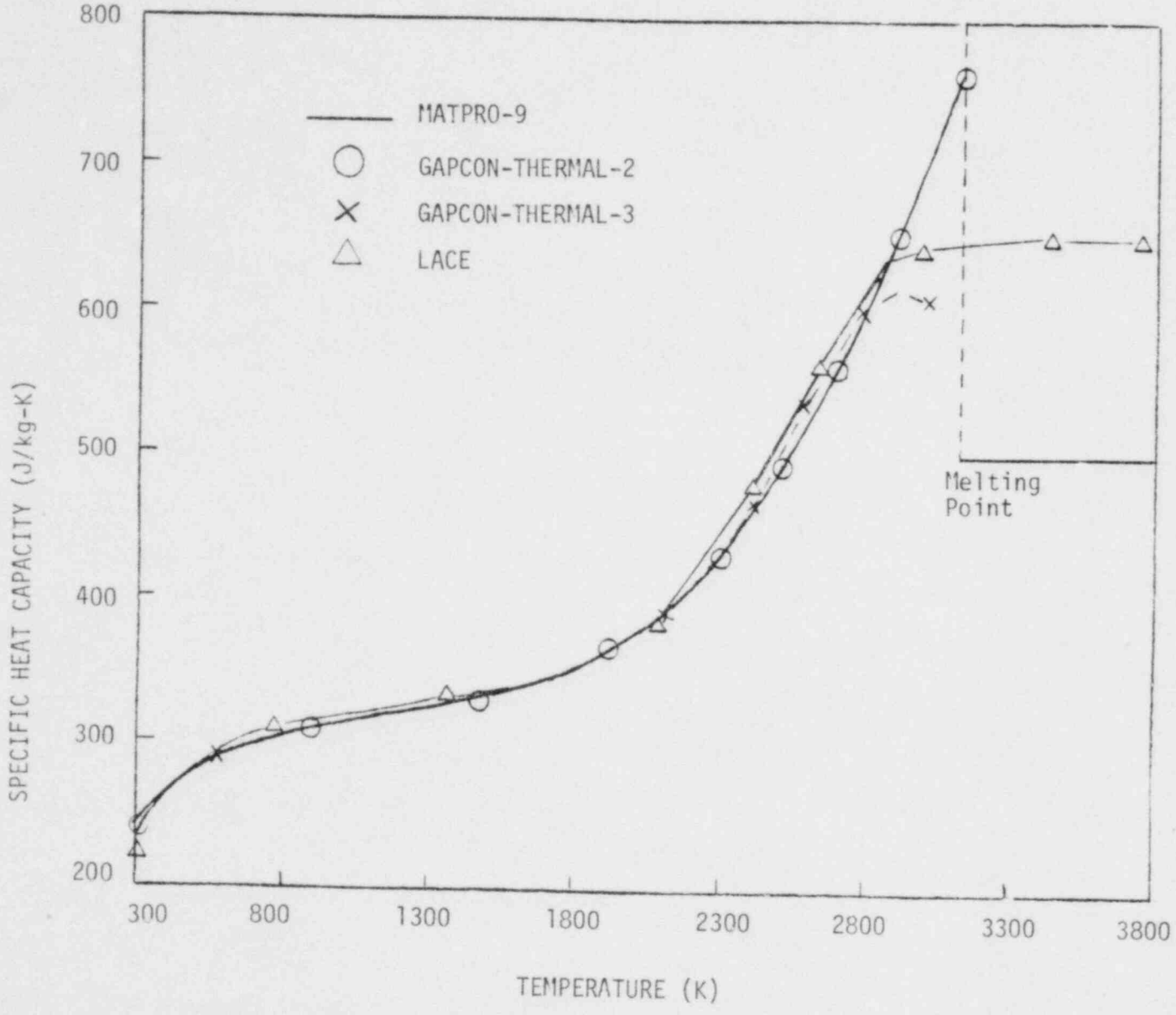

Fig. 16 Fuel heat capacity versus temperature at 95% TD.

3.7 Fuel Elastic Modulus

The uranium dioxide Young's modulus correlation is

$$ES = (1.8863 \times 10^{11} - 9.0627 \times 10^{7}\ T)\ (2.28\ D - 1.28) \text{ for } T < 2000\ K$$

$$= 7.0 \times 10^{8} \text{ for } T > 2000\ K$$

where

ES = Young's modulus for stoichiometric UO_2 (N/m^2)
D = fraction of theoretical density
T = temperature (K).

For a fuel theoretical density of 95%, the FRAP-T4-LACE, MATPRO and GAPCON-THERMAL correlations predict the values shown in Figure 17. The FRAP-T4-LACE correlation appears to be unreasonable when compared to the other more recently developed correlations.

3.8 Fuel Emissivity

The fuel emissivity correlation is

$$\varepsilon = 19.32 - 6.68 \times 10^{-2}T + 9.396 \times 10^{-5}T^2 - 6.397 \times 10^{-8}T^3 + 2.10 \times 10^{11}T^4 - 2.667 \times 10^{-15}T^5$$

This correlation is applied for temperatures between 900 and 2300 K. Above 2300 K, the emissivity is 0.40; below 900 K, it is 0.83.

The FRAP-T4-LACE correlation, along with the MATPRO and GAPCON-THERMAL correlations, are shown in Figure 18. All correlations are similar for temperatures below 1300 K. Examination of more recent

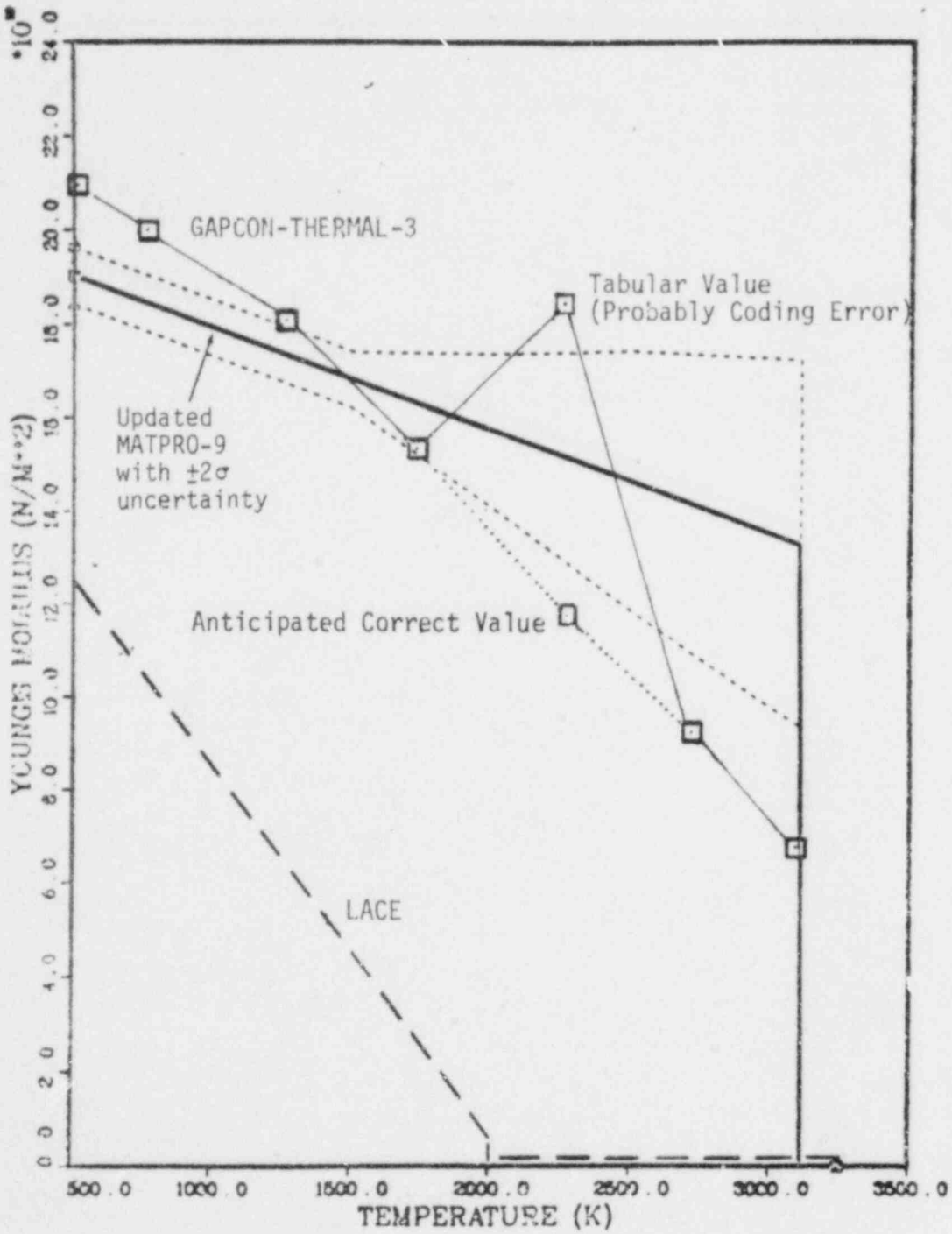

Fig. 17 Fuel elastic modulus versus temperature at 95% TD.

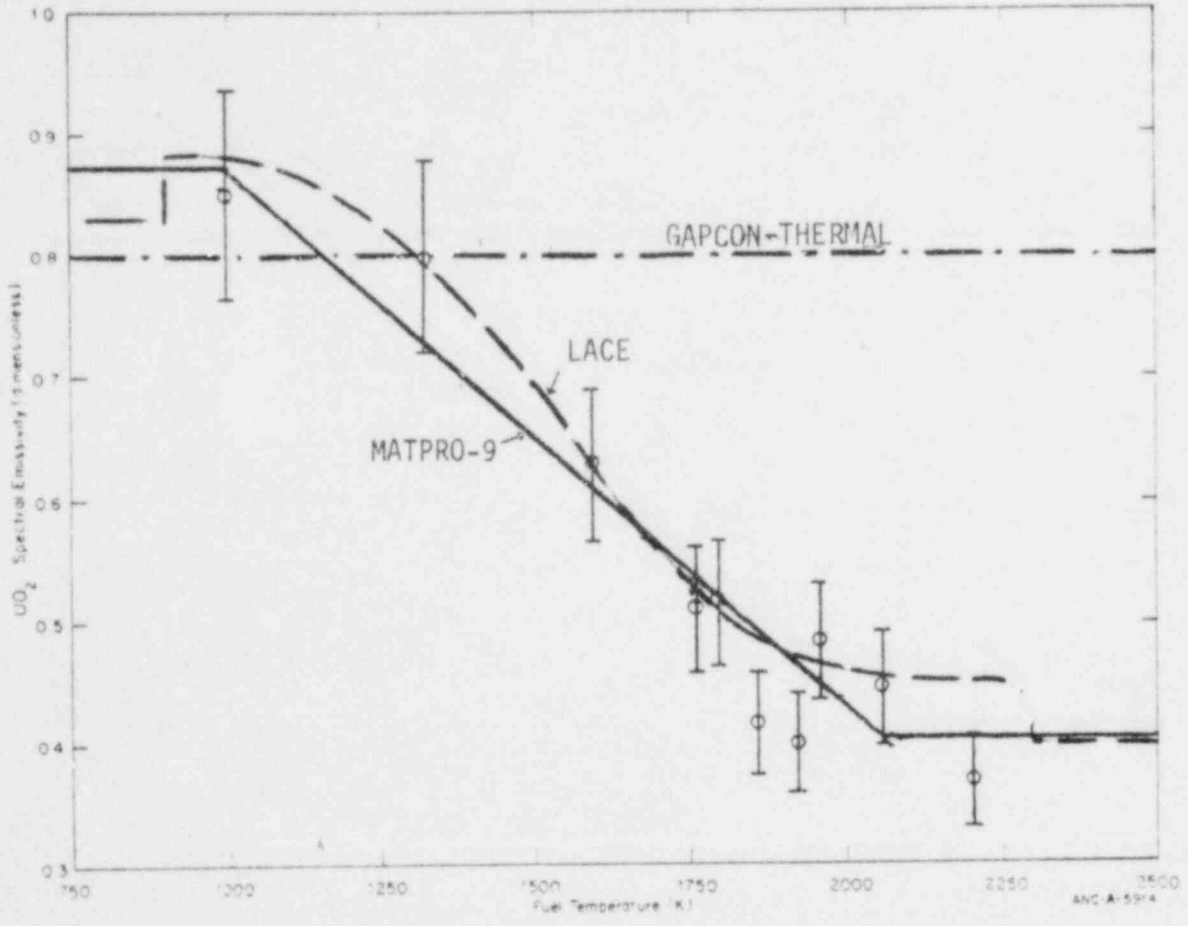

Fig. 18 Fuel emissivity versus temperature.

experimental data indicates that at high temperatures, the MATPRO and FRAP-T4-LACE predictions are too low and the GAPCON-THERMAL predictions are too high.

3.9 Fuel Poisson's Ratio

FRAP-T4-LACE and MATPRO-9 use a constant value of 0.316 to model Poisson's ratio for UO_2 fuel. GAPCON-THERMAL-3 uses a correlation which is a function of temperature and varies from 0.316 to 0.295 from low to high temperatures, respectively.

3.10 Fuel Thermal Conductivity

In compliance with NRC direction, the UO_2 thermal conductivity correlation in FRAP-T4-LACE produces an integral of 93 W/cm from zero to melt temperature. This correlation, a combination of the Lyon's et al[30] and the Maxwell-Eucken correction[31] for porosity, is given by the equation:

$$k_{UO_2} = \frac{1.025}{0.95}(100)\ \frac{D}{1 + (1-D)(0.5)} * \frac{38.24}{[29.4 + T}$$

$$+ (6.125 \times 10^{-13})\ (T^3)$$

where

k_{UO_2} = UO_2 thermal conductivity (W/m-K)

D = fraction of theoretical density

T = temperature (K).

In Figure 19, the FRAP-T4-LACE and MATPRO-9 correlations are compared with the MATPRO-9 data base. The FRAP-T4-LACE values are slightly higher for temperatures up to 2000 K, after which FRAP-T4-LACE

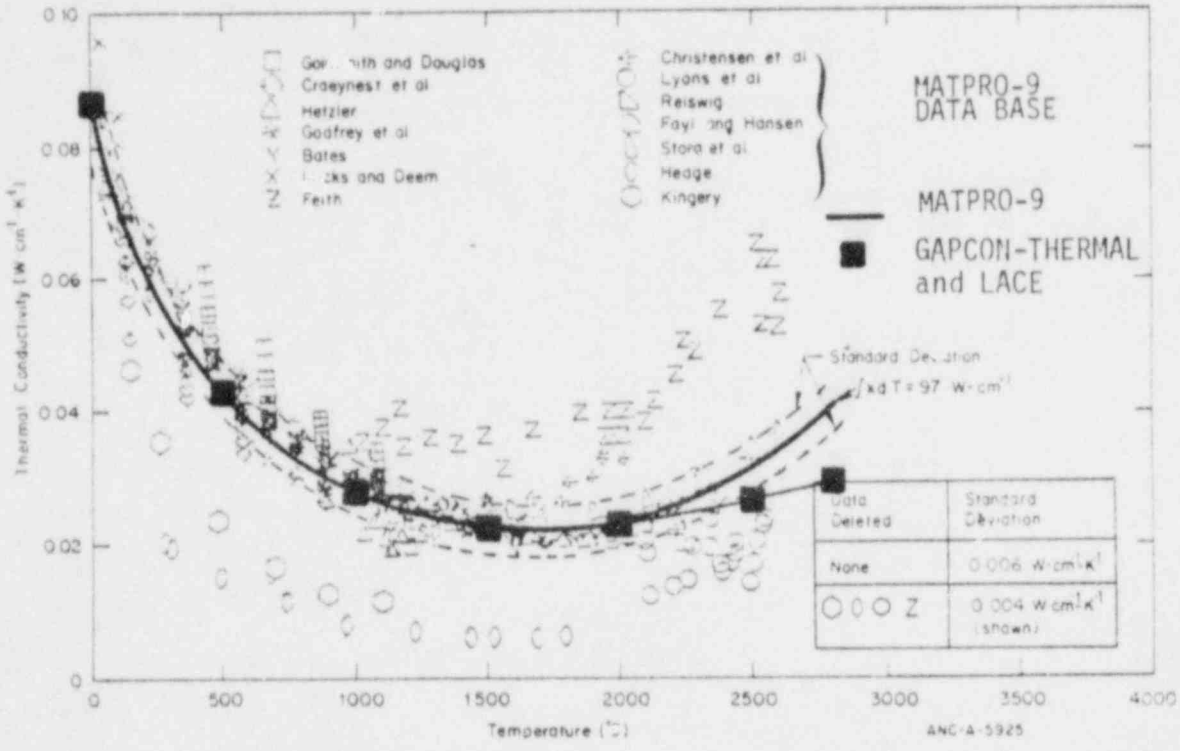

Fig. 19 Thermal conductivity for UO_2 at 95% TD versus temperature.

predicts lower conductivity values. Based on the ten sets of data used to derive the MATPRO-9 correlation, the best estimate value for integral to melt temperature is 97 W/cm.

3.11 Fuel Thermal Expansion

The expression for fuel thermal expansion is

$$\frac{\Delta L}{L} = -1.723 \times 10^{-4} + 6.797 \times 10^{-6} T + 2.896 \times 10^{-9} T^2$$

where

$\frac{\Delta L}{L}$ = linear thermal expansion

T = temperature (^{o}C)

This correlation is compared in Figure 20 with available experimental data and the MATPRO-9 and GAPCON-THERMAL expressions. All expressions are consistent with the data.

3.12 Gas Thermal Conductivity

In FRAP-T4-LACE and also in GAPCON-THERMAL, the gas thermal conductivity correlations are based on Bird, Stewart, and Lightfoot.[32] The basic expression for monatomic gases is

$$k = 1.9 \times 10^{-4} \frac{(T/M)^{1/2}}{\sigma^2 \Omega}$$

where

M = gas molecular weight (g/mole)
σ = Lennard-Jonas constants for monatomic gases
Ω = Lennard-Jonas variable for monatomic gases, a function of temperature.

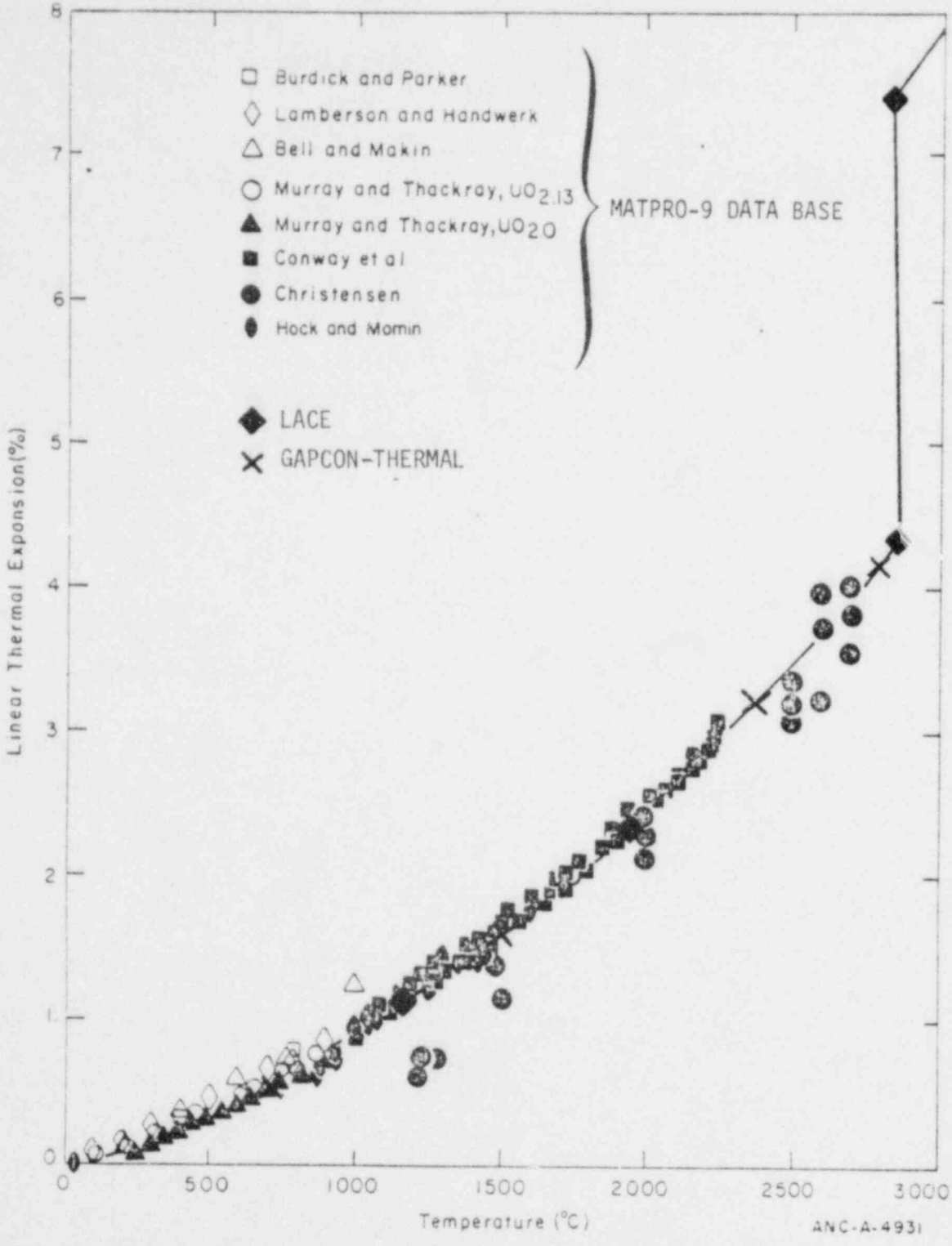

Fig. 20 Fuel linear thermal expansion versus temperature.

The values of σ for each gas are 2.576 for helium, 3.418 for argon, 4.055 for xenon, and 3.498 for krypton. For the diatomic (N_2, H_2, CO_2) gases, the equation is

$$k = (C_p + 1.25\ R)\ \frac{\mu}{M}$$

where

C_p = heat capacity at constant pressure
R = gas constant (1.987 cal/mole-K)
μ = gas viscosity (g/cm-s).

The helium conductivity expression is compared in Figure 21 with experimental data and the MATPRO-9 correlation. The FRAP-T4-LACE expression appears to be best estimate.

When the pellet-cladding gap used in thermal calculations is open, the small gap correction model is used to adjust the gas conductivity value for small gap Knudsen domain effects. Because the correction models in the best estimate and LACE gas conductivity routines are slightly different, gas conductivity predicted by each routine during open gap conditions will be slightly different.

3.13 Correlation Influence Study

The influence of the LACE material property options upon fuel temperatures and stored energy during a typical blowdown calculation was examined. This was accomplished by analyzing a hypothesized LOCA blowdown, using a single LACE material property option while all other options were specified to be best-estimate. All twelve LACE material property options were analyzed in this fashion.

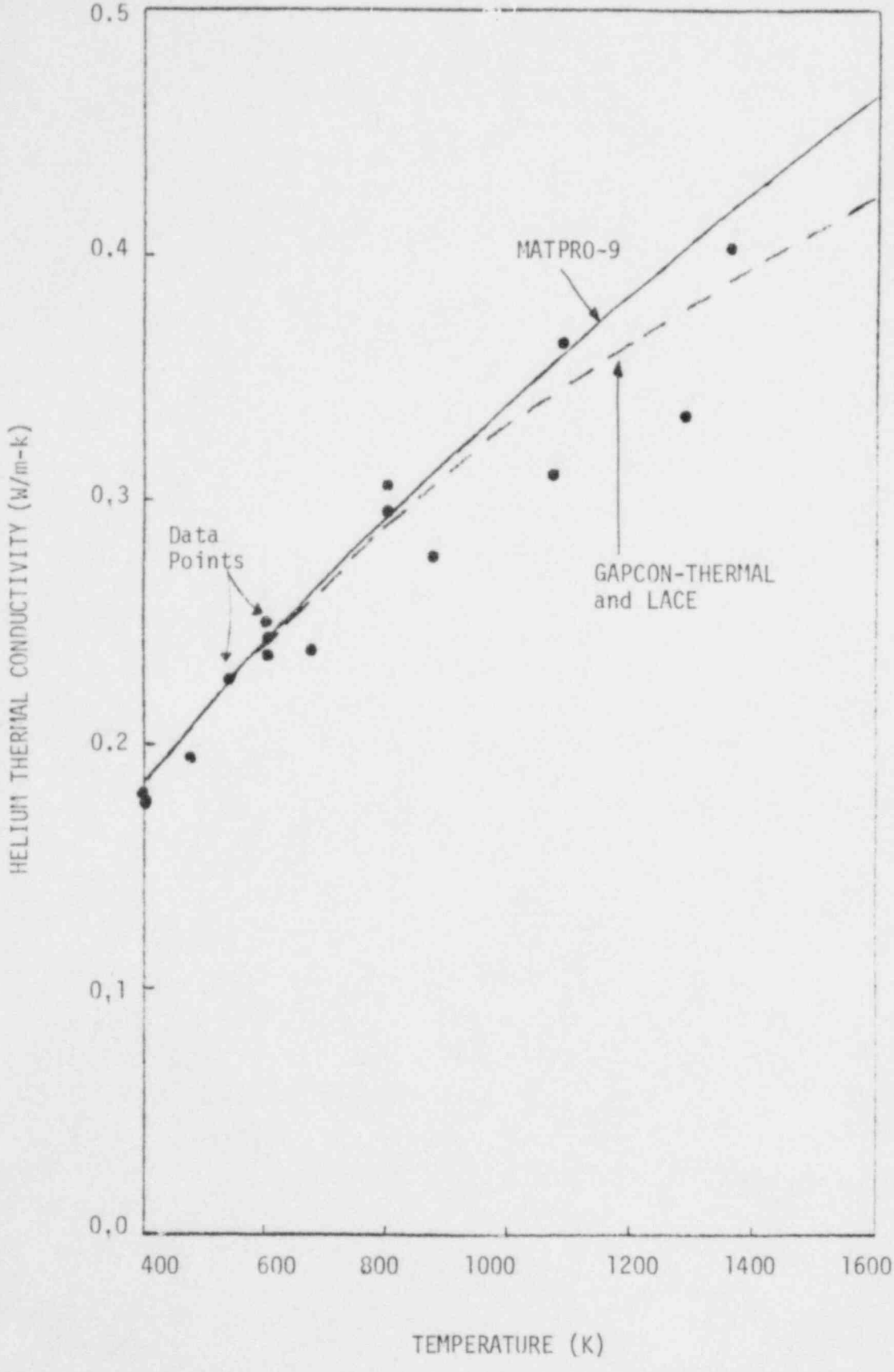

Fig. 21 Helium thermal conductivity versus temperature.

The blowdown problem used in this study is essentially identical to the blowdown portion of the Zion LOCA problem described in Table 4. The basic features of the input are summarized in Table 13. Results of the influence study are given in Table 14. Deviation of the fuel centerline temperature, cladding surface temperature, and fuel stored energy histories from the best estimate values at the peak power axial node are given for three times during the blowdown problem (0, 14, and 28 s).

As can be seen, options 4, 5, 6, 7, 8, 9, 10, 11, 13, and 16 perturb the fuel temperature histories by amounts less than 5 K. For these, the stored energy history is perturbed less than 1 Btu/lbm. This is expected since many FRAP-T4-LACE correlations are essentially identical to the best estimate correlations. Only two options perturb the best estimate predicted temperatures more than 5 K during blowdown, the cladding thermal expansion and fuel thermal conductivity. The LACE cladding thermal expansion correlation (Option 3) tends to decrease slightly the rod temperature and the fuel stored energy. This results from the LACE diametral expansion correlation predicting less cladding strain than the best estimate MATPRO-9 correlation, resulting in a smaller pellet-cladding gap, higher gap conductance values, and lower fuel temperatures. Lower than best estimate temperatures are also seen when the fuel thermal conductivity correlation (Option 12) is used. The temperature reduction occurs because this correlation (due to Lyon) predicts slightly higher fuel conductivity values at low temperatures (<1800 K) than the MATPRO-9 correlation, after which point the MATPRO correlation predicts higher conductivity values. Since fuel temperatures during the example blowdown problem are always below 2000 K, the Lyon's correlation in this temperature region causes the fuel temperatures to be lower overall.

TABLE 13

BLOWDOWN PROBLEM BASE CASE INPUT

UO_2 fueled, zircaloy clad, fuel rod
Rod dimensions - 3.658 m length
0.01072 m diameter
94.5% TD fuel
0.0108 cm radial gap
0.0604 cm cladding thickness
0.9296 cm pellet diameter

Best-Estimate Options Specified:

Ross and Stoute gap conductance model
Cracked fuel conductivity model
Cathcart cladding oxidation model
FRACAS-I mechanical deformation model coupled with fuel pellet relocation model
Pure helium fill gas

TABLE 14

RESULTS OF THE OPTION INFLUENCE STUDY

Deviation From Best Estimate At Peak Power Node

Option(s)	Fuel Centerline Temperature (K)			Cladding Surface Temp (K)			Fuel Stored Energy (Cal/g)			Net Increase Or Decrease
	t = 0 sec T_{base} = 1908	12 1117	28 967	0 T_{base} = 608	12 901	28 855	0 E_{base} = 68	12 49	28 42	
3	-9	-6	-3	0	-2	-2	-0.4	-0.3	-0.3	Decrease
4	0	0	0	0	0	0	0	0	0	0
5	0	0	0	0	0	0	0	0	0	0
6	+2	+1	+1	0	0	0	0	0	0	Increase
7	+1	+1	+1	0	+1	+1	0	0	[illegible]	Increase
8	0	+2	+2	0	+1	+1	0	0	0	Increase
9*	0	0	0	0	0	0	0	0	0	0
10	0	0	0	0	0	0	0	0	0	0
11	0	0	0	0	0	0	0	0	0	0
12	-16	-6	-3	0	-6	-3	-0.4	0	0	Decrease
13	+3	+2	+1	0	+1	+1	0	0	0	Increase
16	-5	-5	-3	0	-2	-2	-0.5	-0.3	-0.2	Decrease

In summary, four FRAP-T4-LACE correlations tend to increase rod temperature and stored energy, three tend to decrease them, and five have no noticeable effect for this example blowdown problem. However, only two options caused significant perturbations, cladding thermal expansion and fuel thermal conductivity.

III. CHECKOUT OF FRAP-T4-LACE AGAINST STANDARD PROBLEMS

The full set of LACE options in FRAP-T4-LACE was exercised for ten different standard problems. These standard problems cover a wide range of hypothesized reactor transient conditions, and constitute the standard problem set against which each succeeding version of the best-estimate code FRAP-T is benchmarked. These comparisons provide a quantitative measure of the conservatism of the LACE evaluation models, and permit a qualitative assessment of the reasonableness of the FRAP-T4-LACE calculations to be made.

1. DESCRIPTION OF STANDARD PROBLEMS

Complete listings of input and output for the ten problems are given on the microfiche attached to this report. The ten problems are summarized in Table 15. They exercise the LACE models over a broad range of coolant conditions, power, and fuel rod design. Five of the problems involve LOCA conditions. Two of the problems involve the reflood stage of a LOCA. All of the problems except Number 10 model beginning-of-life (BOL) events. Both the LACE and BE calculations used the FLECHT correlation for computing the post blowdown cladding surface heat transfer coefficient. A complete list of the models used for the LACE and BE calculations is shown in Table 16.

2. SUMMARY OF COMPARISON RESULTS

The LACE and BE results for the ten standard problem runs are compared in Table 17. A more detailed presentation of the results consisting of plots with overlaid LACE and BE predicted fuel rod response is given in Appendix D. For pressurized fuel rods, the LACE predictions of fuel centerline temperature at accident initiation are about 150 to 300^{o}F higher than the BE predictions . For unpressurized fuel rods, the LACE and BE predicted fuel centerline temperatures at accident initiation are about the same. For all of

TABLE 15

STANDARD PROBLEMS FOR LACE CHECKOUT

Problem	LACE Models Not Used	Comments
ZION PWR LOCA	Infinite operating time for decay heat	Calculations through reflood, LOCA caused by double-ended cold leg break, blo down coolant conditions from RELAP4/MOD5, BOL fuel rod
LOFT 2-2 Test	Infinite operation time for decay heat	Calculations through reflood, blowdown coolant conditions from RELAP4/MOD6, BOL fuel rod
Simplified PWR LOCA	Cladding surface heat transfer coefficient, decay heat	FRAP-T Standard Problem #1, calculations through blowdown, RELAP3 computed coolant conditions input on cards, BOL fuel rod
PBF Test LOC-11C	Infinite operating time for decay heat	Radiation to flow shroud not modeled, coolant conditions from RELAP4/MOD6, BOL fuel rod
TREAT LOCA Test	Cladding oxidation, cladding surface heat transfer coefficient, decay heat	Test designed to simulate post blowdown behavior of BWR fuel rod, coolant conditions computed by FRAP-T
PBF Test PCM 8-1	Decay heat	Sustained film boiling occurs, BOL fuel rod
BWR ATWS	Decay heat	ATWS caused by accidental closure of main stream line isolation valve, fuel-cladding interaction occurs, BOL fuel rod
BWR Hot Standby RIA	Decay heat, transient power	Fuel-cladding interaction occurs, BOL fuel rod
Halden Test HPR-80, rod HBC	Decay heat	Calculation of fuel centerline temperature versus power for unpressurized rod, BOL fuel rod
PWR EOL Power Ramp	Decay heat	Calculation of fuel centerline temperature versus power for end of life pressurized rod, initial conditions obtained from FRAP-S3

TABLE 16

LIST OF MODELS FOR LACE AND BE CALCULATIONS

Phenomenon	LACE Model	BE Model
Gap Conductance	Modified Ross and Stoute	Modified Ross and Stoute
Plenum Gas Temperature	Subroutine PLNT	Subroutine PLNT
Metal-Water Reaction	Baker-Just	Cathcart
Internal Pressure	Ideal gas law, no gas flow	Ideal gas law, no gas flow
Cladding Deformation	Input tables of: Rupture temperature versus ΔP Rupture strain versus ΔP	FRACAS-I, BALOON subcodes
Fuel Deformation	GAPCON model	Free thermal expansion (MODFD=0)
Decay Heat	1.2 x ANS	1.0 x ANS
Critical Heat Flux Correlation	CaW-2	B&W-2
Flow Film Boiling Correlation	Dougall-Rohsenow	Dougall-Rohsenow
Pool Film Boiling Correlation	Modified Bromley ($\alpha \leq 0.6$) Free Convection ($\alpha > 0.6$)	Modified Bromley ($\alpha \leq 0.3$) Free Convection ($\alpha > 0.3$)
Reflood Heat Transfer Model	FLECHT, TOODEE steam cooling model	FLECHT, TOODEE steam cooling
Fuel, Cladding, and Gas Properties	LACE	MATPRO-10
Water Properties	Wagner steam table	Wagner steam table

TABLE 17

COMPARISON OF FRAP-T4 LACE AND BE CALCULATIONS

Problem		Peak Power At Accident Start/Node (kW/ft)[a]	Centerline Temp At Peak Power Node At Accident Start (°F)	Internal Pressure At Accident Start (psia)	Peak Cladding Temp/Node (°F)	Time of Peak Cladding Temp (s)	Time of Cladding Failure (s)	Cladding Oxide Thickness At Problem End (mil)	Maximum Uniform Permanent Hoop Strain/ Node	Cladding Temp At Time of Cladding Failure (°F)
ZION PWR LOCA	LACE	11.2/8	3225	1234	1500/8	4.5	--	0.09	0.007/12	--
	BE	11.2/8	3060	1212	1405/8	4.5	--	0.01	0.017/12	--
LOFT 2-2	LACE	8.2/5	2593	51.7	1300/5	10.0	--	0.0	0.0	--
	BE	8.2/5	2414	44.3	1195/5	9.0	--	0.0	0.0	--
Simplified	LACE	17.7/5	4511	2065	2405/6	10.3	7.6	0.74	0.26/5	1740
PWR LOCA	BE	17.7/5	4231	1945	2000/6	10.3	8.7	0.23	0.073/5	1720
PBF LOC 11C	LACE	22.6/6	5021	1334	2106/6	29.5	14.25	0.68	0.303/6	1690
	BE	22.6/6	4546	1305	1664/6	21.5	17.75	0.19	0.156/6	1550
TREAT LOCA	LACE	0	286	105	2440/5	50.0	29.80	--	0.475/5	2010
	BE	0	286	105	2370/5	40.0	29.00	--	0.092/5	1910
PBF-PCM 8-1	LACE	19.5/9	4443	1610	2350/10	72.0	--	0.85	0.0	--
	BE	19.5/9	4110	1608	2300/9	84.0	--	0.65	0.013/10	--
BWR ATWS	LACE	16.5/4	4516	39.9	1644/4	7.4	--	0.05	0.0	--
	BE	16.5/4	4569	42.1	1154/4	18.0	--	0.0	0.003/4	--
BWR RIA	LACE	b/4	534	28.3	2449/4	1.00	--	0.05	0.0	--
	BE	b/4	534	28.1	2130/4	1.37	--	0.0	0.008/4	--
Halden Rod HBC	LACE	14.8/4	3027	48.2	--	--	--	0.38	--	--
	BE	14.8/4	3026	56.6	--	--	--	0.13	--	--
PWR EOL Power	LACE	12.7/5	2959	1510	--	--	--	--	--	--
Ramp	BE	12.7/5	2741	1644	--	--	--	--	--	--

a Nominal rod power shown. If LACE power model used, the decay heat portion of power multiplied by 1.2, the total power by 1.02.

b Energy input was 250 cal/g in 0.37 s.

the problems involving LOCA conditions, the LACE predicted peak cladding temperatures were 100 to 400°F higher than BE. The LACE and BE models predicted cladding rupture at approximately the same time. The LACE models predicted more cladding plastic strain than the BE models. The LACE models consistently predicted more cladding oxidation than the BE models.

A more detailed study of the LACE models was made with the ZION PWR LOCA transient. This transient was analyzed for three different levels of initial fuel rod power. The three linearly averaged power levels were 9.33 (normal power case), 10.4 and 11.28 (high power cases) kW/ft, respectively. The corresponding peak fuel rod powers were 11.2, 12.45, and 13.5 kW/ft, respectively. An operating time of 10 hr was assumed for the calculation of decay heat (exception to Appendix K rule). This transient was also analyzed for two different flooding rates. In one case, the flooding rate after 106 s of flooding was maintained at a value of 1.001 in./s. In the other case, it was maintained at a value of 0.99 in./s after 106 s of flooding. The two flooding histories are shown in Table 18. For both cases, the flooding began 40 s after initiation of the LOCA. In all cases, the problem was analyzed out to 250 s after initiation of the LOCA. All of the cases used the same blowdown coolant condition history.

The results of the calculations are summarized in Table 19. For an average fuel rod power of 10.4 kW/ft, neither the BE or LACE calculations predicted cladding failure. For an average fuel rod power of 11.28 kW/ft, the BE calculations predicted significant plastic deformation of the cladding, but no failure. For the same power, the LACE calculations predicted cladding failure 104 s after the LOCA initiation.

As shown by the last two cases in Table 19, the peak cladding temperature is sensitive to the flooding rate. In one case, the flooding rate is kept greater than 1 in./s. For this case, the steam cooling model is never used. In the other case, the flooding rate

TABLE 18

FLOODING HISTORY FOR ZION PWR LOCA

Time from Reflood Start (s)	Case 1 Flooding Rate (in./s)	Case 2 Flooding Rate (in./s)
0	10.8	10.8
0.1	11.2	11.2
0.5	7.66	7.66
5.0	1.57	1.57
10.0	1.37	1.37
20.0	1.27	1.27
30.0	1.17	1.17
40.0	1.14	1.14
50.0	1.11	1.11
100.0	1.03	1.03
110.0	1.001	0.99
1000.0	1.001	0.99

TABLE 19

INITIAL POWER AND FLOODING RATE STUDY FOR ZION PWR LOCA

Initial Average Fuel Rod Power (kW/ft)	Flooding Rate After 1 min (in./s)	Type of Calculation	Peak Cladding Temp/Node (°F)	Time of Peak Cladding Temp (s)	Maximum Uniform Permanent Hoop Strain /Node	Time of Cladding Failure (s)	Cladding Oxide Thickness At Problem End (mils)
9.33	1.001	BE	1405/8	4.5	0.014/11	--	0.01
9.33	1.001	LACE	1500/8	4.5	0.007/12	--	0.09
10.4	1.001	BE	1447/8	5.0	0.10/12	--	0.04
10.4	1.001	LACE	1582/12	110	0.03/12	--	0.18
11.28	1.001	BE	1520/8	5.0	0.24/10	--	0.07
11.28	1.001	LACE	1655/12	104	0.35/12	104	0.25
11.28	0.99	LACE	2130/13	250	0.34/12	104	0.84

drops to a little less than 1 in./s. For this case, the steam cooling model is used to compute the cladding surface heat transfer coefficient above the failure elevation. This model predicts significantly less cooling of the fuel rod than the FLECHT correlations. As shown in Figure 22 for the 1.001 in./s case, the cladding temperature above the rupture elevation begins to cool about 100 s after accident initiation. For the 0.99 in./s case, the cladding temperature rises at a rate of 4.7°F/s after the flooding rate drops to less than 1 in./s at a time of 146 s. The cladding temperature rises at a rate of 4.7°F/s for 100 s and then levels off. As shown in Figure 23, the steam cooling model initially predicts a heat transfer coefficient of 4.2 Btu/ft^2-hr-°F, while the FLECHT predicted value is 7.3 BTU/ft^2-hr-°F. At a time of 247 s, the steam cooling predicted heat transfer coefficient increases to 6.7 Btu/ft^2-hr-°F, and the cladding temperature rise is decreased to less than 0.1 °F/s.

The significant increase in the steam cooling predicted heat transfer coefficient at a time of 247 s is due to the increase in the FLECHT predicted heat transfer coefficient at the rupture node (Node 12). A plot of the heat transfer coefficient history at Node 12 is shown in Figure 24. The steam heat capacity in the steam cooling model is adjusted so that the heat transfer coefficient calculated by the Dittus-Boelter correlation gives the same value as the FLECHT correlation at the rupture node. When the FLECHT correlation predicts a rise in the heat transfer coefficient at the rupture node, the steam heat capacity in the Dittus-Boelter correlation rises. At a time of 245 s, the heat capacity used in the Dittus-Boelter correlation is 0.063 Btu/lbm-°F (unadjusted value of 0.516 Btu/lbm-°F). At a time of 250 s, the heat capacity used in the Dittus-Boelter correlation is 0.117 Btu/lbm-°F. This higher heat capacity raises the heat transfer coefficient from 4 to 7 Btu/ft^2-hr-°F.

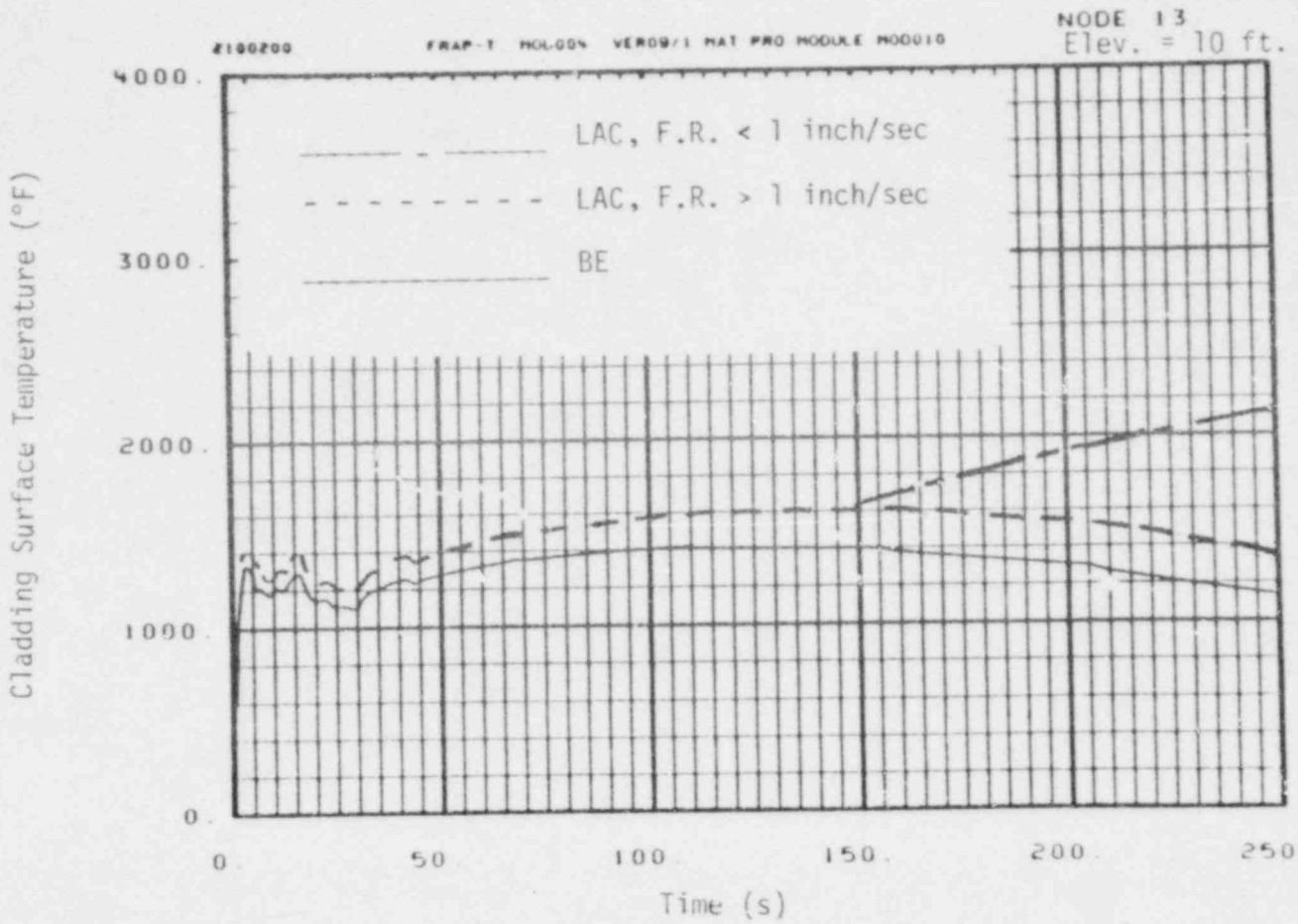

Fig.22 Effect of flooding rate on transient cladding surface temperature (PWR LOCA, high power case)

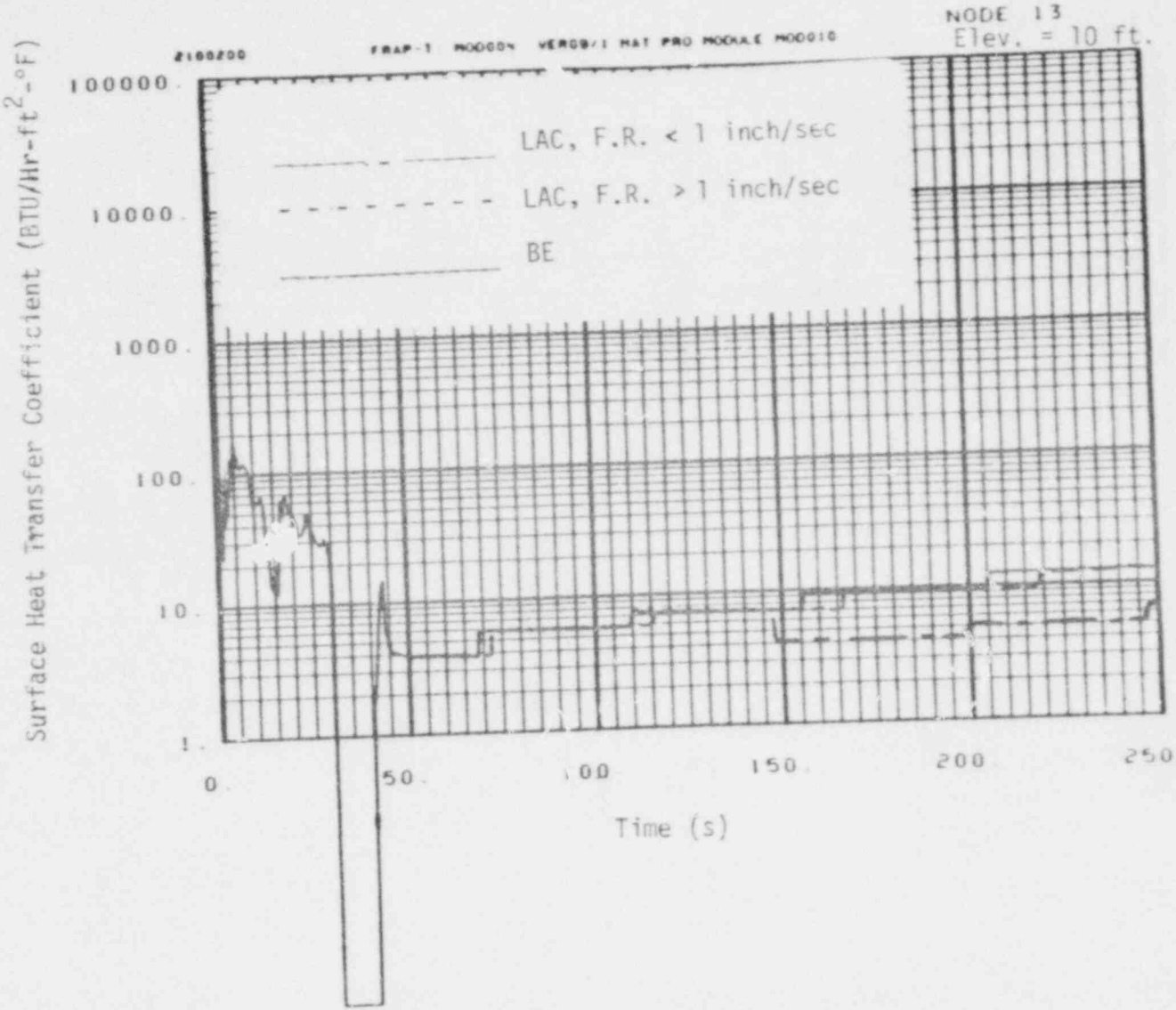

Fig. 23 Effect of flooding rate on transient cladding surface heat transfer coefficient (PWR LOCA, high power case).

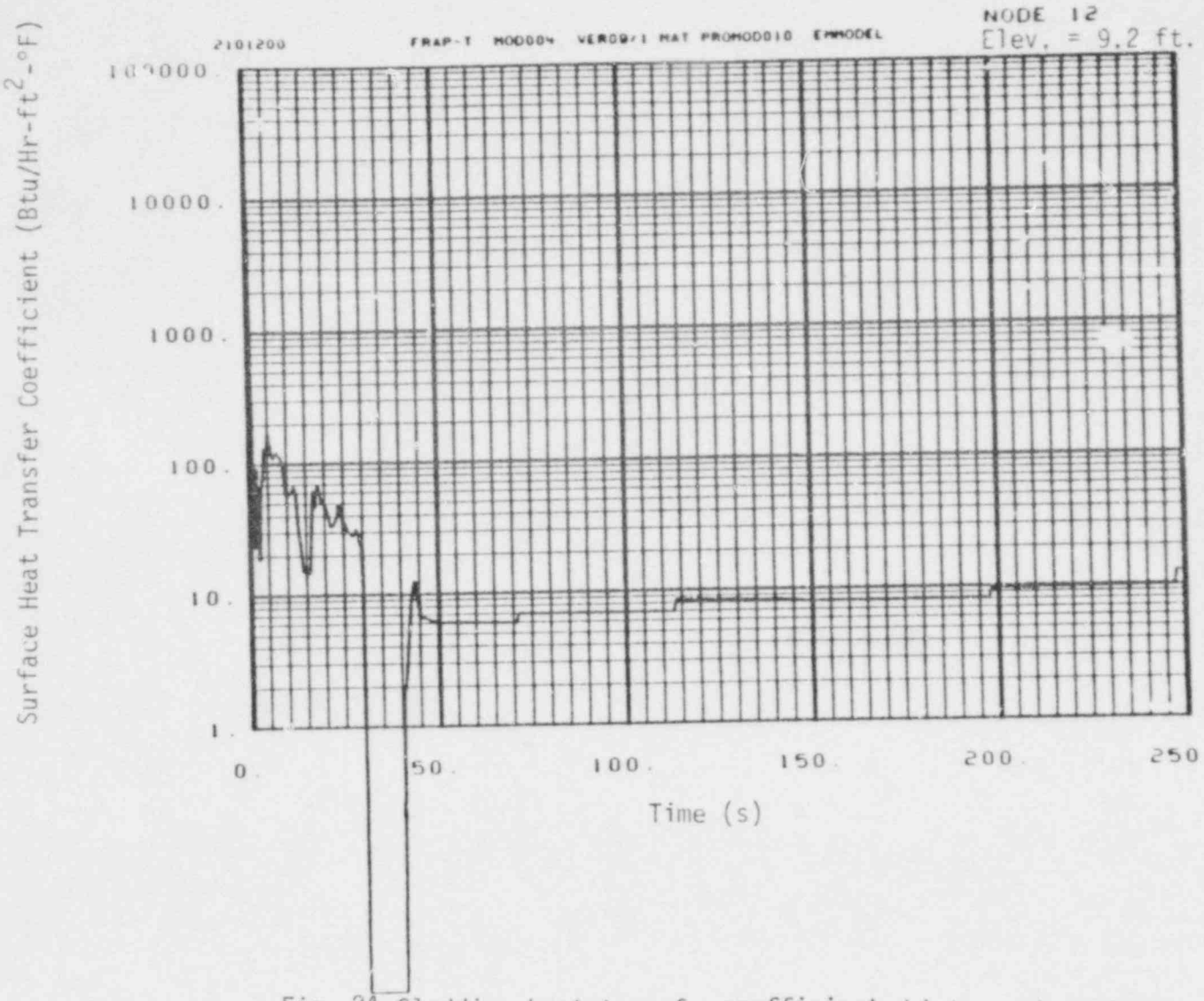

Fig. 24 Cladding heat transfer coefficient history at rupture node (PWR LOCA, high power, 0.99 (in./s case).

The flow blockage has a significant effect on the cladding surface temperature. This is shown in Figure 25, where the variations with elevation of the cladding surface temperature and heat transfer coefficient at a time of 250 s. are plotted. The quench height at this time is almost 6 ft above the bottom of the fuel rod. The cladding ruptured at an elevation of 9.2 ft. The heat transfer coefficient is 50 Btu/ft^{2}hr-°F from the bottom of the fuel rod to the quench height. From the quench height to the rupture plane, the heat transfer coefficient decreases from 50 to 12.5 Btu/ft^2-hr-°F. The heat transfer coefficient is calculated by the FLECHT correlation in this elevation range. Above the rupture plane, the heat transfer coefficient is calculated by the steam cooling model. The heat transfer coefficient decreases to 6.7 Btu/ft^2-hr-°F at the first axial node above the rupture plane, then increases to 12 Btu/ft^2-hr-°F at the top of the rod. The decrease in the heat transfer coefficient is due to flow blockage in the vicinity of the rupture plane. The steam cooling model varies the flow blockage with elevation. At an elevation of 1 ft above the rupture plane, about half of the steam flow is diverted from the fuel rod. At an elevation of 2.5 ft above the rupture plane, little diversion of the steam flow occurs. The flow diversion has a significant affect on the cladding temperature. At th first axial node above the rupture plane, where the flow diversion is the greatest, the cladding temperature is 600°F higher than at the rupture plane.

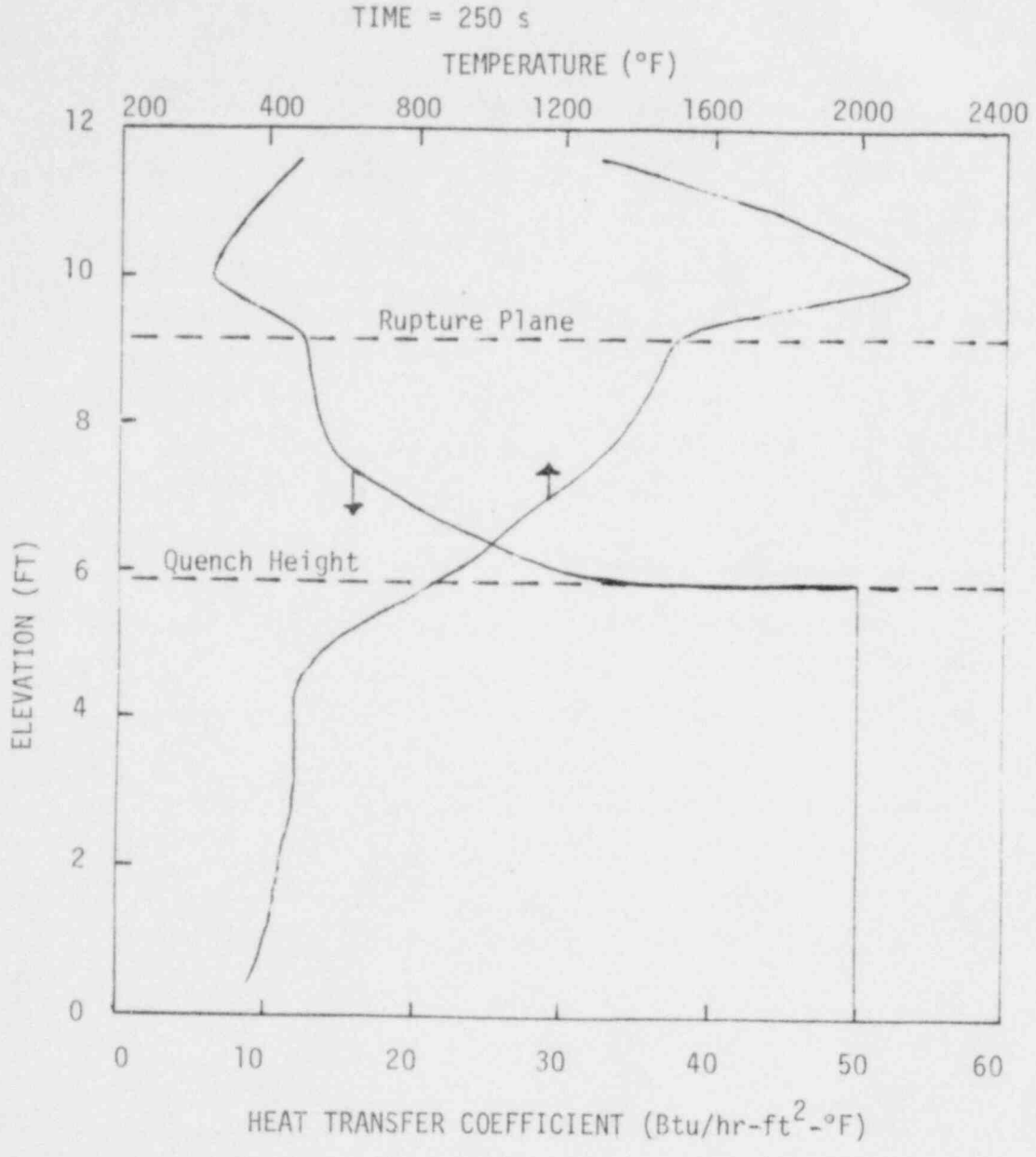

Fig. 25 Cladding surface temperature and heat transfer coefficient profile (time - 250 s).

IV. COMPARISONS WITH FRAP-T4 UNCERTAINTY ANALYSIS PREDICTIONS

1. DESCRIPTION OF THE UNCERTAINTY ANALYSIS OPTION

A FRAP-T5[24] uncertainty analysis option has been developed that allows a user to obtain estimates of the uncertainty in calculated code outputs as a function of known uncertainties in the code input variables. The option has been specifically designed so that any user may perform an uncertainty analysis on any FRAP problem in an understandable, systematic manner. Default uncertainty values for approximately 50 input variables have been built into the code. The option provides for a sequential development of output complexity by allowing the user to restart and continue an analysis from intermediate points. A complete description of the option is available in Reference 33.

The uncertainty analysis option is based on the Response Surface Method. Any of the output variables of the computer code may be termed a response. There is some functional relationship between a response and the input variables. In the space of the input variables, this relationship defines a surface, and hence the term "response surface." When the code is rather simple, this surface may be determined analytically over the entire range of the input variables. More often, as in the case of the FRAP code, the surface may be known only through the code, and the range of inputs and problem types is very large. Thus, the complete true response surface cannot be determined analytically. The response surface method of uncertainty analysis is based on a systematic sampling of the true surface which is then approximated by a polynomial equation in the independent (input) variables. In effect, the true surface is approximated by a smooth surface.[33,34]

The polynomial equation is obtained by truncating a Taylor's series expansion at second order terms. The coefficients of the

equation are estimated from sample values of the true response surface obtained by perturbing the nominal code inputs. For a second order polynomial to reasonably approximate the true response surface, the region of the surface being sampled must be small enough so that large irregularities are not present. Developmental verification efforts have shown that an analysis of residuals, that is, the difference between code and response equation predictions, will verify the adequacy of the response equation fit.

The polynomial approximation to the true response surface may be used to examine the behavior of the true surface in the region of the sample space without the burden of excessive cost. In particular, the polynomial can be used to study the propagation of errors through the code and their effect on the uncertainty in computed outputs. Thus, an estimate of response uncertainty and the relative contributions of the input variables to this uncertainty may be obtained using the response surface method.

Once the user has selected a base case problem and made a choice of output responses and input variables, the following procedures will automatically be followed by the code to obtain the response uncertainties.

(1) An experimental design is computed. This is simply a pattern for perturbing the independent variables of the problem. The pattern is obtained in matrix format where the columns correspond to inputs and the rows correspond to the individual analyses that must be computed. The problem is automatically run as many times as the design dictates, each time varying the input variable perturbations according to the pattern.

(2) The response surface equations are then generated by the code using the information derived from step one.

Basically, a multiple regression routine is used with certain simplifications arising from orthogonal properties of the experimental design.

(3) The code uses the response surface equations to generate uncertainty distributions for the response parameters. Second order error propagation analysis is used to estimate the means and variances of the responses.

(4) Finally, estimates of the fractional contribution of each input uncertainty to the response variances are computed to indicate the relative importance of individual input variables.

2. UNCERTAINTY ANALYSIS OF A LOCA THROUGH REFLOOD

An uncertainty analysis of the best estimate 200% cold leg break Zion LOCA through reflood was performed in order to quantify the degree of conservatism inherent in the LACE calculations for the same problem. The problem analyzed was essentially identical to a standard problem discussed in Section III, specifically using flooding rate history case 2 from Table 18 and a linear average power of 10.0 kW/ft. Probability density distributions were estimated for most of the BE thermal and mechanical code outputs. By comparing the LACE calculated outputs with these distributions, estimates of the probability that the LACE values might occur as a result of uncertainty in the code inputs can be made.

The estimated output uncertainties are strongly dependent on the input uncertainties chosen for the analysis. In this case, seven input variables, or factors, were chosen specifically with the idea of examining the reflood portion of the analysis. Five variables (flooding rate, flow blockage, FLECHT heat transfer correlation, carryout fraction, and the ANS decay heat curve) were thought to most

significantly affect reflood calculations. Two additional variables (gap heat transfer and fuel thermal conductivity) were included because of their known importance in blowdown uncertainty analysis. The variables and their respective uncertainty estimates are shown in Table 20. The analysis was completed in eight executions of FRAP-T5 fitting response equations at two second intervals over a 250 s history for each of the responses. An analysis of residuals (see Reference 34 for a discussion of developmental verification of the method) indicated that the majority of thermal responses were well fit by a linear response equation but that the mechanical responses would probably benefit from a continued analysis and higher order response equations.

Figure 26 compares the BE and LACE calculations for cladding surface temperature during the LOCA history. The dashed lines about the BE curve correspond to plus and minus one standard deviation from the BE calculation. Notice that the LACE calculation lies approximately two standard deviations above the BE curve. If the distribution is approximately normal, this corresponds to a 98% probability that the actual value lies below the LACE value.

Figure 27 illustrates the fractional contributions to the variance (the square of the standard deviation) from each of the inputs during the LOCA history. Notice that during the blowdown portion of the LOCA, when the rod contains significant stored energy, the uncertainties in gap heat transfer and fuel thermal conductivity dominate the calculated uncertainty in cladding surface temperature. Later, however, the reflood variables assume greater importance, and flooding rate in particular contributes almost 90% of the calculated variance by the end of the transient.

Figure 28 compares the LACE and BE calculated fuel centerline temperature with dashed lines showing one sigma uncertainty bands as before. Again, notice that the LACE calculation lies approximately

TABLE 20

REFLOOD LOCA UNCERTAINTY FACTORS*

1. FLOOD RATE	10%
2. FLOW BLOCKAGE PERCENTAGE	5%
3. FLECHT HEAT TRANSFER	10%
4. CARRYOUT FRACTION	10%
5. GAP HEAT TRANSFER	25%
6. FUEL THERMAL CONDUCTIVITY	0.4 (W/m-K)
7. ANS DECAY HEAT CURVE	6.7%

* Normal distributions, one standard deviation

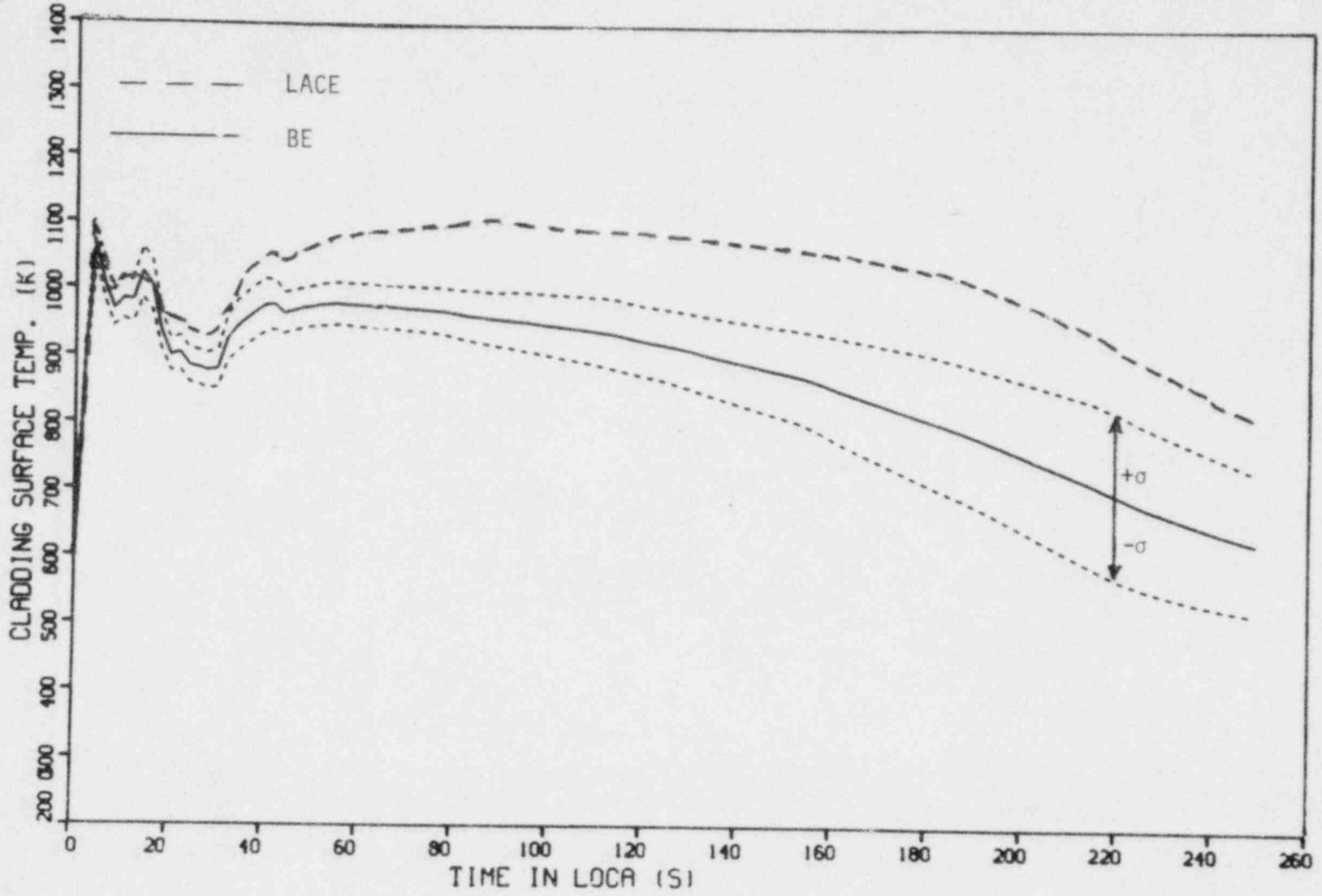

Fig. 26 Comparison of BE and LACE calculated cladding surface temperature.

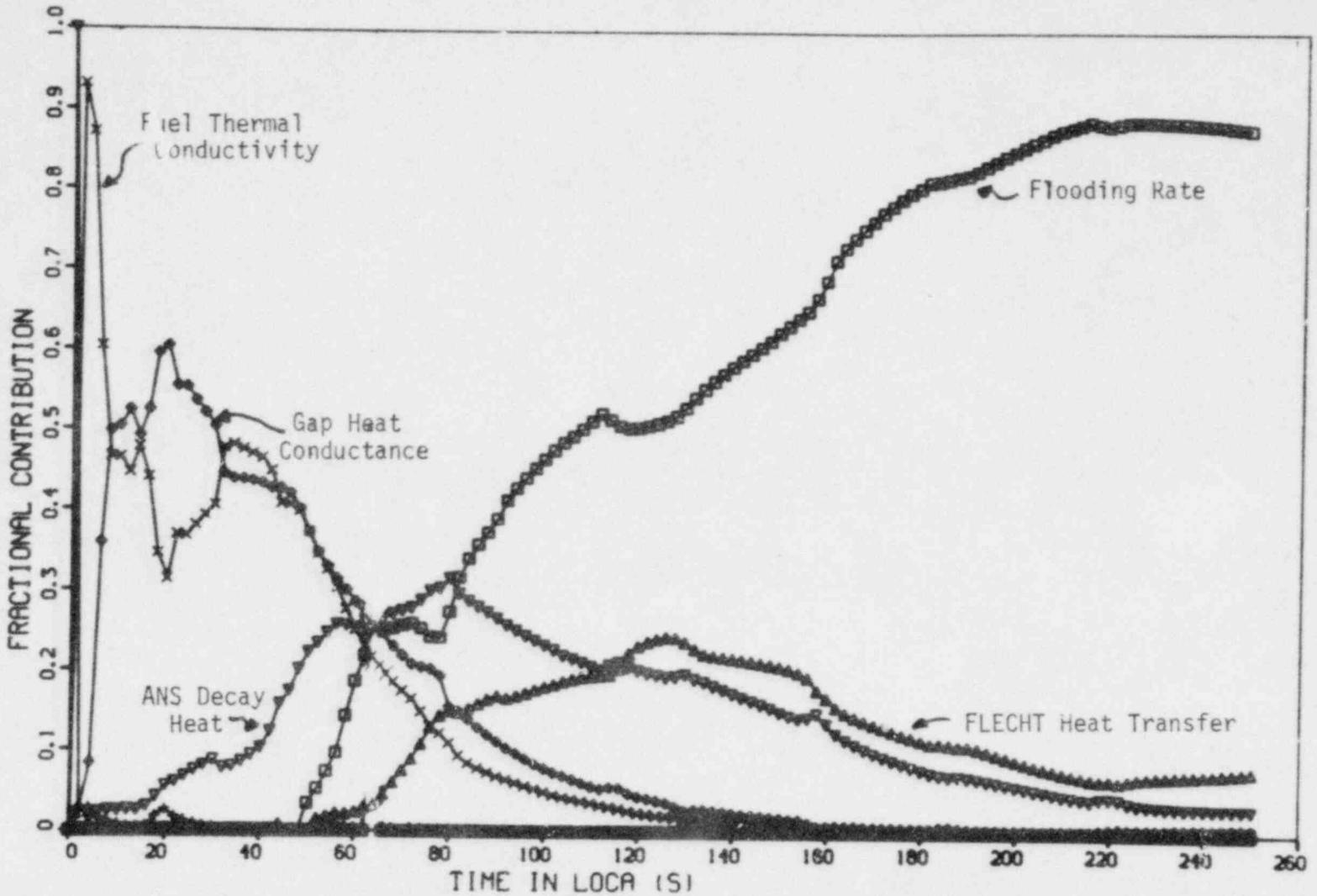

Fig. 27 Fractional contributions to the variance of cladding surface temperature from each input.

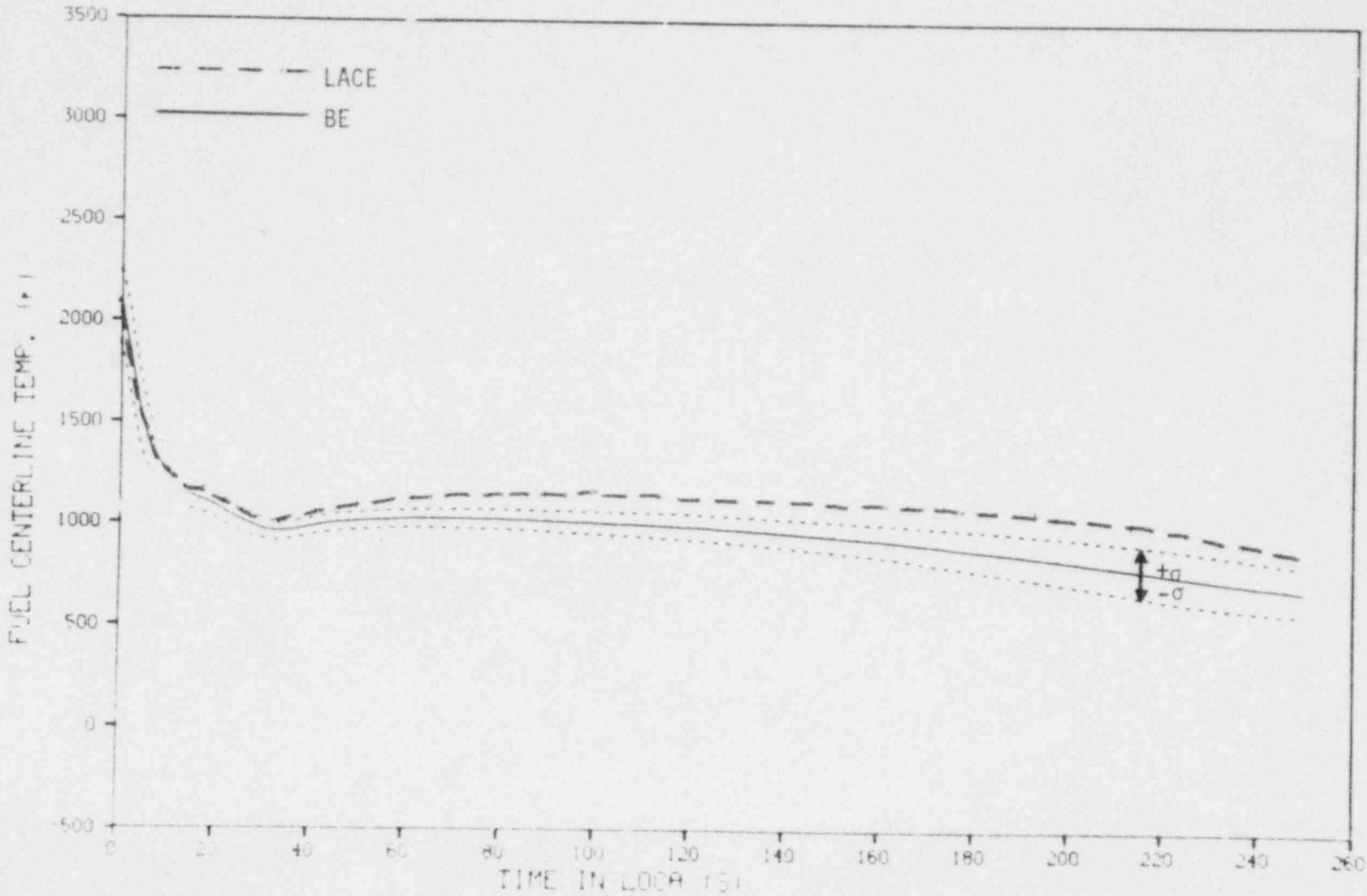

Fig. 28 Comparison of BE and LACE calculated fuel centerline temperature.

two standard deviations more above the BE curve indicating that, as a result of random variations in the inputs, the true value of the BE calculation has a 98% chance of falling below the LACE value. Figure 29 illustrates the fractional contributions of the inputs to the variance of the fuel centerline temperature, with a distribution similar to that for cladding surface temperature. The dominating effect of flooding rate on the calculated uncertainties indicates a clear need to reduce the uncertainty in this model as opposed to the uncertainty in the other variables.

3. ADDITIONAL COMMENTS

The thermal response of the FRAP-T5 calculations using the LACE options lies approximately two standard deviations or more above the corresponding BE calculations. This means that the true BE value that might occur as a result of the assumed random variations in the input variables has a 98% probability of being less than the LACE value if a normal probability distribution is assumed.

The above results apply to errors propagated through the code, and must not be confused with random measurement errors (for example, thermocouple measurement uncertainty), or systematic code error (incorrect modeling). All of these errors sum to determine a total error of simulation, and must be evaluated when code comparisons with independent data are made. For the purpose of comparison of code calculations, however, an evaluation of propagated error through the code is entirely sufficient.

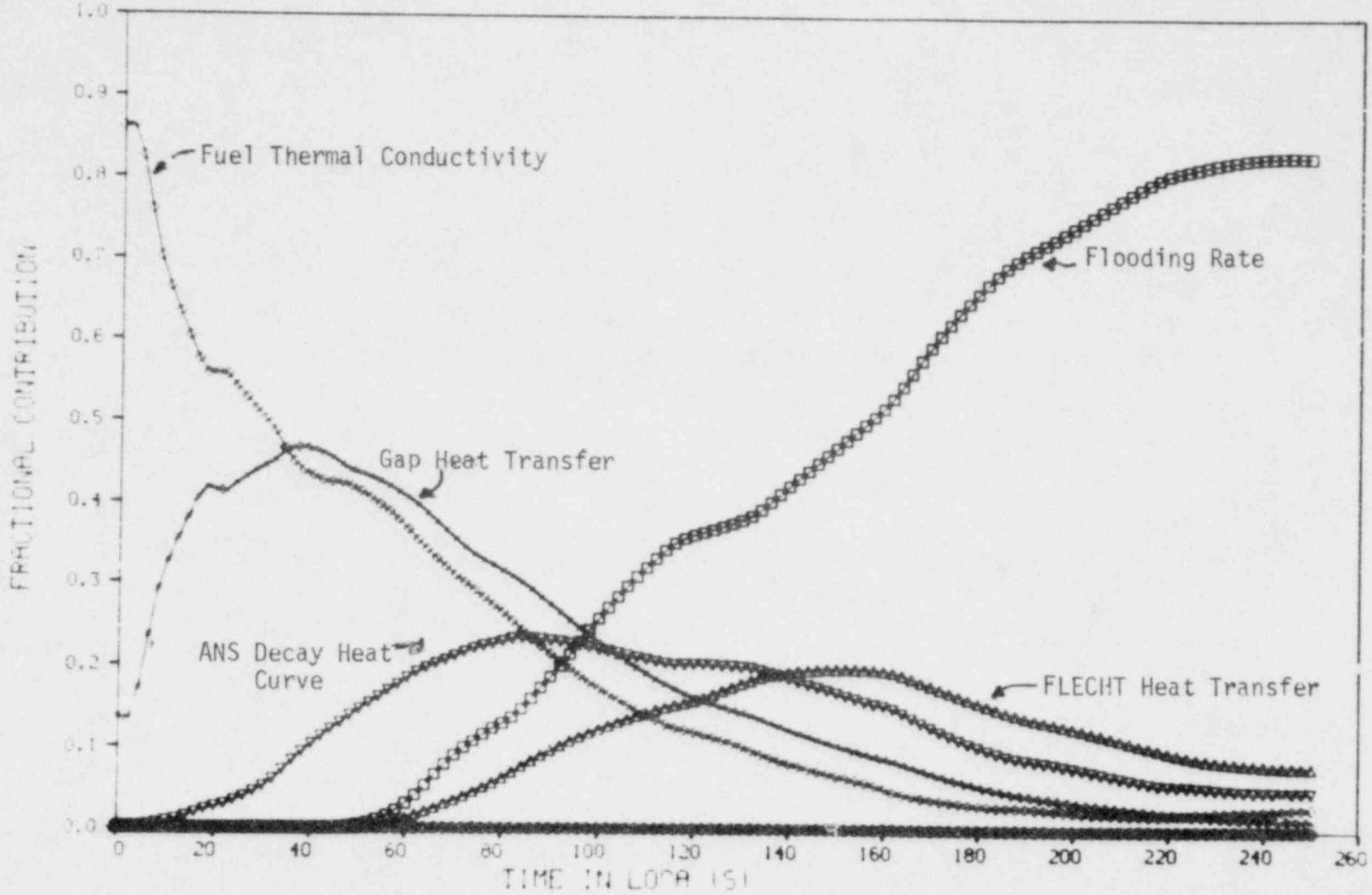

Fig. 29 Fractional contributions to the variance of fuel centerline temperature from each input.

V. CONCLUSIONS AND RECOMMENDATIONS

This report has presented a detailed description of the LACE options incorporated in the fuel rod code FRAP-T4. In addition, the results of a number of studies and comparison problems were presented to benchmark the FRAP-T4-LACE calculations and illustrate some inherent limitations in the LACE models. The conclusions from these checkout studies are summarized below:

(1) The LACE option package as incorporated in FRAP-T4 is performing as intended. Computed cladding temperatures during the LOCA transients studied were always higher than the corresponding best-estimate calculations.

(2) In none of the other types of reactor transients examined (PCM, ATWS, RIA) was the LACE prediction of peak cladding temperature below that predicted by the best-estimate calculations. However, there was little or no conservatism present in peak cladding temperature for these other transients. Modifications to the LACE models would be required for conservative calculations in the other transients.

(3) The LACE material property models are all in reasonable agreement with the corresponding best-estimate models. Varying the LACE models in a one-at-a-time fashion showed that only two of the twelve LACE material property options had any significant effect on the calculation of peak cladding temperature during a typical hypothesized LOCA transient. These two options (cladding thermal expansion and cladding fuel thermal conductivity) tended to slightly decrease peak cladding temperature and initial stored energy. Due to the very small effect that the special LACE material property options have on a typical

LOCA transient, it is recommended that any future LACE option utilize best-estimate material properties.

(4) The LACE and best-estimate FRACAS-I mechanical deformation subcodes were found to be in reasonable agreement, although the LACE failure logic tended to delay the onset of failure. Final cladding diametral strains at failure were in reasonable agreement for the sample LOCA transient examined.

(5) The LACE reflood model was found to be very sensitive to the rate of reflooding. Above flooding rates of 1 in./s, adequate cooling occurs. Below 1 in./s, the FLECHT correlation is used and the steam cooling model is used and deficient cooling results.

(6) During LOCA reflood, the interaction between the steam cooling model and the flow blockage model appears to be performing as designed. For the LOCA transient examined, a temperature increase is calculated immediately above the rupture plane, which is physically expected due to flow diversion around a region of flow blockage.

(7) Comparison of the conservative LACE cladding temperature predictions with those using the FRAP uncertainty analysis option shows that that, for the same input base, the LACE predictions are approximately two standard deviations above the best estimate calculations for the hypothesized LOCA transient examined. On this basis, the results would imply that there is a 98% probability that the actual value would be less than the LACE predicted value. The uncertainty in the best estimate calculation (from which the above conclusion is drawn) is dominated by the uncertainty in the input flooding rate, which is sensitive to the 1 in./s criteria discussed above.

As has been seen, the LACE option package provides a reasonable degree of conservatism in the calculation of peak cladding temperatute during the hypothesized LOCA transients examined. However, no conservatism is provided in the calculation of temperature during a PCM, ATWS, or RIA.

VI. REFERENCES

1. WREM: Water Reactor Evaluational Model (Revision 1), NUREG-75/056 (May 1975).

2. C. R. Hann, C. E. Beyer, L. J. Parchen, GAPCON-THERMAL-1: A Computer Program for Calculating the Gap Conductance in Oxide Fuel Pins, BNWL-1778 (September 1973).

3. J. A. Dearien et al., FRAP-T1: A Computer Code for the Transient Analysis of Oxide Fuel Rods, TREE-NUREG-1041 (February 1977).

4. G. A. Reymann et al., MATPRO-Version 10: A Handbook of Materials Properties for Use in the Analysis of Light Water Reactor Fuel Rod Behavior, TREE-NUREG-1180 (February 1978).

5. D. G. Hardy, "Burst Testing of Zircaloy Cladding for Irradiated Pickering-Type Fuel Bundles", Symposium on the Effects of Radiation on Substructure and Mechanical Properties of Metals and Alloys, Los Angeles, June 25-30, 1972, ASTM-STP 529 (1973) pp 415-435.

6. ANS Standard Decay Energy Release Rates Following Shutdown of Uranium-Fueled Thermal Reactors, ANS-5.1 (October 1971).

7. RELAP4/MOD5: A Computer Program for Transient Analysis of Nuclear Reactors and Related Systems User's Manual, Volume 1, RELAP4/MOD5 Description, ANCR-NUREG-1335 (September 1976).

8. E. D. Hughes, A Correlation of Rod Bundle Critical Heat Flux for Water in the Pressure Range 150 to 725 psia, IN-1412 (July 1970).

9. P. G. Barnett, A Correlation of Burnout Data for Uniformly Heated Annuli and Its Use for Predicting Burnout in Uniformly Heated Rod Bundles, AEEW-R463 (1966).

10. J. S. Gellerstedt et al, "Correlation of Critical Heat Flux in a Bundle Cooled by Pressurized Water", Two-Phase Flow and Heat Transfer in Rod Bundles, Symposium presented at the Winter Annual Meeting of the American Society of Mechanical Engineers, Los Angeles, California, (November 1969) pp 63-71.

11. L. S. Tong, Boiling Crisis and Critical Heat Flux, TID-25887 (August 1972).

12. S. A. Eide and R. G. Gottula, Evaluation and Results of LOFT Steady State Departure from Nucleate Boiling Tests, TREE-NUREG-1043 (Apr 1977).

13. B. C. Slifer and J. E. Hench, Loss-of-Coolant Accident and Emergency Core Cooling Models for General Electric Boiling Water Reactors, NEDO-10329 (April 1971).

14. D. H. Knoebel et al, Forced Convection Subcooled Critical Heat Flux, D_2O, and H_2O Coolant With Aluminum and Stainless Steel Heaters, DP-1306 (February 1973).

15. C E-1: Critical Heat Flux Correlation for CE Fuel Assemblies with Standard Spacer Grids, CENPD-162-P-A, Supplement 1-A (February 1977).

16. F. W. Dittus and L. M. K. Boelter, Heat Transfer in Automobile Radiators of the Tubular Type, University of California Publications, 2 (1930) pp 443-461.

17. J. R. S. Thom et al, "Boiling in Subcooled Water During Flow Up Heated Tubes or Annuli", Proceedings Instrumentation of Mechanical Engineers, (London), 180 (Part 3C) (1966) pp 226-246.

18. V. H. Schrock and L. M. Grossman, Forced Convection Boiling Studies, Final Report on Forced Convection Vaporization Project, TID-14632 (1959).

19. J. B. McDonough, W. Milich, E. C. King, Partial Film Boiling with Water at 2000 psia in a Round Tube, MSA Research Corporation, Technical Report 62 (1958).

20. D. C. Groeneveld, An Investigation of Heat Transfer in the Liquid Deficient Regime, AECL-3231 (Rev.) (December 1968: Revised August 1969).

21. RELAP4/MOD6 UPDATE Version III, Idaho National Engineering Laboratory Configuration Control Number H00441IB.

22. R. L. Dougall and W. M. Rohsenow, Film Boiling on the Inside of Vertical Tubes with Upward Flow of the Fluid at Low Qualities, MIT-TR-9079-26 (1963).

23. F. F. Cadek et al, PWR FLECHT Final Report Supplement, WCAP-7931 (October 1972).

24. L. J. Siefken et al., FRAP-T5 A Computer Code for the Transient Analysis of Oxide Fuel Rods, NUREG/CR-0840, TREE-1281 (June 1979).

25. J. C. Lin, Reflood Heat Transfer and Carryover Rate Fraction Correlations for LOFT Evaluation Model Calculations. LOFT Technical Report 20-96 (March 1979).

26. Ibid Reference 25, Page 44.

27. C. E. Beyer et al., GAPCON-THERMAL-2: A Computer Program for Calculating the Thermal Behavior of an Oxide Fuel Rod, BNWL-1898 (November 1975).

28. D. D. Lanning et al, GAPCON-THERMAL-3: A Computer Program for Calculating the Thermal Behavior of Oxide Fuel Rods, PNL-2434 (February 1978).

29. Ibid Reference 1, Page 2-30.

30. M. F. Lyon's et al., UO_2 Pellet Thermal Conductivity from Irradiation With Central Melting, GEAP-4624 (July 1964).

31. A. Eucken, Forsch. Geb. Ingenieurw, B3, Forschungschaft No. 353 (1932).

32. R. B. Bird et al., Transport Phenomena, John Wiley and Sons, New York, 1966.

33. S. O. Peck, FRAP Uncertainty Analysis Option, CDAP-TR-78-024 (July 1978).

34. N. D. Cox, "Comparison of Two Uncertainty Analysis Methods", Nuclear Science and Engineering, 64 (September 1977) pp 258-265.

APPENDIX A

CORRECTIONS TO LACE MODELS IN FRAP-T4

The LACE models added to FRAP-T4 were taken from an earlier code, REMFRAP[A-1], which was developed for licensing purposes but was never extensively evaluated. In the process of reviewing these models for incorporation into FRAP-T4, a few coding errors were found, as well as instances where the models were hardwired with values applicable only to one standard problem. These problems have been corrected in the final version of the LACE models documented in the body of this report.

This appendix references equations in the main report body* over which questions may still arise or which may be incorrect or different in the RELAP4-EM[A-2] or TOODEE[A-3] codes.

1. FUEL EXPANSION MODEL

The LACE model for thermal expansion is based on the GAPCON-THERMAL-1 model as described fully in the body of the report. It is expressed in Equation 1 as:

$$\Delta R = (\Delta R_L)_{max} + \sum_{i=1}^{L} \Delta t_i \quad . \qquad (A\text{-}1)$$

This expression lacks an additional term which subtracts one-half of Δt_L which is shown in the GAPCON-THERMAL-1 equation. However, this term has been shown to be insignificant computationally.

The original coding of this correlation was in error and was corrected to comply with Equation A-1. This calculation should also be checked in the RELAP4-EM and the TOODEE codes for consistency.

---

* Equation numbers with no letter prefix refer to equations in the main body of this report.

2. CLADDING THICKNESS CALCULATION

The calculation for cladding thickness assumes the change in thickness is proportional to the thermal strain and inversely proportion to hoop strain and is defined in Equation 11 as:

$$\Delta t = \frac{(R_o - R_i)\ (1 + \varepsilon_{TH})}{(1 + \varepsilon_H)} \quad . \tag{A-2}$$

A more exact calculation would be

$$\Delta t = (R_o - R_i)\ (1 + \varepsilon_{TH} + \varepsilon_r) \tag{A-3}$$

However, substitution of Equation A-3 into a FRAP-T4-LACE analysis of a typical LOCA transient analysis showed no significant difference in the thermal response or failure. This is because the elastic strains are very small and also because Equation A-2 approximates Equation A-3. One argument in favor of Equation A-2 is that only hoop strain, ε_H, contains the plastic strain component causing cladding thickness, Δt, to reduce as plastic strain is predicted.

3. INTERFACE PRESSURE CALCULATION

In the original coding of PRSINF, the interface pressure was calculated due to interference fit but the contribution due to gas pressure was not added. This must be added because the deformed fuel dimensions are used in the interference calculation. The total interface pressure must be calculated as shown in Equation 16 so that

$$P = P_{gas} + P_i \tag{A-9}$$

The RELAP4 and TOODEE codes may have this same error. However, it is not significant in LOCA conditions because lockup is never predicted.

4. PREDICTION OF STRAIN AFTER FAILURE

The plastic strain in EMSTRN is a function of the failure strain, F, for the current temperature and pressure and is obtained from the failure tables. Plastic strain is defined in Equation 19 as

$$\epsilon_p = \frac{F \exp(-0.0153\ \Delta T)}{5}. \qquad \text{(A-5)}$$

At the timestep when failure occurs and ΔT is less than or equal to zero, the plastic strain is one-fifth of the strain at failure from the tabulated strain at failure data and is shown in Equation 20 as

$$\epsilon_p = F/5. \qquad \text{(A-6)}$$

At time steps subsequent to failure, ϵ_p equals F so that the total strain approximately equals that predicted in the total strain at failure tables. The total strain may not be handled in this way in the RELAP4 or TOODEE codes.

5. REFERENCES

A-1 R. C. Young, REMFRAP - A Computer Code for the Time Dependent Analysis of Fuel Rods, RE-N-77-004, EG&G Idaho, Inc. (January 1977).

A-2 RELAP4/MOD5: A Computer Program for Transient Thermal-Hydraulic Analysis of Nuclear Reactors and Related Systems User's Manual, ANCR-NUREG-1335 (September 1976).

A-3 G. N. Lauben, TOODEE-II: A Two Dimensional Time Dependent Fuel Element Heat-up Code for PWR Reflood Analysis, USAEC Regulatory Staff (January 1974).

APPENDIX B

CHECKOUT OF SHORT CORE FLECHT MODEL

The generalized FLECHT correlation and the integral power method in FRAP-T4-LACE were verified by comparison with Semiscale data and the calculations of Lin.[B-1] To perform the comparisons, a driver program was written for the reflood subcode of FRAP-T5. The driver program reads the FLECHT or Semiscale axial power profile and test conditions from card input. The program then repeatedly cycles through a loop in which time is increased and the REFLOOD heat transfer subcode of FRAP-T5 is called to calculate the heat transfer coefficient.

The heat transfer coefficient (HTC) histories calculated by the FRAP-T5 REFLOOD subcode for Semiscale Tests S-03-A and S-03-1 are shown in Figure B-1 through Figure B-4. The test conditions are shown in Table B-1. The HTC histories are plotted at the 20 and 29 in. elevations. The measured HTC and the HTC calculated by Lin are also shown in the plots. The FRAP-T5 REFLOOD subcode calculations agree well with the Lin calculations. The agreement is very close from the start of reflood to the start of quenching. After the start of quenching, the HTC calculated by the FRAP-T5 REFLOOD subcode is less than that calculated by Lin. This difference in calculated HTC is due to differences in approximating the Semiscale axial power profile.

The generalized FLECHT correlation was further checked by comparison with the FLECHT correlation originally put into the FRAP-T4 code. The original correlation was taken from the TOODEE-2 code. The reflood heat transfer for the LOFT 2-2 test was predicted with both FLECHT correlations. The results are compared in Figures B-5 and B-6, in which the heat transfer coefficient of the hot rod is plotted as a function of time. The reflood heat transfer regime begins at 40 s. The heat transfer coefficient predicted by the generalized FLECHT

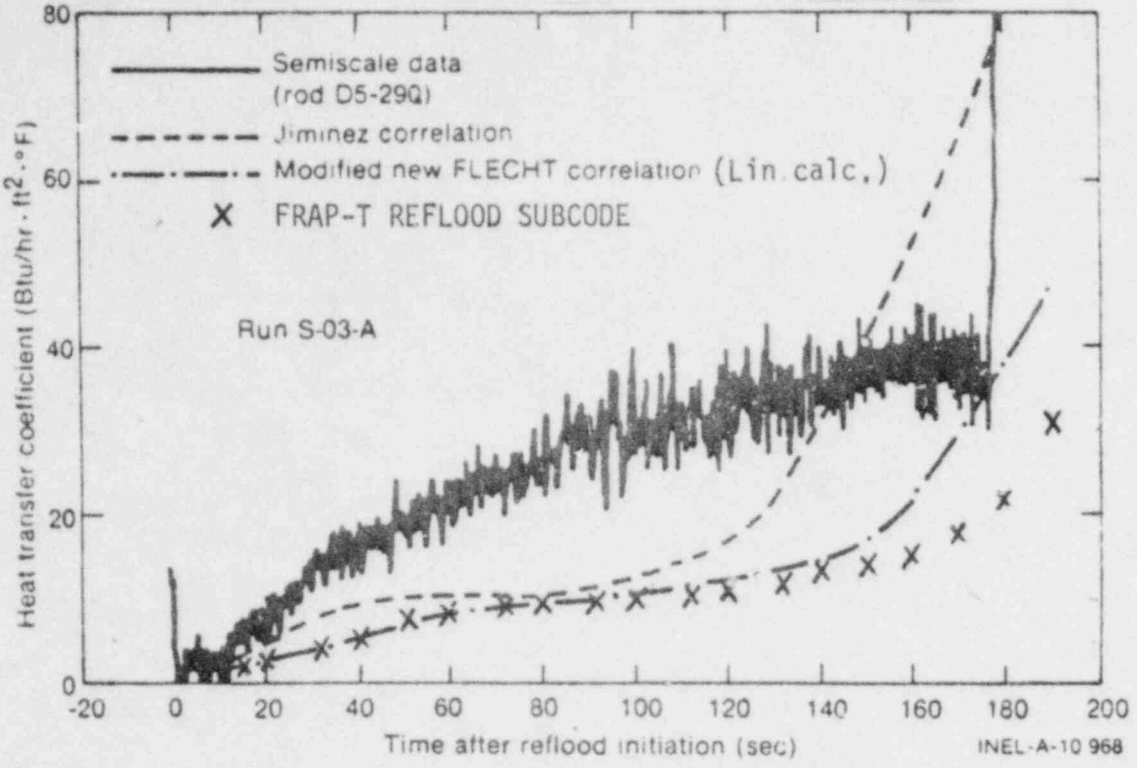

Fig. B-1 Heat transfer coefficient history of Semiscale Test S-03-A at 29 in. elevation.

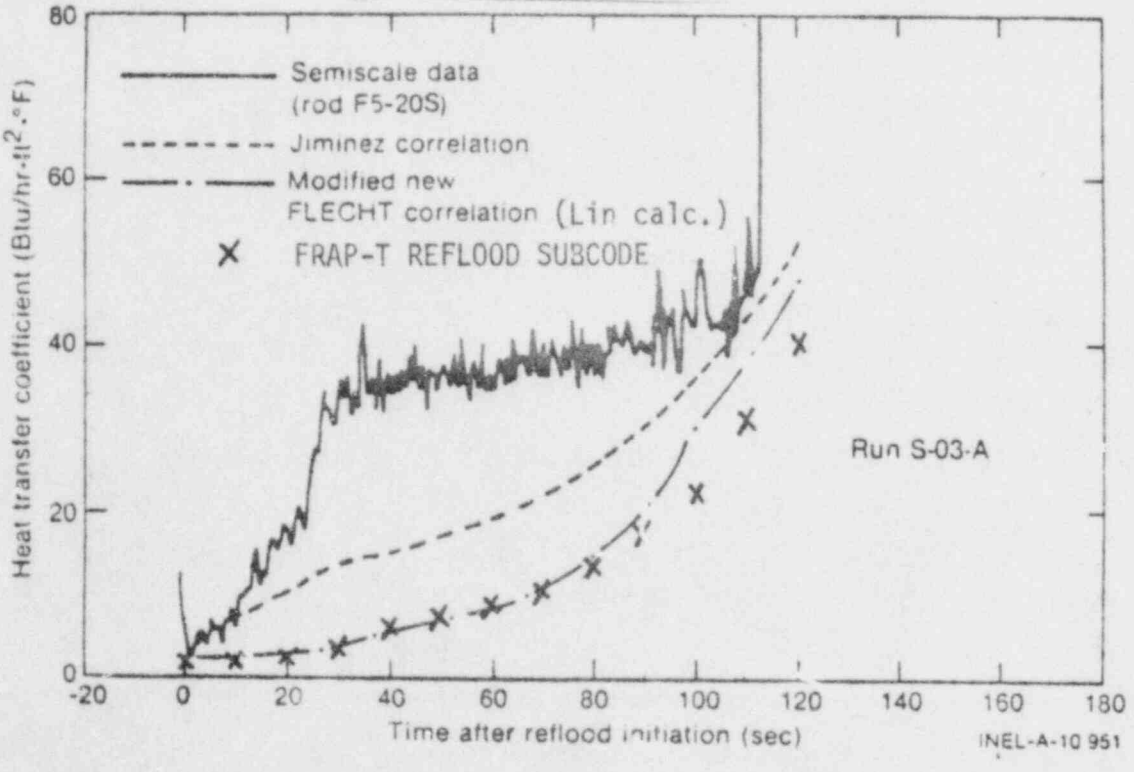

Fig. B-2 Heat transfer coefficient history of Semiscale Test S-03-A at 20 in. elevation.

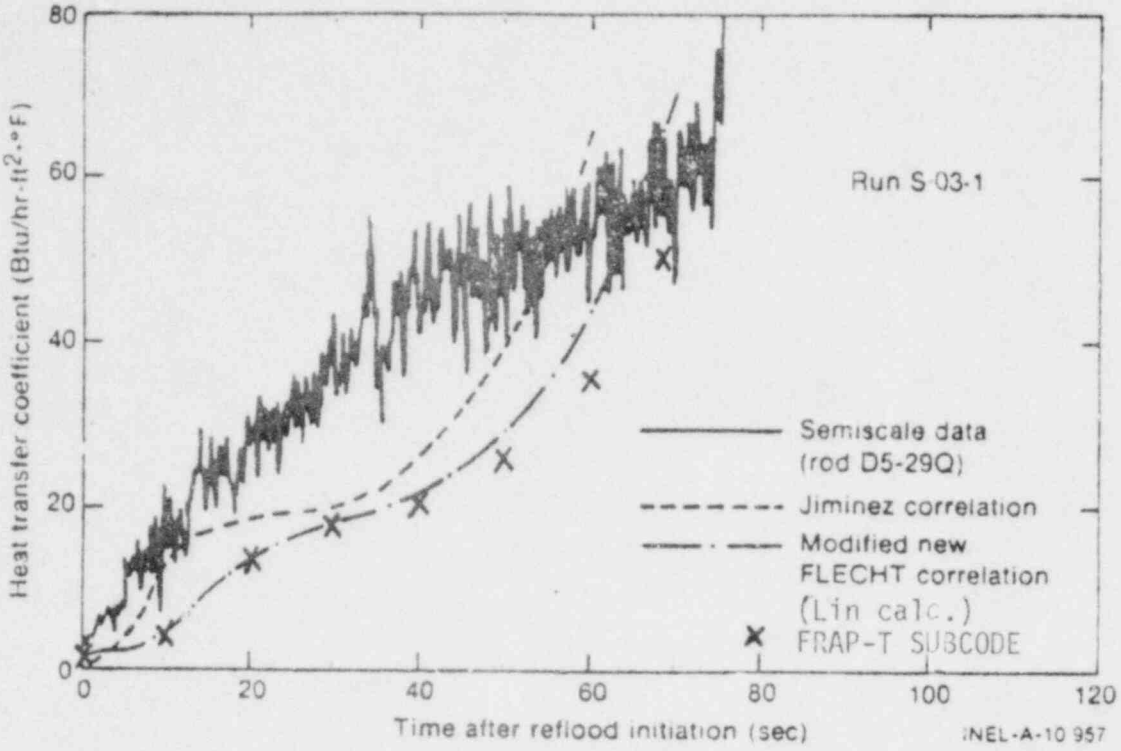

Fig. B-3 Heat transfer coefficient history of Semiscale Test S-03-1 at 29-in. elevation.

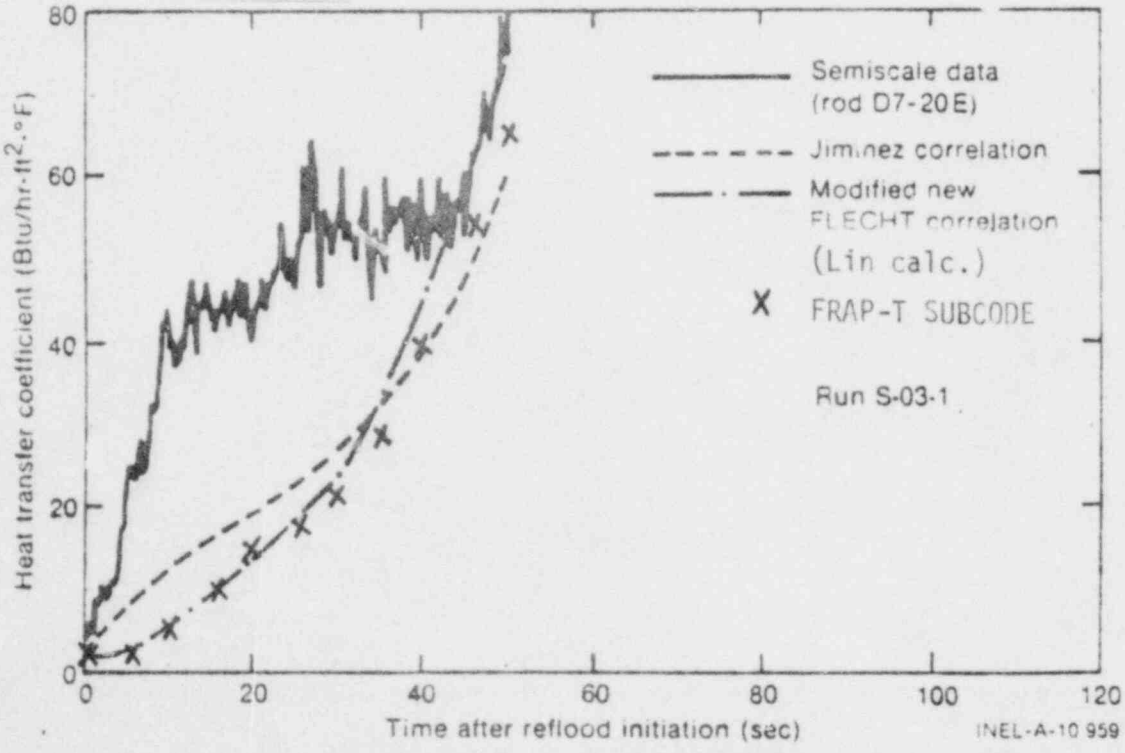

Fig. B-4 Heat transfer coefficient history of Semiscale Test S-03-1 at 20-in. elevation.

TABLE B-1
SEMISCALE TEST CONDITIONS

PARAMETER	TEST S-03-A	TEST S-03-1
Cold reflood rate (in./s)	1.0	1.8
Maximum rod power (kW/ft)	0.7	0.7
Core radial power profile	Flat	Flat
Maximum initial cladding temperature (°F)	1400	1400
Reflood water subcooling (°F)	140	140
Vessel pressure (psia)	20	60

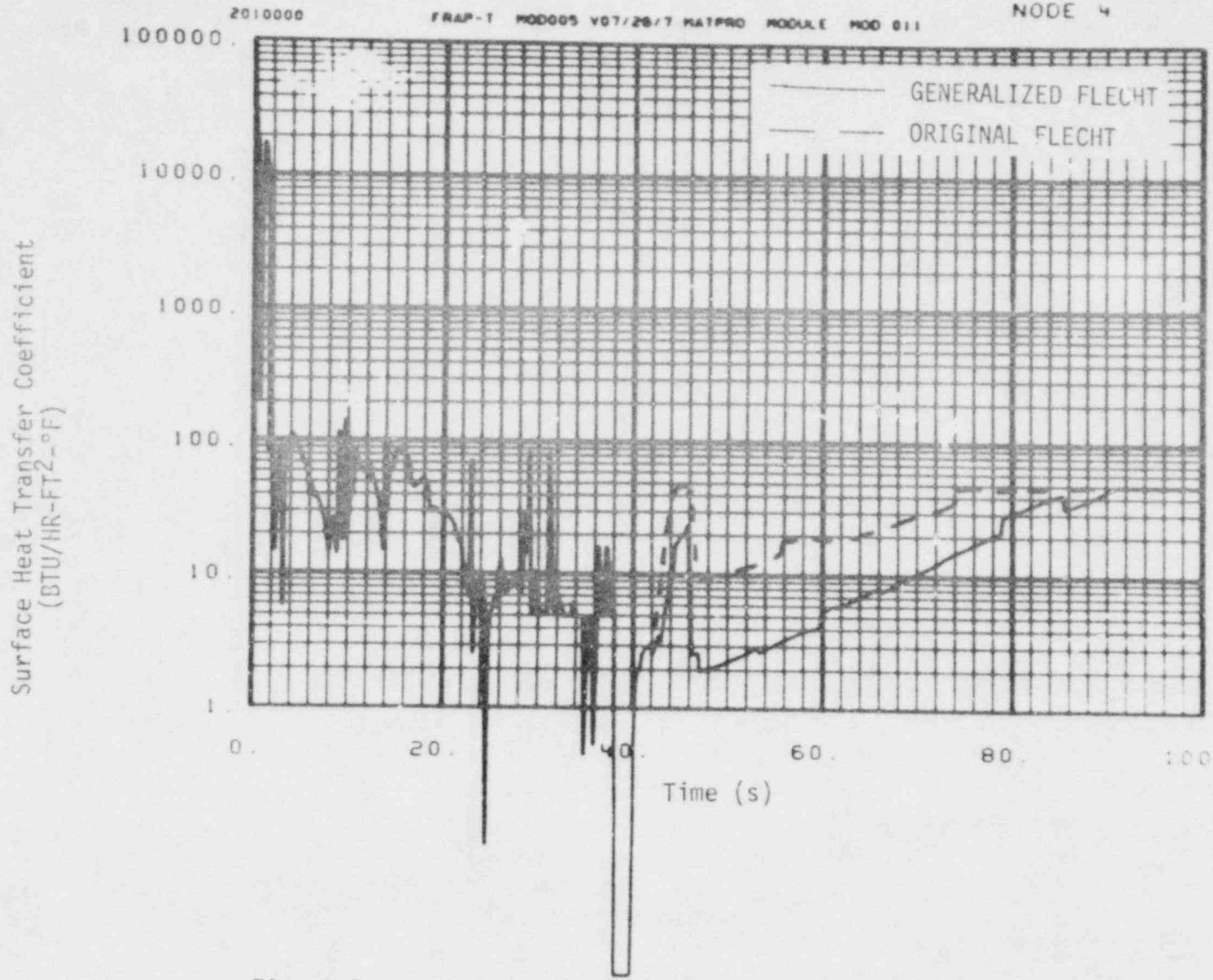

Fig. B-5 Comparison of original and generalized FLECHT correlations for LOFT 2-2 test hot rod at elevation of 1.6 ft.

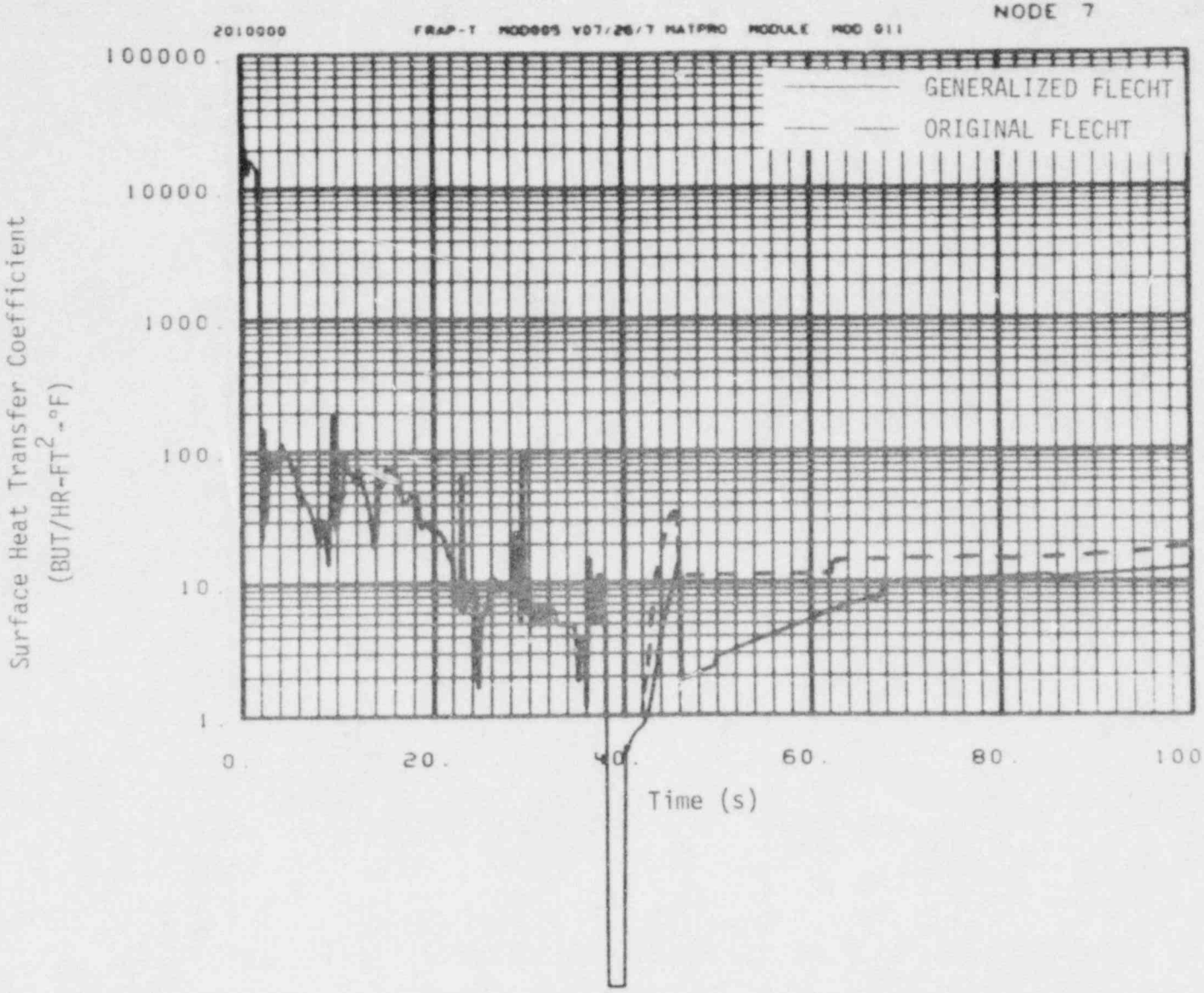

Fig. B-6 Comparison of original and generalized FLECHT correlations for LOFT 2-2 test hot rod at elevation of 3.0 ft.

correlation is less than or equal to that of the original FLECHT correlation over the entire time span of reflooding. The differences between the two correlations are the greatest at the start of reflooding and least at the end of reflooding. Both correlations show a pulse of cooling to occur for 2 s at the start of reflooding.

The cladding surface temperature histories corresponding with the heat transfer coefficient histories shown in Figure B-6 are shown in Figure B-7. After 60 s of reflooding, the cladding surface temperature calculated using the generalized FLECHT correlation is 150°F higher than that calculated using the original FLECHT correlation.

REFERENCES

B-1. J. C. Lin, Reflood Heat Transfer and Carryover Rate Fraction Correlations for LOFT Evaluation Model Calculations, LTR-20-96 (March 1979).

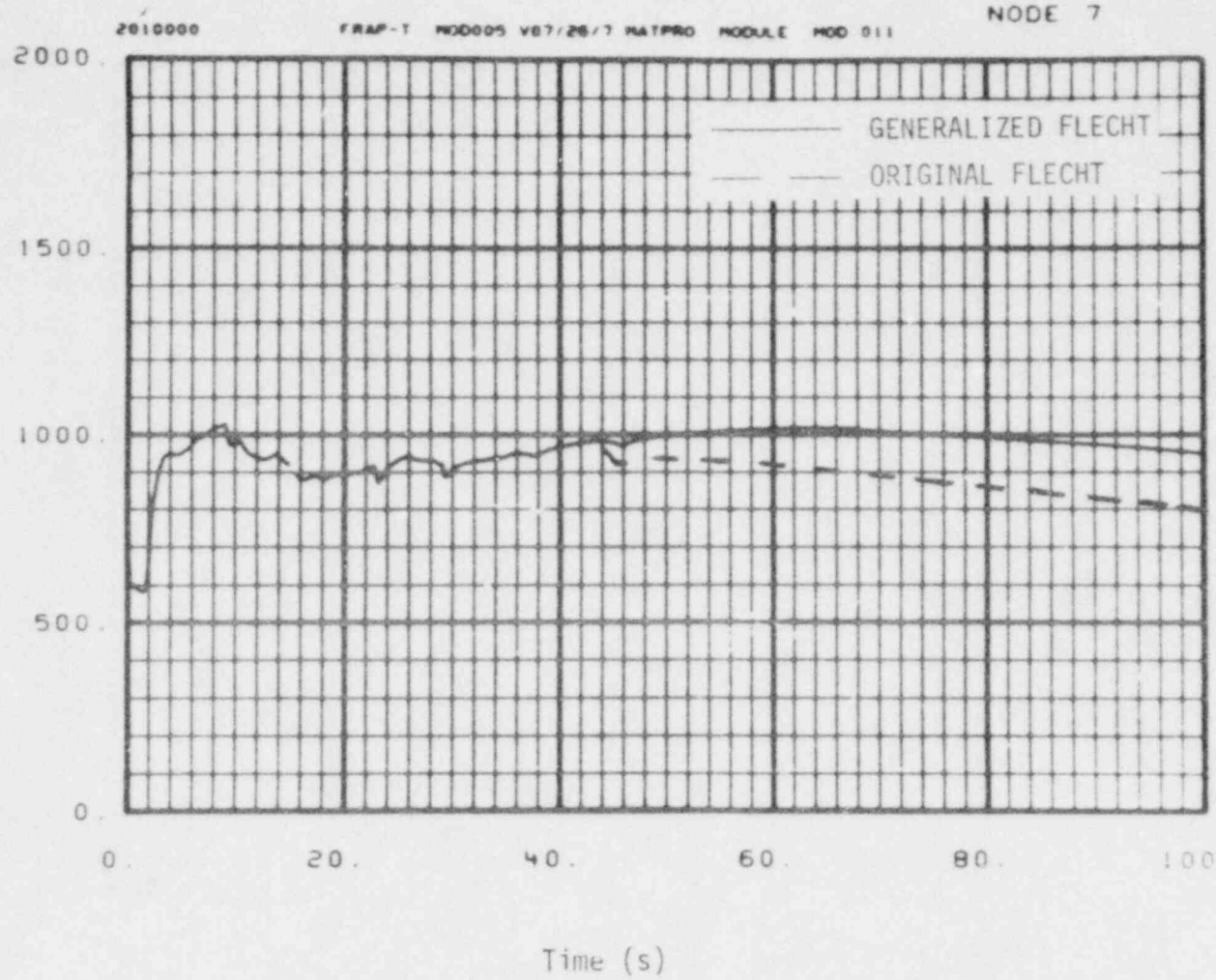

Fig. B-7 Comparison of cladding surface temperature for the original and generalized FLECHT correlations for LOFT 2-2 test hot rod at elevation of 3.0 ft.

APPENDIX C

Additional Input Data for Short Core FLECHT Correlation

If reflood heat transfer is calculated by the generalized FLECHT correlation, some additional input to the FRAP-T5 code is required. The additional input occurs in Card Group 1.20. There are two additional variables on Card 1.20.1 and a new card after Card 1.20.5. The contents of these cards are shown below.

Card 1.20.1

Columns	Format	Name	Quantity
5	I	NFLEC	Switch for selection of FLECHT correlation. If NFLEC = 0, the generalized FLECHT correlation is used. If NFLEC = 1, the FRAP-T4 version of the FLECHT correlation is used.
10-11	A	NSWRLD	Input the character string ON in Columns 10-11.
15-24	F	EMPYTM	Problem time, in seconds, at which the core is dry and begins adiabatic heatup.
27-36	F	REFDTM	Problem time, in seconds, at which flooding of fuel rods begins.
39-48	F	HRAD	Radiation heat transfer coefficient. If HRAD < 0.0, HRAD is computed. (BtU/hr-ft^2-°F)

51-55	I	NBR1	Number of inlet temperature (^{o}F) versus time (sec) pairs, NBR1 $\leq$ 20.
55-60	I	NBR2	Number of flooding rate (in./s) versus time (s) pairs, NBR2 $\leq$ 100.
66-70	I	NBR4	Number of reactor vessel pressure (psia) versus time (s) pairs, NBR4 $\leq$ 20.
71-75	I	NBR5	Number of collapsed liquid level (ft) versus time (s) pairs, NBR5 $\leq$ 50. If the carryover rate fraction is to be computed by the FRAP-T4 correlation for carryover rate fraction, set NBR5 = 0.

Card(s) 1.20.6 Collapsed Liquid Level History (If NBR5 = 0 on Card 1.20.1, omit this card.)

Columns	Format	Name	Quantity
1-10	F	HLIQ(1)	Collapsed liquid level at time TIME (1) (ft).
11-20	F	TIME(1)	Time from beginning of reflood (s) (must be 0.0).
21-30	F	HLIQ(2)	Collapsed liquid level at time TIME (2) (ft).
31-40	F	TIME(2)	Time into reflood (s).

41-50	F	HLIQ(3)	Collapsed liquid level at time TIME (3) (ft).
51-60	F	TIME(3)	Time into reflood (s).

Continue on additional cards until NBR5 pairs have been entered. A maximum of 16 and two-thirds cards are allowed.

APPENDIX D

LACE Analysis of Standard Problems

The fuel rod response is presented for each standard problem, and the LACE and BE calculated responses are overlaid. The LACE and BE calculations used the same models for calculating the post blowdown cladding surface heat transfer coefficient.

1. Zion PWR LOCA Problem

Plots of the computed fuel response are shown in Figures D-1 through D-13 for initial average fuel rod powers of 9.33 (normal power case) and 11.28 (high power case) kW/ft. For the normal power case, the fuel rod response is plotted for axial node 8, which is 6 ft. above the bottom of the fuel rod. This is the elevation at which both peak fuel rod power and peak transient cladding temperature occur. For the high power case, plots are shown for Nodes 8, 12, and 13, which have elevations of 6, 9.2, and 10.0 ft., respectively. For the BE calculations for the high power case, the peak cladding temperature occurred at Node 8. For the LACE calculations with flooding rate greater than 1 in./s, the peak cladding temperature occurred at Node 12. For the LACE calculations with a flooding rate less than 1 in./s, the peak cladding temperature occurred at Node 13. For all cases, the peak cladding deformation occurred at Node 12.

As shown in Figures D-1 through D-4, the LACE predicted cladding surface temperature is always greater than the BE predicted temperature. For the most part, the differences between LACE and BE predicted temperatures range from 100 to 200°F. The LACE and BE calculations both predict film boiling to start at the same time. As shown in Figures D-5 through D-8, the LACE predicted fuel centerline temperatures also are 100 to 200°F greater than the BE predicted temperatures.

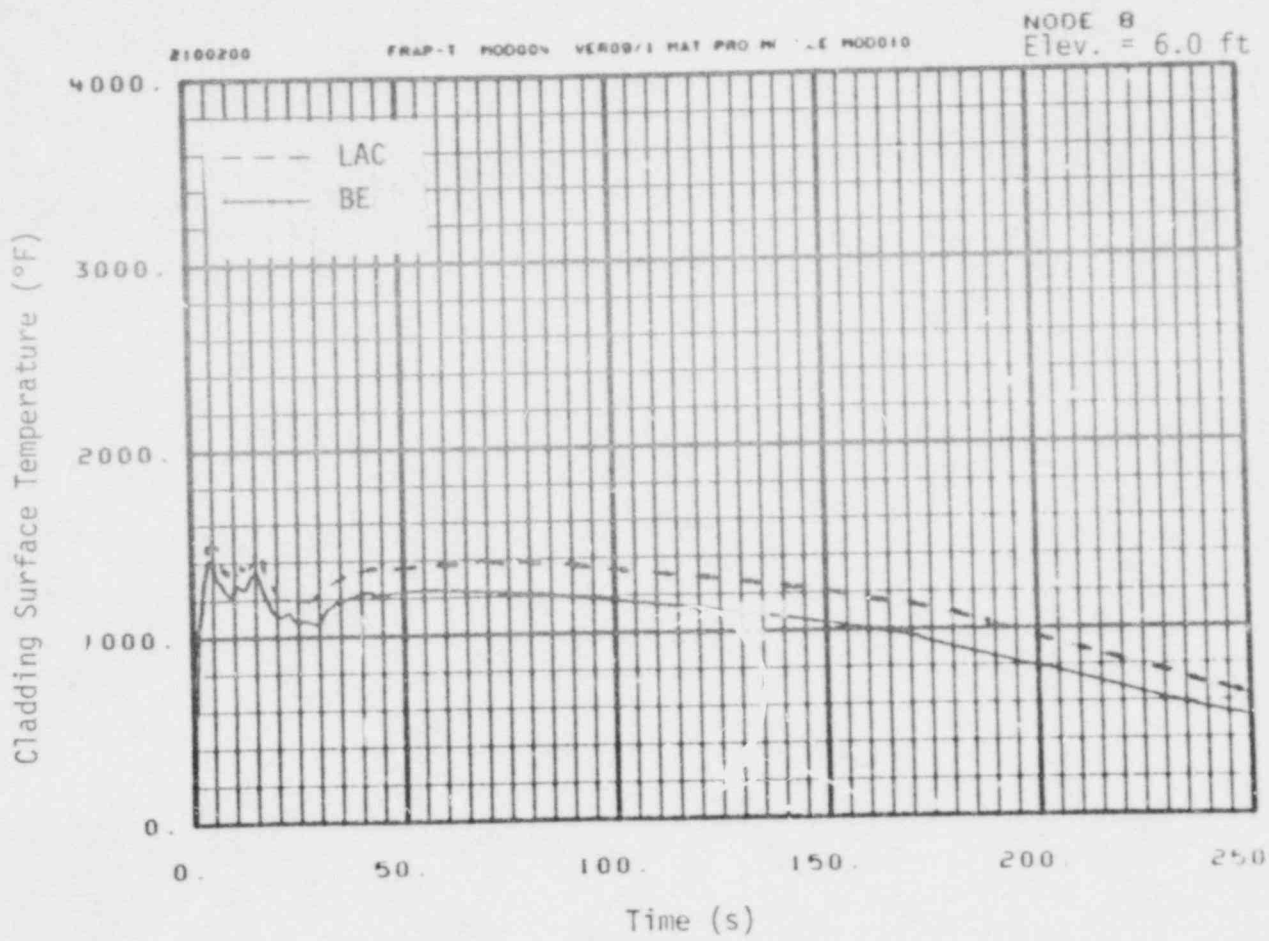

Fig. D-1 Cladding surface temperature history (PWR LOCA, normal power case).

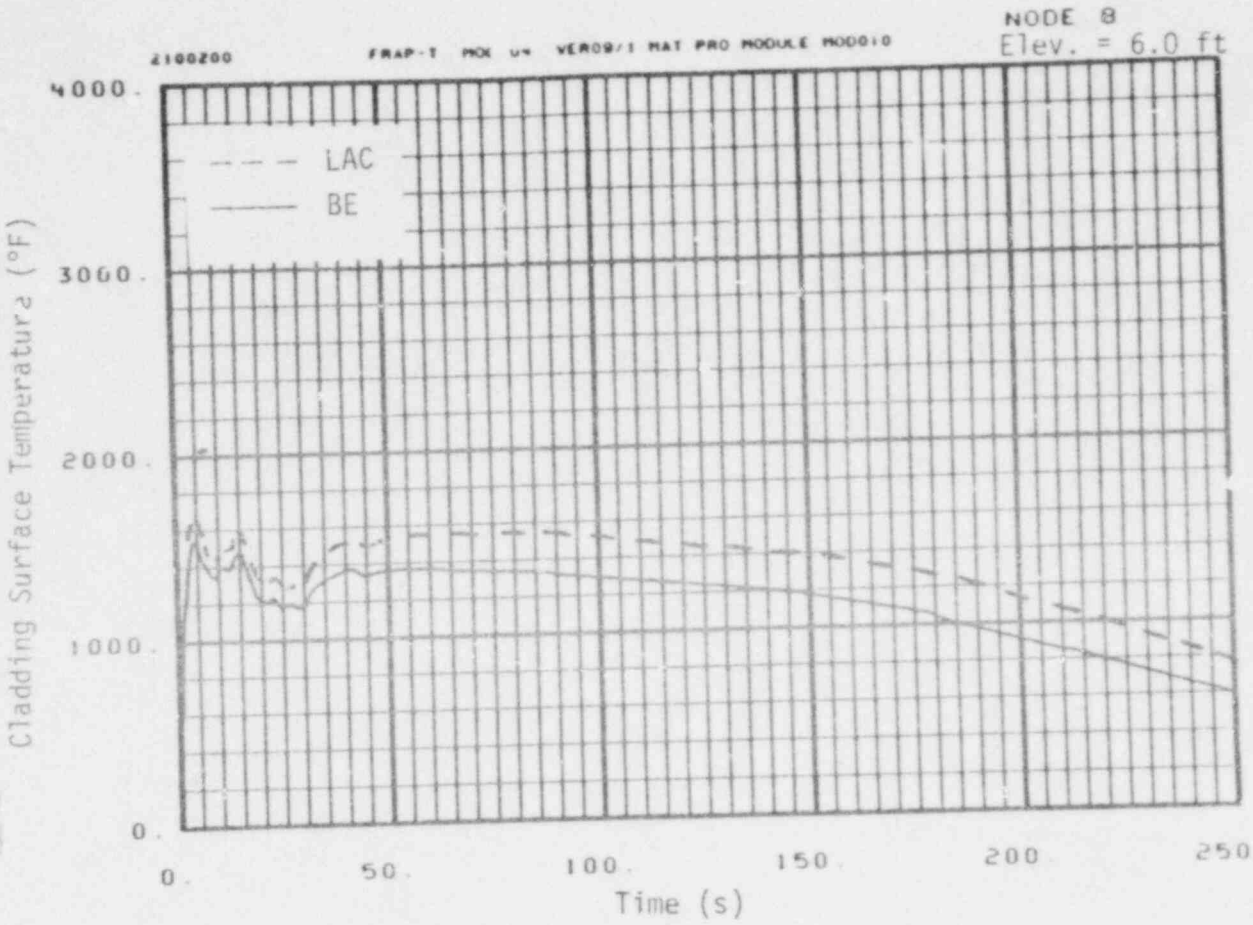

Fig. D-2 Cladding surface temperature history at peak power node (PWR LOCA, high power case).

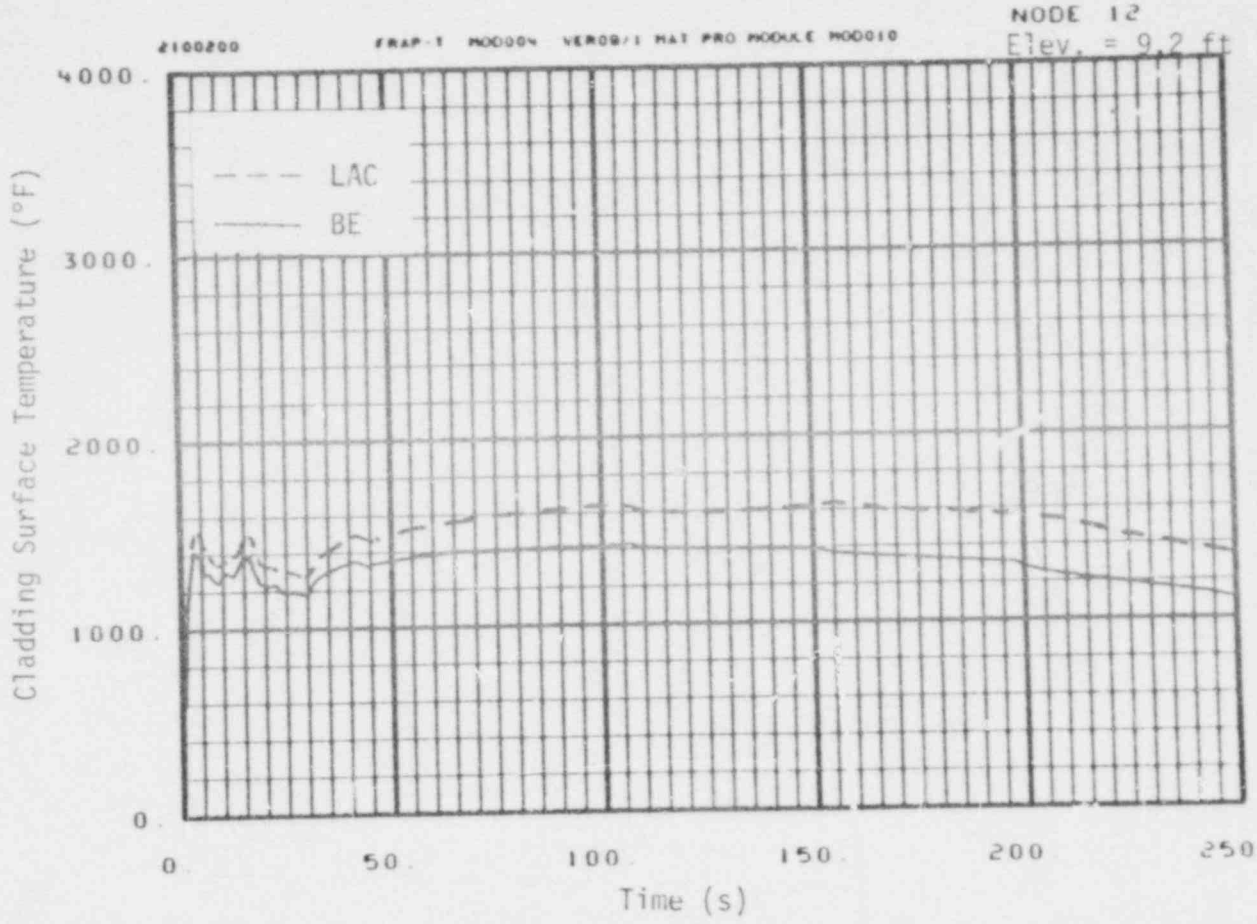

Fig. D-3 Cladding surface temperature history at rupture node (PWR LOCA, high power case).

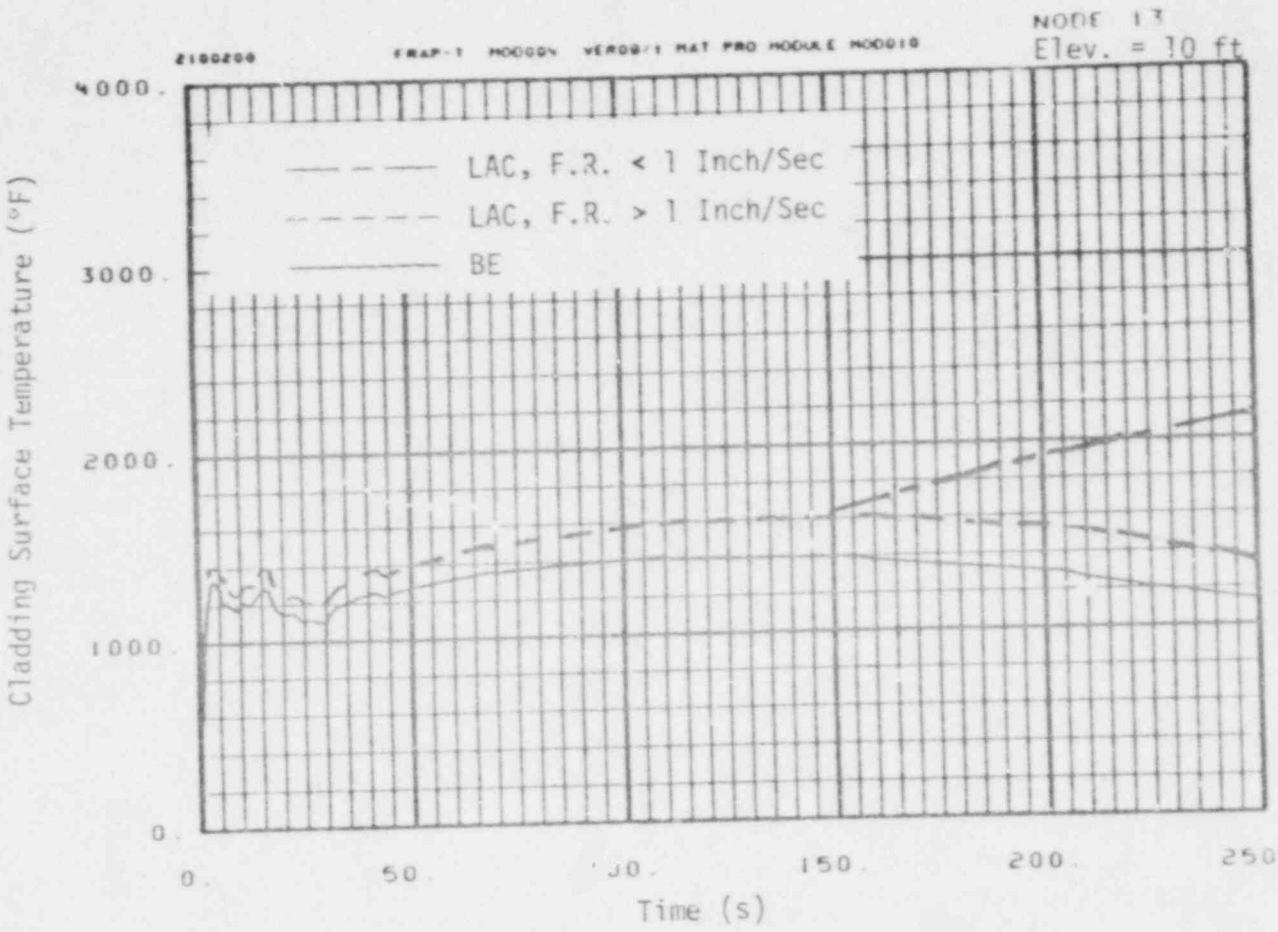

Fig D-4 Cladding surface temperature history at node with peak cladding temperature (PWR LOCA, high power case).

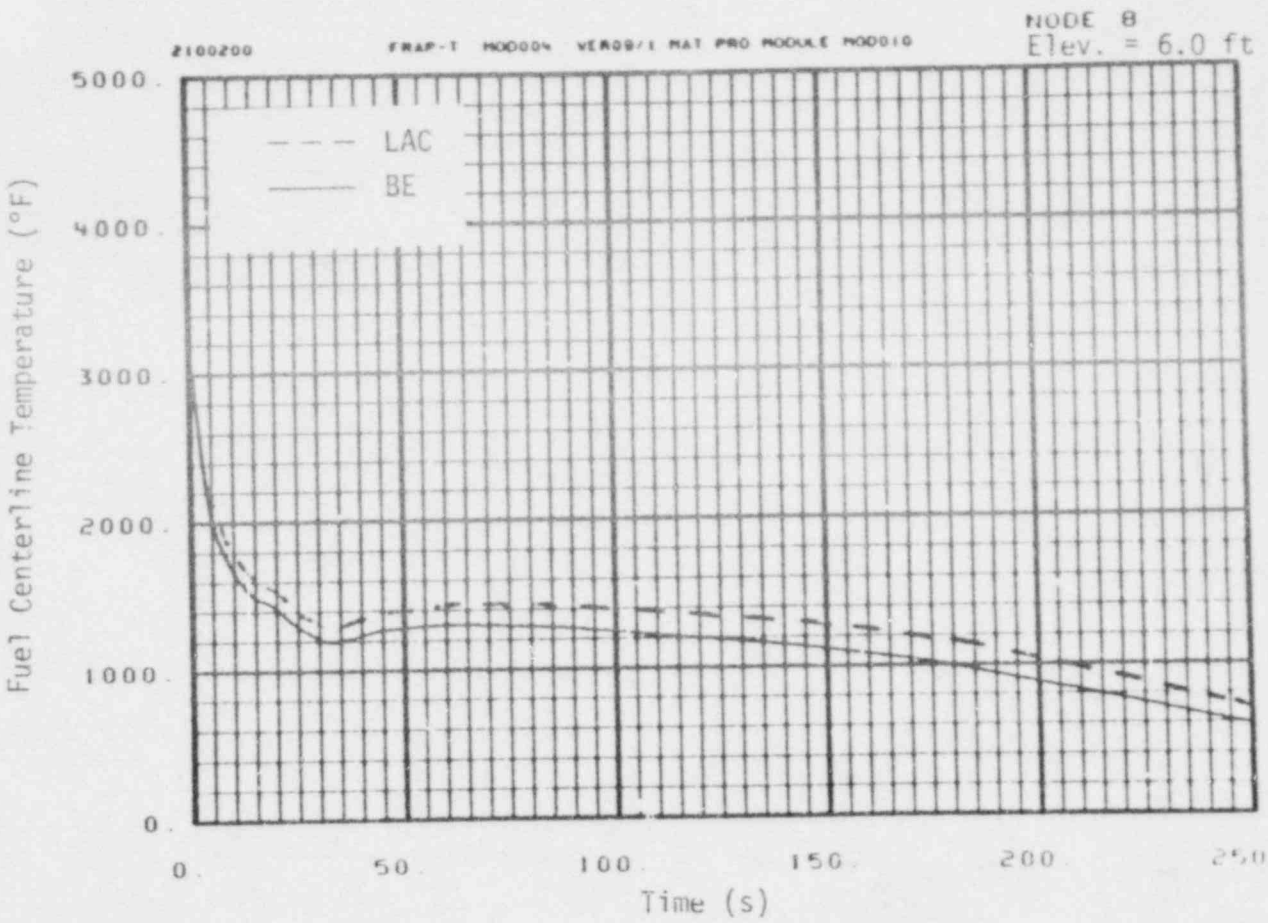

Fig. D-5 Fuel centerline temperature history (PWR LOCA, normal power case).

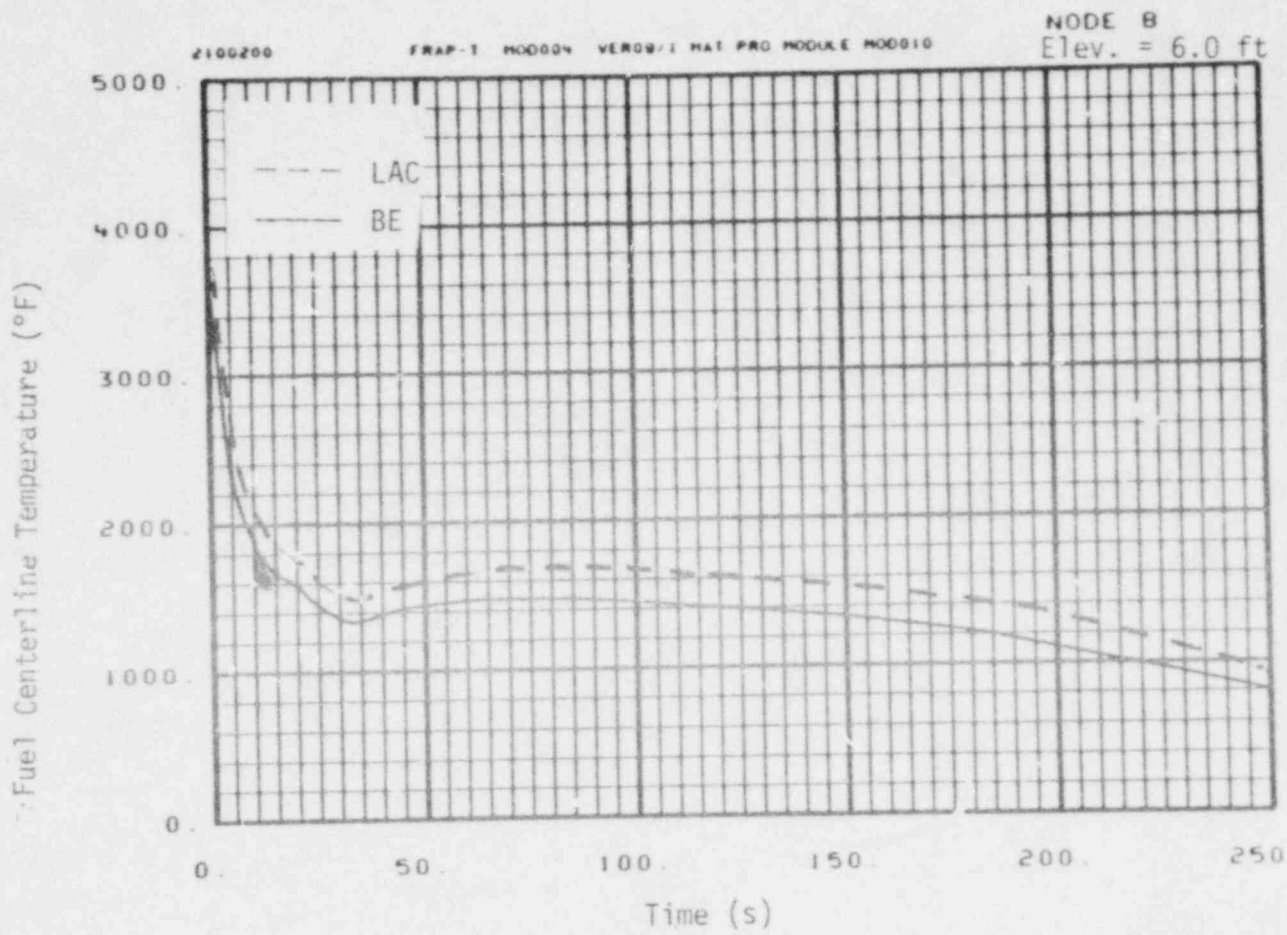

Fig. D-6 Fuel centerline temperature history at peak power node (PWR LOCA, high power case).

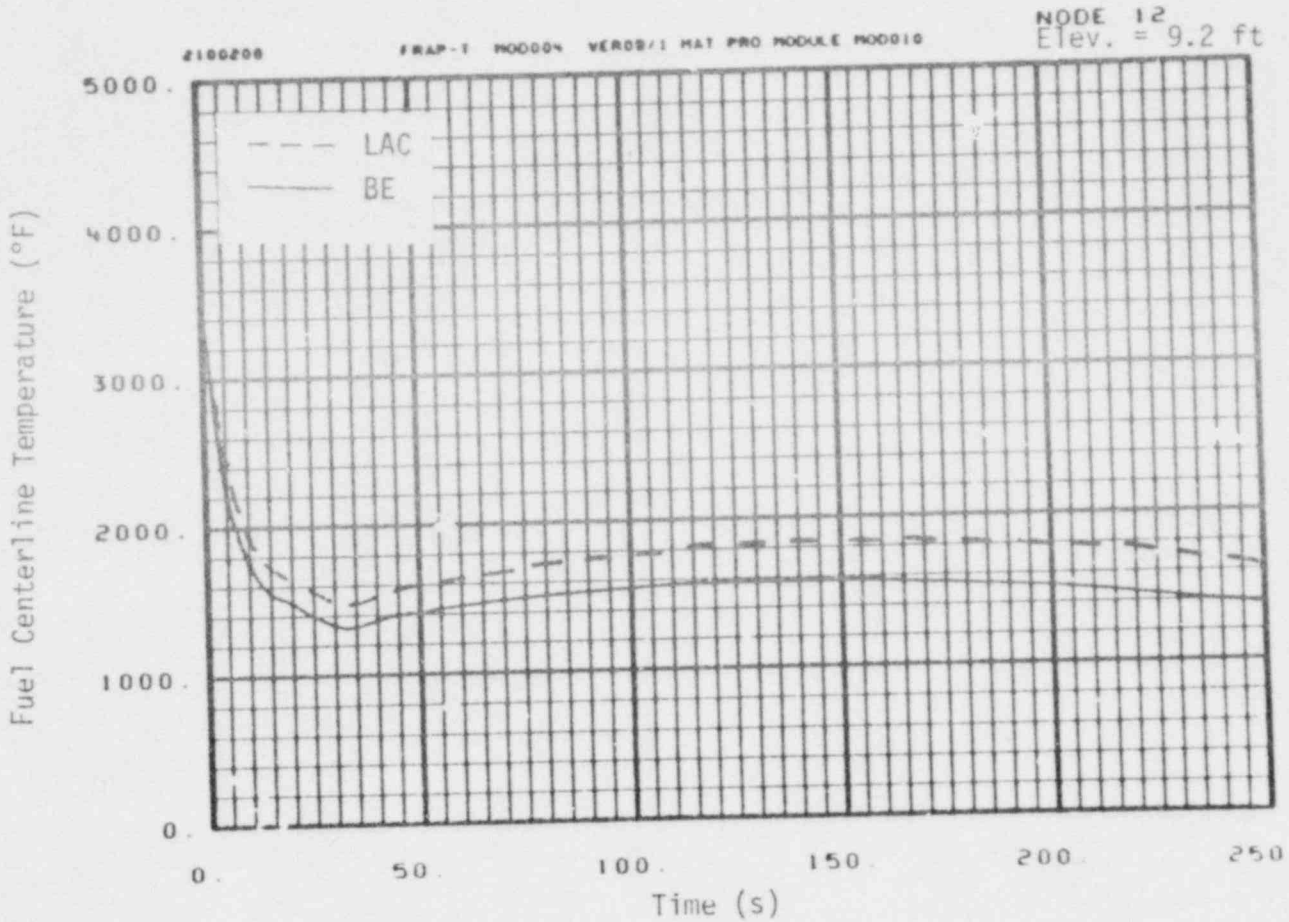

Fig. D-7 Fuel centerline temperature history at rupture node (PWR LOCA, high power case).

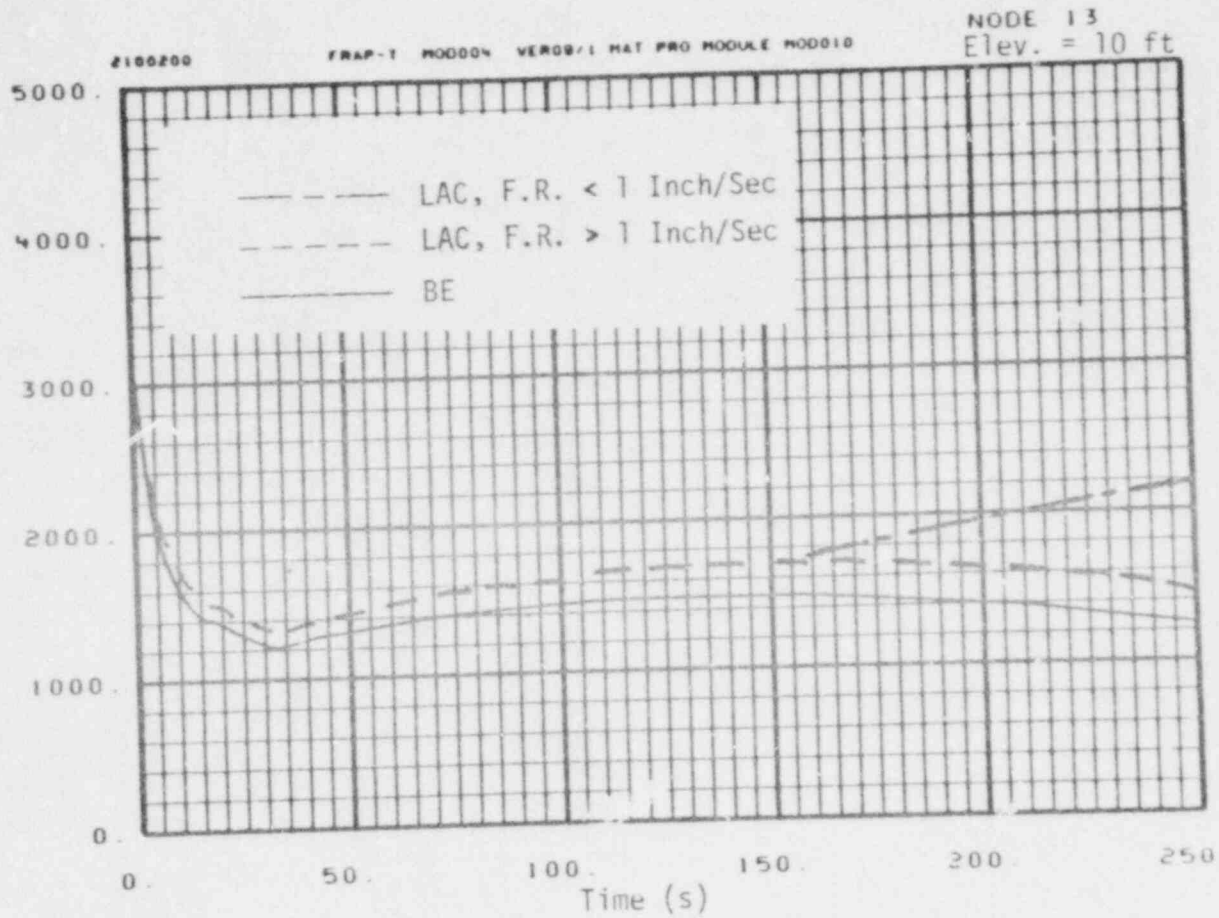

Fig. D-8 Fuel centerline temperature history at node with peak cladding temperature (PWR LOCA, high power case).

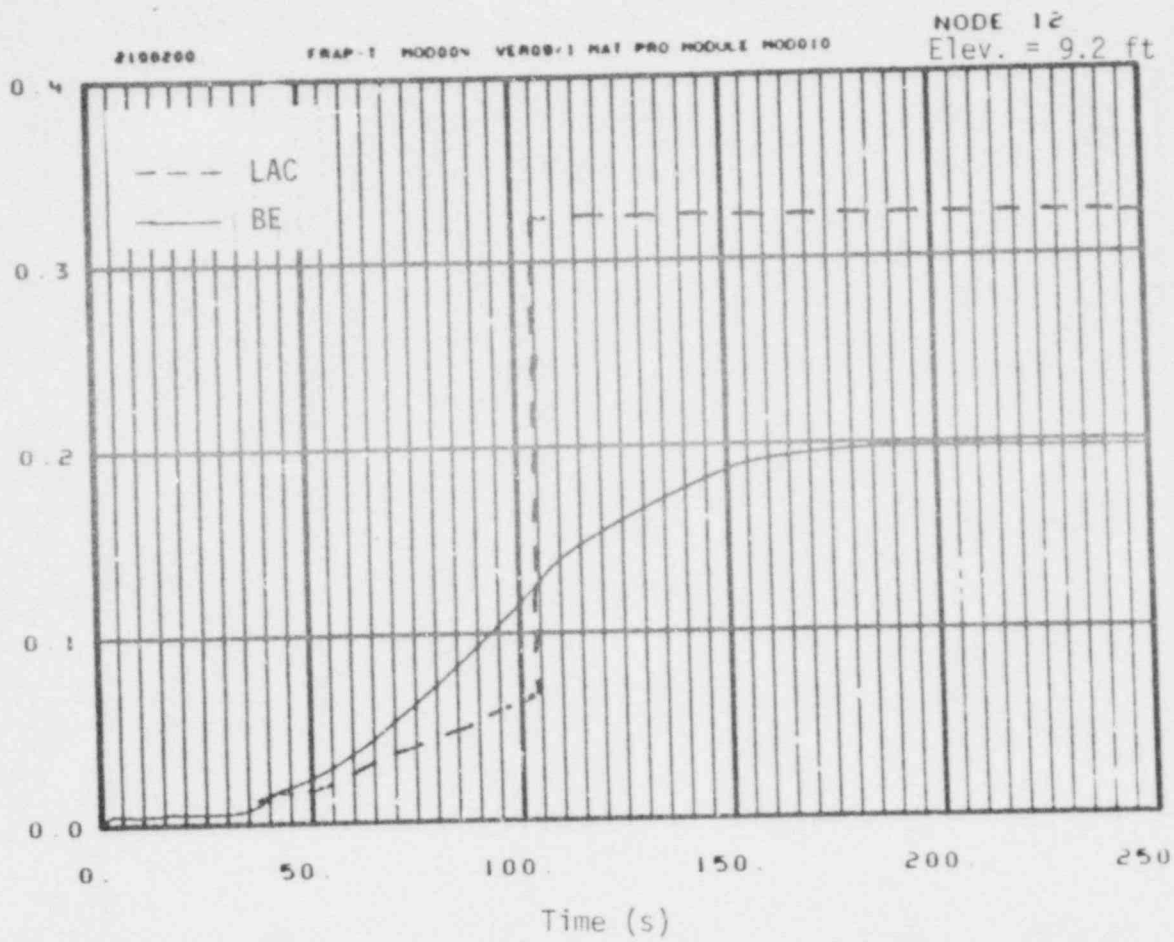

Fig. D-9 Cladding hoop strain history at rupture node (PWR LOCA, high power case).

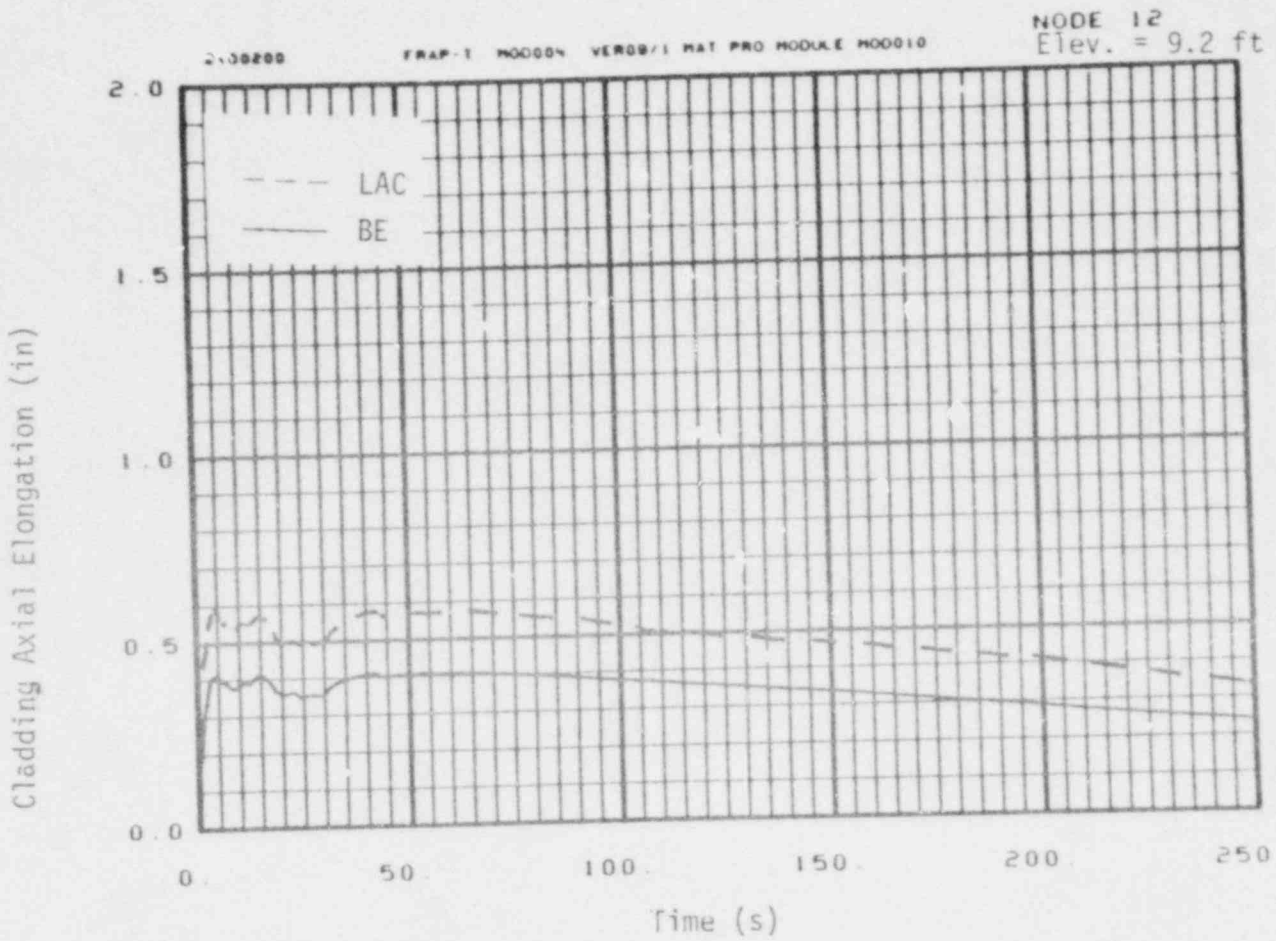

Fig. D-10 Cladding elongation history (PWR LOCA, high power case).

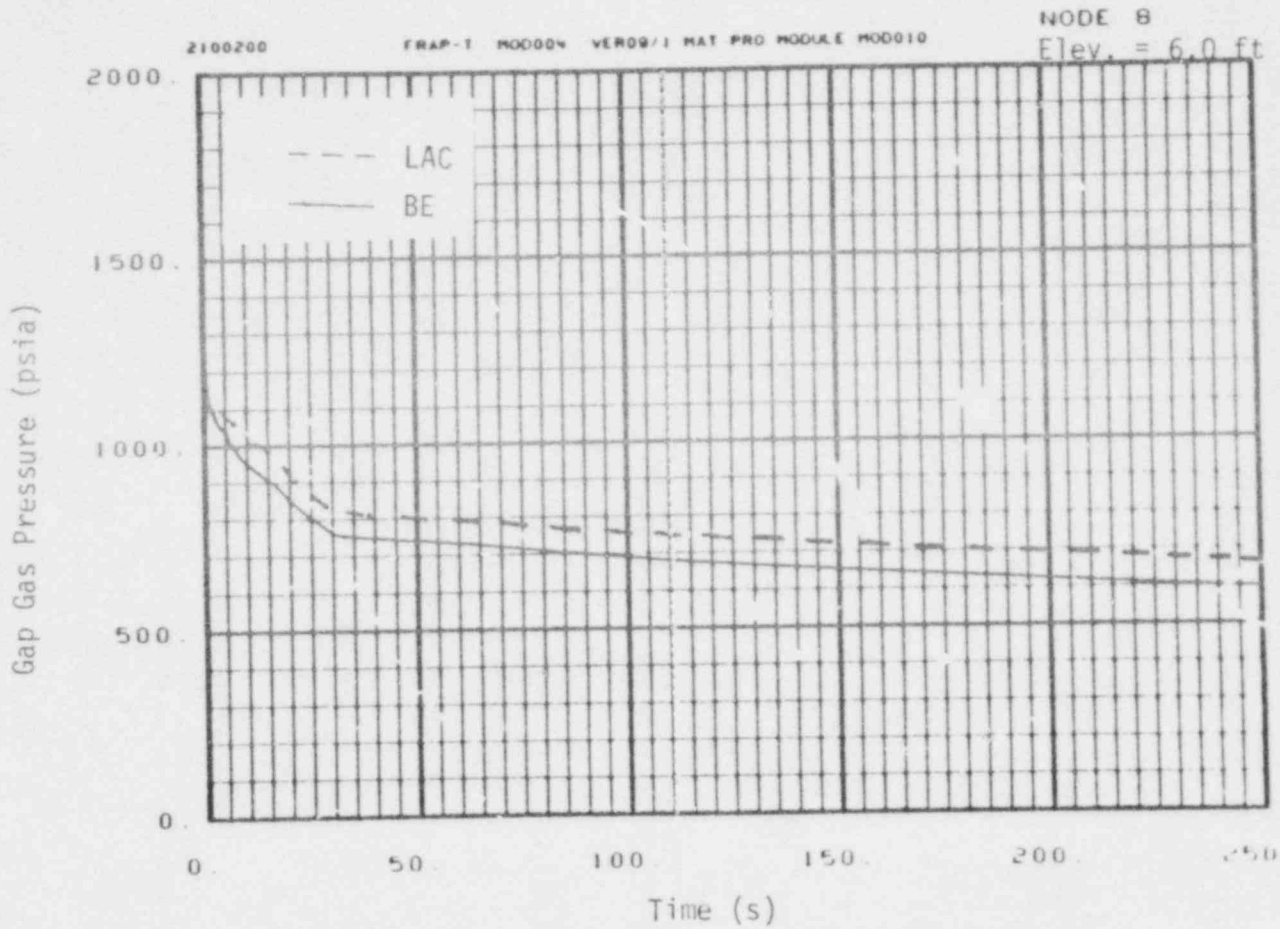

Fig. D-11 Internal pressure history (PWR LOCA, normal power case).

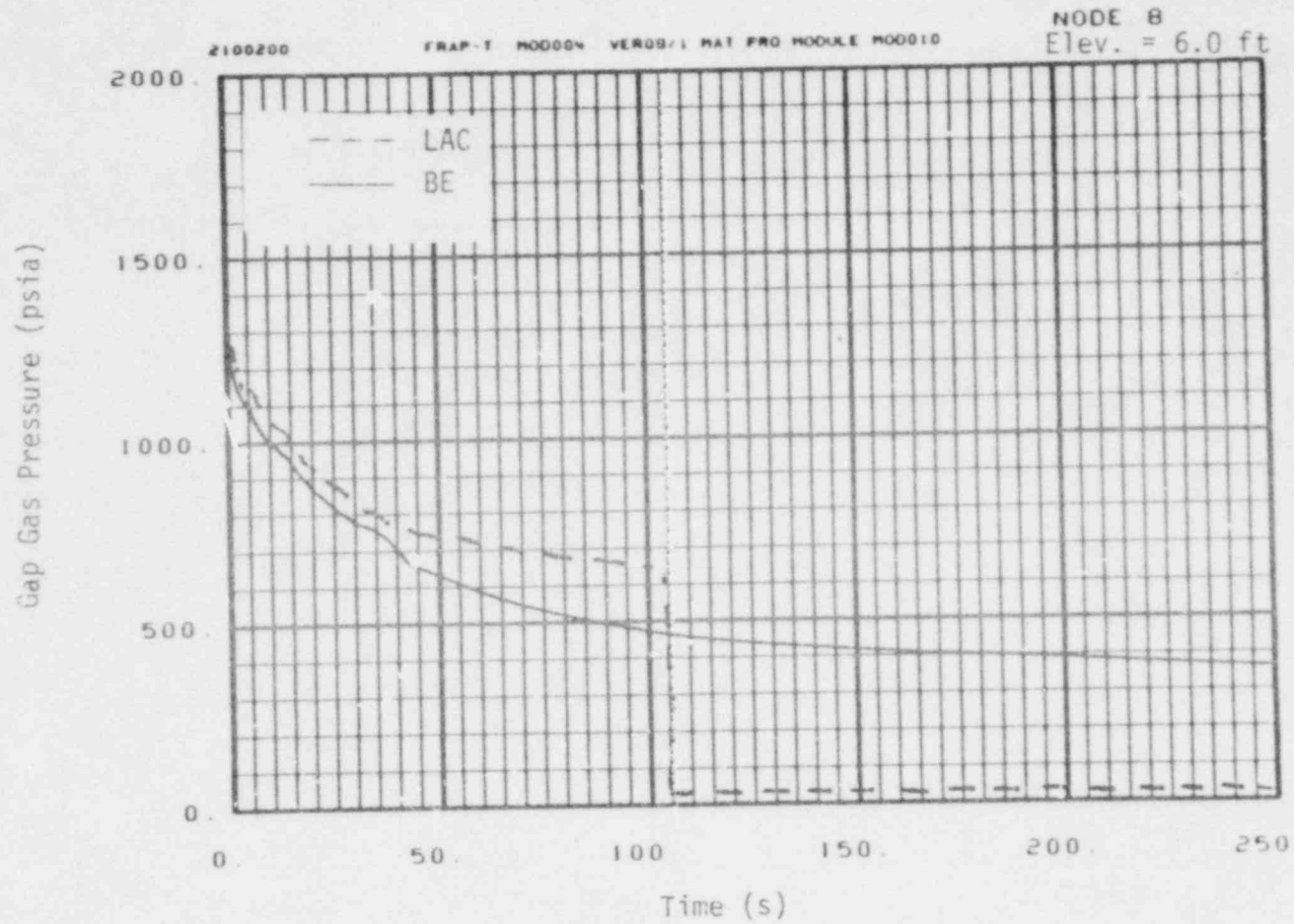

Fig. D-12 Internal pressure history (PWR LOCA, high power case).

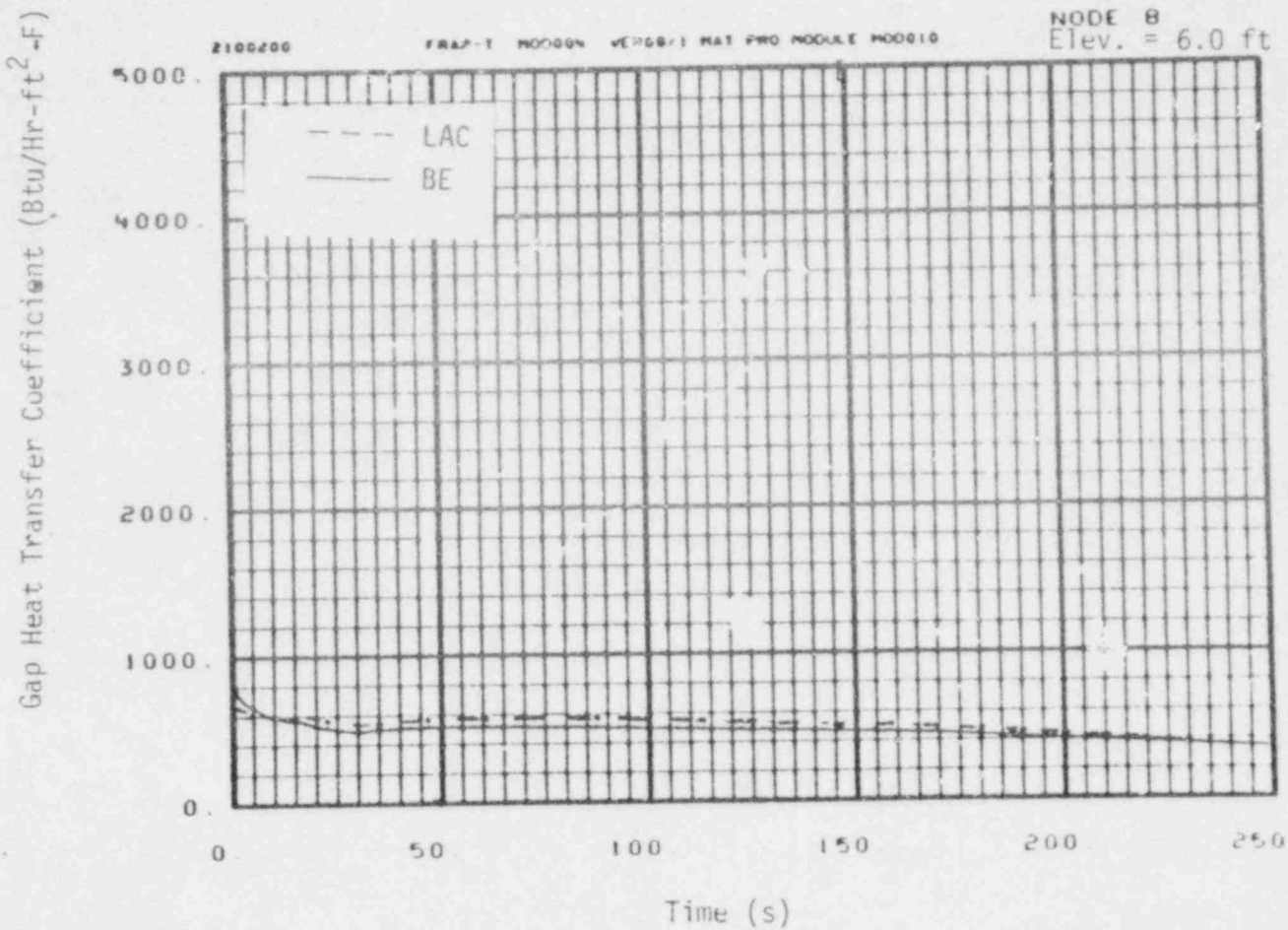

Fig. D-13 Gap conductance history at peak power node (PWR LOCA, normal power case)

The cladding hoop strain history for the high power case is shown in Figure D-9. Both the BE and LACE calculations predict cladding plastic deformation to initiate at a time of 35 s. The LACE predicted cladding deformation is initially less than the BE predicted deformation, but then becomes significantly greater. The LACE calculations predict cladding failure at a time of 105 s. The cladding temperature at time of failure is 1660°F. The flow blockage is 36%. The BE calculations do not predict failure. This is because the BE predicted cladding temperature is about 200°F lower than the LACE predicted temperature.

The cladding axial elongation history for the high power case is shown in Figure D-10. The LACE and BE curves are about the same shape, but the LACE calculations predict about 0.1 in. more elongation than the BE calculations.

The internal gas pressures for the normal and high power cases are shown in Figures D-11 and D-12. The LACE calculations predict about a 2% higher internal gas pressure at accident initiation than the BE calculations. The pressure difference tends to get greater with an increase in time.

The gap conductance history for the normal power case is shown in Figure D-13. At accident initiation, the LACE and BE predicted gap conductance values are 784 and 873 Btu/ft^2-hr-°F, respectively. During the LOCA, the LACE and BE predicted gap conductance are about the same.

2. LOFT 2-2 Test

Plots of the computed fuel rod response are shown in Figures A-14 through D-18. The fuel rod response is plotted for axial Node 5, which is 2.063 ft. above the bottom of the 5.5 ft. long fuel rod. This is the elevation at which peak fuel rod power occurs. The

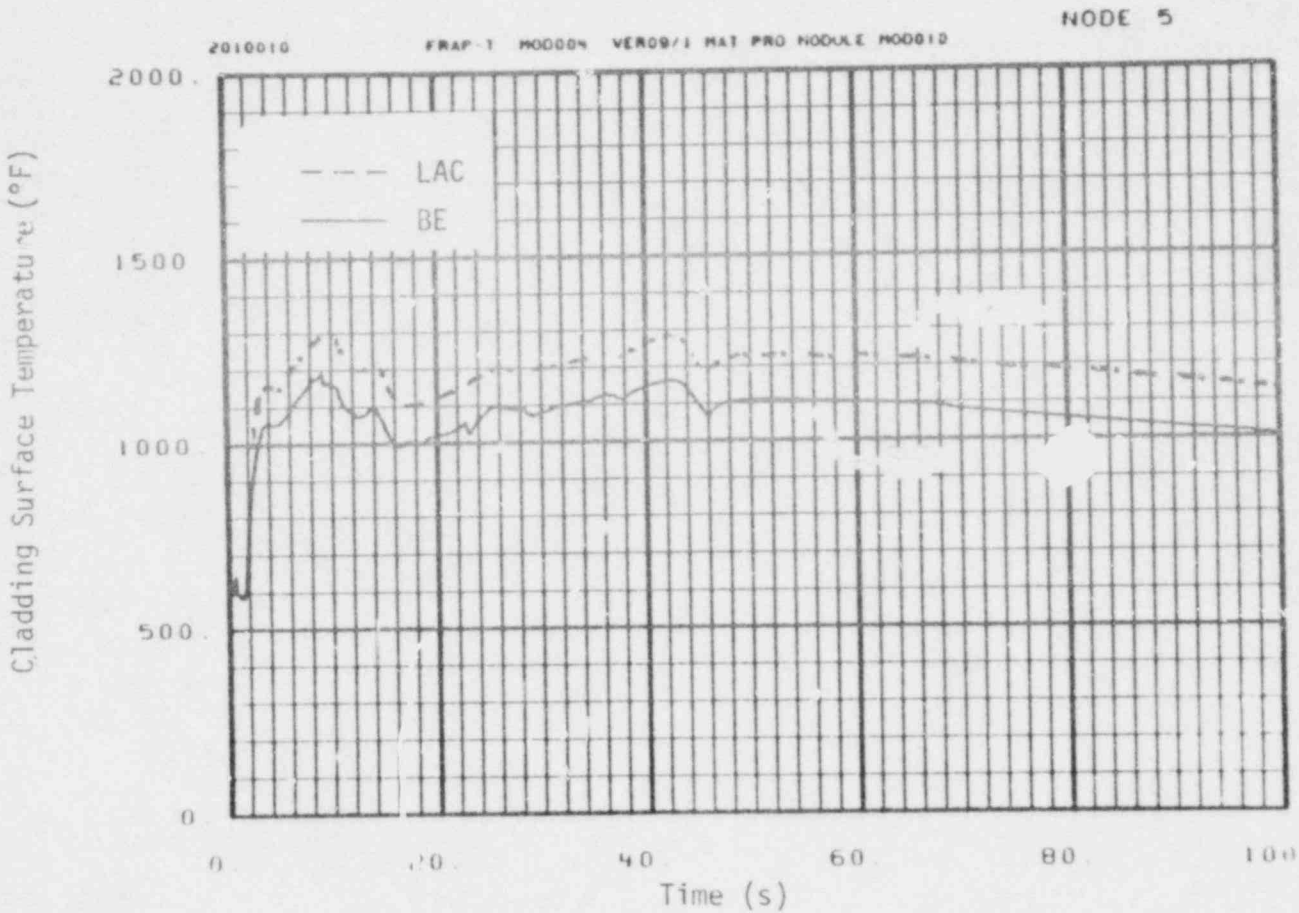

Fig. D-14 Cladding surface temperature history (LOFT 2-2 Test).

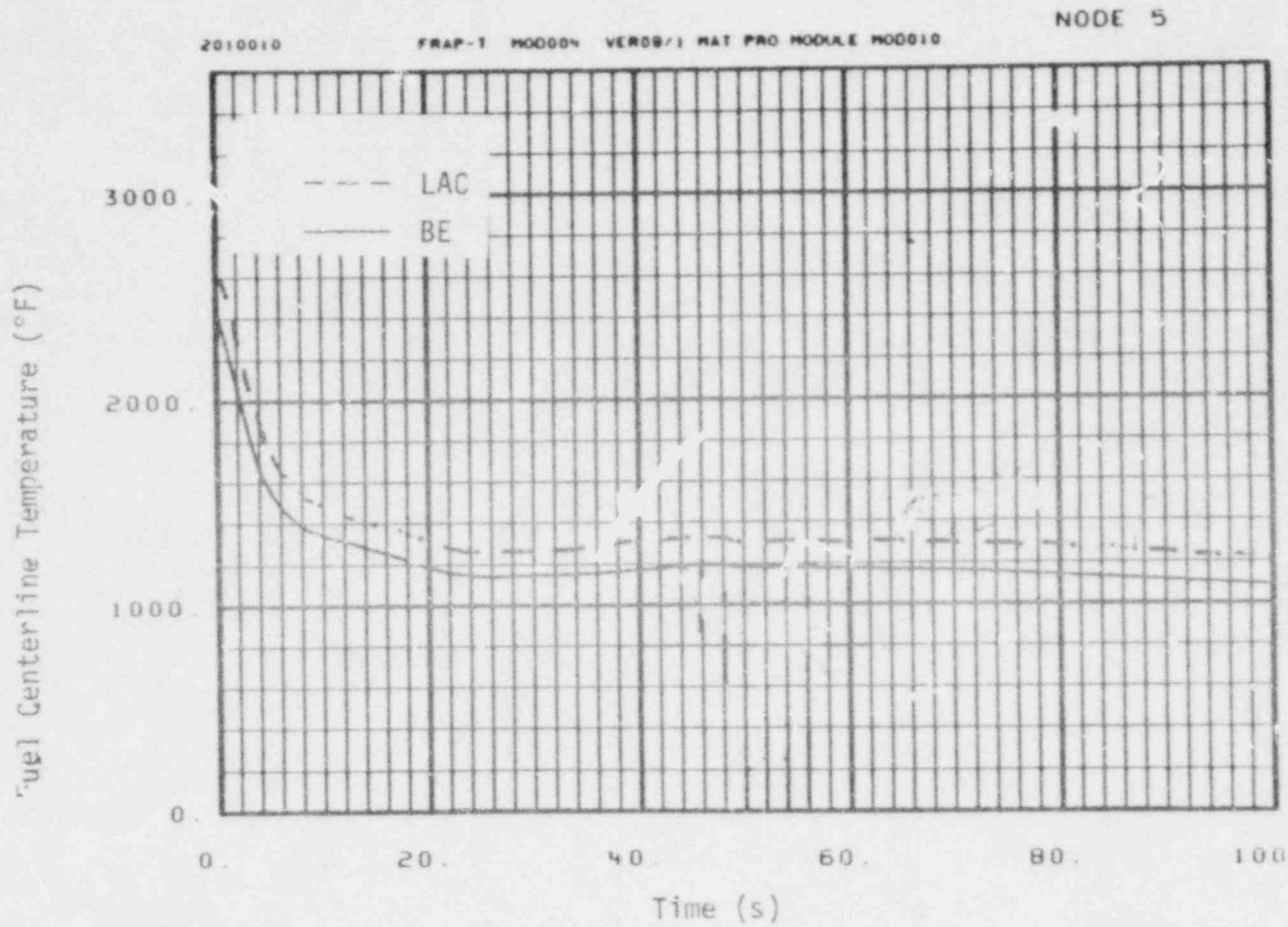

Fig. D-15 Fuel centerline temperature history (LOFT 2-2 Test).

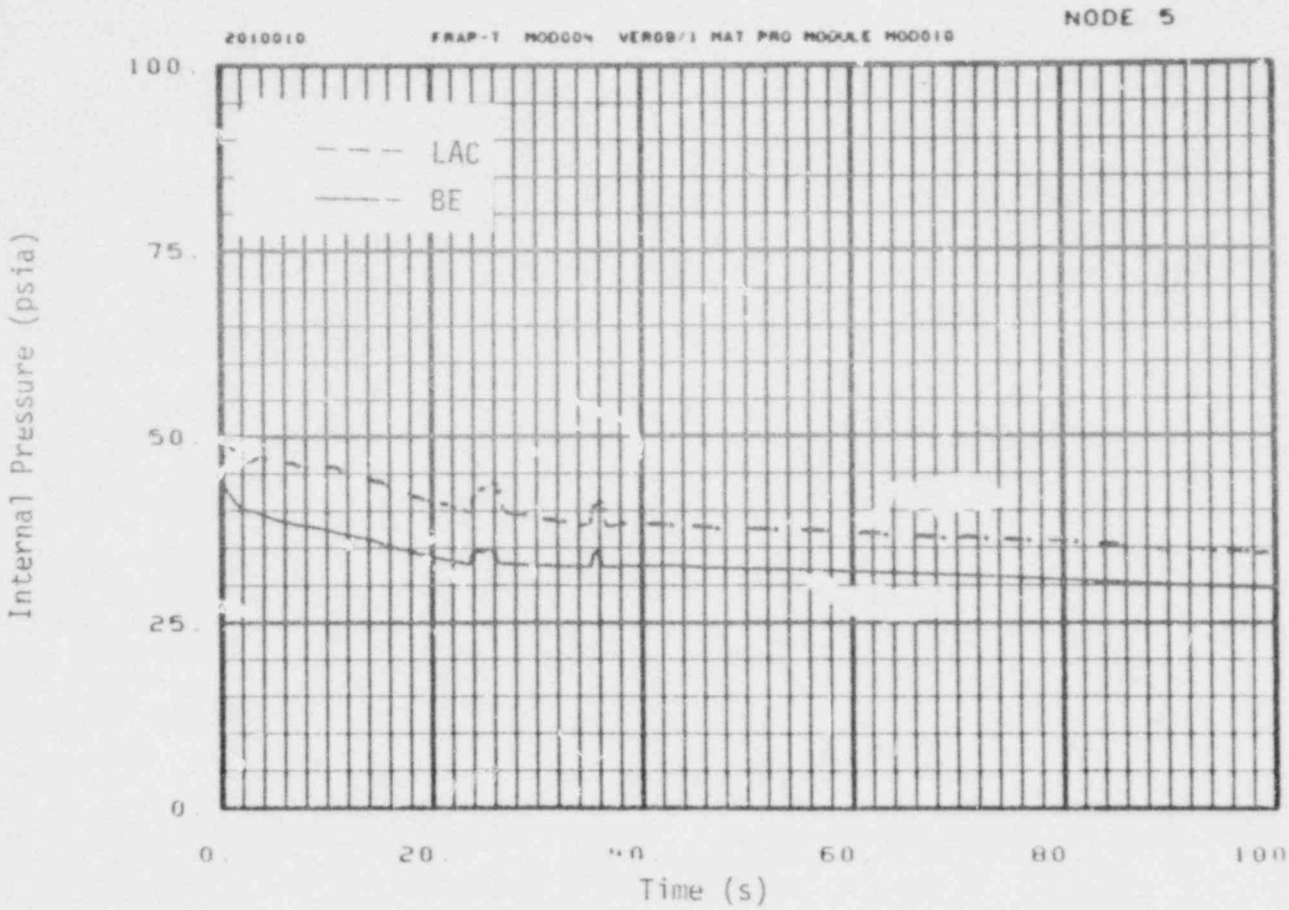

Fig. D-16 Internal pressure history (LOFT 2-2 Test).

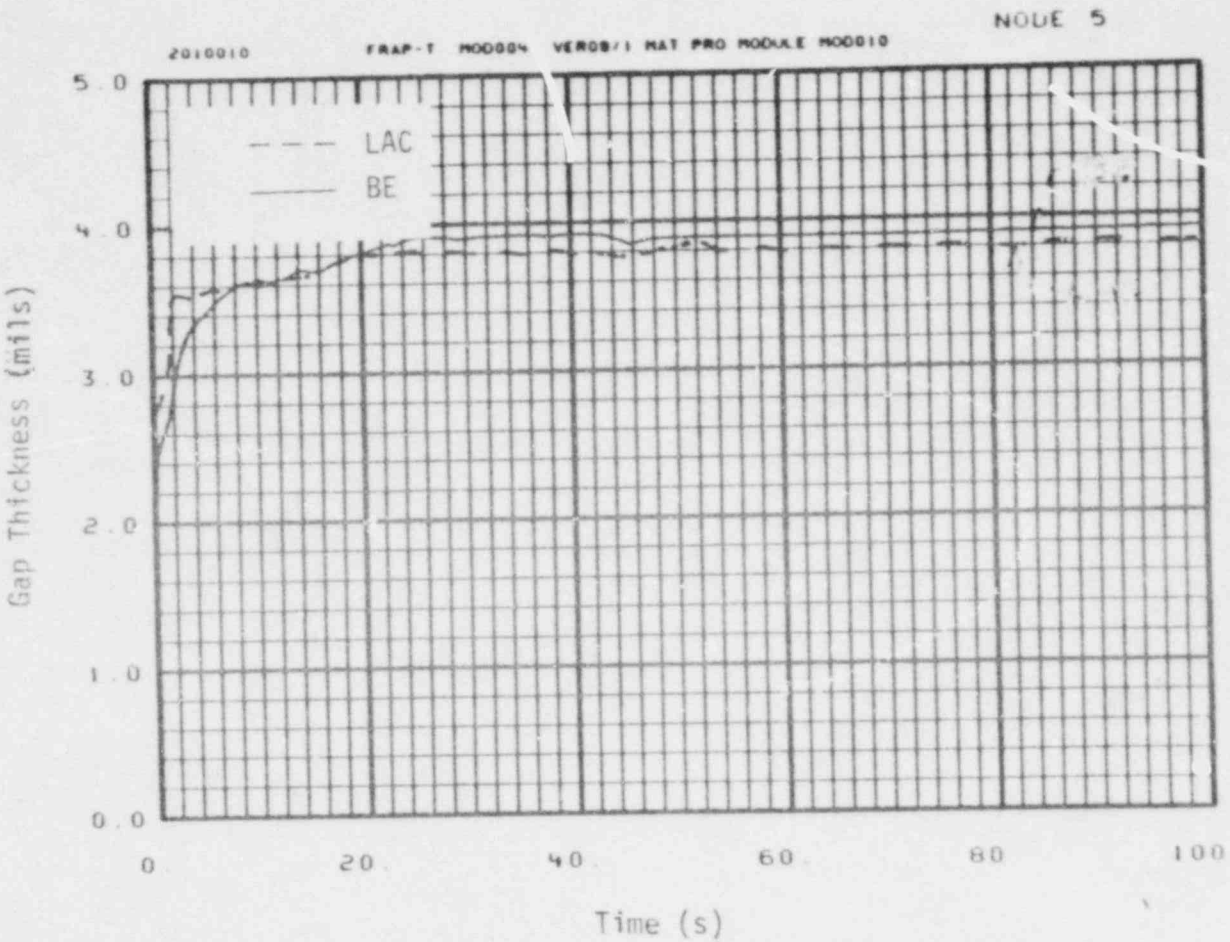

Fig. D-17 Gas gap size history (LOFT 2-2 Test).

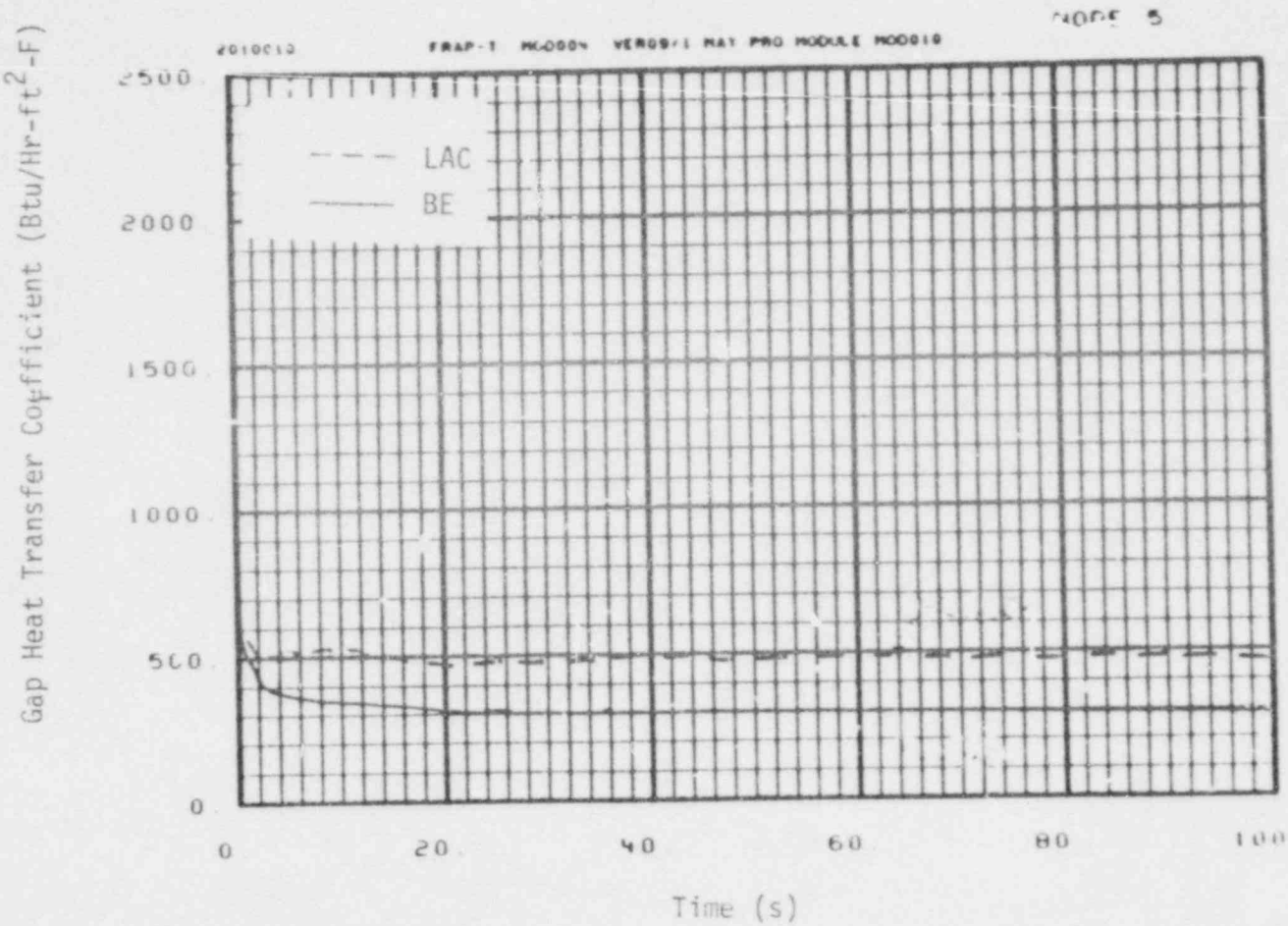

Fig. D-18 Gap conductance history (LOFT 2-2 Test).

calculations apply to the fuel rods in the center fuel module of the LOFT reactor. The coolant conditions were from RELAP4/MOD6 pretest predictions.

As shown in Figure D-14, the LACE and BE calculations predict film boiling to begin at the same time. After film boiling has begun, the LACE predicted cladding temperature is about 150°F above the BE predicted temperature for the duration of the calculations. As shown in Figure D-15, the LACE predicted fuel centerline temperature is about 100°F above the BE predicted temperature.

As shown in Figure D-16, the LACE predicted fuel rod gas pressure is about 20% higher than the BE predicted pressure. When the fuel rod gas plenum is surrounded by superheated steam, the LACE and BE calculations both show an increase in gas pressure. This occurs at times of 24 and 35 s, respectively.

The gas gap histories for the LACE and BE calculations are shown in Figure D-17. At the start of the test transient, the LACE and BE predicted gaps are 2.6 and 2.3 mils, respectively. The corresponding gap conductances are 618 and 723 Btu/ft^2-hr-°F, respectively. As shown in Figure D-18, however, the LACE predicted gap conductance becomes greater than the BE predicted value shortly after the LOCA initiation.

3. Simplified PWR LOCA

Plots of the computed fuel rod response are shown in Figures D-19 through D-26. The plots are shown for axial Node 5 and 6, which are located 4.25 and 4.75 ft above the bottom of the fuel rod, respectively. The peak fuel rod power and cladding rupture occurred at Node 5. The peak cladding temperature occurred at Node 6.

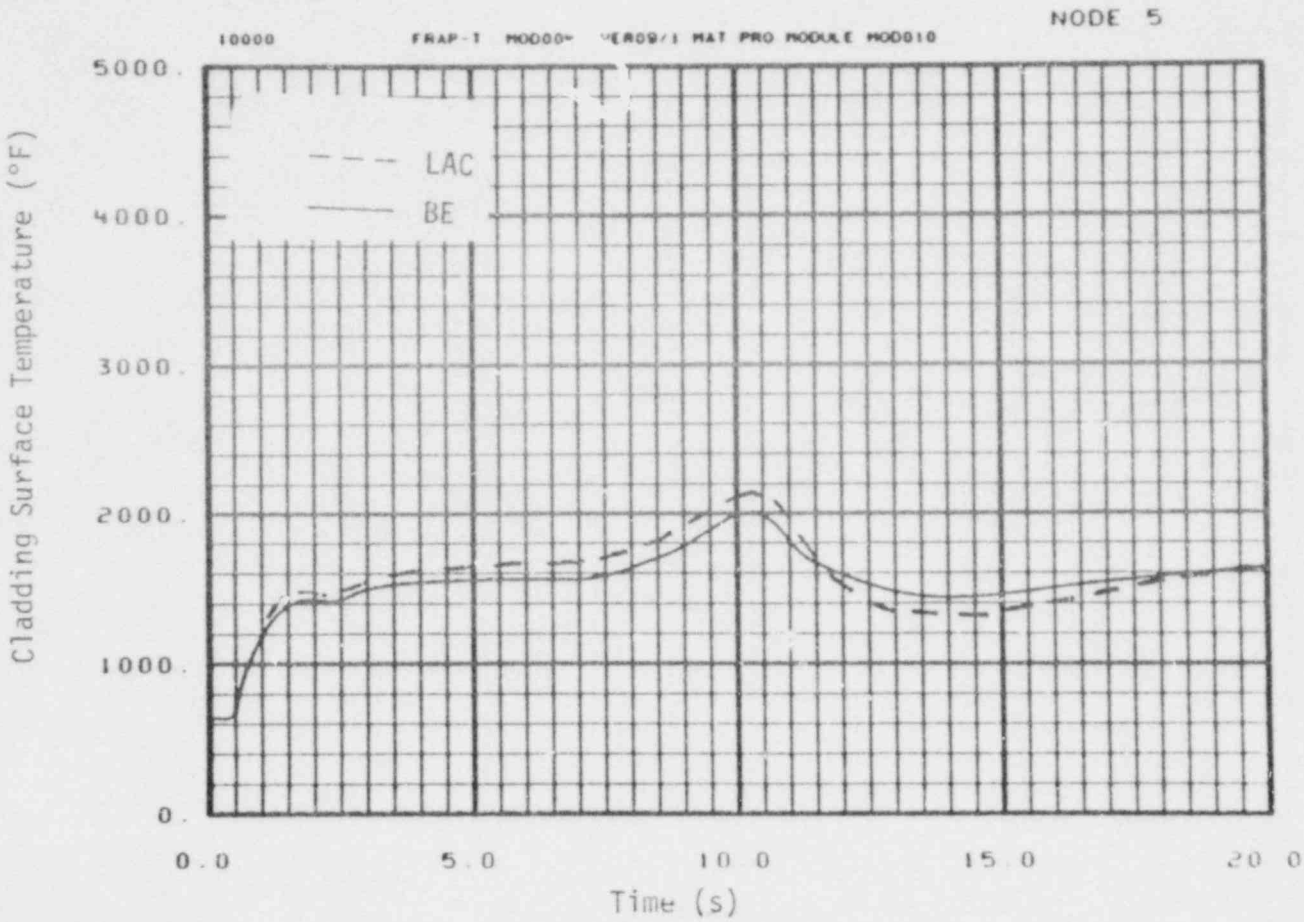

Fig. D-19 Cladding surface temperature history at peak power node (simplified PWR LOCA).

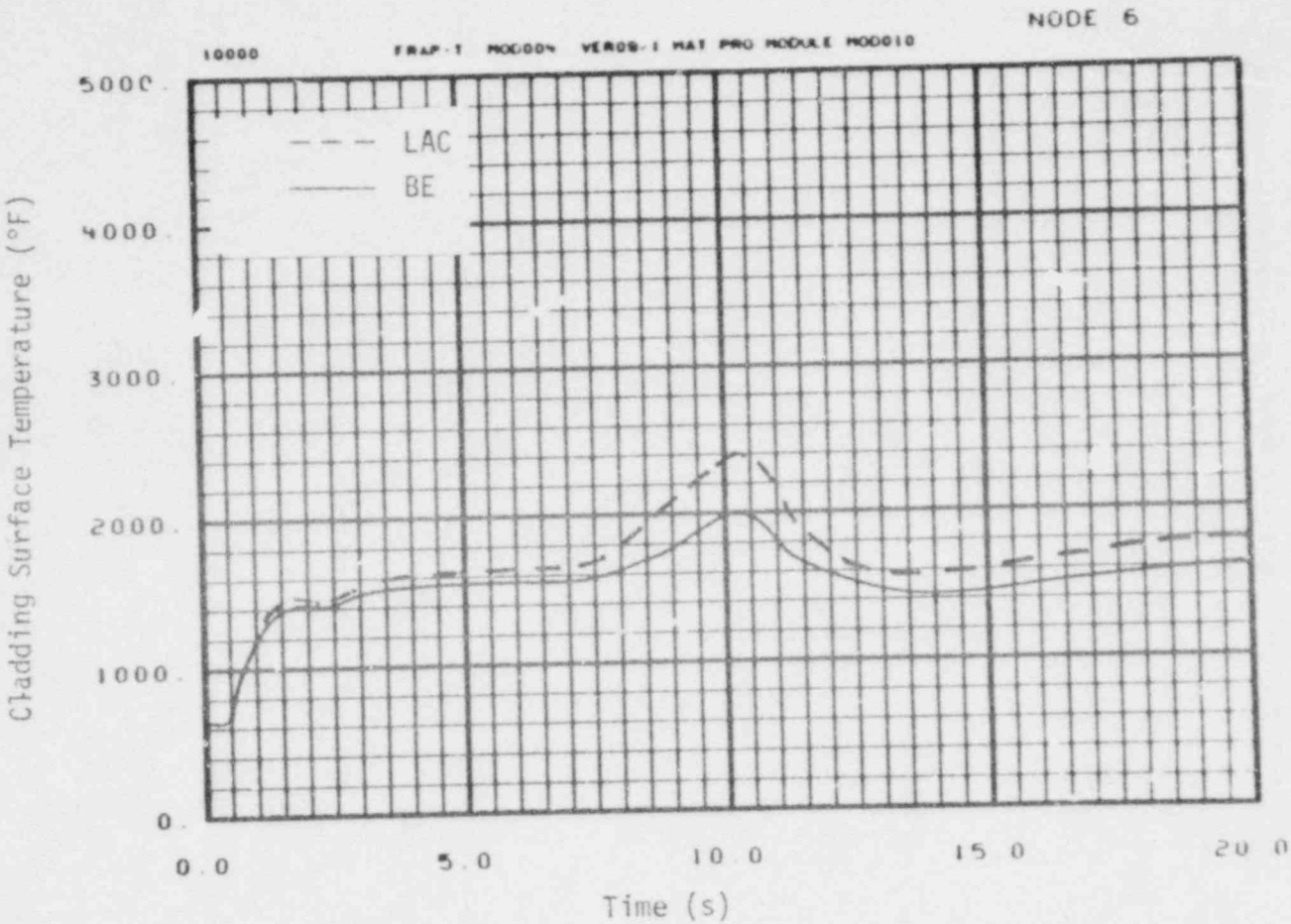

Fig. D-20 Cladding surface temperature history at peak cladding temperature node (simplified PWR LOCA).

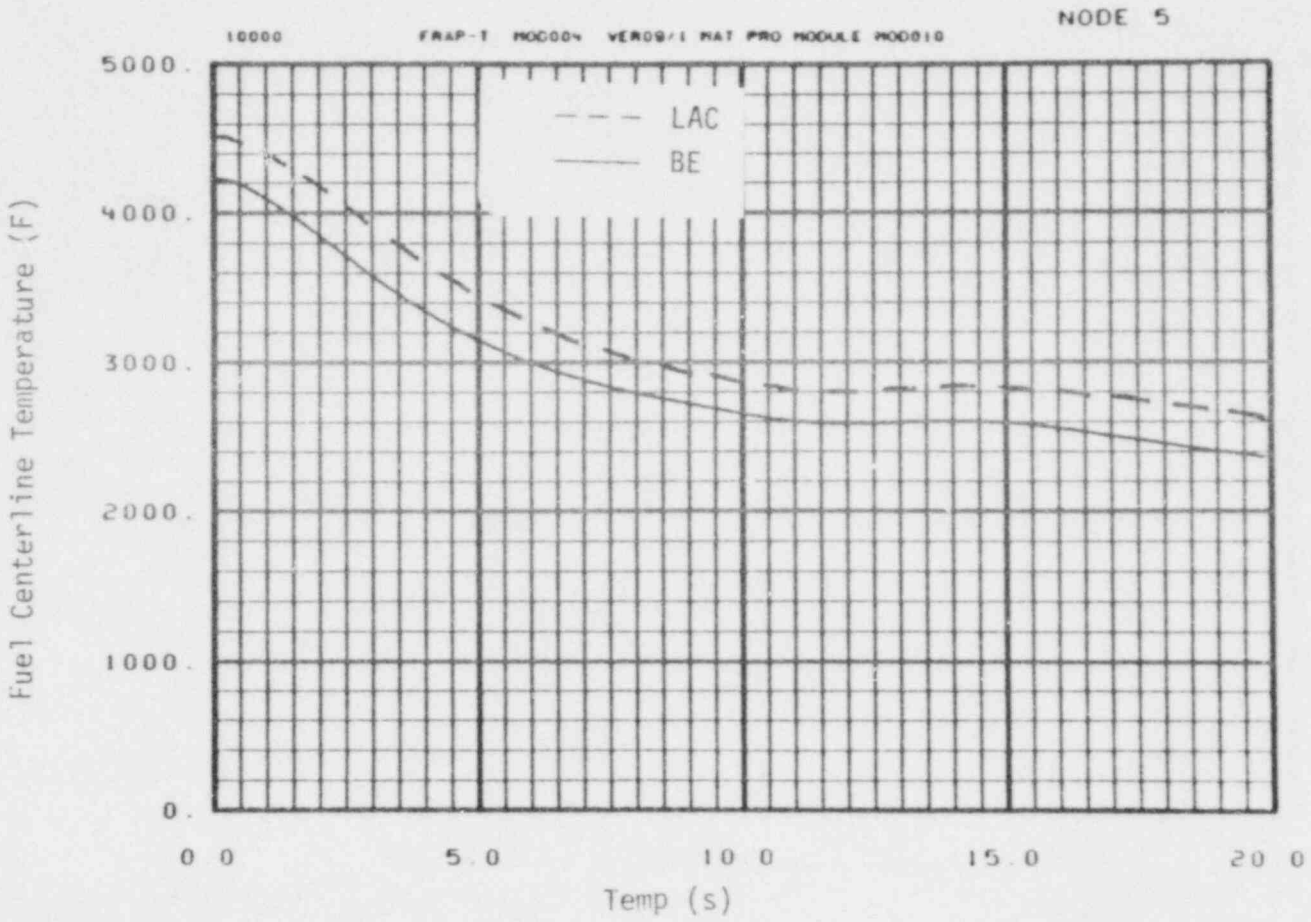

Fig. D-21 Fuel centerline temperature history at peak power node (simplified PWR LOCA).

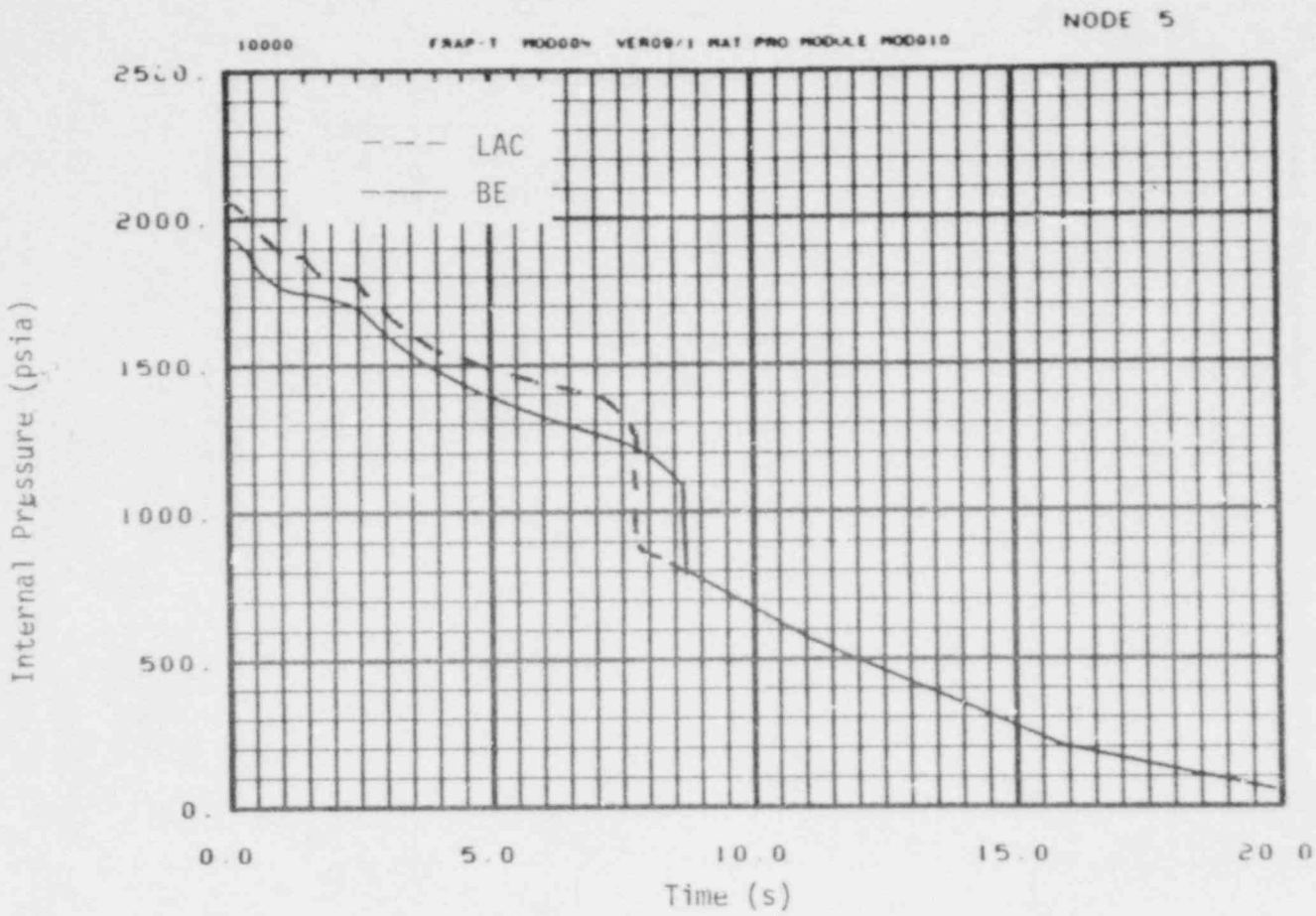

Fig. D-22 Internal pressure history (simplified PWR LOCA).

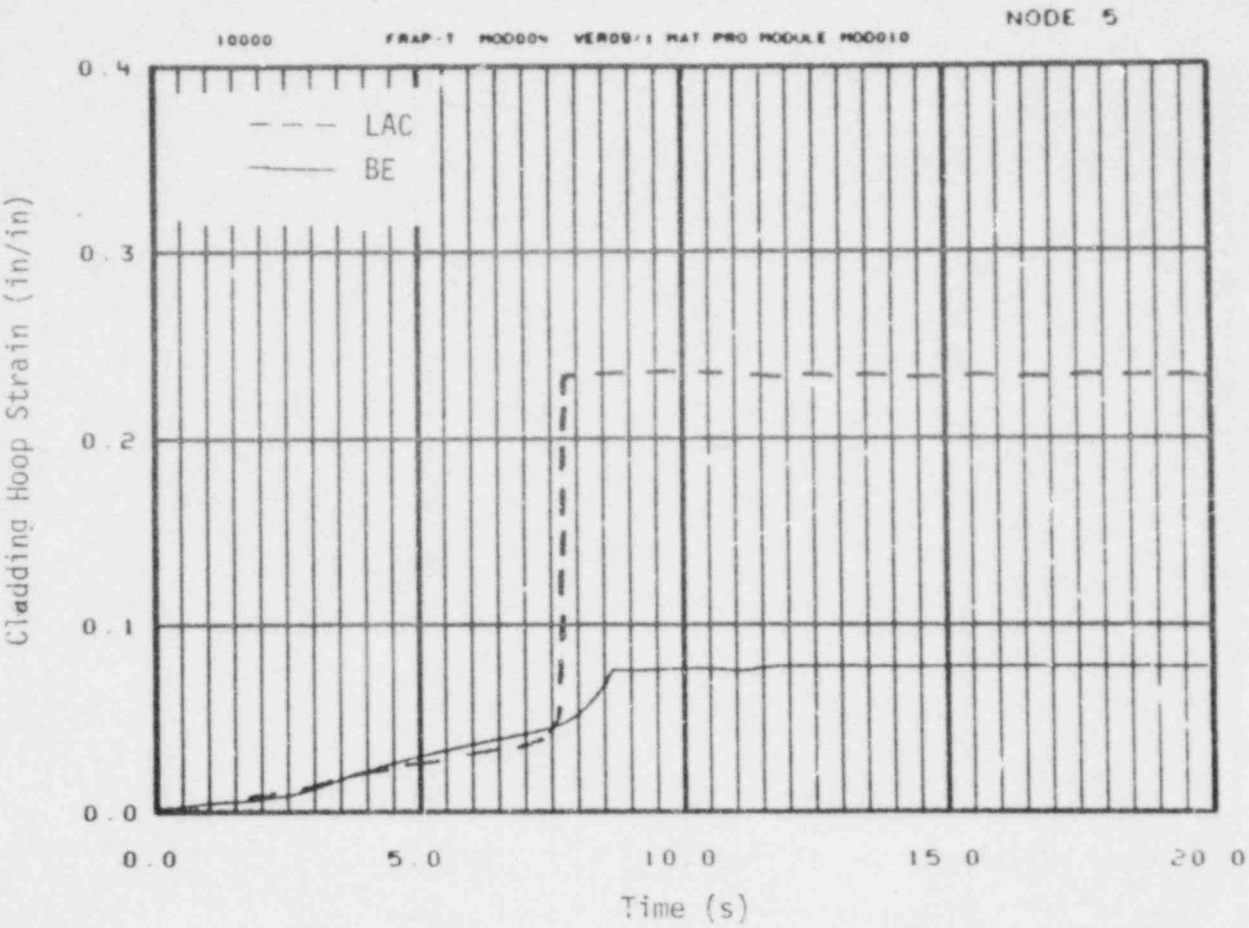

Fig. D-23 Cladding hoop strain history at rupture node (simplified PWR LOCA).

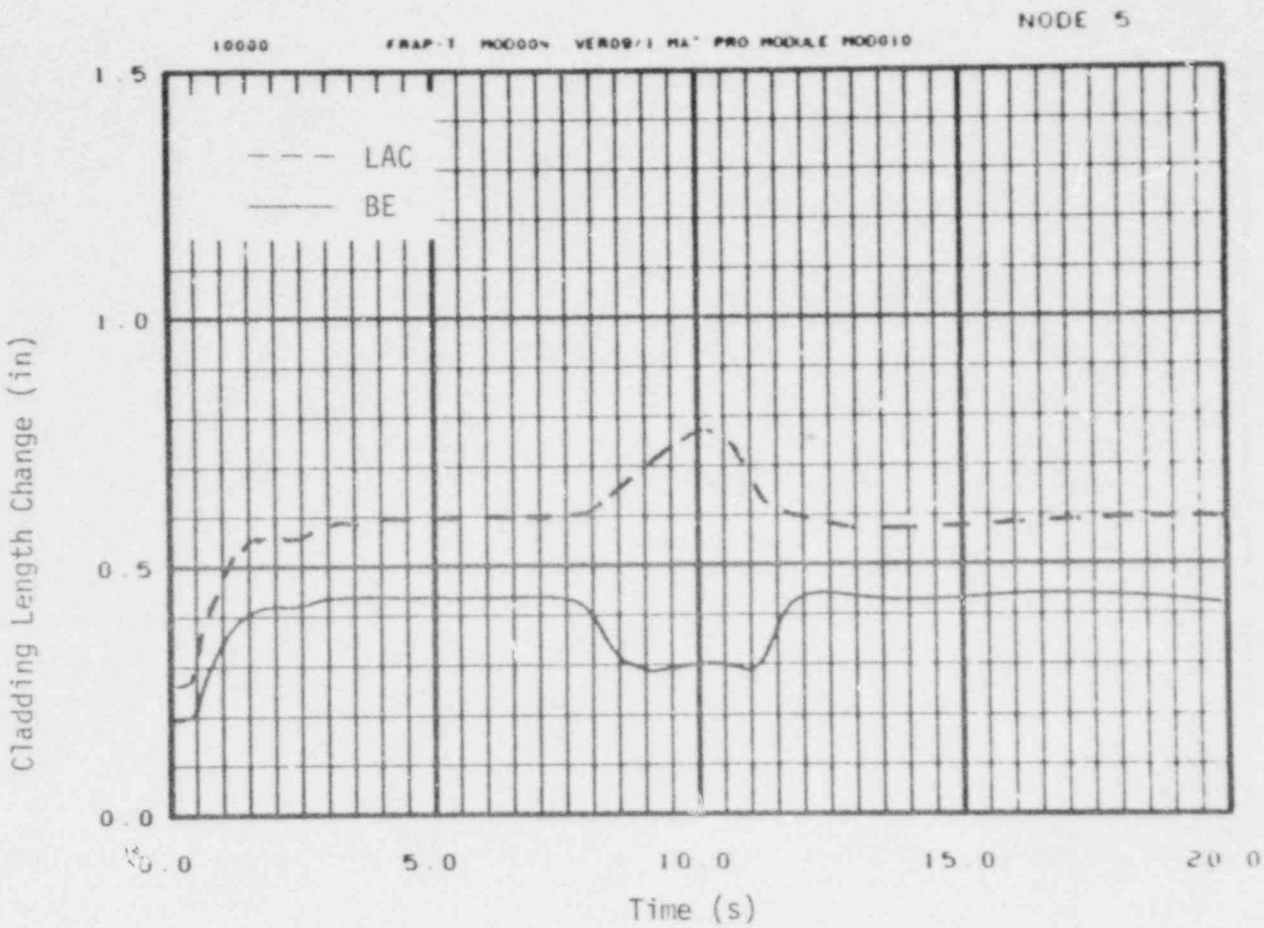

Fig. D-24 Cladding elongation history (simplified PWR LOCA).

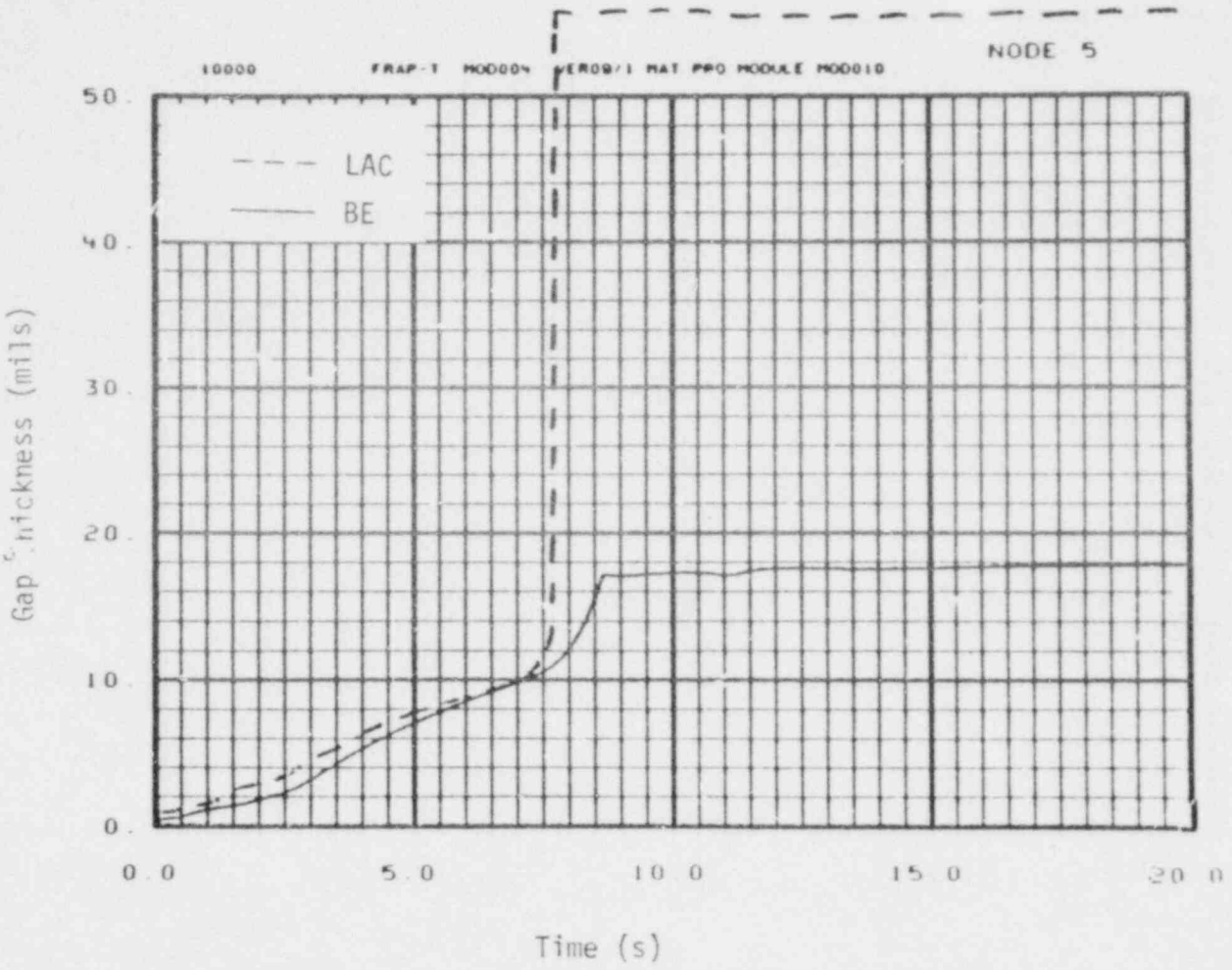

Fig D-25 Gas gap size history at peak power node (simplified PWR LOCA).

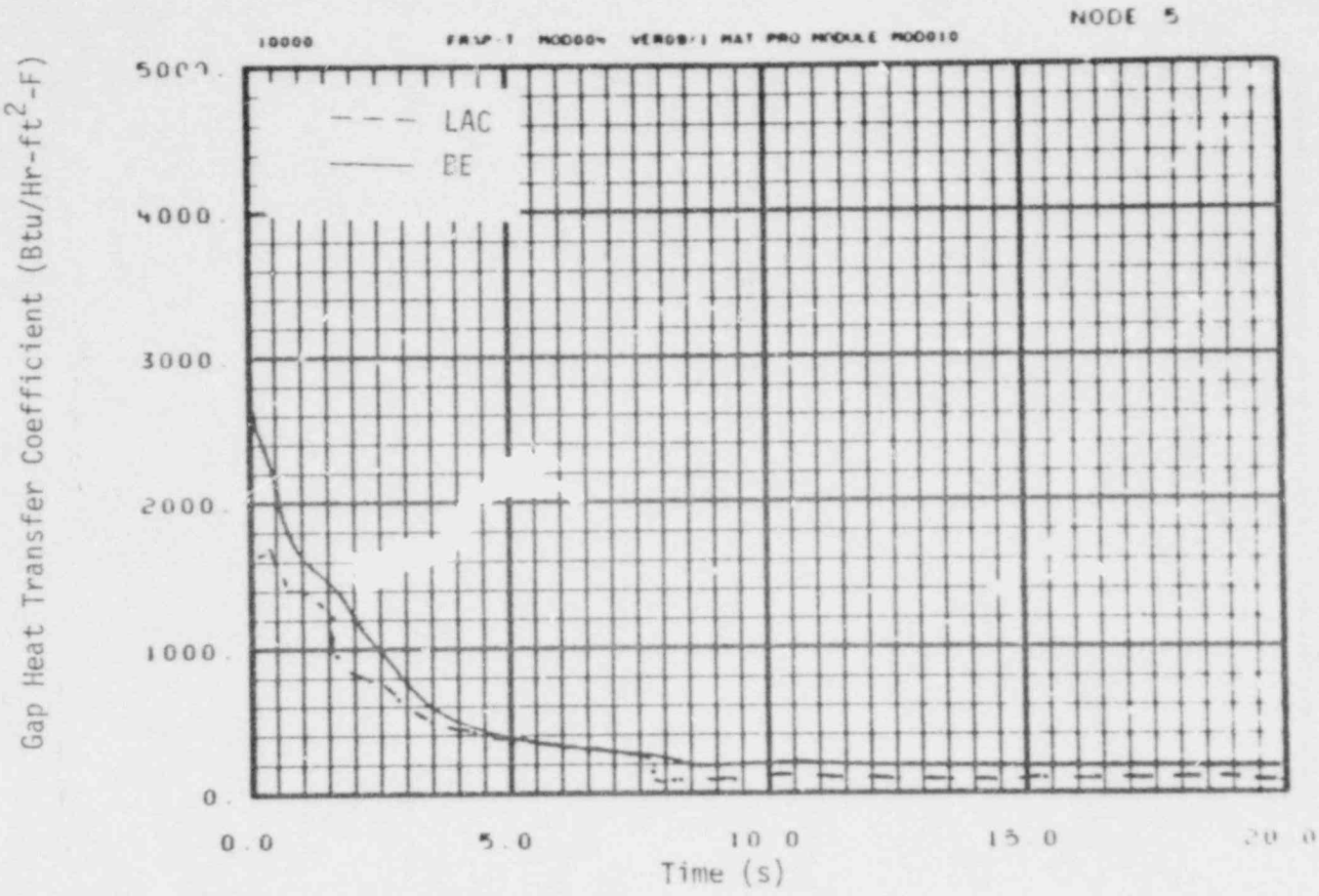

Fig. D-26 Gap conductance history at peak power node (simplified PWR LOCA).

As shown in Figure D-19, the LACE predicted cladding temperature is a slightly greater than the BE predicted temperature from the time film boiling begins until cladding rupture or [illegible]s. The LACE calculations predict cladding rupture to occur at a time of 7.7 s. At that time the LACE predicted temperature is less than the BE predicted temperature. This is becuase the LACE calculations predict more cladding deformation, which leads to more cooling of the cladding. After cladding rupture has occurred, the location of peak cladding temperature shifts from Node 5 to Node 6. As shown in Figure D-20, the LACE calculations predict a peak cladding temperature at Node 6 of 2400°F, while the BE peak temperature is 2000°F. As shown in Figure D-21, the LACE calculations predict a fuel centerline temperature at LOCA initiation that is 300°F higher than the BE predicted temperature. This temperature difference is maintained for the time span of the calculations.

The LACE and BE internal pressure histories are shown in Figure D-22. The LACE calculations predict an internal pressure of 2065 psia at the time of the LOCA initiation, while the BE calculations predict a pressure of 1945 psia. The internal pressure drops sharply at the time of cladding rupture. The LACE predicted time of cladding rupture is 7.7 s, while the BE predicted time is 8.6 s. The combination of higher internal presssure and higher cladding temperature cause the LACE calculations to predict cladding rupture earlier than the BE calculations.

The LACE and BE cladding hoop strain histories are shown in Figure D-23. The LACE and BE calculations both predict cladding plastic deformation to begin about 2.5 s after initiation of the LOCA. The LACE calculations initially predict slightly less plastic deformation than the BE claculations. After unstable ballooning to rupture initiates at 7.6 s, however, the LACE calculations predict significantly more plastic deformation than the BE calculations. This is because the LACE models assume the cladding deformation to remain

uniform until cladding rupture occurs. The BE model or the other hand, assumes the cladding deformation is uniform only until the cladding instability strain is exceeded. Then localized non-axisymmetric wall thinning is modeled as the cladding strains out to rupture. (This localized straining is not included in the plotted BE hoop strain history.)

The cladding length change history is plotted in Figure D-24. The LACE calculated elongation parallels the BE calculated elongation until the cladding temperature exceeds 1500°F. It is about 30 % greater than the BE calculated elongation, however. As the cladding temperature increases from 1500 to 1800°F, the alpha to beta phase transition takes place and the LACE calculations show no increase in cladding elongation, while the BE claculations show a decrease. This variance is consistent with the LACE and BE models for cladding thermal expansion. The LACE model shows no thermal exapnsion during the temperature range of the alpha to beta phase transition (1500 to (1780°F), while the BE model shows a decrease in thermal expansion.

The gas gap history is plotted in Figure D-25. At the time of LOCA initiation, the LACE calculated gas gap is 0.92 mils, and the BE gap is 0.36 mils. After the LOCA initiation, the LACE calculated gap continues to stay slightly larger than the BE calculated gap until cladding rupture is predicted. After rupture it is significantly bigger than the BE calculated gap.

The gap conductance history is plotted in Figure D-26. At the time of LOCA initiation, the LACE calculated gap conductance is 1680 Btu/ft^2-hr-°F, while the BE calculated value is 2470 Btu/ft^2-hr-°F. During the LOCA, the LACE calculated gap conductance continues to stay less than the BE calculated value.

4. PBF LOC 11C Test

Plots of the computed fuel rod response are shown in Figures D-27 through D-31. The plots are shown for axial Node 6, which is located 1.38 ft above the bottom of the 3 ft long test rod. The fuel rod peak power, cladding temperature, and deformation all occur at axial Node 6. The calculation apply to the medium pressure test rod (fill gas pressure of 312 psia).

The LACE and BE calculated cladding surface temperature histories are compared in Figure D-27. The fuel centerline temperature histories are shown in Figure D-28. At the time of LOCA initiation, the LACE and BE calculated fuel centerline temperatures are 5021 and 4546°F, respectively. At the end of blowdown, the LACE and BE calculated temperatures are 2150 and 1890°F, respectively.

The LACE and BE calculated rod pressure and cladding deformation histories are compared in Figure D-29 and D-30. Both the rod pressure and cladding hoop strain are similiar for the two calculations until the LACE calculations predict cladding rupture. The BE calculations predict cladding rupture 3.5 s later. The post-rupture LACE calculated cladding hoop strain is 30%, while the BE calculated value is 16%.

The LACE and BE calculated gap conductance histories are compared in Figure D-31. At the time of LOCA initiation, the LACE calculated gap conductance is 2710 Btu/ft^2-hr-°F, while the BE calculated value is 6800 Btu/ft^2-hr-°F.

5. TREAT LOCA Test FRF-2

Plots of the computed fuel rod responses are shown in Figures D-32 through D-37. The plots are shown for axial Node 5, which is 0.94 ft above the bottom of the 2.08 ft long test rods. The

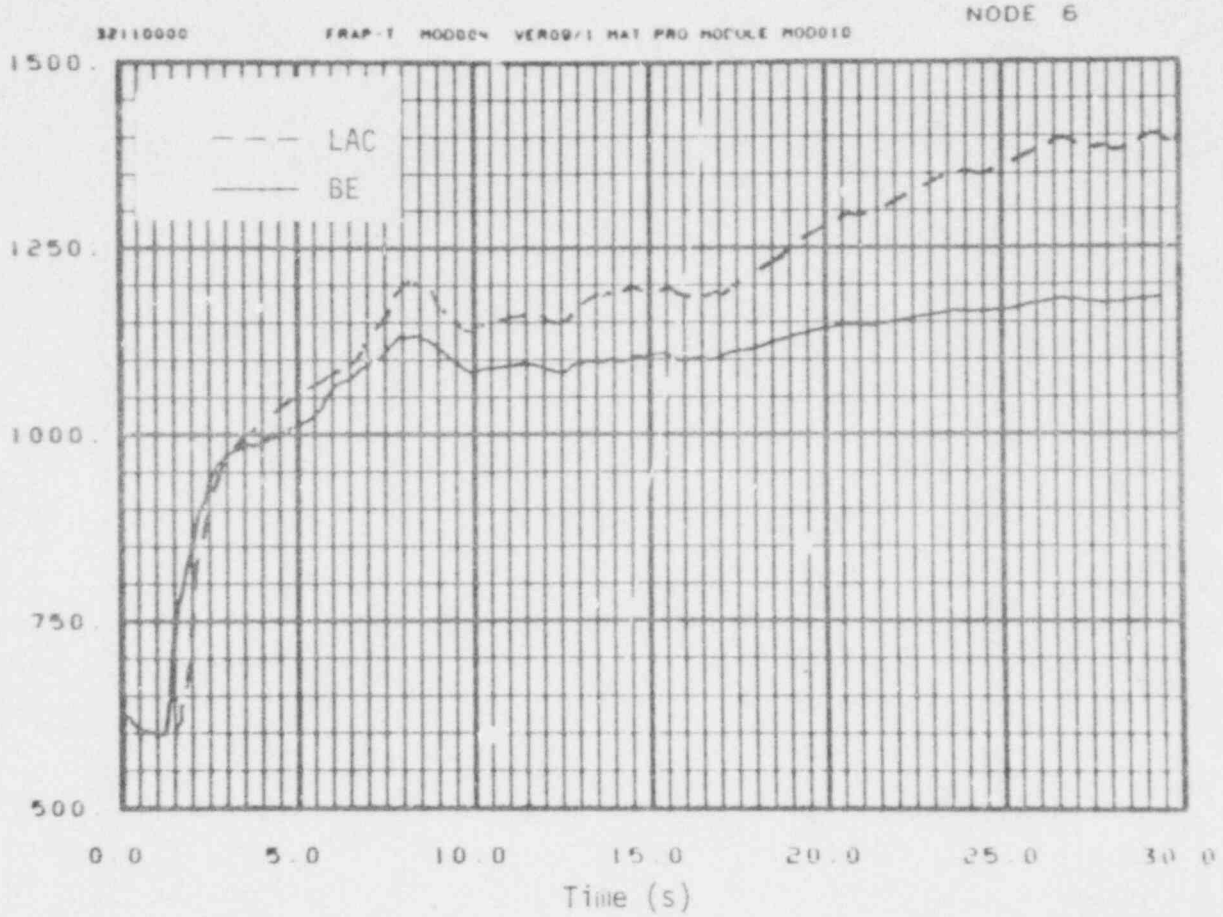

Fig. D-27 Cladding surface temperature history (PBF LOC 11C Test).

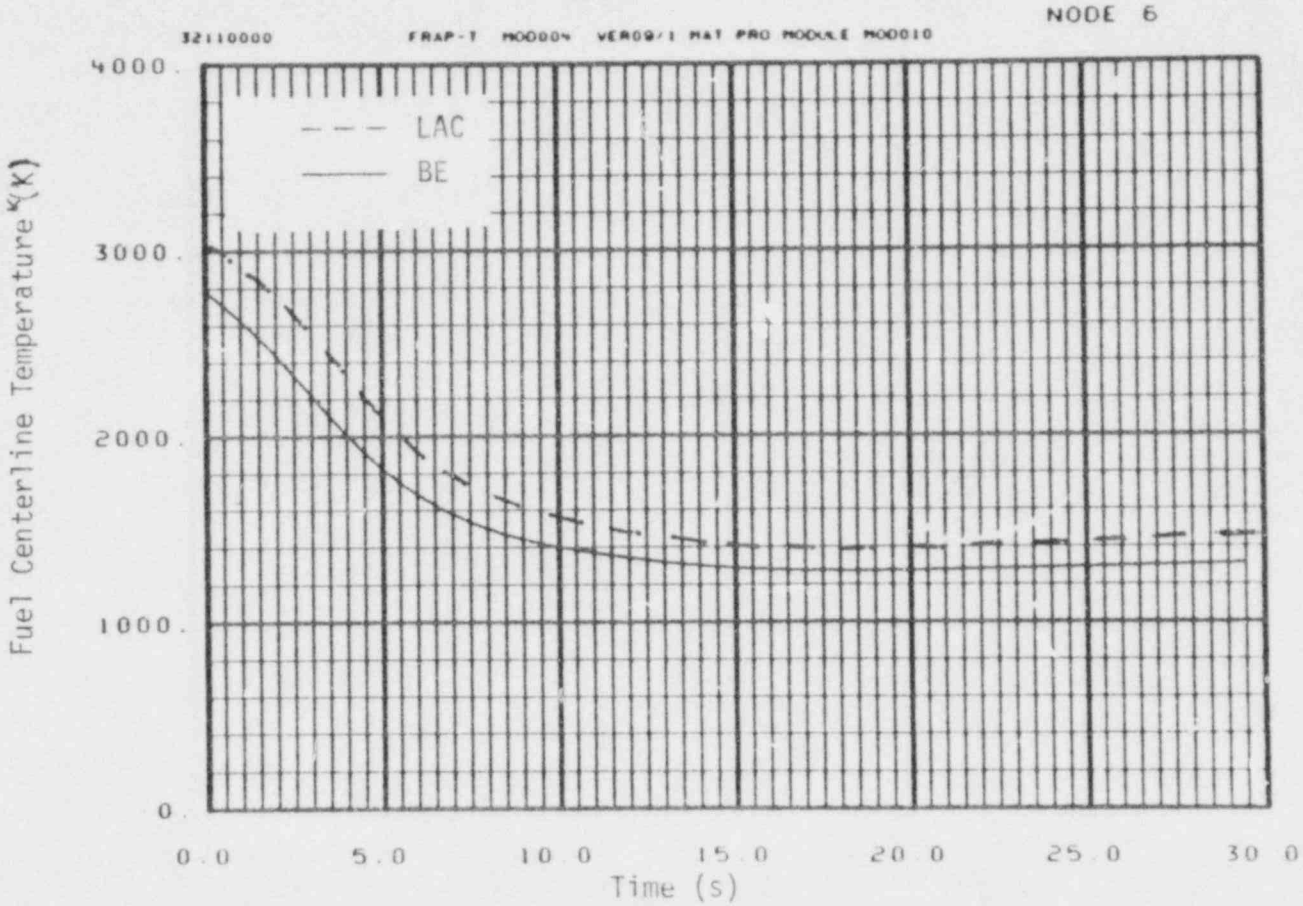

Fig. D-28 Fuel centerline temperature history (PBF LOC 11C Test)

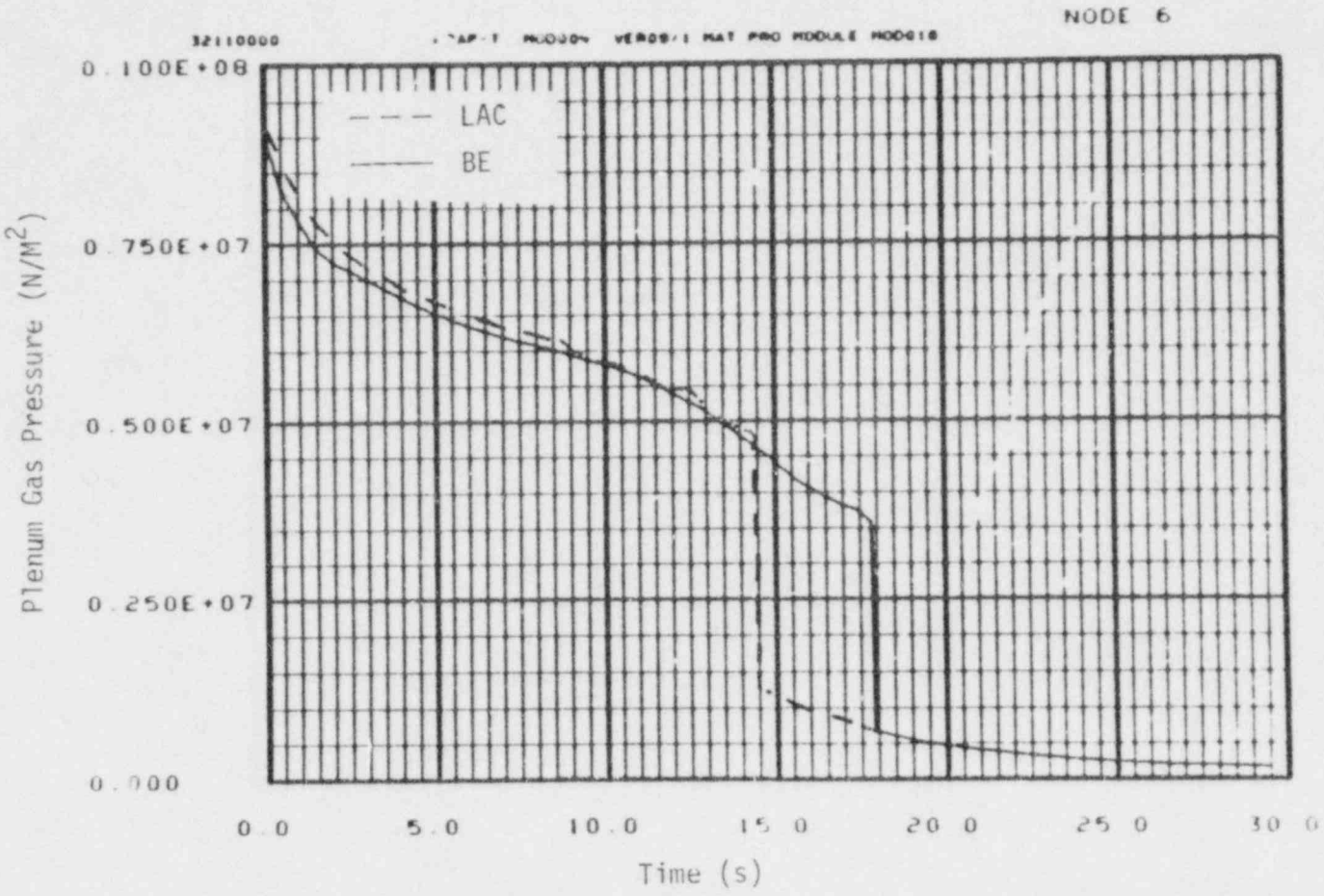

Fig. D-29 Internal pressure history (PBF LOC 11C Test).

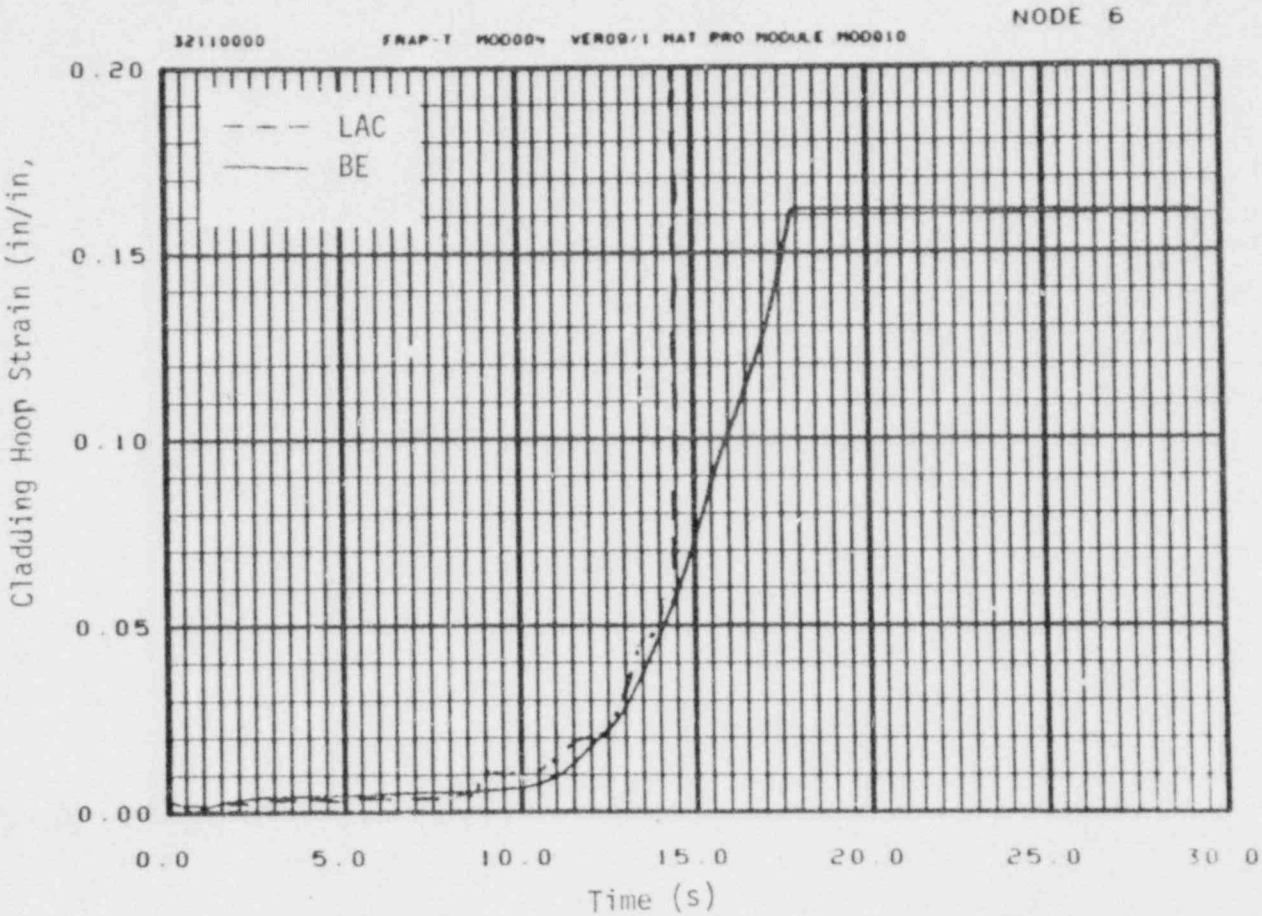

Fig. D-30 Cladding hoop strain history (PBF LOC 11C Test).

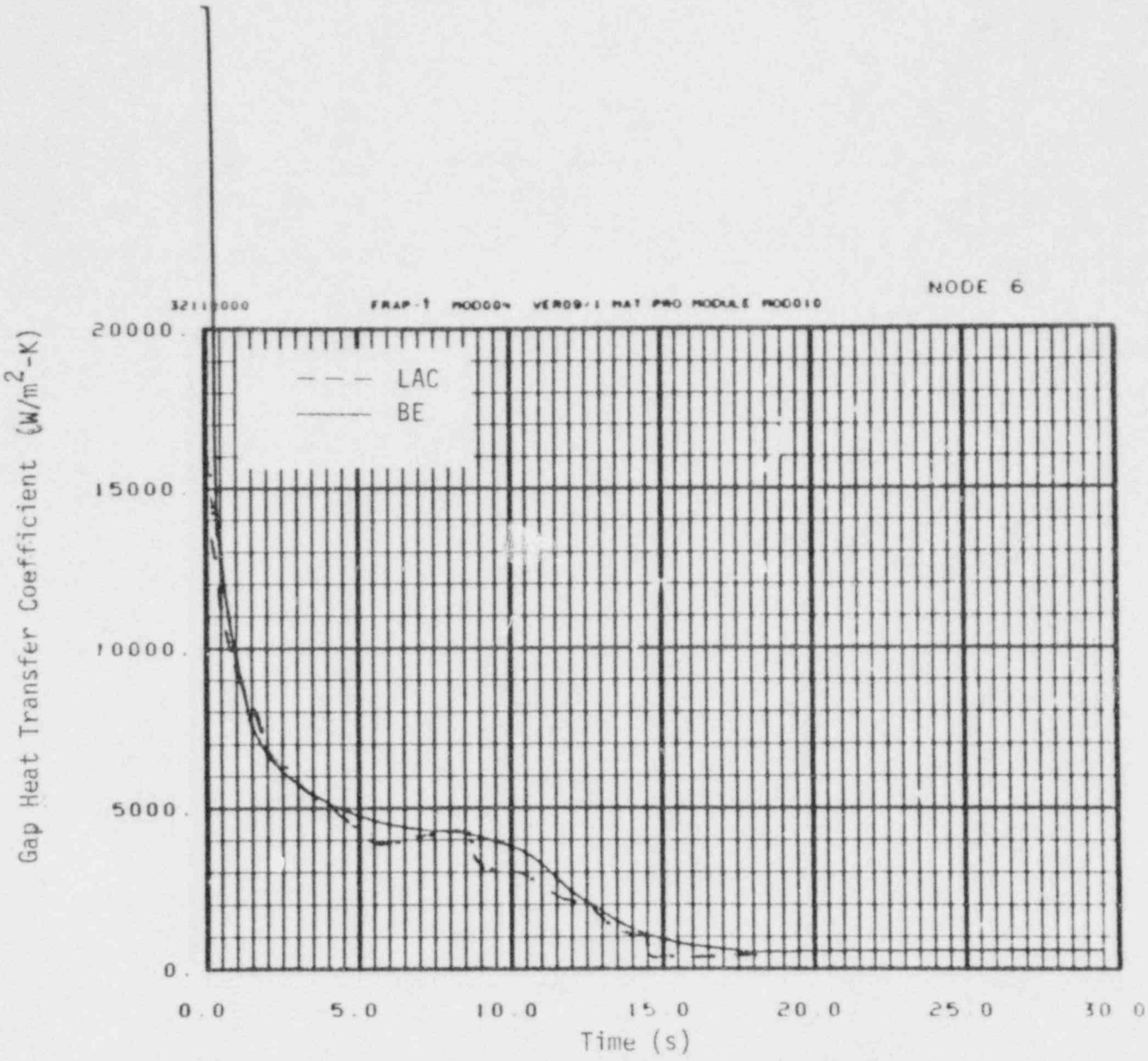

Fig. D-31 Gap conductance history (PBF LOC 11C Test).

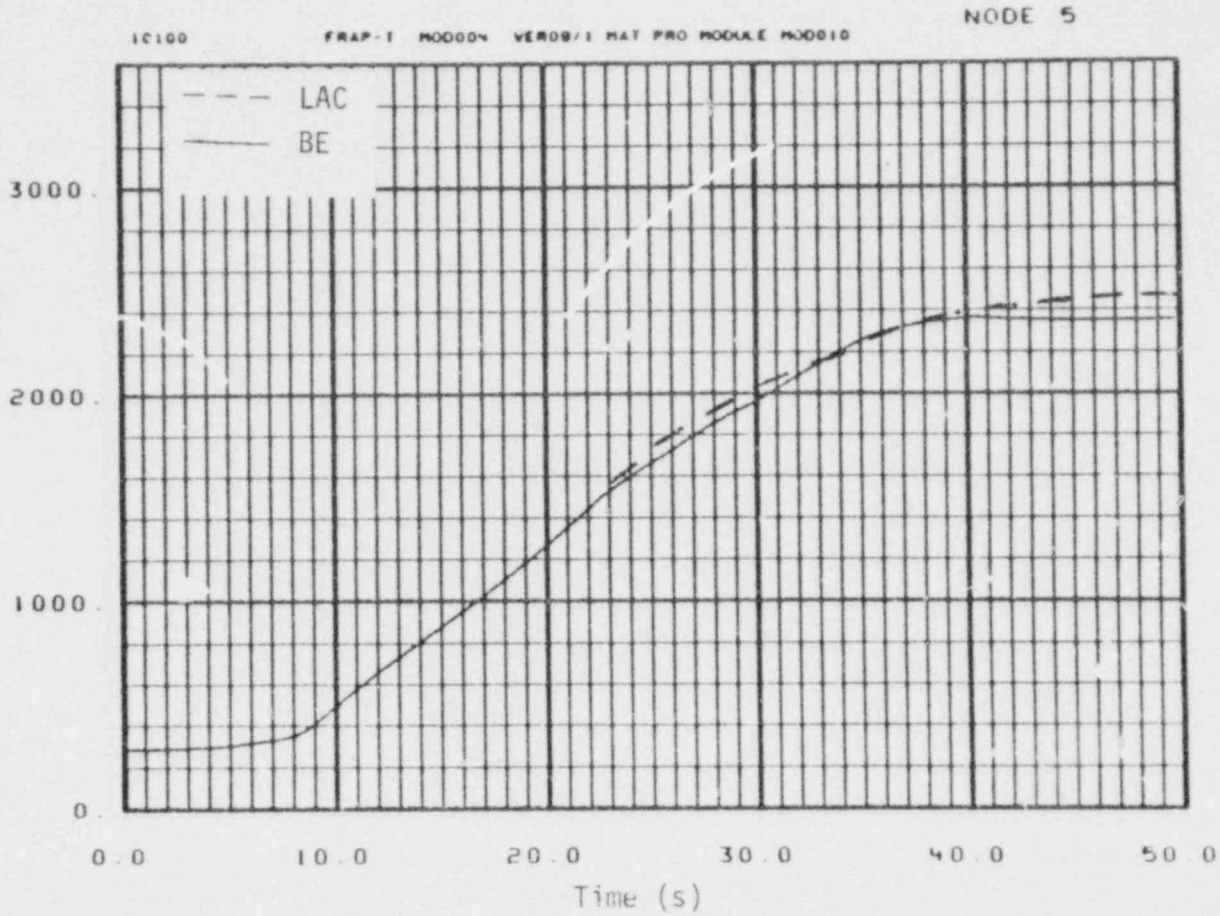

Fig. D-32 Cladding surface temperature history (TREAT LOCA Test).

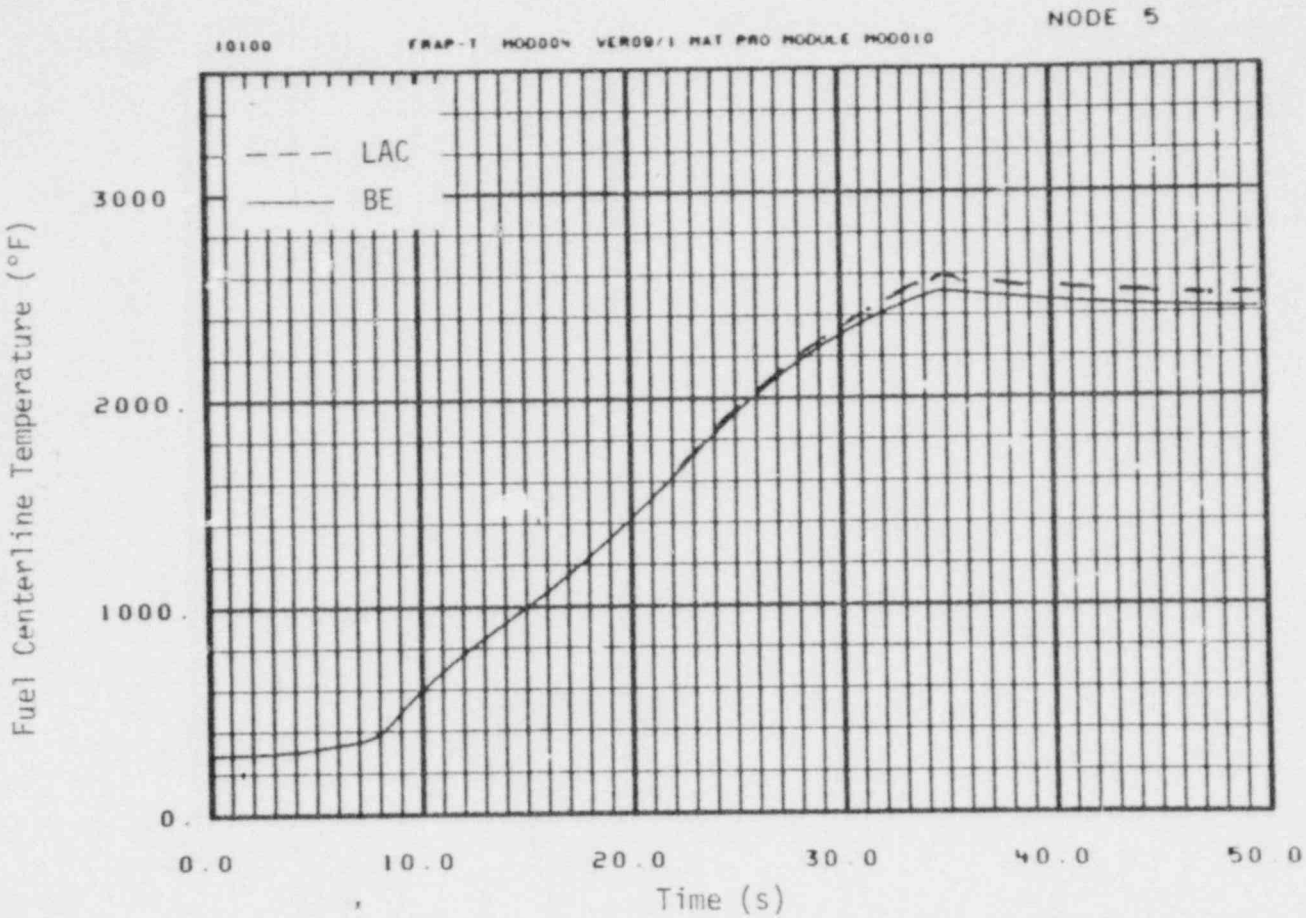

Fig. D-33 Fuel centerline temperature history (TREAT LOCA Test).

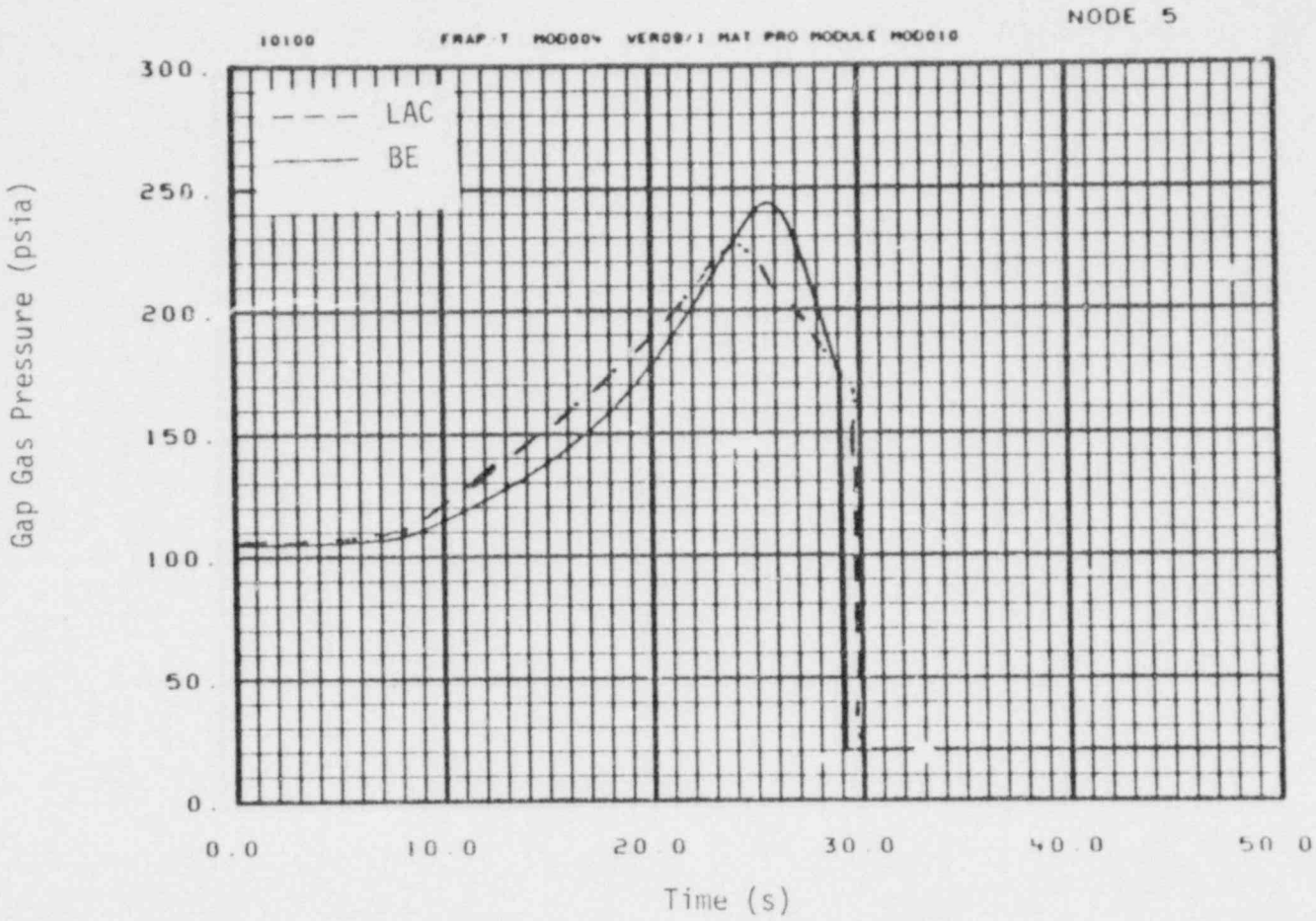

Fig. D-34 Internal pressure history (TREAT LOCA Test).

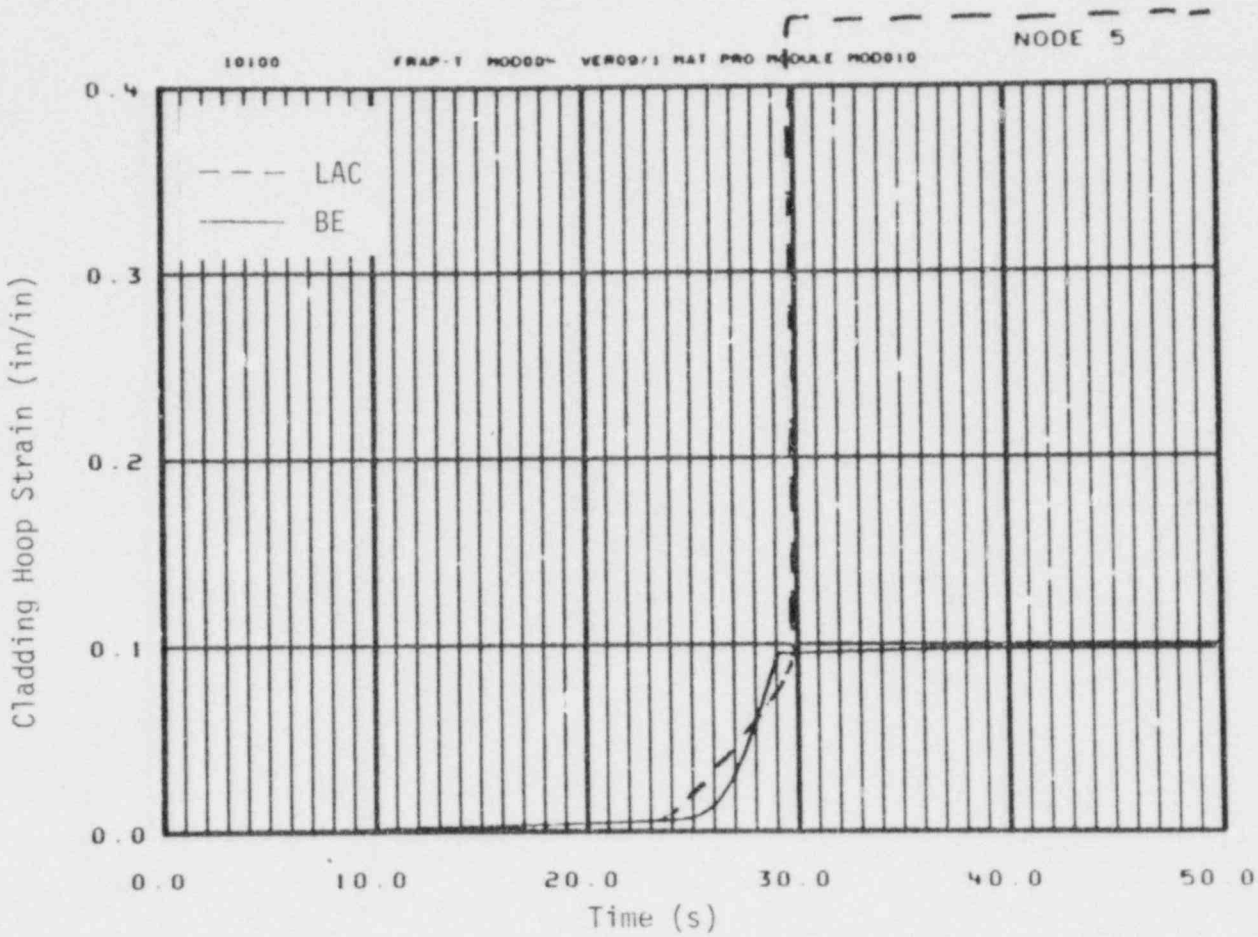

Fig. D-35 Cladding hoop strain history (TREAT LOCA Test).

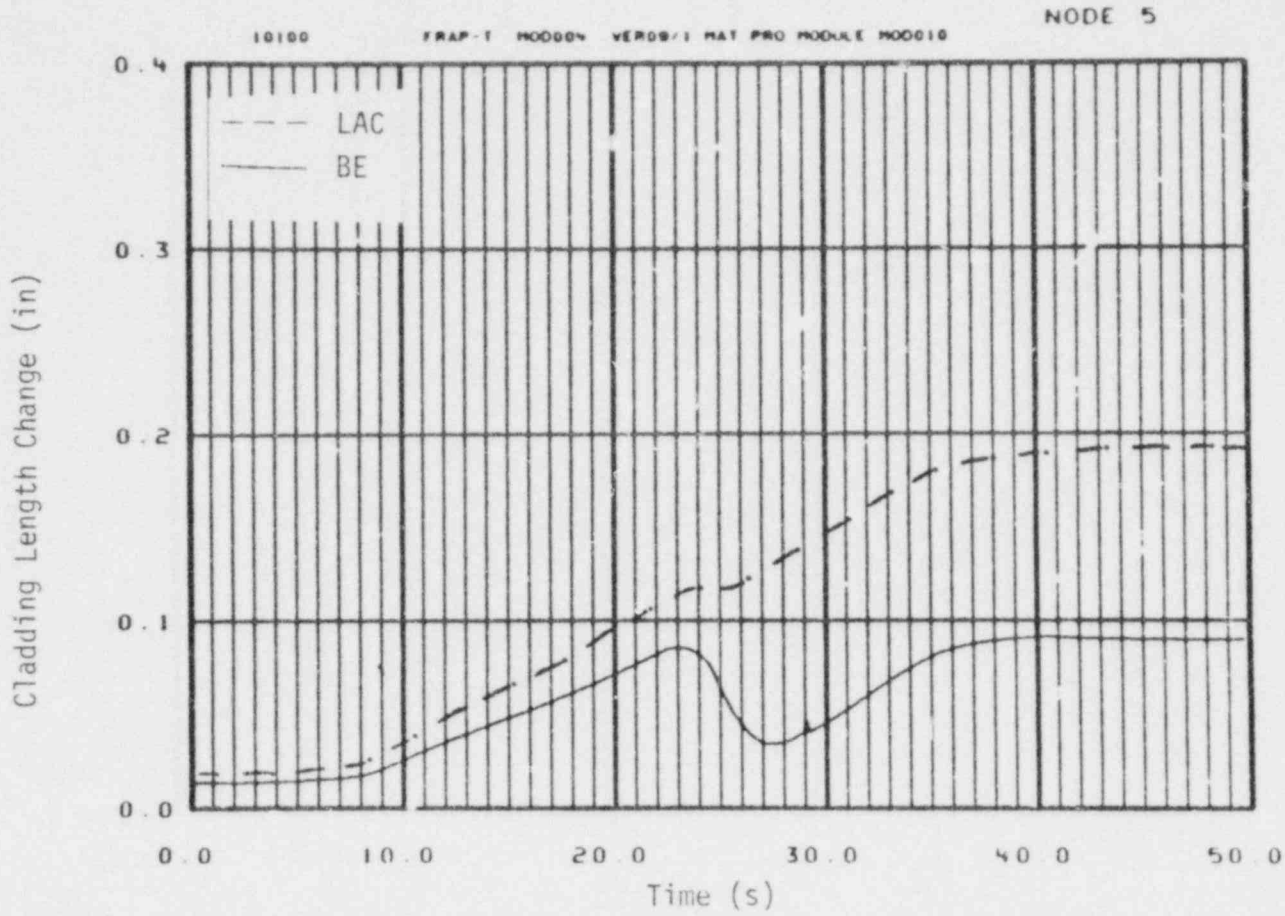

Fig. D-36 Cladding elongation history (TREAT LOCA Test).

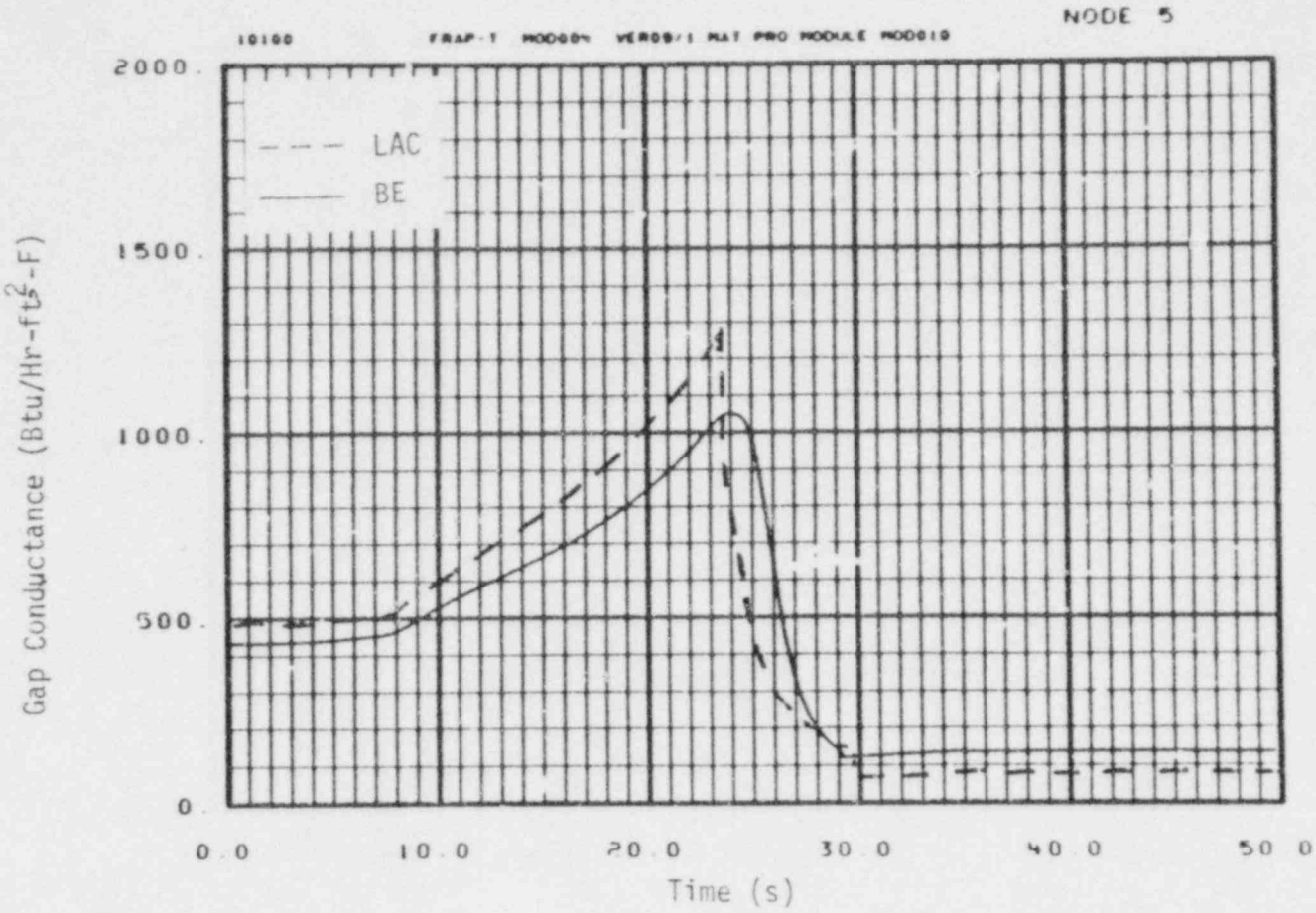

Fig. D-37 Gap conductance history (TREAT LOCA Test).

test rod peak power and predicted cladding rupture occurred at Node 5. At the start of the test, the fuel and cladding are at a temperature of 286°F. Then a power pulse with an amplitude of about 6 kW/ft and a duration of 25 s is applied to the fuel rod. This results in a fuel stored energy roughly comparable to that expected in a commercial reactor fuel rod at the end of the blowdown phase of a LOCA. The test fuel rods are cooled by superheated steam the duration of the test. The temperature of the steam is calculated by FRAP-T.

Metal-water reaction was precluded in both the LACE and BE calculations. This prevented the calculated fuel rod temperatures from exceeding the measured temperatures, and compensated for not modeling radiation heat transfer to the flow shroud. Also, steam flow during the test is low enough that steam limiting of the metal-water reaction will occur. (FRAP-T assumes no steam limiting.)

The LACE and BE calculated cladding surface temperature histories are compared in Figure D-32. The fuel centerline temperature histories are compared in Figure D-33. Power input to the fuel rod stopped at a time of 35 s. The LACE and BE calculated fuel centerline temperatures at this time were 2580 and 2555°F, respectively. The LACE and BE calculated cladding temperatures are almost the same out to 38 s. Then the LACE calculated temperature steadily becomes greater than the BE calculated temperature. At a time of 50 s, the LACE and BE calculated cladding surface temperatures are 2480 and 2360°F, respectively.

The LACE and BE calculated internal pressure histories are compared in Figure D-34, while the cladding hoop strain histories are compared in Figure D-35. Even though the LACE calculated cladding temperature is a little higher than the BE calculated temperature, the LACE calculations predicted cladding rupture 1 s later than the BE calculations. The rupture temperature is about 2000°F. The LACE calculations, however, predict a larger post-rupture hoop strain than the BE calculations.

The LACE and BE calculated cladding length change histories are compared in Figure D-36. This plot clearly shows the differences in the LACE and BE models for cladding thermal expansion during the alpha to beta phase transition. The LACE model predicts no expansion during the transition, while the BE model predicts a contraction.

The LACE and BE gap conductance histories are compared in Figure D-37. The LACE calculations predict a gap conductance that is 10 to 20% higher than the BE calculations.

6. PBF Test PCM 8-1

Plots of the calculated fuel rods response for this test are shown in Figures D-38 through D-39. The LACE calculations predict film boiling to initiate about 3 s later than the BE claculations. After film boiling has stabilized, the LACE calculated cladding temperatue is about 50°F higher than the BE calculated temperature.

7. BWR ATWS Problem

Plots of the calculated fuel rod response are shown in Figures D-40 through D-43. The fuel rod is not pressurized. At accident initiation, the LACE calculated fuel centerline temperature is about 50°F lower than the BE calculated temperature. The LACE calculated peak cladding temperature, however, is about 500°F higher than the BE calculated temperature. This difference is partly due to the higher transient fuel temperature predicted by the LACE calculations. It is also due to the delayed film boiling predicted by the BE calculations.

8. BWR RIA Problem

Plots of the calculated fuel rod response are shown in Figures D-44 through D-50. The fuel rod is not pressurized. The LACE

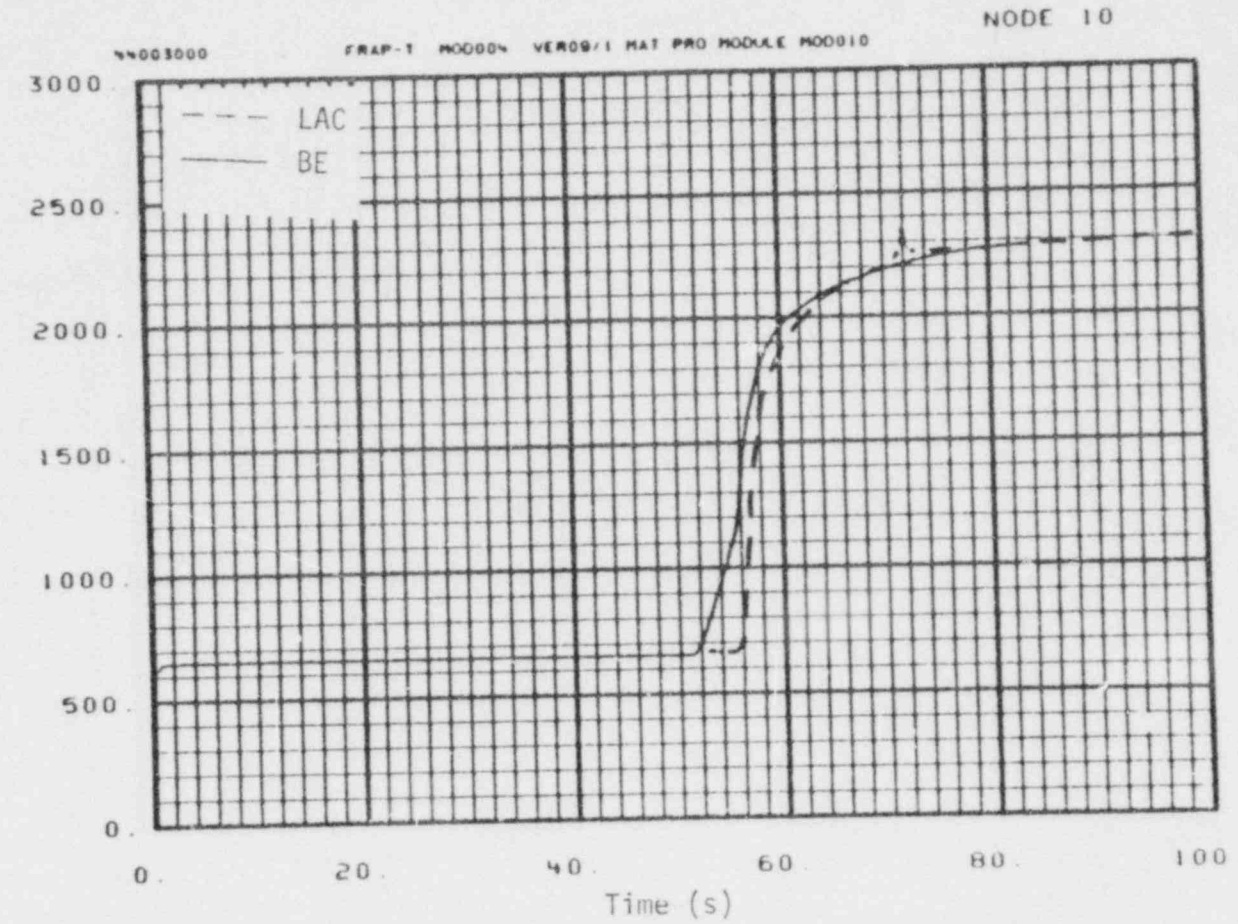

Fig.D-38 Cladding surface temperature history (PBF Test PCM 8-1).

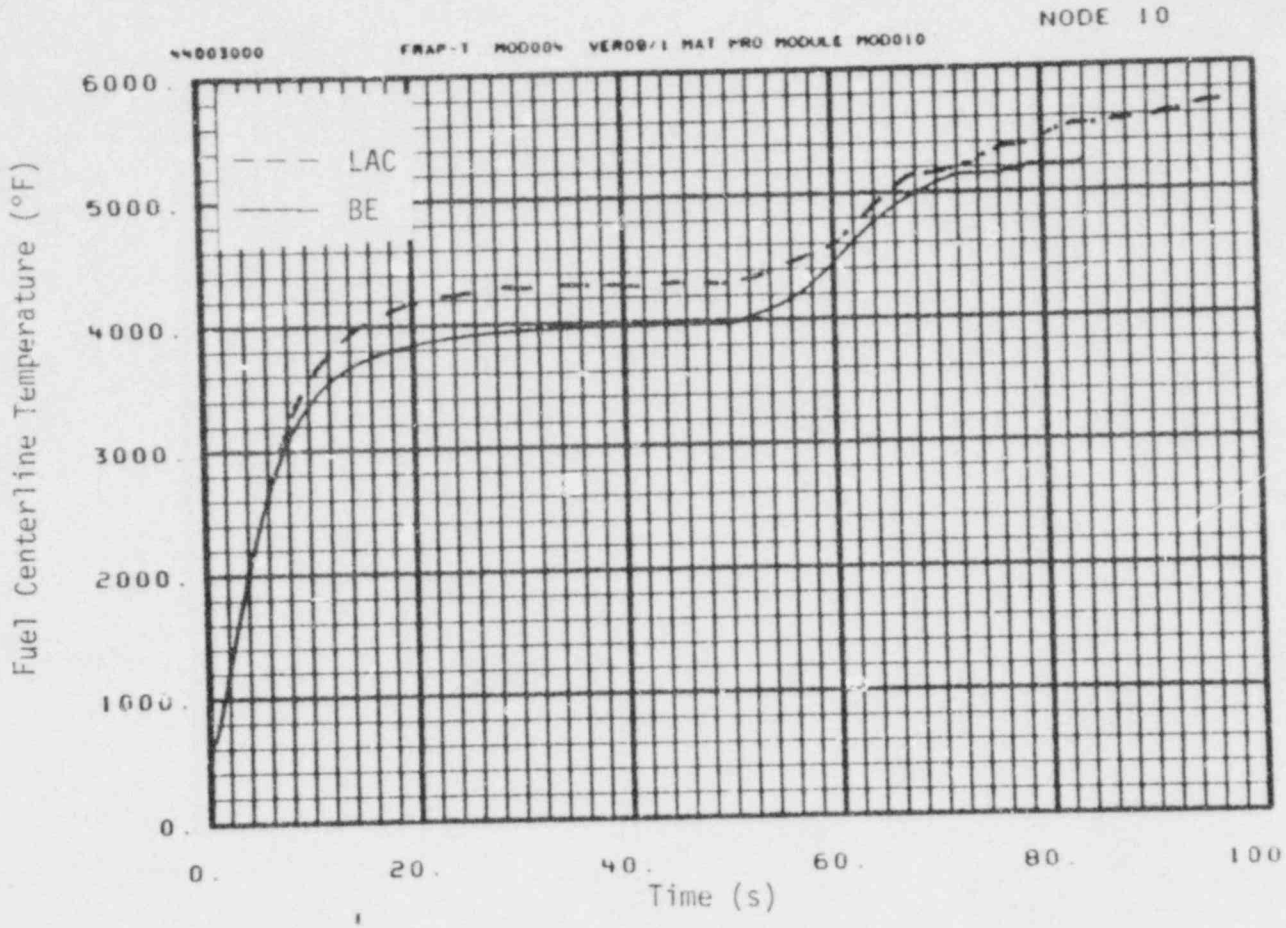

Fig. D-39 Fuel centerline temperature history (PBF Test PCM 8-1).

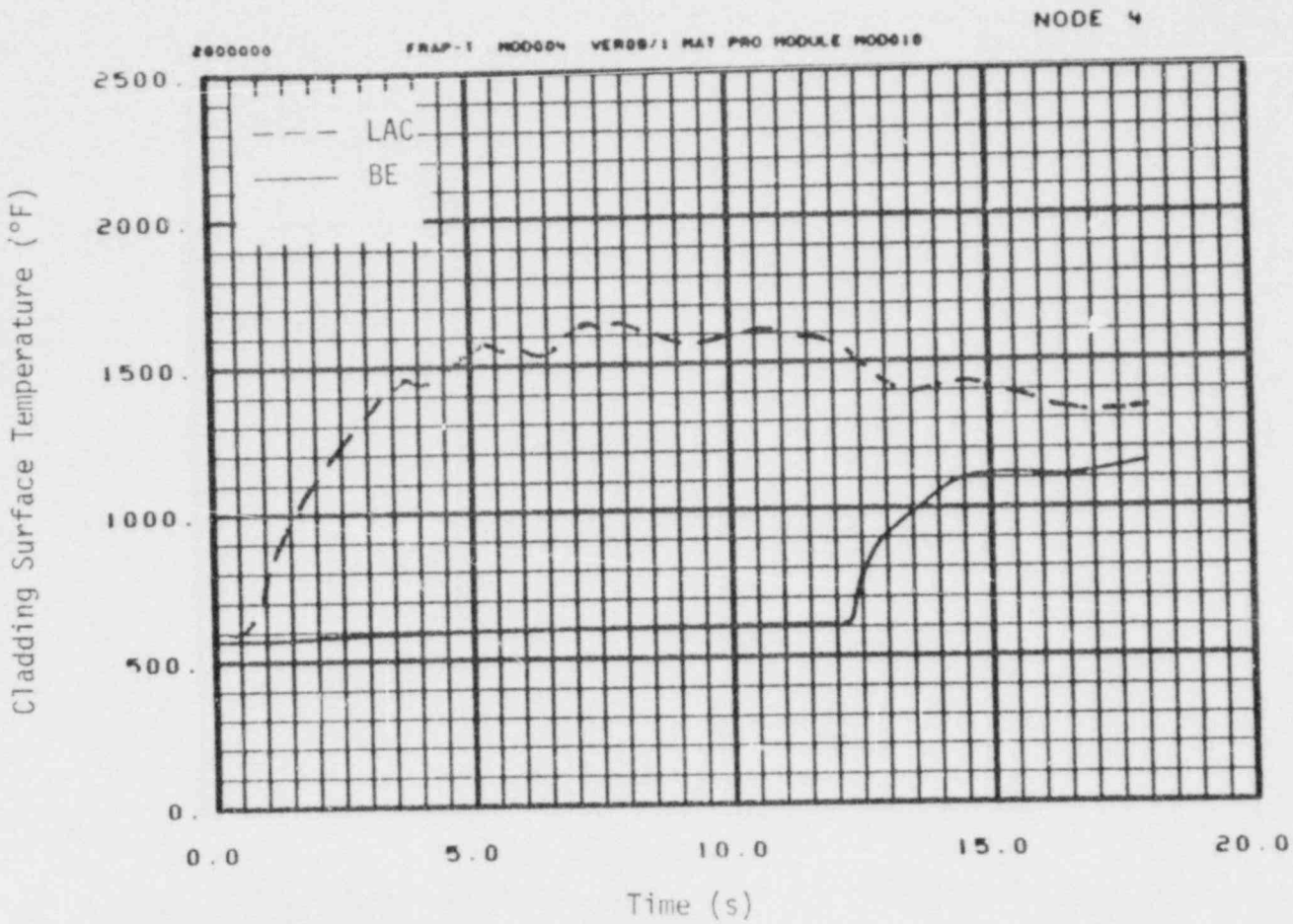

Fig. D-40 Cladding surface temperature history (BWR ATWS).

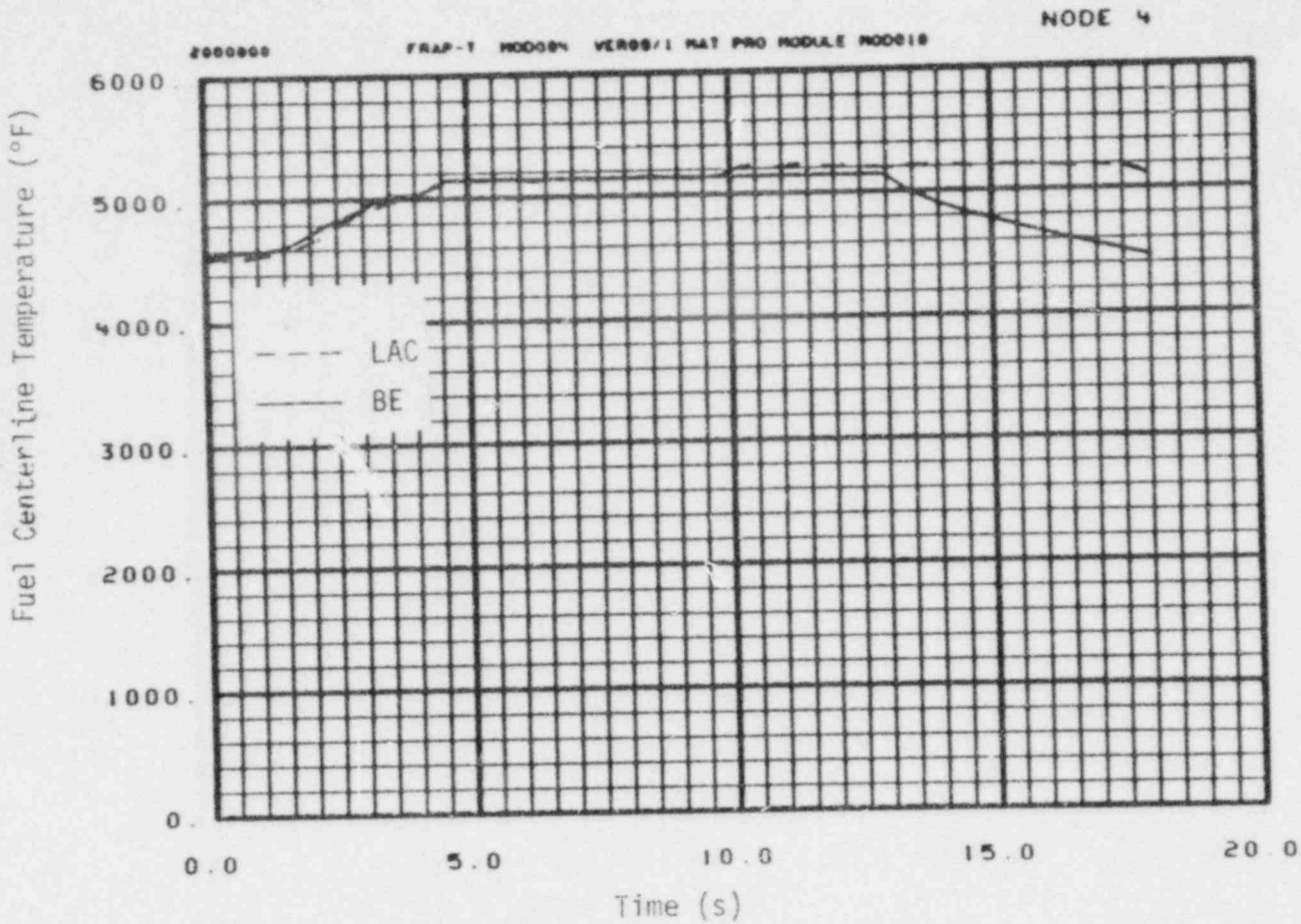

Fig. D-41 Fuel centerline temperature history (BWR ATWS).

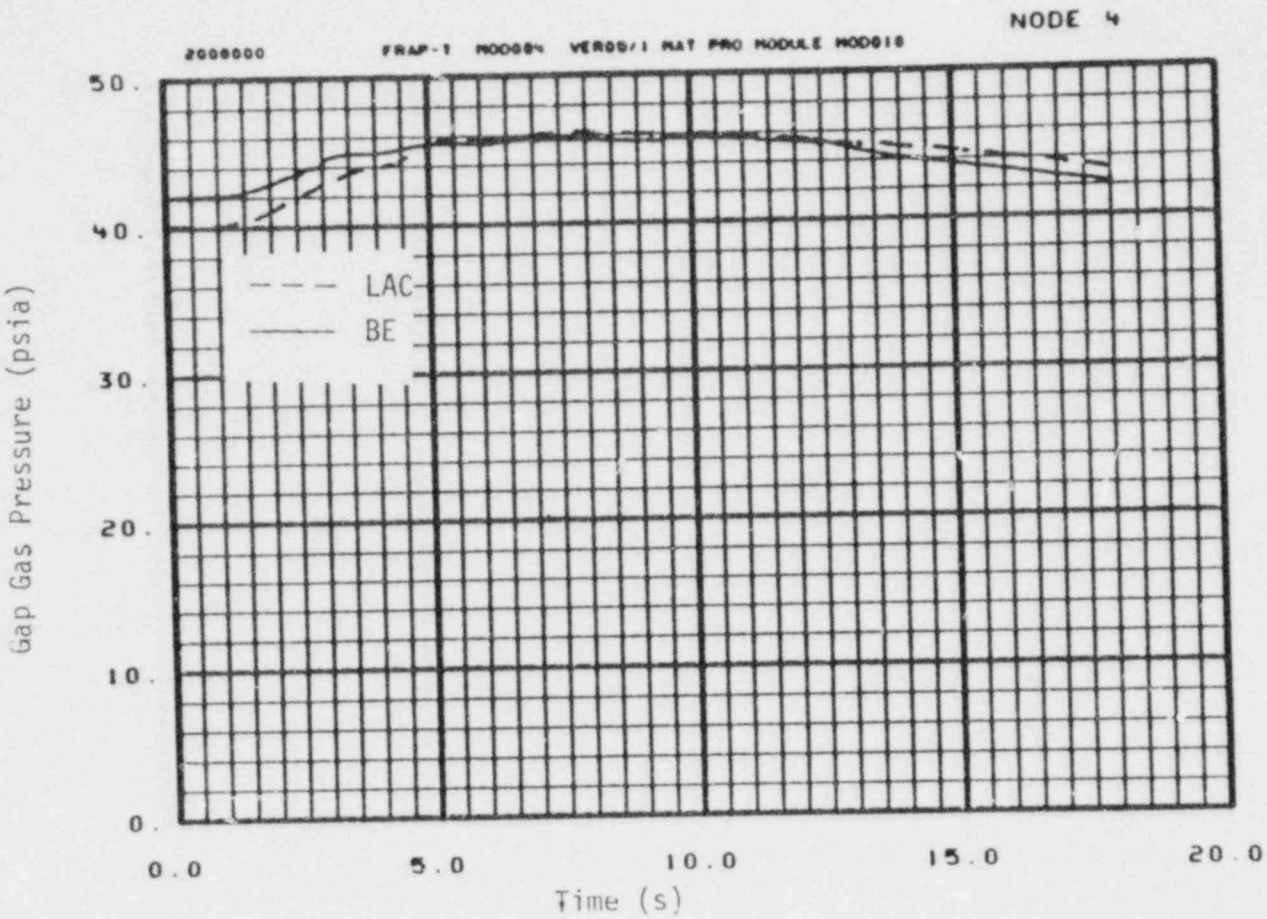

Fig. D-42 Internal pressure history (BWR ATWS).

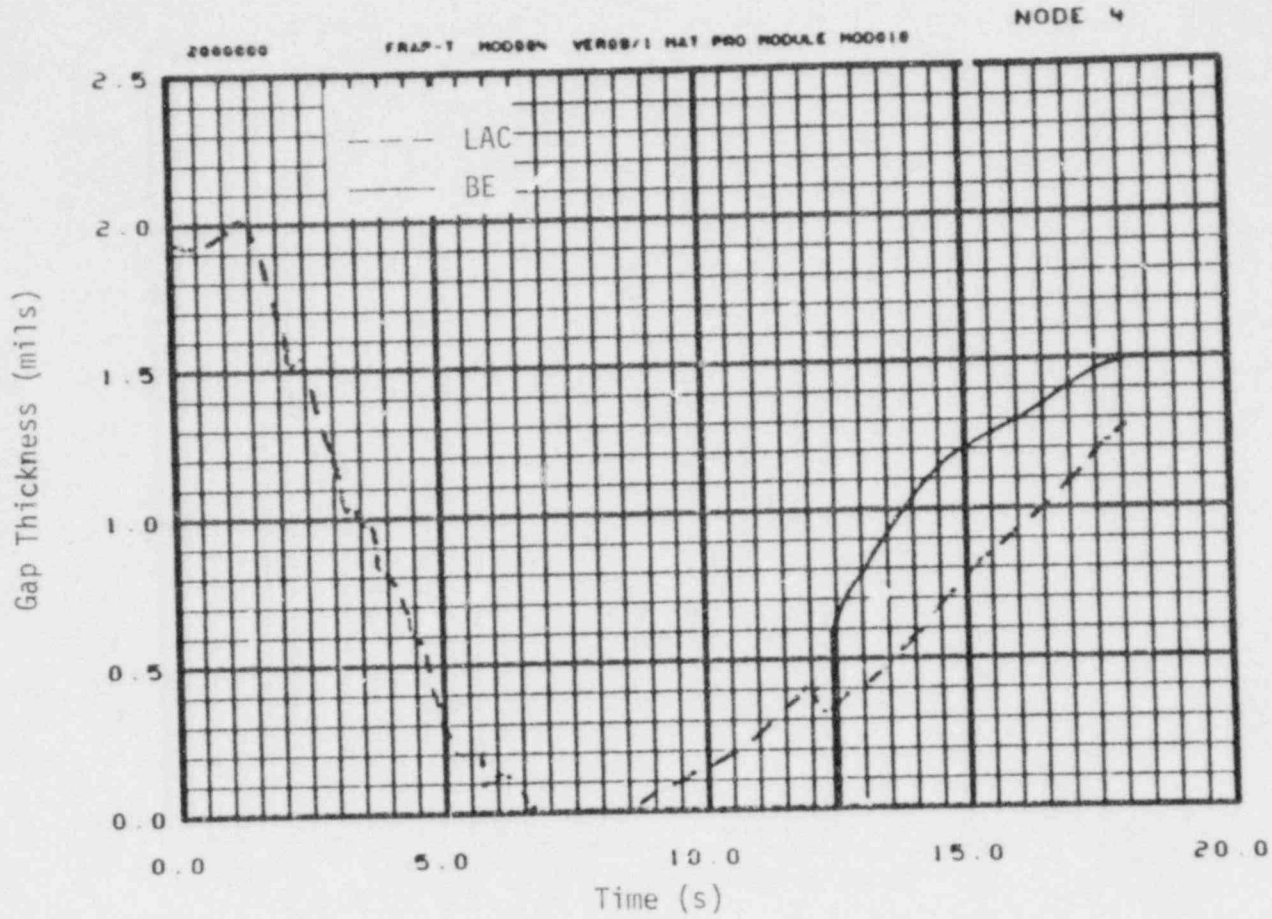

Fig. D-43 Gas gap size history (BWR ATWS).

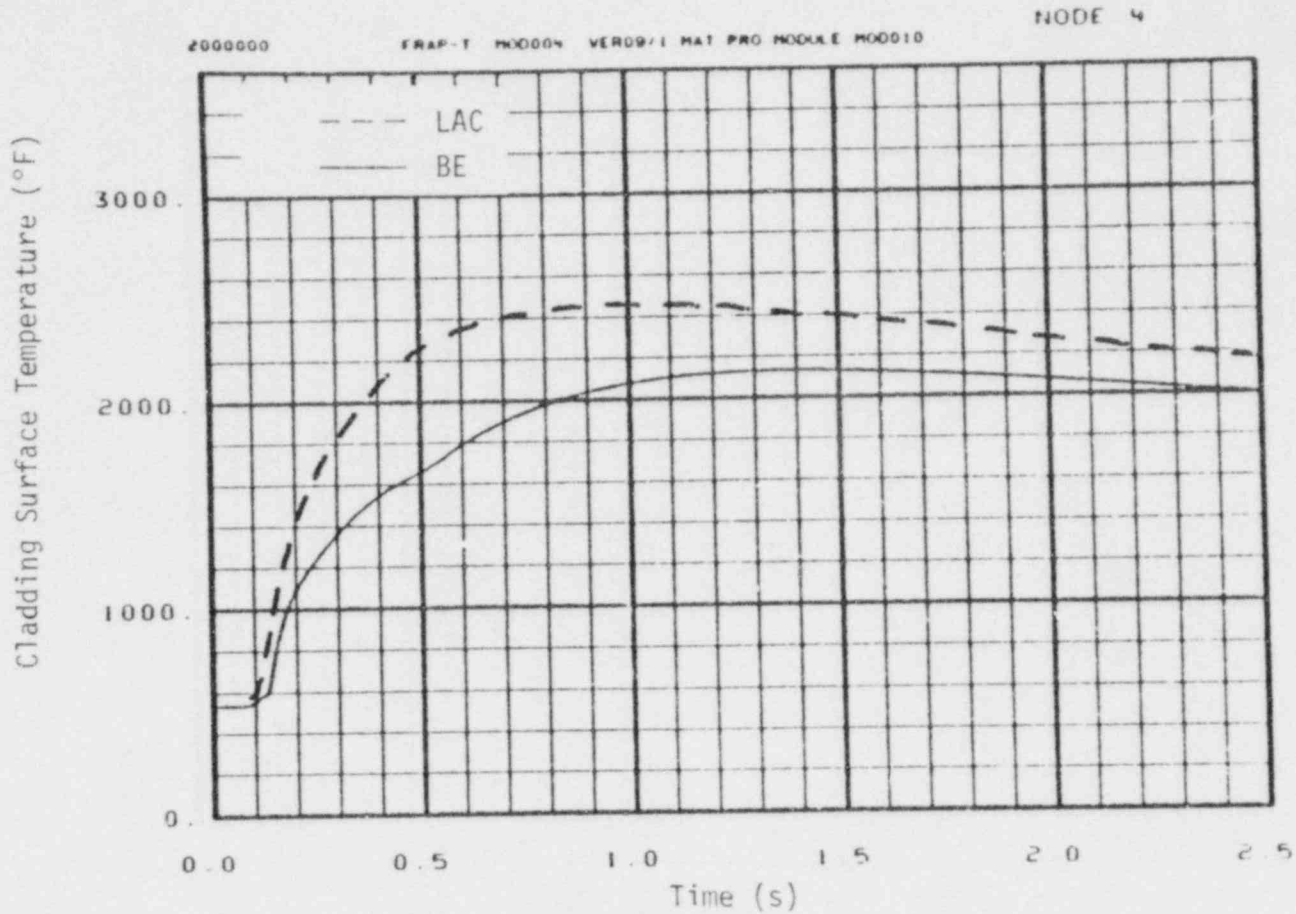

Fig. D-44 Cladding surface temperature history (BWR RIA).

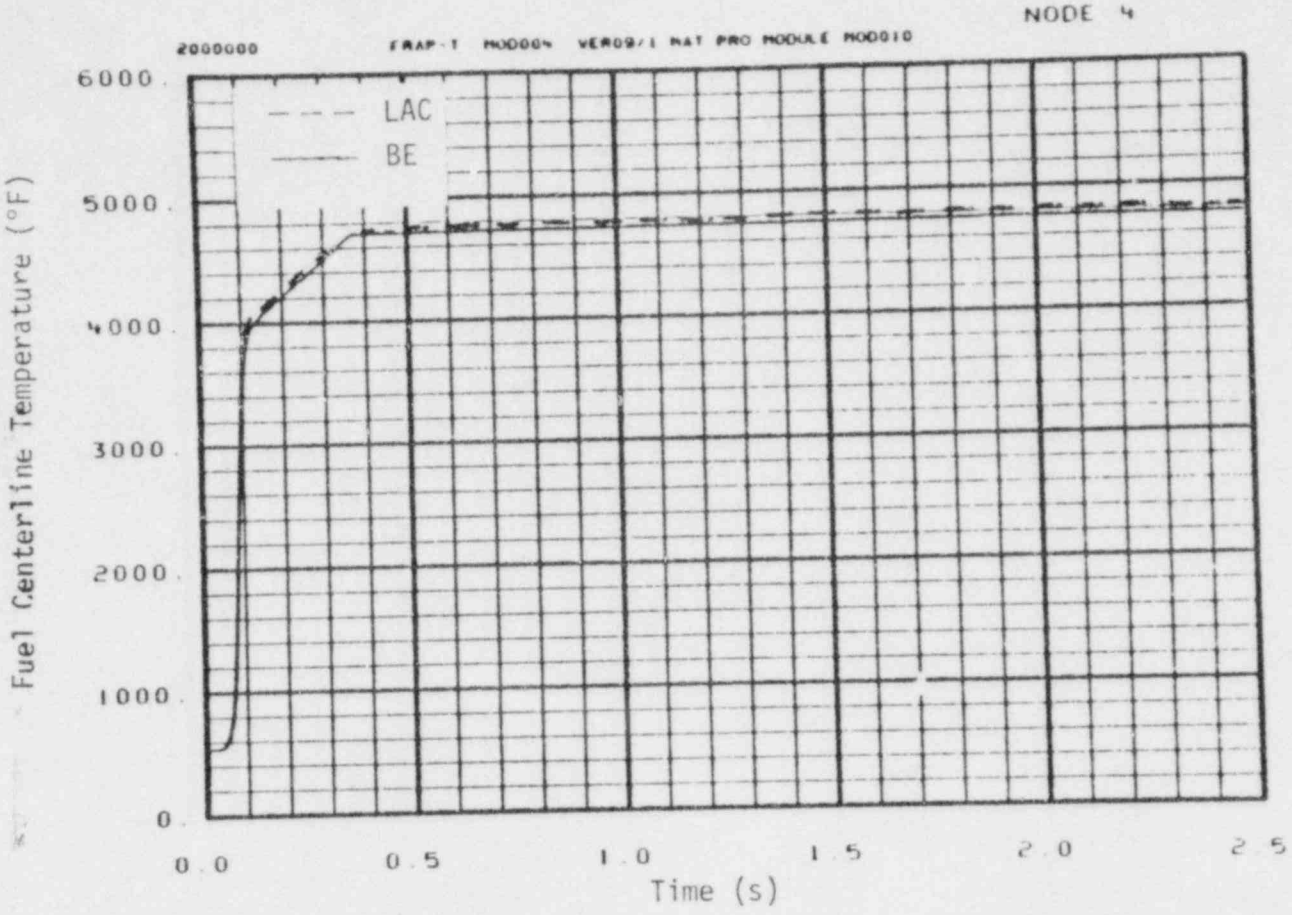

Fig. D-45 Fuel centerline temperature history (BWR RIA).

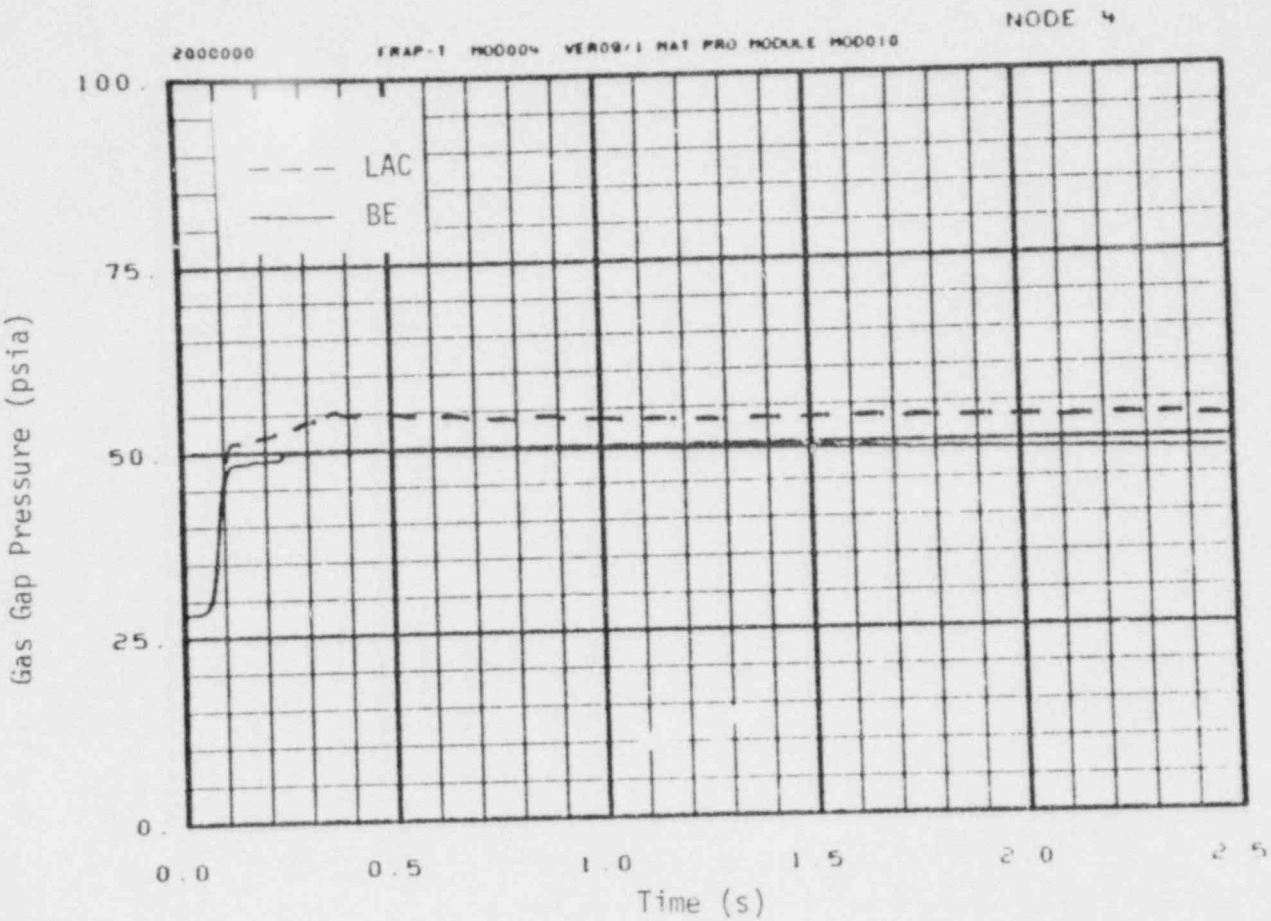

Fig. D-46 Internal pressure history (BWR RIA).

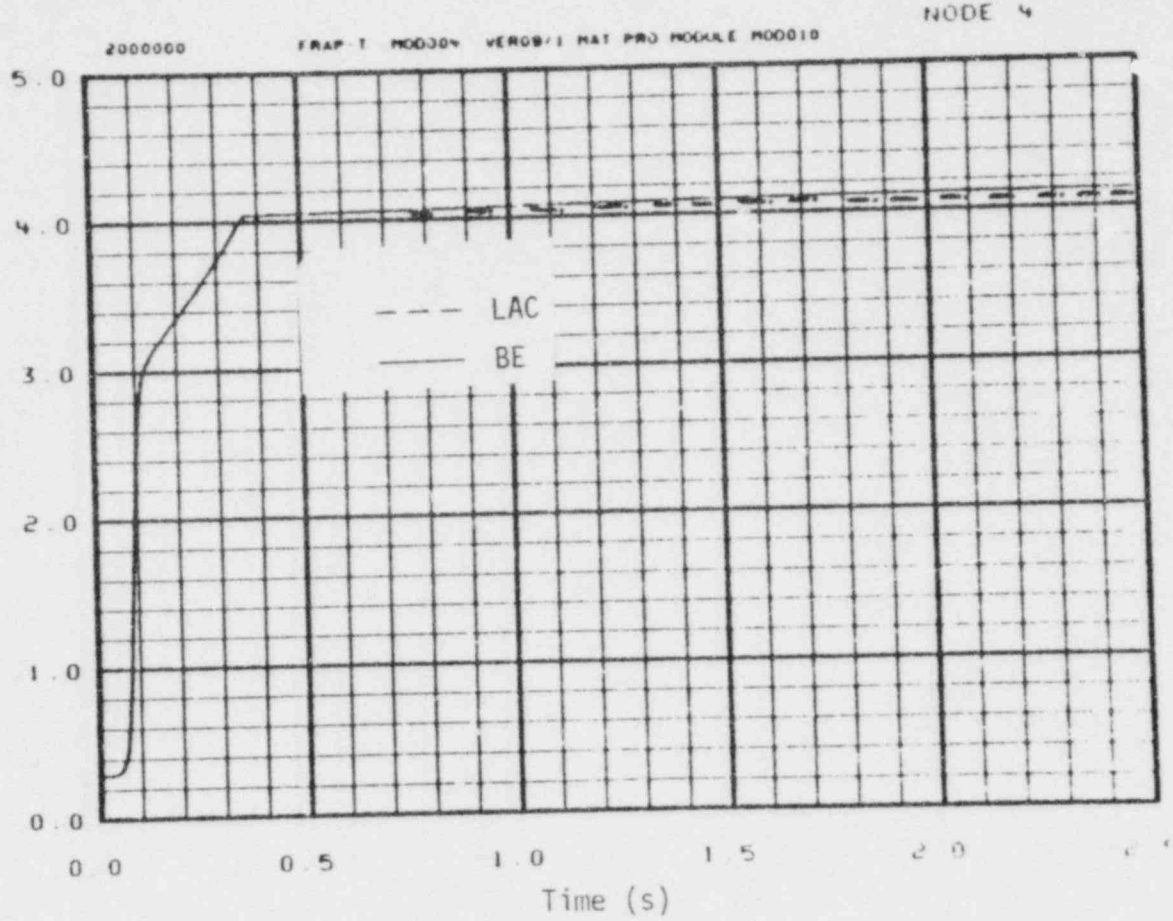

Fig. D-47 Fuel stack elongation history (BWR RIA).

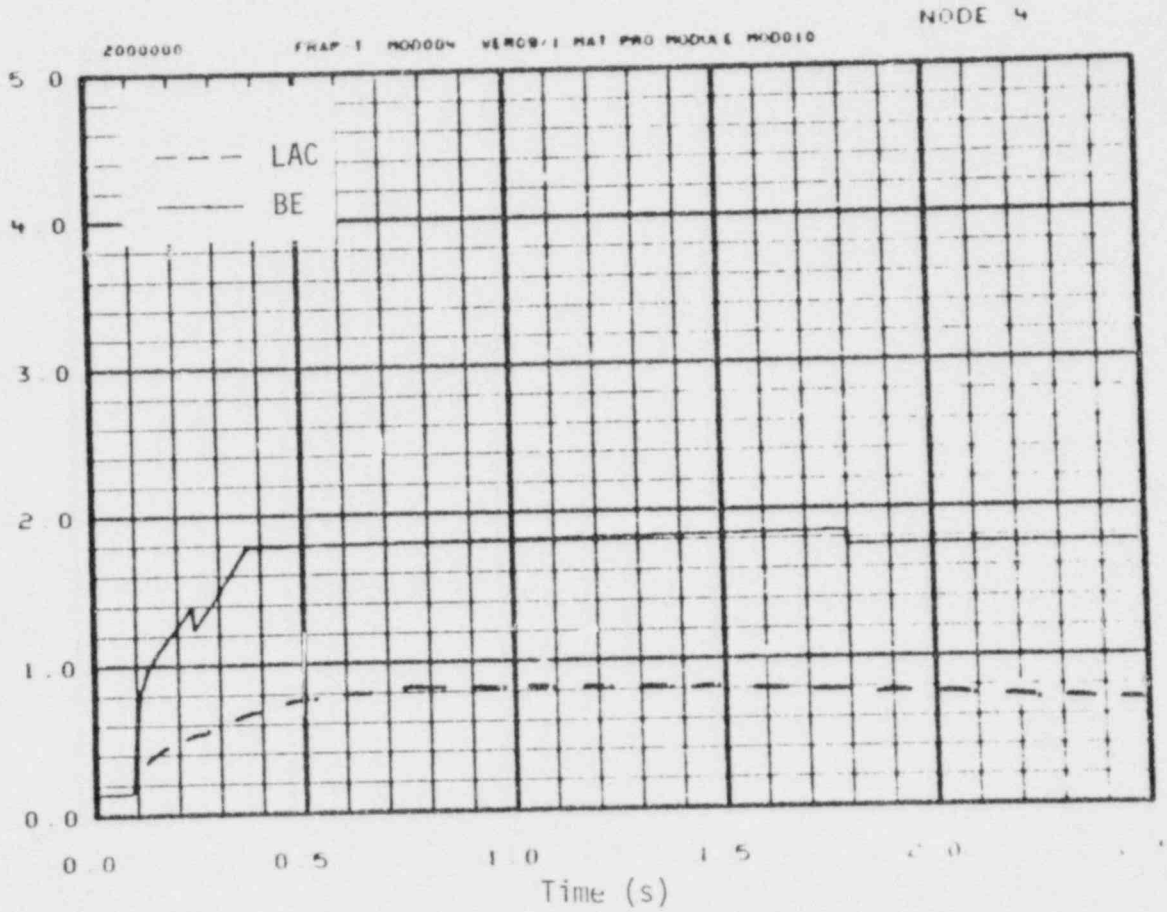

Fig. D-4. Cladding elongation history (BWR RIA).

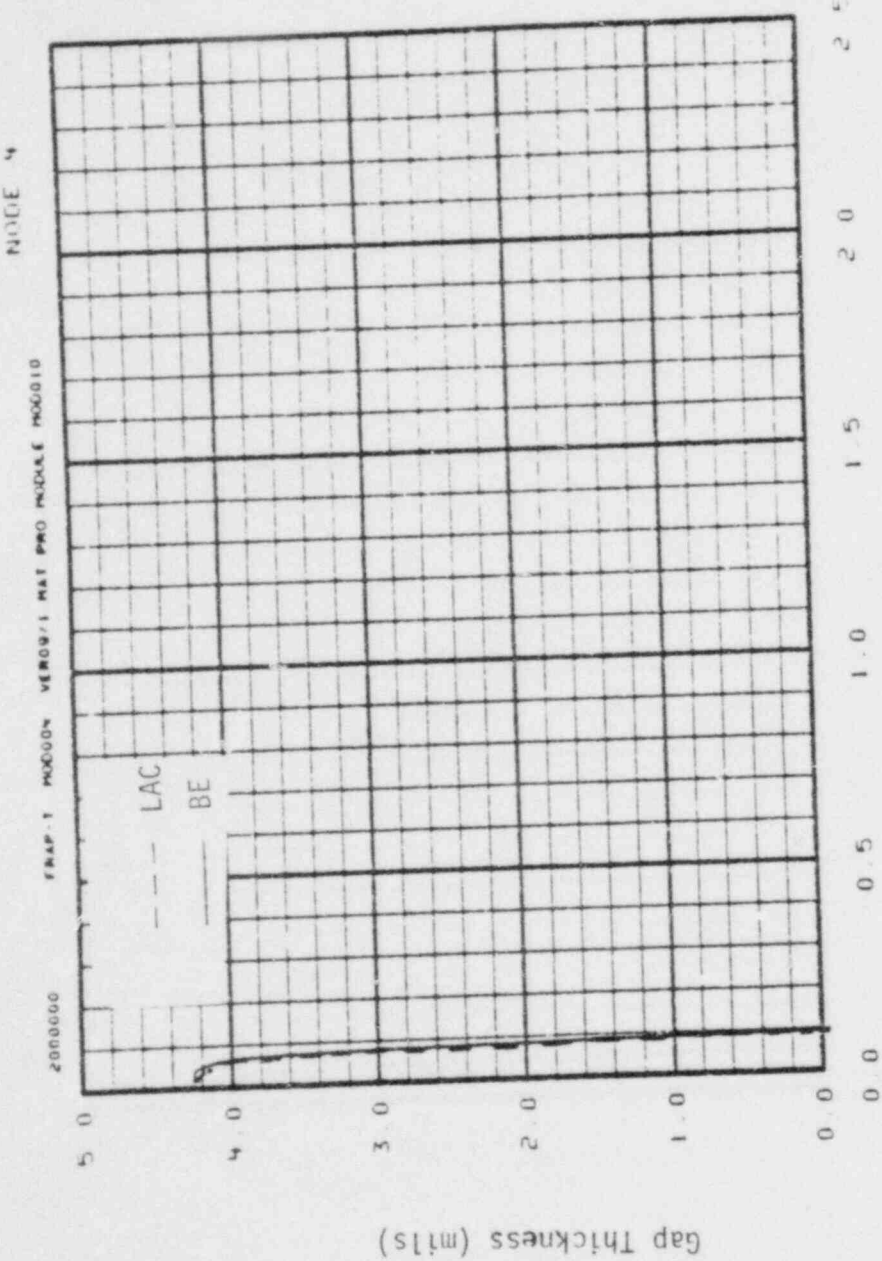

Fig. D-49 Gas gap size history (BWR RIA).

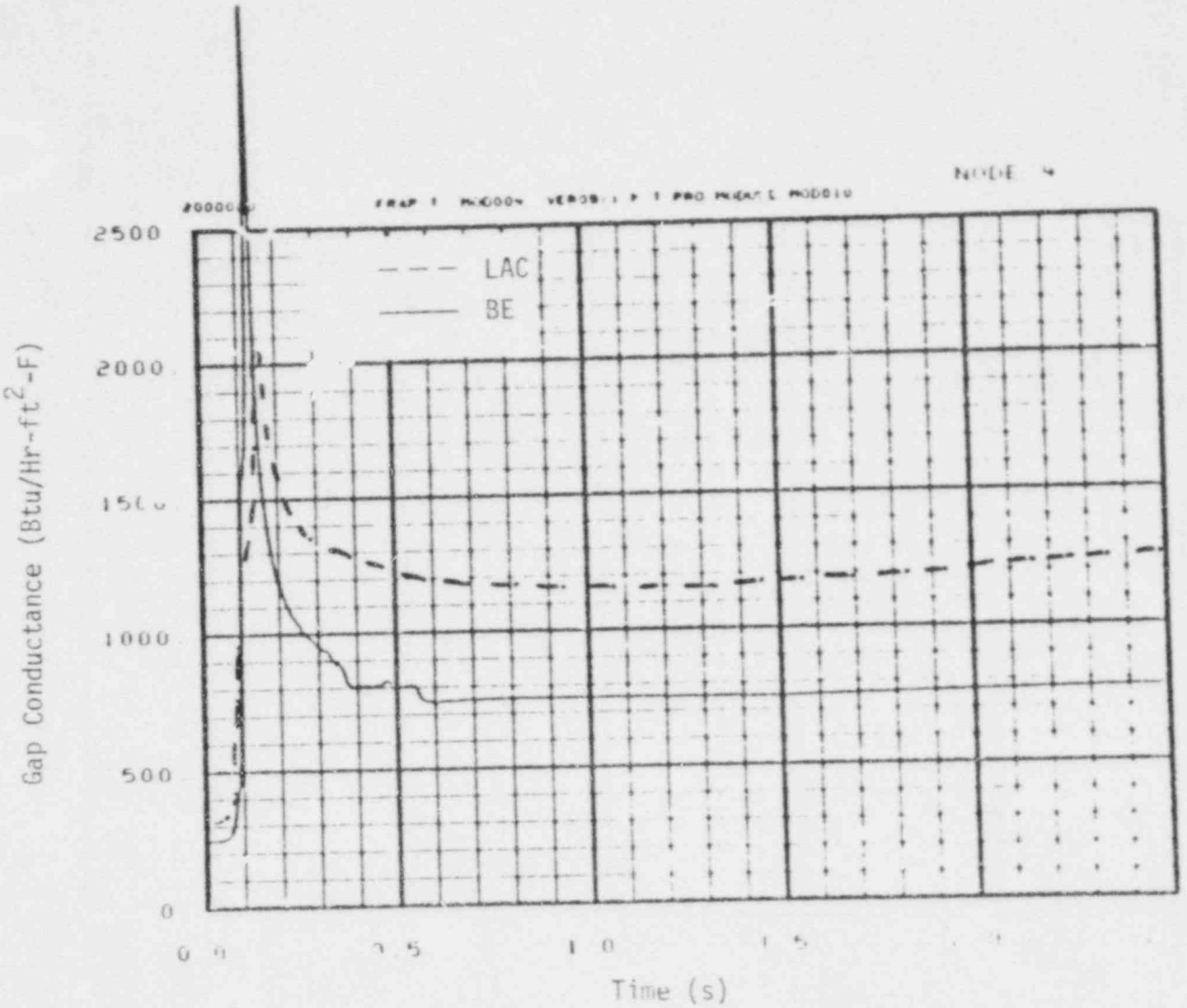

Fig. D-50 Gap conductance history (BWR RIA).

and BE calculated fuel centerline temperature histories are about the same. The LACE calculated peak cladding temperature is about 300°F higher than the BE calculated temperaure. This is due to the higher gap conductance predicted by LACE calculations after the power pulse has ended and the fuel and cladding are in contact. The gap conductance histories are plotted in Figure D-50.

9. Halden Test HPR-80

Plots of the calculated fuel centerline temperature versus fuel rod power for test rod HBC of the HPR-80 test are shown in Figure D-51. The fuel rod is not pressurized. At a peak linear rod power of 14.8 kW/ft, the LACE and BE calculated temperatures are virtually the same.

10. PWR End of Life Power Ramp

The LACE and BE calculated fuel centerline temperatures versus fuel rod power are plotted in Figure D-52 for an end of life PWR fuel rod. The fuel rod was assumed to have 875 days of burnup. The initial conditions were given by the FRAP-S3 code, which computed the fuel rod fission gas inventory, fuel swelling and densification, and cladding creep. These quantities were written to a FRAP-T4 restart tape.

As shown in Figure D-52, the LACE calculated fuel centerline temperature is greater than the BE for the complete range of power. The differences between the LACE and BE calculated temperatures decrease with an increase in fuel rod power. At a local fuel rod power of 10 kW/ft, the LACE and BE fuel centerline temperatures are 2430 and 2120°F, respectively. At a local fuel rod power of 14 kW/ft, the LACE and BE temperatures are 3220 and 3060°F, respectively.

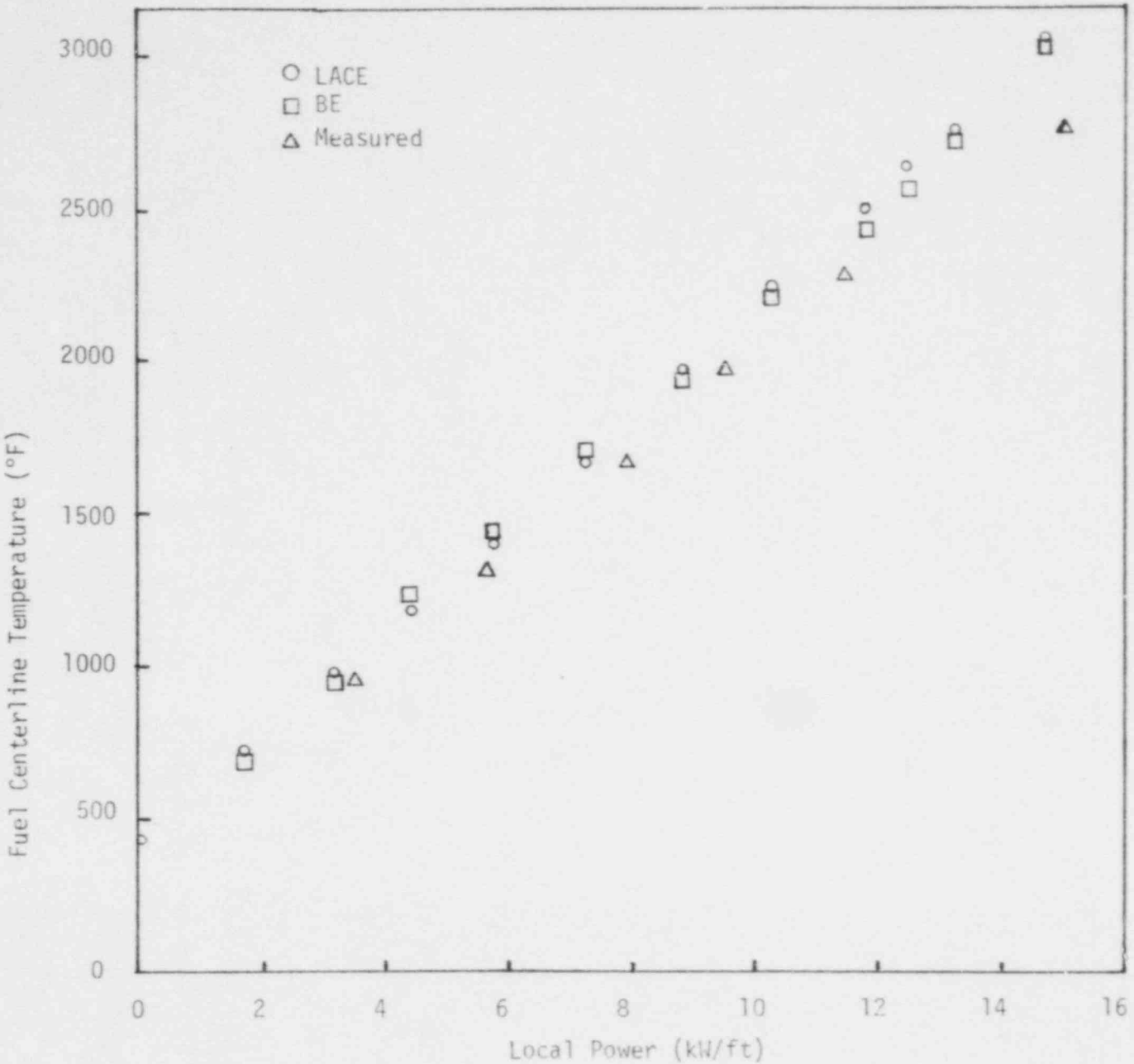

Fig. D-51 Fuel centerline temperature versus power (Halden Test HPR-80).

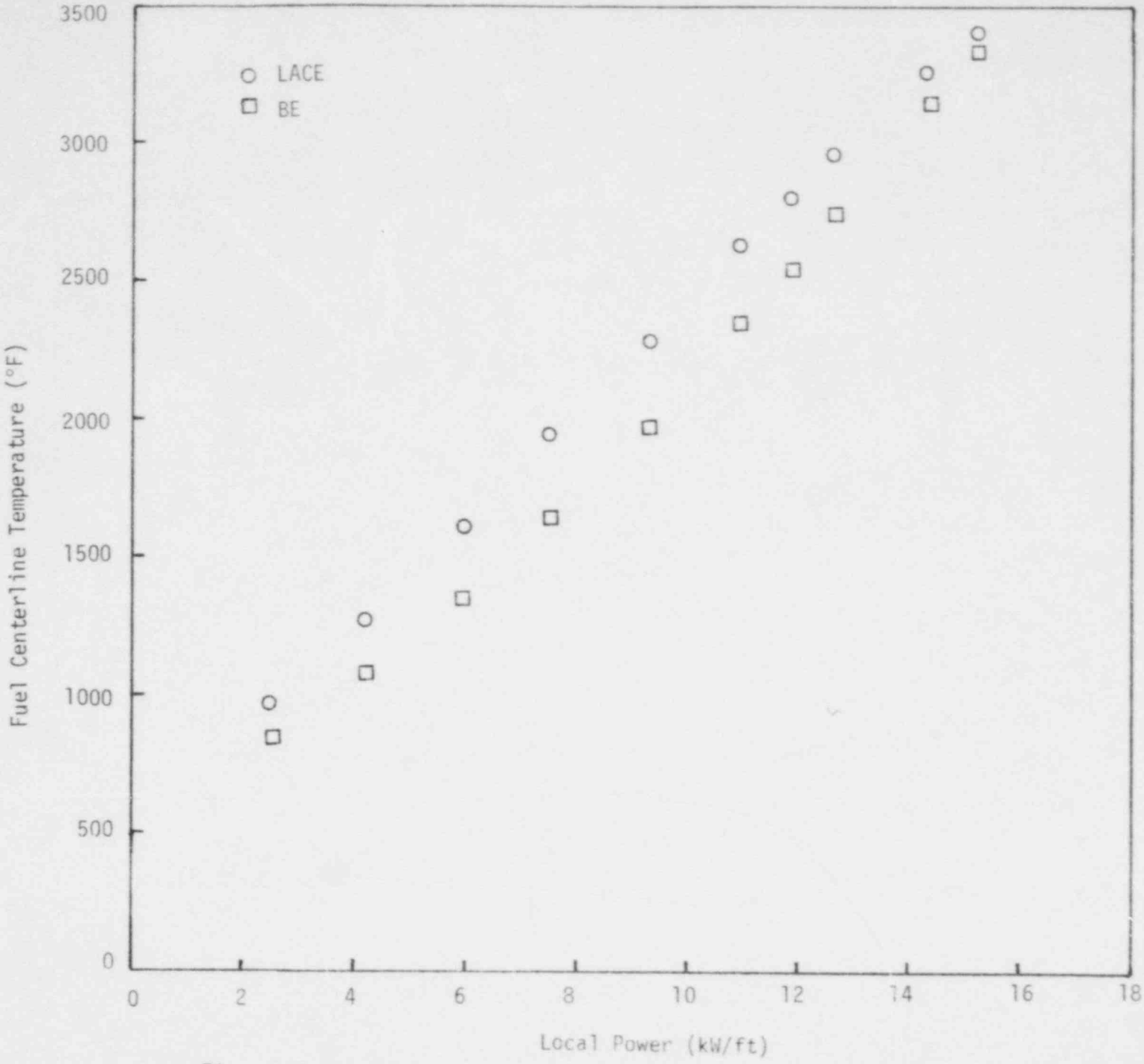

Fig. D-52 Fuel centerline temperature versus power (PWR EOL Power Ramp).